Institut für
Chemische und Thermische
Verfahrenstechnik ICTV

Sven Gutperl

Separation Performance Measurements in Distillation: Finite and Infinite Reflux Ratio Operation

ICTV – Schriftenreihe Band 55
Hrsg. Stephan Scholl und Wolfgang Augustin

Technische Universität Braunschweig

Bibliografische Information der Deutschen Nationalbibliothek
Die Deutsche Nationalbibliothek verzeichnet diese Publikation in der Deutschen Nationalbibliografie; detaillierte bibliografische Daten sind im Internet über http://dnb.dnb.de abrufbar.
1. Aufl. – Göttingen: Cuvillier, 2026
Zugl.: (TU) Braunschweig, Univ., Diss., 2024

Herausgeber:
Stephan Scholl, Wolfgang Augustin
ICTV – Institut für Chemische und Thermische Verfahrenstechnik
Langer Kamp 7
38106 Braunschweig
Telefon + 49 (0)531 391 2781
Telefax + 49 (0)531 391 2792
ictv@tu-braunschweig.de
www.ictv.tu-bs.de

CUVILLIER VERLAG GmbH, Göttingen 2026
Nonnenstieg 8, 37075 Göttingen
Telefon: 0551-54724-0
Telefax: 0551-54724-21
www.cuvillier.de

Diese Publikation wurde durch Mittel aus dem Publikationsfonds NiedersachsenOPEN unterstützt, der von zukunft.niedersachsen finanziert wird.

1. Auflage, 2026
Gedruckt auf umweltfreundlichem, säurefreiem Papier aus nachhaltiger Forstwirtschaft.

ISSN 1860-1316
eISSN 3053-8300
ISBN 978-3-68952-338-1
eISBN 978-3-68952-339-8
ORCID https://orcid.org/0000-0002-6301-873X
DOI https://doi.org/10.61061/ISBN_9783689523381

Separation Performance Measurements in Distillation: Finite and Infinite Reflux Ratio Operation

Von der Fakultät für Maschinenbau

der Technischen Universität Braunschweig

zur Erlangung der Würde

eines Doktor-Ingenieurs (Dr.-Ing.)

genehmigte Dissertation

von:	Sven Gutperl
geboren in:	Bad Hersfeld

eingereicht am:	16.07.2024
mündliche Prüfung am:	18.10.2024

Vorsitz:	Prof. Dr.-Ing. Rolf Radespiel
Gutachter:	Prof. Dr.-Ing. Stephan Scholl
Gutachter:	Prof. Dr.-Ing. Eugeny Kenig

2026

Abstract

Although separation performance for multistage distillation processes can be sufficiently predicted within a margin of $\pm 25\,\%$ for most industrial applications, deviations of up to $\pm 80\,\%$ occur in some cases. Such separation problems include foaming mixtures, mixtures with a high water content or systems with an elevated mixture viscosity. To systematically address elevated mixture viscosities in separation performance experiments, polymer-enhanced test mixtures need to be used to achieve liquid viscosities greater than $5 \ldots 6\,\mathrm{mPa\,s}$ at operating conditions. However, the plant setup conventionally used for separation performance measurements is not suitable for such mixtures, since a bottom product purge is required to prevent the accumulation of the non-volatile mixture component in the bottom section of the distillation column. This purge results in separation performance experiments with partial reflux operating conditions, which are rarely described in the literature.

Therefore, to systematically address separation performance at partial reflux operating conditions, an alternative plant setup similar to a stripping column was developed in this work. After commissioning and operational characterization, separation performance experiments with both total and partial reflux operating conditions were successfully conducted using the well-established test mixture chlorobenzene/ethylbenzene. Experiments were evaluated based on McCabe-Thiele stage constructions to determine the number of theoretical stages and express separation performance in terms of HETP. In addition, experimental results are compared to the separation performance predicted with the Delft mass transfer model.

Compared to total reflux experiments, the HETP values obtained for partial reflux are about 2.7 times increased, indicating a substantially reduced separation performance due to a smaller driving concentration potential which was not yet addressed in the literature. The effect of partial reflux is even more pronounced when predicting the separation performance using the Delft model. While experimental and predicted separation performances are in good agreement for total reflux experiments, the Delft model underestimates HETP values for partial reflux operating conditions by a factor of up to six. Although such an effect is generally assumed in the literature, since most mass transfer models have been developed and validated using results of total reflux experiments, the specific magnitude of the difference in separation performance caused by the reflux condition has not been systematically investigated before.

Kurzfassung

Obwohl die Trennleistung von Rektifikationsprozessen für die meisten industriellen Anwendungsfälle mit einer Genauigkeit von etwa $\pm 25\,\%$ hinreichend beschrieben werden kann, treten in manchen Fällen Abweichungen von bis zu $\pm 80\,\%$ auf. Solche Trennprobleme umfassen u.a. schäumende Stoffgemische, Stoffgemische mit einem erhöhten Wasseranteil oder Stoffgemische mit erhöhter Viskosität. Für systematische Untersuchungen der Rektifikation viskoser Systeme mit Gemischviskositäten von mehr als $5 \ldots 6\,\mathrm{mPa\,s}$ unter Rektifikationsbedingungen ist jedoch die Verwendung von polymer-haltigen Stoffgemischen erforderlich. Um dabei eine Akkumulation der nicht-verdampfenden Gemischkomponente im Kolonnensumpf zu vermeiden, ist eine Ausschleusung von Sumpfprodukt nötig, sodass die üblicherweise für Trennleistungsmessungen genutzten Anlagenaufbauten nicht eingesetzt werden können. Aus der Sumpfproduktausschleusung resultiert zudem ein Anlagenbetrieb mit partiellem Rücklauf, welcher in der Literatur bislang kaum beschrieben ist.

Zur systematischen Untersuchung des Einflusses von partiellem Rücklauf auf die Trennleistung wurde im Rahmen dieser Arbeit daher ein alternatives Anlagenkonzept in Anlehnung an eine Abtriebskolonne entwickelt. Nach Inbetriebnahme und Charakterisierung der Anlage wurden erfolgreich Trennleistungsmessungen mit dem etablierten Stoffsystem Chlorbenzol/Ethylbenzol sowohl unter vollständigem als auch unter partiellem Rücklauf durchgeführt. Die Auswertung der Experimente erfolgte mittels Stufenkonstruktionen, um die Anzahl der theoretischen Trennstufen zu bestimmen und anschließend die erzielte Trennleistung in Form von HETP-Werten auszudrücken. Darüber hinaus wurde die Trennleistung mithilfe des Delft-Modells vorausberechnet und mit den experimentellen Ergebnissen verglichen.

Bezogen auf die bei totalem Rücklauf erreichte Trennleistung ergeben sich für partiellen Rücklauf um den Faktor 2,7 erhöhte HETP-Werte, was eine stark reduzierte Trennleistung aufgrund kleinerer treibender Konzentrationsdifferenzen verdeutlicht und bislang kaum in der Literatur beschrieben ist. Der Einfluss partiellen Rücklaufs ist bei der Vorhersage von HETP-Werten mittels Delft-Modell noch deutlich stärker ausgeprägt. Zwar werden für totalen Rücklauf gute Vorhersagegenauigkeiten erzielt, jedoch unterschätzt das Delft-Modell die HETP-Werte bei partiellem Rücklauf um einen Faktor von bis zu sechs. Da die meisten Stoffübergangsmodelle nur für totalen Rücklauf entwickelt und validiert wurden, wurde ein solches Verhalten zwar bereits in der Literatur vermutet, die genaue Größenordnung der Abweichung zwischen experimentell ermittelter und vorausberechneter Trennleistung in Abhängigkeit des Rücklaufverhältnisses ist bislang aber nicht systematisch untersucht worden.

Preface and Acknowledgements

This dissertation was created during my time as a research assistant at the Institute for Chemical and Thermal Process Engineering of TU Braunschweig. The work is primarily based on the research project "Theoretical and experimental investigation of distillation of viscous systems in packed columns" funded by the German Research Foundation (DFG, grant: SCHO 842/12-3), but also addresses some questions raised during the project "Reduction of climate-relevant process emissions through an improved design of structured packing columns (ReProvAP)" funded by the Federal Ministry of Education and Research (BMBF, grant: 01LJ2002G).

First, I would like to thank my doctoral supervisor Prof. Dr.-Ing. Stephan Scholl and my research group leader Dr.-Ing. Katharina Jasch for their trust, the constant support, the great collaboration and the countless open-minded discussions. I would also like to thank Prof. Dr.-Ing. Eugeny Kenig for taking on the role of second reviewer and Prof. Dr.-Ing. Rolf Radespiel for chairing the examination board.

Since the research questions addressed in this work would probably have not been revealed without the aforementioned DFG project, I would also like to thank Christian Bradtmöller and my two reviewers for successfully acquiring the funding as well as for the open discussions and exchange of ideas during the research project. In this context, I would also like to thank the mechanical and electrical workshops at the institute for their support in realizing the plant concept proposed in this work. Thanks are also due to my colleagues Natalie Schwerdtfeger and Luca Jäger for debugging the plant control system and implementing several hotfixes during the experiments.

As listed in the appendix, I had the pleasure to supervise several students contributing to my research activities. It was a great experience to see how all of them contributed their individual approaches and ideas to answer the research questions. Nonetheless, special thanks are due to my former student and current colleague Martin Wolke, who did not only conduct most of the separation performance experiments of this work during his master's thesis and his subsequent research internship, but also contributed helpful improvements, ideas and discussions.

I thank my colleagues Katharina Jasch, Christoph Spiegel, Rolf Staud, David Appelhaus, Natalie Schwerdtfeger and Luca Jäger for several research and non-research related discussions and mastering the daily pitfalls at the institute, the university and the lectures together. In this context, I would also like to thank Prof. Dr.-Ing. Otto Carlowitz and Dr. Sven Meyer, who offered me an early behind-the-scenes look at everyday research activities at the Institute for Environmental Sciences of Clausthal University of Technology during my bachelor's thesis as well as my subsequent student job. Furthermore, thanks are due to Christian Bradtmöller,

Alina Uhlendorf, Prof. Dr.-Ing. Stephan Scholl and Prof. Dr.-Ing. Thomas Turek for their joint supervision of my master's thesis at the Institute of Chemical and Thermal Process Engineering, which can certainly be considered as the starting point of my research activities at TU Braunschweig.

Furthermore, I thank Holly Huellemeier, Katharina Jasch, David Appelhaus, Martin Wolke, Rolf Staud, Luca Jäger, Hannah Maul, Mauritio Müller, Caroline Otto and my dad for proof-reading and commenting the original manuscript. Last but not least, many thanks are also due to my parents and my uncle "Fitti" for awakening my curiosity for nature, science and technology as well as countless calm explanations about how things work.

Braunschweig, September 2025
Sven Gutperl

Contents

List of Symbols

Latin Symbols

symbol	unit	meaning
a	$\mathrm{m^2\,m^{-3}}$	specific surface area, specific interfacial area
A_{col}	$\mathrm{m^2}$	cross-sectional area of distillation column
$\dot{B}$	$\mathrm{kmol\,h^{-1}}$	molar flow rate of bottom product
c_{p}	$\mathrm{J\,kg^{-1}\,K^{-1}}$	specific heat capacity
c_i	-	sensitivity coefficient of uncertainty component i
d_{col}	m	column diameter
$d_{\mathrm{h,c,G}}$	m	hydraulic diameter of a gas flow channel (packing geometry)
d_{p}	m	diameter of packing element
D°_{ij}	$\mathrm{m^2\,s^{-1}}$	mutual diffusion coefficient for binary mixture with components i and j
D_{ij}	$\mathrm{m^2\,s^{-1}}$	corrected diffusion coefficient for binary mixture with components i and j
$\dot{D}$	$\mathrm{kmol\,h^{-1}}$	molar flow rate of distillate
f_{G}	$\mathrm{Pa^{0.5}}$	f-factor
$\dot{F}$	$\mathrm{kmol\,h^{-1}}$	molar flow rate of feed
$\dot{F}\,\dot{D}^{-1}$	$\mathrm{kmol_F\,kmol_D^{-1}}$	molar stream ratio
Fr	-	Froude number
g	$\mathrm{m\,s^{-2}}$	gravity of Earth ($g = 9.806\,65\,\mathrm{m\,s^{-2}}$)
$\dot{G}$	$\mathrm{kmol\,h^{-1}}$	molar flow rate of gas (in rectifying section)
$\dot{G}'$	$\mathrm{kmol\,h^{-1}}$	molar flow rate of gas (in stripping section)
h	m	height
h_i	$\mathrm{J\,kmol^{-1}}$, $\mathrm{J\,kg^{-1}}$	molar / specific enthalpy of component or mixture i

(continued)

symbol	unit	meaning
h_i'	$\mathrm{J\,kmol^{-1}}$, $\mathrm{J\,kg^{-1}}$	molar / specific enthalpy of component or mixture i (as boiling liquid)
h_i''	$\mathrm{J\,kmol^{-1}}$, $\mathrm{J\,kg^{-1}}$	molar / specific enthalpy of component or mixture i (as saturated vapor)
h_L	-	liquid hold-up
H_bed	m	height of packed bed
HETP	m	height equivalent to a theoretical plate
HTU	m	height of a transfer unit
i	-	iteration / summation variable
IQR	same as quartiles	interquartile range
j	-	iteration / summation variable
k	$\mathrm{m\,s^{-1}}$	mass transfer coefficient
k	-	index, iteration / summation variable
K_i	-	distribution coefficient of component i
l	m	length
$\dot{L}$	$\mathrm{kmol\,h^{-1}}$	molar flow rate of liquid (in rectifying section)
$\dot{L}'$	$\mathrm{kmol\,h^{-1}}$	molar flow rate of liquid (in stripping section)
m	-	slope of equilibrium line
m_i	kg	mass of i
$\dot{m}_i$	kg/h	mass flow rate of component or stream i
$\dot{m}_\mathrm{F}\,\dot{m}_\mathrm{D}^{-1}$	$\mathrm{kg_F\,kg_D^{-1}}$	stream ratio
M_i	$\mathrm{kg\,kmol^{-1}}$	molar mass of component or mixture i
n	-	index, iteration / summation variable, exponent
$\dot{n}$	$\mathrm{kmol\,h^{-1}}$	molar flow
N	-	number of data points, upper summation limit, number of replicates, number of (considered) equilibrium stages
N_c	-	number of mixture components
N_MC	-	number of samples used for Monte Carlo methods / simulations
N_p	-	number of packing elements

(continued)

symbol	unit	meaning
N_{th}	-	number of theoretical stages
$N_{\mathrm{th,dec}}$	-	number of theoretical stages (fractional stage considered)
NTSM	-	number of theoretical stages per meter
NTU	-	number of transfer units
p	bar(a), mbar(a), Pa	pressure
p_i	Pa	partial pressure of component i
p_i^0	Pa	vapor pressure of component i
$p_i^{(j)}$	Pa	partial pressure of component i in phase j
q	-	feed condition
$Q_i(\cdot)$	same as $\cdot$	i-th quartile of $\cdot$ (Q_1: 25 %, Q_2: 50 %, Q_3: 75 %)
R	$\mathrm{kJ\,kmol^{-1}\,K^{-1}}$	universal gas constant ($R = 8.314\,\mathrm{kJ\,kmol^{-1}\,K^{-1}}$)
$\dot{R}$	$\mathrm{kmol\,h^{-1}}$	molar flow rate of reflux
Re	-	Reynolds number
$s(\cdot)$	same as $\cdot$	standard deviation of $\cdot$
s_{c}	m	channel side length (packing geometry)
S_{MC}	%	success ratio of Monte Carlo methods / simulations
$\dot{S}$	$\mathrm{kmol\,h^{-1}}$	molar flow rate of side stream
Sc	-	Schmidt number
Sh	-	Sherwood number
T	K	temperature
$T_i^{(j)}$	K	temperature of component i in phase j
u	$\mathrm{m\,s^{-1}}$	flow velocity
$u(\cdot)$	same as $\cdot$	standard uncertainty of $\cdot$
$u_{\mathrm{c}}(\cdot)$	same as $\cdot$	combined standard uncertainty of $\cdot$
u_{A}	same as measurand	type A standard uncertainty
u_{B}	same as measurand	type B standard uncertainty
$U(\cdot)$	same as $\cdot$	expanded uncertainty of $\cdot$
V	$\mathrm{cm^3\,mol^{-1}}$	(molar) volume
$\dot{V}_i$	$\mathrm{m^3\,h^{-1}}$	volumetric flow rate of component or stream i

(continued)

symbol	unit	meaning
w_i	$\mathrm{kg_i\,kg_{tot}^{-1}}$	mass fraction of component i
w_L	$\mathrm{m^3\,m^{-2}\,h^{-1}}$	liquid load
w_c	m	width of packing channel
We	-	Weber number
x_i	depends on measurand	i-th measurand / input (uncertainty quantification)
x_i	$\mathrm{kmol_i\,kmol_{tot}^{-1}}$	liquid phase molar fraction of component i, liquid phase molar fraction of more volatile component in stream i
x_n	$\mathrm{kmol_i\,kmol_{tot}^{-1}}$	liquid phase molar fraction of more volatile component on stage n
$\overline{x}$	same as x	arithmetic average of x
y_i	$\mathrm{kmol_i\,kmol_{tot}^{-1}}$	vapor phase molar fraction of component i, vapor phase molar fraction of more volatile component in stream i
y_n	$\mathrm{kmol_i\,kmol_{tot}^{-1}}$	vapor phase molar fraction of more volatile component on stage n

Greek Symbols

symbol	unit	meaning
α_{ij}	-	nonrandomness parameter in NRTL model
α_{L}	$^\circ$	effective liquid flow angle
α_{p}	$^\circ$	angle of inclination (packing geometry)
α_{12}	-	relative volatility of binary mixture
$\tan\beta$	-	slope
γ_i	-	activity coefficient of component i
δ	%	relative deviation
δ_{L}	m	thickness of liquid film
δ_{p}	m	sheet thickness of corrugated sheet packings
Δg_{ij}	K	interaction energy parameter in NRTL model
Δh_{vap}	$\mathrm{J\,kmol^{-1}}$, $\mathrm{J\,kg^{-1}}$	specific / molar enthalpy of vaporization
Δp	mbar	differential pressure
Δp_{bed}	$\mathrm{mbar\,m^{-1}}$	specific pressure drop
ΔT_{F}	K	feed subcooling
Δx	$\mathrm{kmol_i\,kmol_{tot}^{-1}}$	gradient / difference of molar fractions in liquid phase (driving concentration potential)
Δy	$\mathrm{kmol_i\,kmol_{tot}^{-1}}$	gradient / difference of molar fractions in vapor phase (driving concentration potential)
ε	depends on measurand	absolute deviation
ε_{p}	-	void fraction (packing geometry)
η	Pa s, mPa s	dynamic viscosity
ϑ	$^\circ$C	temperature
$\vartheta_{\mathrm{tr,col}}$	$^\circ$C	setpoint temperature of trace heating column
$\vartheta_{\mathrm{tr,h}}$	$^\circ$C	setpoint temperature of trace heating column head
λ	-	stripping factor
$\mu_i^{(j)}$	$\mathrm{J\,mol^{-1}}$	chemical potential of component i in phase j
ν	-	(external) reflux ratio
ν'	-	reboil ratio, stripping ratio
ξ_{GL}	-	gas/liquid friction factor

(continued)

symbol	unit	meaning
π	-	mathematical constant π
ρ	$\mathrm{kg\,m^{-3}}$, $\mathrm{g\,cm^{-3}}$	density
σ	$\mathrm{N\,m^{-1}}$	surface tension
ϕ_i	-	dimensionless association factor of component i
φ_i	-	fugacity coefficient of component i
$\varphi_{\mathrm{c,L}}$	-	fraction of cross-sectional area occupied by liquid film
Ω_{p}	-	fraction of surface area occupied by holes (packing geometry)

Subscripts

subscript	meaning
0	x-intercept (x_0), y-intercept (y_0)
1	mixture component 1, equilibrium stage 1
2	mixture component 2, equilibrium stage 2
3	mixture component 3, equilibrium stage 3
4	equilibrium stage 4
12	binary mixture with components 1 and 2
A	at position A
b	below packed bed
B	bottom product, at position B
boil	boiling
c	packing channel, critical
CB	chlorobenzene
D	distillate
Delft	calculated based on Delft model
drv	driving
EB	ethylbenzene
eff	effective
exp	experiment, experimental
F	feed
G	gas, vapor
h	column head, above packed bed
i	mixture component i, iteration / summation variable
ij	binary mixture with components i and j
integration	calculated based on integration
is	intersection (between feed line and operating lines)
j	mixture component j, iteration / summation variable
k	iteration / summation variable
L	liquid
lam	laminar

(continued)

subscript	meaning
m	molar
max	maximum
mb	at mid-bed position
meas	measured
min	minimum
mix	mixture
n	stage n, iteration / summation variable
nom	nominal
oG	overall gas phase
oL	overall liquid phase
Onda	calculated with Onda correlation
original	calculated with original mass transfer correlation (Delft model)
p	packing element
pred	predicted
ref	reference
rel	relative
revised	calculated with revised mass transfer correlation (Delft model)
s	superficial
sep	separation
stages	calculated based on McCabe-Thiele stage constructions
success	successful
tot	total
turb	turbulent
vap	vaporization

Superscripts

superscript	meaning
(1)	phase 1
(2)	phase 2
(3)	phase 3
(j)	phase j
b	bulk
E	excess
eq	equilibrium
i	interface
op	operating

List of Abbreviations

abbreviation	meaning
abs	absolute
BIPM	International Bureau of Weights and Measures (Bureau International des Poids et Mesures)
C6	cyclohexane
C7	n-heptane
CB	chlorobenzene
CC	CHEMCAD
CH	cyclohexanol
CLI	command-line interface
CP	cyclopentanol
CPU	central processing unit
DC	direct current
DDBST	Dortmund Data Bank Software and Separation Technology
dif	differential
DIPPR	Design Institute for Physical Properties
EB	ethylbenzene
EoS	equation of state
FL	feed line, q-line
FRI	Fractionation Research Inc.
FUG	Fenske-Underwood-Gilliland (shortcut method)
FUGK	Fenske-Underwood-Gilliland-Kirkbride (shortcut method)
GUM	Guide to the expression of uncertainty in measurement
HDF	Hierarchical Data Format (a binary file format used to store structured experiment data)
HETP	height equivalent to a theoretical plate

(continued)

abbreviation	meaning
HTU	height of a transfer unit
Ipopt	interior point optimizer (a solver for non-linear optimization problems)
JCGM	Joint Committee for Guides in Metrology
JuMP	Julia for Mathematical Programming (a modeling language for the Julia programming language to solve optimization problems)
lit	literature
LPU	law of propagation of uncertainty
MCM	Monte Carlo method, Monte Carlo experiments
MES	material, equilibrium and summation equations
MESH	material, equilibrium, summation and enthalpy equations
MWR	minimum wetting range
NCBI	National Center for Biotechnology Information
NIST	National Institute of Standards and Technology
NRTL	non-random two-liquid model
NTSM	number of theoretical stages per meter
NTU	number of transfer units
ODR	orthogonal distance regression
PBD	polybutadiene
PDF	probability density function
PVP	polyvinylpyrrolidone
ROL	rectifiying section operating line, enrichment line, top operating line
RTD	resistance temperature detector, resistance thermometer
SOL	stripping section operating line, stripping line, bottom operating line
SRP	Separations Research Program
SSR	sum of squared residuals
TC	thermocouple
UNIQUAC	universal quasichemical
UQ	uncertainty quantification
VLE	vapor-liquid equilibrium

(continued)

abbreviation	meaning
YAML	YAML Ain't Markup Language, Yet Another Markup Language (a human-readable data format used for configuration files)

List of Figures

List of Tables

List of Listings

1. Introduction

Distillation, also known as rectification, multistage or fractional distillation, is one of the most essential and widespread unit operations in the chemical process industry (Beneke et al., 2013; Billet, 1979; Fair, 2001; Kister, 1992; Mix et al., 1978; Moran, 2017; Stichlmair et al., 2021; Weiß, 1996). The underlying mechanism of distillation, separating a (binary) homogeneous liquid mixture based on its relative volatility, dates back to around 1200 BCE in ancient Mesopotamia where archaeological findings show simple distillation setups for perfume production (Levey, 1955). Detailed descriptions and illustrations of early distillation setups were presented by e.g. (Fairley, 1907; Kockmann, 2014). Throughout history, the best known application of a distillation process is presumably the alcohol enrichment of beverages. Distillation stills comparable to modern setups were developed in the early 19th century: A continuously operated distillation apparatus based on a vertical column was proposed in 1813. Mass transfer enhancing *column internals* like *packings* or *trays* were firstly used in 1820 and 1822, respectively (Kister, 1992).

Several generations of improved structured packings have been developed since the late 1950s, resulting in increased separation capacities and reduced costs which has led to the widespread application of structured packings in both absorption and distillation processes (Mendes, 2011; Spiegel and Meier, 2003). A mature understanding of the underlying mass and heat transfer phenomena as well as improved mass transfer correlations was developed in the last decades. According to (Schultes, 2013), the established models predict the separation performance for up to 90 % of the relevant industrial processes with an error margin of around 25 %, but deviations of up to 80 % are observed for the remaining applications. In the latter cases, column design needs to be supported with experimental separation performance investigations.

Such separation performance experiments are commonly carried out with standardized binary test mixtures under total reflux operating conditions and are widely discussed in the known literature. Despite its widespread use in industrial and academic settings, the conventional total reflux setup is not suitable for some specific use cases. As discussed by (Böcker and Ronge, 2005; Bradtmöller, 2017; Gutperl et al., 2022), it cannot be used for test mixtures with inert or non-volatile components which are, however, required to systematically investigate the separation of viscous mixtures with viscosities greater than $5 \ldots 6\,\mathrm{mPa\,s}$ at operating conditions (Böcker and Ronge, 2005; Bradtmöller, 2017; Bradtmöller and Scholl, 2016; Manivannan et al., 2019). Furthermore, total reflux conditions do not represent the conditions present in production columns which require product draws and are thus operated with finite reflux ratios.

This work, therefore, focuses on an alternative methodology suitable for separation perfor-

mance experiments with both finite and infinite reflux operating conditions. The developed plant setup is derived from the approach presented by (Böcker and Ronge, 2005) and is similar to a stripping column, inasmuch as product recycles are used to reduce the required amount of feedstock, and the feed inlet is located above the packed bed. After successful plant commissioning and characterization, the effect of reflux operating condition on separation performance was systematically investigated using the proposed experimental approach.

To support method development and experiment evaluation, relevant fundamentals of multistage distillation and separation performance measurements with total and partial reflux are summarized in chapter 2. As separation performance is commonly expressed in terms of the *height equivalent to a theoretical plate (HETP)* or the *height of a transfer unit (HTU)*, a link between both concepts is presented to point out the characteristics specific to each approach and to provide some background information addressing the question *Which measure should be preferred over the other?*. Furthermore, best practices and recommendations for designing and operating distillation plants for separation performance measurements are covered, since such information is required to ensure a robust plant design and operation. Use cases for which separation performance measurements at partial reflux are relevant are introduced in chapter 3 to not only highlight the necessity of such experiments, but also to derive the research hypotheses and objectives of this work. In addition, the developed plant concept, the corresponding plant setup and the experimental procedures used for the separation performance experiments, sample analyses and experiment evaluation are presented in detail. In particular, separation performance is evaluated in terms of HETP values, which are calculated based on the number of theoretical stages determined from *McCabe-Thiele stage constructions* and predicted with the *Delft mass transfer model*. Experimental and predicted results are compared to each other to address the applicability of the Delft model with respect to partial reflux experiments. A consistent propagation of relevant uncertainties allows assessing the robustness of the experimental results. Therefore, all calculation routines were implemented in and fully automated using the *Python* programming language. The results obtained from plant characterization and separation performance experiments with total and partial reflux operating conditions are discussed in chapter 4. As partial reflux experiments are commonly considered less sound than total reflux experiments, special attention is paid to the uncertainty components related to the reflux condition. Furthermore, the proposed plant concept, experimental setup and corresponding experimental procedures are evaluated based on the obtained experimental results to not only identify potential improvements increasing the applicability and usability of the presented methodology, but also highlight future research activities enabled by separation performance measurements with partial reflux.

2. Theoretical Background and Literature Review

2.1. Distillation and Separation Fundamentals

2.1.1. Equilibrium Thermodynamics

Mixture separation of binary mixtures is primarily based on the differing *distribution coefficients* K_i of each mixture component (Sorensen, 2014). The distribution coefficient, also abbreviated as the *K-value*, of a given mixture component i depends on both temperature and pressure and is defined as (Kister, 1992; Sorensen, 2014):

$$K_i = \frac{\text{molar fraction of component } i \text{ in vapor phase}}{\text{molar fraction of component } i \text{ in liquid phase}} = \frac{y_i}{x_i} \tag{2.1}$$

A high K-value indicates a high volatility, or tendency of the component to vaporize and accumulate in the vapor phase, whereas less volatile components show lower K-values. For a binary mixture containing components 1 and 2, its relative volatility α_{12} is defined as (Kister, 1992):

$$\alpha_{12} = \frac{K_1}{K_2} = \frac{y_1 \cdot x_1^{-1}}{y_2 \cdot x_2^{-1}} = \frac{y_1 \cdot x_2}{y_2 \cdot x_1} = \frac{y_1 \cdot (1 - x_1)}{x_1 \cdot (1 - y_1)} \tag{2.2}$$

Equation (2.2) can be rearranged to express the *vapor-liquid-equilibrium (VLE)*, so that y_1 is calculated in terms of x_1 and α_{12} (Kister, 1992; Sorensen, 2014):

$$y_1 = \frac{\alpha_{12} \cdot x_1}{1 + (\alpha_{12} - 1) \cdot x_1} \tag{2.3}$$

This expression is often used in conjunction with *xy-diagrams*, which are also known as *equilibrium diagrams* and are especially relevant for *McCabe-Thiele stage constructions*, see section 2.2.1.2. As shown in figure 2.1, higher relative volatilities result in more convex equilibrium curves with higher molar fractions present in the vapor phase than lower relative volatilities. Therefore, binary mixtures with a high relative volatility require less separation effort to obtain pure components than binary mixtures with low volatility (Kister, 1992).

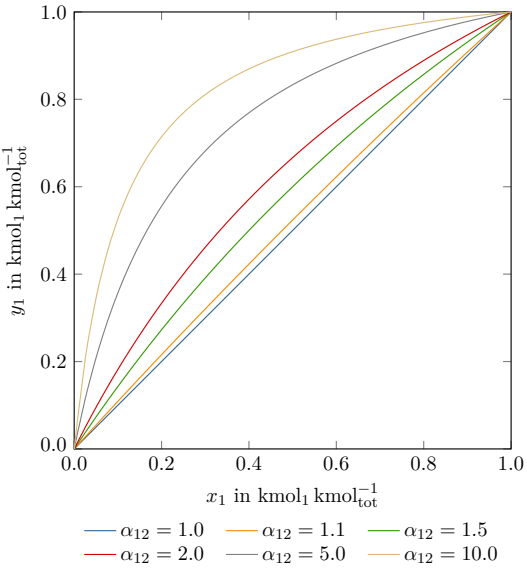

Figure 2.1.: Equilibrium curve in dependence of relative volatility α_{12}, calculated according to equation (2.3)

However, for most mixtures, the relative volatility α_{12} varies with mixture composition and temperature. To describe this behavior, different approximations have been established; a detailed discussion can be found in e.g. (Kister, 1992). A simple approximation is based on the geometrically averaged relative volatility $\overline{\alpha}_{12}$ as given in equation (2.4) (King, 1980). $\alpha_{12,\mathrm{I}}$ and $\alpha_{12,\mathrm{II}}$ represent the relative volatilities at minimum as well as maximum mixture composition and an arithmetically averaged mixture temperature (King, 1980).

$$\overline{\alpha}_{12} = \sqrt{\alpha_{12,\mathrm{I}} \cdot \alpha_{12,\mathrm{II}}} \tag{2.4}$$

The liquid phase is generally described by *Raoult's law* which defines a relation between the partial pressure p_i of component i, its vapor pressure p_i^0 and its molar fraction x_i. Deviations from ideal behavior ($\gamma_i = 1$) are described by the activity coefficient γ_i which is a function of temperature T and liquid phase composition x_i (Kleiber, 2020; Sorensen, 2014):

$$p_i = x_i \cdot p_i^0 \cdot \gamma_i(T, x_i) \tag{2.5}$$

For the vapor phase, *Dalton's law* provides a relation between partial pressure p_i, molar fraction in vapor phase y_i and the total pressure p_{tot}:

$$p_i = y_i \cdot p_{\mathrm{tot}} \tag{2.6}$$

Similar to activity coefficients, nonidealities of the vapor phase can be expressed by fugacity coefficients φ_i. According to (Sorensen, 2014) nonidealities become relevant at elevated operating pressures of $p \geq 7 \ldots 10\,\mathrm{bar(a)}$. Since all experiments presented in this work were conducted with $p = 100\,\mathrm{mbar(a)}$ an ideal vapor phase can be assumed, and thus fugacity coefficients are not considered.

Inserting equations (2.5) and (2.6) into equation (2.2) expresses the relative volatility as a function of activity coefficients γ_i and vapor pressures p_i^0 (Kister, 1992; Sorensen, 2014):

$$\alpha_{12} = \frac{\gamma_1(T, x_1) \cdot p_1^0}{\gamma_2(T, x_2) \cdot p_2^0} \tag{2.7}$$

The activity coefficients needed to describe nonideal mixture behavior are commonly estimated by using either g^E *models* or *equations of state (EoS)*[1].

g^E models are based on the relation between the excess Gibbs energy g^E and activity coefficient γ_i (Gmehling and Kleiber, 2014):

$$g^\mathrm{E} = \sum_i x_i \cdot g_i^\mathrm{E} = R\,T \sum_i x_i \cdot \ln \gamma_i \Longleftrightarrow \ln \gamma_i = \frac{g_i^\mathrm{E}}{R\,T} \tag{2.8}$$

For a pure liquid, the excess Gibbs energy g^E needs to satisfy the following condition (Gmehling et al., 2019):

$$g^\mathrm{E}(x_i = 1) \to 0. \tag{2.9}$$

For a binary liquid mixture with components 1 and 2, the *Porter equation* given in equation (2.10) fulfills this requirement. It is often considered as the simplest *activity coefficient model*, because it contains only a single model parameter A:

$$\frac{g^\mathrm{E}}{R\,T} = A\,x_1\,x_2 \tag{2.10}$$

Due to its simplicity, the Porter equation can only be applied to a very limited number of nonideal liquid mixtures, and thus more versatile approaches are required (Gmehling et al., 2019). A general algebraic approach to describe nonideal binary mixtures using series expansion was proposed by (Redlich and Kister, 1948a):

$$\frac{g^\mathrm{E}}{R\,T} = x_1\,x_2\,\left[A + B\,(x_1 - x_2) + C\,(x_1 - x_2)^2 + \ldots\right] \tag{2.11}$$

Despite the versatility of equation (2.11), this approach is only applicable to binary mixtures and the influence of temperature on the activity coefficient is neglected (Gmehling et al., 2019). Therefore, improved activity coefficient models, such as the *Wilson equation* (Wilson, 1964), the

[1] EoS are not in scope of this work, and thus not elaborated further. Refer to e.g. (Gmehling and Kleiber, 2014; Gmehling et al., 2019; Kleiber, 2020; Stichlmair et al., 2021) for details on EoS.

NRTL model (Non-random two-liquid model) (Renon and Prausnitz, 1968) and the *UNIQUAC approach (universal quasichemical)* (Abrams and Prausnitz, 1975), are commonly used today. These models contain additional parameters which consider local concentrations around mixture molecules and allow for an improved description of mixture nonidealities.

2.1.2. Continuous Distillation

Continuous multistage distillation operates under countercurrent flow conditions and can be illustrated as a cascade of multiple *equilibrium stages*, see figure 2.2 (Vogelpohl, 2021).

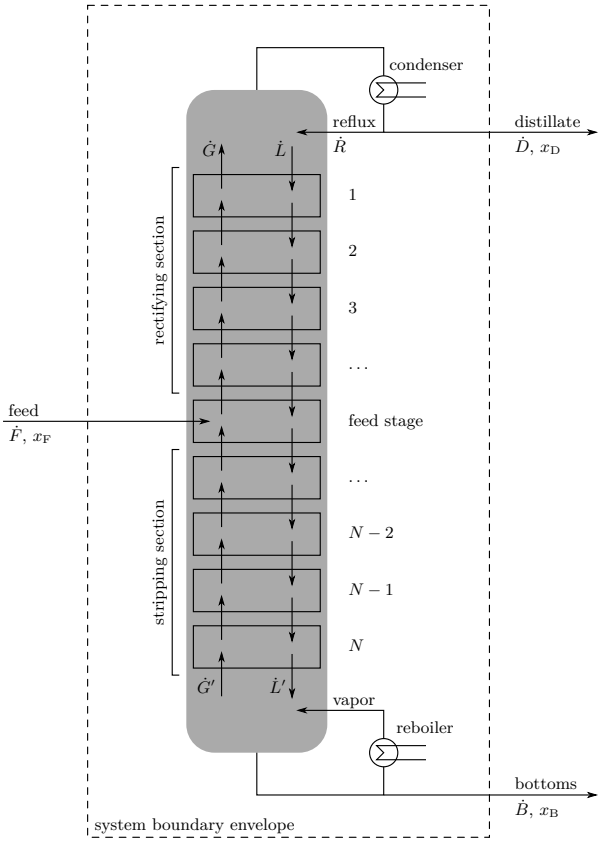

Figure 2.2.: Multistage distillation represented as a cascade of equilibrium stages, based on (Kister, 1992; Sorensen, 2014; Stichlmair et al., 2021; Vogelpohl, 2021)

According to (Kister, 1992), each equilibrium stage operates in steady state resulting in

constant vapor and liquid output streams. Since input streams are assumed being perfectly mixed after entering the stage, equilibrium between the vapor and liquid output streams is achieved instantaneously (Kister, 1992). The separation is accomplished by feeding vapor from the reboiler to the bottom stage[2] N. As liquid from stage N comes into contact with the vapor, partial condensation occurs. As a result, some liquid is vaporized due to the released heat of condensation, whereby volatile mixture components are enriched in the vapor. This condensation and vaporization continues throughout every stage, resulting in a purified vapor stream leaving the top stage. The overhead vapor is then (partially) condensed and either drawn from the system as the *distillate* or returned to the top stage as the *reflux*. Since the reflux trickles down inside the column, it also provides liquid in each stage. Liquid leaving the bottom stage is either drawn from the system as the *bottom product*, also referred to as *bottoms*, or returned to the reboiler.

Using the system boundary drawn in figure 2.2 and assuming a steady-state operation, such that there is no accumulation inside the system boundary, the *molar balance of a continuous distillation* can be written as:

$$\dot{F} = \dot{D} + \dot{B} \tag{2.12}$$

Furthermore, the *reflux ratio* ν is defined based on the molar flow of reflux $\dot{R}$ and distillate $\dot{D}$ as shown in equation (2.13) (Kister, 1992; Sorensen, 2014). For a boiling liquid reflux, the reflux ratio can also be expressed with the internal liquid stream $\dot{L}$, since $\dot{R} = \dot{L}$ (Schönbucher, 2002):

$$\nu = \frac{\dot{R}}{\dot{D}} = \frac{\dot{L}}{\dot{D}} \tag{2.13}$$

Equation (2.13) is also referred to as the *external reflux ratio* and takes values of $\nu > 0$ (Sorensen, 2014). Alternatively, the *internal reflux ratio* ν_{int} with values of $0 \leq \nu_{\text{int}} \leq 1$ is described as (Sorensen, 2014):

$$\nu_{\text{int}} = \frac{\dot{L}}{\dot{G}} \tag{2.14}$$

Similarly, the *reboil ratio* ν', also known as the *stripping ratio*, is given based on the molar flow of vapor $\dot{G}'$ and the bottoms $\dot{B}$ (Kister, 1992; Sorensen, 2014):

$$\nu' = \frac{\dot{G}'}{\dot{B}} \tag{2.15}$$

[2]Throughout this work, stages are numbered from top to bottom (stage 1 at the top and stage N at the bottom of the column) which is in accordance with e.g. (Kister, 1992; McCabe and Thiele, 1925; Sorensen, 2014). However, numbering from bottom to top is also possible and can be found in e.g. (Kleiber, 2020; Stichlmair et al., 2021). Furthermore, indices referring to a stage number indicate the stage where the designated flow originates. For example, $\dot{L}_4$ denotes the molar liquid flow leaving stage 4 and entering stage 5, whereas $\dot{G}_4$ is the molar vapor flow from stage 4 into stage 3.

Special attention should be focused on the feed stage. As shown in figure 2.2, stages above the feed stage are called the *rectifying section*, while stages below the feed stage belong to the *stripping section*. Furthermore, internal molar vapor flows $\dot{G}'$ and $\dot{G}$ as well as liquid flows $\dot{L}'$ and $\dot{L}$ depend on the *feed condition* q, which results in $\dot{G}' \neq \dot{G}$ or $\dot{L}' \neq \dot{L}$ for most cases. The feed condition is defined by the molar enthalpy at the bubble point h'_{F}, the molar enthalpy as saturated vapor h''_{F}, the molar enthalpy at feed condition h_{F} and the molar enthalpy of vaporization $\Delta h_{\mathrm{vap,F}}$ (Billet, 1979):

$$q = 1 + \frac{h'_{\mathrm{F}} - h_{\mathrm{F}}}{\Delta h_{\mathrm{vap,F}}} = 1 + \frac{h'_{\mathrm{F}} - h_{\mathrm{F}}}{h''_{\mathrm{F}} - h'_{\mathrm{F}}} \tag{2.16}$$

General trends for the resulting flows of vapor $\dot{G}'$ and $\dot{G}$ as well as liquid $\dot{L}'$ and $\dot{L}$ are summarized in table 2.1.

Table 2.1.: Feed conditions, based on (Billet, 1979; Sorensen, 2014; Stichlmair et al., 2021)

feed condition	h_{F}	q	vapor streams	liquid streams
subcooled liquid	$h_{\mathrm{F}} < h'_{\mathrm{F}}$	$q > 1$	$\dot{G}' > \dot{G}$	$\dot{L}' > \dot{L}$
boiling liquid	$h_{\mathrm{F}} = h'_{\mathrm{F}}$	$q = 1$	$\dot{G}' = \dot{G}$	$\dot{L}' > \dot{L}$
wet vapor	$h'_{\mathrm{F}} < h_{\mathrm{F}} < h''_{\mathrm{F}}$	$0 < q < 1$	$\dot{G}' < \dot{G}$	$\dot{L}' > \dot{L}$
saturated vapor	$h_{\mathrm{F}} = h''_{\mathrm{F}}$	$q = 0$	$\dot{G}' < \dot{G}$	$\dot{L}' = \dot{L}$
superheated vapor	$h_{\mathrm{F}} > h''_{\mathrm{F}}$	$q < 0$	$\dot{G}' < \dot{G}$	$\dot{L}' < \dot{L}$

2.1.3. Multistage Distillation Apparatus

Multistage distillation is commonly performed in *distillation columns*. Since instantaneous equilibrium can only be reached in theory, phase contact between vapor and liquid streams inside the column needs to be intensified for which different types of *mass transfer equipment*, *column internals* and accessory devices were developed in the past. While *trays*, *unstructured packings* and *structured packings* are the most common types of mass transfer equipment used for multistage distillation, this work focuses on structured packings only. Equipment design and selection varies based on several factors such as feedstock properties, product specification, operating conditions and process complexity, process efficiency, capacity and throughput, capital expenses and operating costs as well as in-house expertise (Kister, 1992; Olujić, 2014). Detailed discussions and comparisons of widely used mass transfer equipment as well as column internals and accessories can be found in e.g. (Billet, 1979; Billet, 1995; Górak and Olujić, 2014; Kister, 1992).

To ensure efficient column operation with respect to its capacity and an optimal mixture separation, the *gas load* $u_{\mathrm{G,s}}$ and *liquid load* w_{L} need to be considered. The gas load is defined as a superficial gas velocity $u_{\mathrm{G,s}}$, and thus based on the volumetric vapor or gas flow rate $\dot{V}_{\mathrm{G}}$

and the cross-sectional area of the (unpacked) column A_{col}:

$$u_{\mathrm{G,s}} = \frac{\dot{V}_{\mathrm{G}}}{A_{\mathrm{col}}} \tag{2.17}$$

Alternatively, gas load can be expressed in terms of the f-factor f_{G} based on superficial gas velocity $u_{\mathrm{G,s}}$ and gas density ρ_{G}:

$$f_{\mathrm{G}} = u_{\mathrm{G,s}} \cdot \rho_{\mathrm{G}}^{0,5} \tag{2.18}$$

Similar to equation (2.17), the liquid load w_{L} is defined using the volumetric liquid flow rate $\dot{V}_{\mathrm{L}}$:

$$w_{\mathrm{L}} = \frac{\dot{V}_{\mathrm{L}}}{A_{\mathrm{col}}} \tag{2.19}$$

These loads depend on the column configuration and operation, and thus can vary along the column height. In such cases, representative column sections should be considered. The valid operating range for a given type of structured packings can be described based on the *load diagram* (Kleiber, 2020):

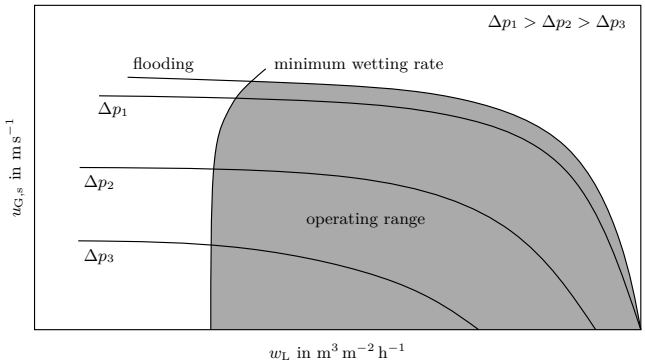

Figure 2.3.: Load diagram for structured packings, based on (Kleiber, 2020; Molzahn and Schmidt, 1975; Stichlmair et al., 2021)

The lower limit of the operating region is defined by the *minimum liquid load* (Kleiber, 2020; Sattler, 2001) or *minimum wetting rate (MWR)* where the packing surface is not wetted sufficiently and *underwetting* occurs (Kister, 1992). This results in a small effective mass transfer area, and thus a poor separation efficiency. In contrast, at high liquid or gas loads, entrainment increases successively, resulting in *flooding* or *phase inversion* which is considered the upper boundary of the operating region (Billet, 1995; Kister, 1992; Sattler, 2001).

Depending on liquid load w_{L} and gas load $u_{\mathrm{G,s}}$, the following operating regimes can commonly

be identified for structured packings (Kister, 1992):

- Turndown maldistribution regime: At low column load, separation efficiency is reduced due to the turndown limit of the packing and/or the liquid distributor. If proper liquid distribution is ensured, the upper boundary of this region represents the MWR of the packing.
- Preloading regime: Separation efficiency is constant and independent of column load due to a turbulent liquid film, good surface wetting and a good mass transfer. Most columns are designed to operate within this region.
- Loading regime: The column transitions from normal to flooded operation. As the liquid holdup increases, the separation efficiency reaches its maximum and drops thereafter due to large entrainment. Even though maximum efficiency can be achieved in this region, it is not commonly used in column design due to its proximity to the flood point.
- Flooding regime: Instable column operation and poor efficiency occur due to heavy entrainment and flooding. Therefore, this region is avoided.

The achieved separation efficiency is related to the fluiddynamic conditions inside the packed bed (Kister, 1992): With higher column loads, the effective interfacial area increases, and thus mass transfer is enhanced, which improves efficiency. In contrast, an increased vapor load decreases the residence time of the vapor phase, which in turn results in a decreased efficiency. Since both effects are balanced for most corrugated-sheet packings, the overall efficiency is widely independent of both the vapor and liquid loads, resulting in a constant separation efficiency in the preloading regime. For some packings, however, a sloped relation between column load and separation efficiency is observed as the decrease in vapor phase residence time can dominate the increasing effect of enhanced mass transfer, resulting in an overall reduced efficiency. Different types of packings, characteristic operating points and operating regimes as well as their corresponding graphical representation in the *efficiency diagram* are discussed by (Kister, 1992).

Proper column design and packing selection are vital for reliable plant operation and mixture separation. This is especially true for demanding separation tasks where low specific pressure drops or high turndown ratios with wide operating ranges are needed. To satisfy these requirements, several generations of structured packings have been developed (Meier et al., 1979; Spiegel and Duss, 2014; Spiegel and Meier, 2003). As further improvements in packing performance seem to be limited by conventional manufacturing processes, additive manufacturing is currently evaluated to realize enhanced packing geometries with improved capabilities; see e.g. (Ashour et al., 2022; Dejean et al., 2020; Neukäufer et al., 2022; Neukäufer et al., 2021; Sarajlic et al., 2022).

Furthermore, improved or alternative distillation apparatuses are the subject of current research activities which focus on process intensification, e.g. wetted wall columns (Reitze et al.,

2020), dividing-wall columns (Kaibel, 2014; Kiss, 2013; Preißinger et al., 2019), rotating packed beds (Skiborowski and Górak, 2022), cyclic distillation (Kiss and Maleta, 2018; Kiss et al., 2021; Rasmussen et al., 2020) or microdistillation (Rieks et al., 2018; Sorensen et al., 2014; Wende et al., 2021).

2.2. Separation Quantification

2.2.1. Number of Theoretical Stages

To quantify the separation effort required to achieve a desired distillate or bottom product composition, the *number of theoretical stages* N_{th} is one of the most common approaches and is based on the concept of equilibrium stages. Several methods estimating N_{th} have been established in the past, of which the *Fenske equation* and the *McCabe-Thiele Method* are referred to as the most basic. In addition, the so-called *MESH equations* are especially relevant for computational calculations and often considered as the basis for rigorous calculations.

2.2.1.1. Fenske Equation

For a cascade of equilibrium stages as already illustrated in figure 2.2, operated under total reflux ($\dot{B} = 0\,\mathrm{kmol\,h^{-1}}$, $\dot{D} = 0\,\mathrm{kmol\,h^{-1}}$ and $\dot{F} = 0\,\mathrm{kmol\,h^{-1}}$), (Fenske, 1932) derived a relation between resulting distillate and bottoms compositions, the number of theoretical stages N_{th} and the relative volatility of the mixture α_{12}. The required assumptions are often simplified to total reflux ($\nu = \infty$), a constant relative volatility ($\alpha_{12} = \text{const.}$) and a binary mixture, but originally included (Fenske, 1932):

- continuous and adiabatic operation
- constant molar reflux and vapor flows (constant molar overflow)
- no heat of mixing
- ideal mixture ($\gamma_i = 1$)
- constant relative volatility ($\alpha_{12} = \text{const.}$)
- total reflux ($\nu = \infty$)
- binary mixture or multi-component mixture from which two key components are considered (components 1 and 2)

If the conditions associated with these assumptions are fulfilled, the relation derived by (Fenske, 1932) can be written as (Haan et al., 2020):

$$\frac{x_{1,\mathrm{D}}}{x_{2,\mathrm{D}}} = \alpha_{12}^{N_{\mathrm{th}}} \frac{x_{1,\mathrm{B}}}{x_{2,\mathrm{B}}} \tag{2.20}$$

Rearranging equation (2.20) gives the Fenske equation[3] as shown in equation (2.21):

$$N_{\mathrm{th}} = \frac{\log\left[\left(\frac{x_{\mathrm{D}}}{1-x_{\mathrm{D}}}\right)\left(\frac{1-x_{\mathrm{B}}}{x_{\mathrm{B}}}\right)\right]}{\log \alpha_{12}} = \frac{\log S}{\log \alpha_{12}} \tag{2.21}$$

The Fenske equation is often used in early-stage column design and is especially relevant for the *Fenske-Underwood-Gilliland (FUG)* or *Fenske-Underwood-Gilliland-Kirkbride (FUGK)* shortcut methods to obtain initial estimates for the required number of theoretical stages, the minimum reflux ratio or the position of the feed inlet (Sorensen, 2014).

Furthermore, equation (2.21) is commonly used to evaluate separation performance experiments based on mixture composition. In such cases, the aforementioned assumptions should be considered for test mixture selection, plant operation and data evaluation. For cases where the assumption of $\alpha_{12} = \text{const.}$ is not fulfilled due to a dependence on temperature or composition, *Winn's modification* to the Fenske equation can be used to achieve improved results; see (Kister, 1992) for details.

2.2.1.2. McCabe-Thiele Method

(McCabe and Thiele, 1925) proposed a graphical method to determine the number of theoretical stages required for mixture separation based on equilibrium diagrams. The following assumptions were made (Kister, 1992; McCabe and Thiele, 1925; Sorensen, 2014):

1. A binary mixture is considered.
2. Complete equilibrium is reached on each theoretical stage.
3. The distillation column is operated in steady state.
4. Internal molar vapor and liquid flows in the rectifying and stripping section are constant, a change only occurs at the feed stage.
5. Heat losses are neglected.
6. Heat of mixing is neglected.
7. Both mixture components show similar boiling points.
8. Both mixture components comply to Trouton's rule[4].
9. Separation is performed at constant pressure, pressure drops along the column are neglected.

[3] Index 1, which denotes the more volatile or light key component, is omitted to improve readability, since the equation is expressed in terms of component 1 only.

[4] (Trouton, 1884) investigated the ratio of enthalpy of vaporization and boiling point of different liquids which resulted in the *Pictet-Trouton rule*: $\Delta S_{\mathrm{vap}} = \Delta H_{\mathrm{vap}}\, T_{\mathrm{boil}}^{-1} \approx 85 \ldots 88\,\mathrm{J\,mol^{-1}\,K^{-1}}$ (Atkins and Paula, 2006; Schönbucher, 2002). Since (McCabe and Thiele, 1925) assumed similar boiling points for the mixture components, Trouton's rule results in similar molar enthalpies of vaporization ($\Delta H_{\mathrm{vap},1} \approx \Delta H_{\mathrm{vap},2}$).

10. The temperature of feed stream is equal to the feed stage temperature.
11. Separation on feed stage occurs after the feed stream is mixed with fluids present on the stage.
12. Total condensation of overhead vapors in condenser without subcooling.
13. The composition of overhead vapors is equal to the distillate composition.
14. Closed loop for utility steam in reboiler (no direct steam distillation).
15. All mixture compositions are expressed as molar fractions of the more volatile component.

In order to determine the number of theoretical stages graphically, three *operating lines* are considered: *rectifying operating line*, *stripping operating line* and *feed line*.

The molar balance and component balance of the top section of the column are defined as:

$$\dot{G} = \dot{D} + \dot{L} \tag{2.22a}$$

$$\dot{G} \cdot y = \dot{D} \cdot x_{\mathrm{D}} + \dot{L} \cdot x \tag{2.22b}$$

The *rectifying section operating line (ROL)*, also known as *enrichment line* or *top operating line* is obtained by rearranging equation (2.22b) and inserting equations (2.13) and (2.22a) (Billet, 1979; King, 1980; Sorensen, 2014; Stichlmair et al., 2021):

$$\begin{aligned} y &= \frac{\dot{L}}{\dot{G}} \cdot x + \frac{\dot{D}}{\dot{G}} \cdot x_{\mathrm{D}} \\ &= \frac{\dot{L}}{\dot{L}+\dot{D}} \cdot x + \frac{\dot{D}}{\dot{L}+\dot{D}} \cdot x_{\mathrm{D}} \\ &= \frac{\nu}{\nu+1} \cdot x + \frac{1}{\nu+1} \cdot x_{\mathrm{D}} \end{aligned} \tag{2.23}$$

By inserting $x = 0$ into equation (2.23), the y-intercept of the rectifying section operating line is defined as:

$$y_{0,\mathrm{ROL}} = \frac{1}{\nu+1} \cdot x_{\mathrm{D}} \tag{2.24}$$

The slope of the rectifying section operating line $\tan\beta_{\mathrm{ROL}}$ is obtained from equation (2.23):

$$\tan\beta_{\mathrm{ROL}} = \frac{\dot{L}}{\dot{G}} = \frac{\nu}{\nu+1} \tag{2.25}$$

Similarly, an envelope over the bottom section of the column gives the following balances:

$$\dot{L}' = \dot{G}' + \dot{B} \tag{2.26a}$$

$$\dot{L}' \cdot x = \dot{G}' \cdot y + \dot{B} \cdot x_\mathrm{B} \tag{2.26b}$$

Using equations (2.26a) and (2.26b) in conjunction with equation (2.15) results in the *stripping section operating line (SOL)*, *stripping line* or *bottom operating line* (Billet, 1979; King, 1980; Sorensen, 2014; Stichlmair et al., 2021):

$$\begin{aligned} y &= \frac{\dot{L}'}{\dot{G}'} \cdot x - \frac{\dot{B}}{\dot{G}'} \cdot x_\mathrm{B} \\ &= \frac{\dot{L}'}{\dot{L}' - \dot{B}} \cdot x - \frac{\dot{B}}{\dot{L}' - \dot{B}'} \cdot x_\mathrm{B} \\ &= \frac{\nu'}{\nu' - 1} \cdot x - \frac{1}{\nu' - 1} \cdot x_\mathrm{B} \end{aligned} \tag{2.27}$$

With $x = 0$, the y-intercept of the stripping line is given as:

$$y_{0,\mathrm{SOL}} = \frac{1}{\nu' - 1} \cdot x_\mathrm{B} \tag{2.28}$$

The slope of the stripping line $\tan\beta_\mathrm{SOL}$ is obtained from equation (2.27):

$$\tan\beta_\mathrm{SOL} = \frac{\dot{L}'}{\dot{G}'} = \frac{\nu'}{\nu' - 1} \tag{2.29}$$

For further considerations, the overall component balance of a continuous distillation is obtained by extending equation (2.12):

$$\dot{F} \cdot x_\mathrm{F} = \dot{D} \cdot x_\mathrm{D} + \dot{B} \cdot x_\mathrm{B} \tag{2.30}$$

The intersection of the operating lines is given by a balance around the feed stage. The assumption of constant molar vapor and liquid flows in the both rectifying and the stripping section (assumption 4) results in:

$$\begin{aligned} &\dot{G}'_\mathrm{N} = \dot{G}'_{\mathrm{N}-1} = \cdots = \dot{G}' = \text{const.} \\ &\dot{L}'_\mathrm{N} = \dot{L}'_{\mathrm{N}-1} = \cdots = \dot{L}' = \text{const.} \\ &\dot{G}_1 = \dot{G}_2 = \cdots = \dot{G} = \text{const.} \\ &\dot{L}_1 = \dot{L}_2 = \cdots = \dot{L} = \text{const.} \end{aligned} \tag{2.31}$$

This is also known as *constant molar overflow* (Kister, 1992; Sorensen, 2014). Therefore, the balances over the feed stage can be written as:

$$\dot{F} + \dot{G}' + \dot{L} = \dot{G} + \dot{L}' \tag{2.32a}$$

$$\dot{F} \cdot x_{\mathrm{F}} - (\dot{L}' - \dot{L}) \cdot x = (\dot{G} - \dot{G}') \cdot y \tag{2.32b}$$

Inserting the feed condition q, see equation (2.16), into equation (2.32b) finally results in:

$$\dot{F} \cdot x_{\mathrm{F}} - q \cdot \dot{F} \cdot x = (1 - q) \cdot \dot{F} \cdot y \tag{2.33}$$

Rearranging equation (2.33) gives the definition of the *feed line (FL)* or *q-line* (Sorensen, 2014):

$$y = \frac{q}{q-1} \cdot x - \frac{1}{q-1} \cdot x_{\mathrm{F}} \tag{2.34}$$

In contrast to the rectifying or stripping operating lines for which the y-intercept was derived, the x-intercept of the feed line is required to construct the McCabe-Thiele diagram. The x-intercept ($y = 0$) is obtained from equation (2.34):

$$x_{0,\mathrm{FL}} = \frac{x_{\mathrm{F}}}{q} \tag{2.35}$$

Furthermore, the slope of the feed line $\tan \beta_{\mathrm{FL}}$ is deduced from equation (2.34):

$$\tan \beta_{\mathrm{FL}} = \frac{q}{q-1} \tag{2.36}$$

The McCabe-Thiele stage construction can be drawn, if any arbitrary point on each operating line and the corresponding slopes are known (Kister, 1992). However, using the intersection of each operating line with the diagonal as fixed points can simplify the construction. The diagonal is defined as:

$$y = x \tag{2.37}$$

The intersection of the rectifying section operating line with the diagonal is dependent on condenser operation. For total condensation, there is no external equilibrium stage[5] and the intersection is directly defined based on equations (2.23) and (2.37) (Kister, 1992; McCabe and Thiele, 1925):

$$x = y = \frac{\dot{D}}{\dot{G} - \dot{L}} \cdot x_{\mathrm{D}} \underset{(2.22a)}{=} x_{\mathrm{D}} \tag{2.38}$$

However, for partial condensation, an additional equilibrium between the remaining overhead vapors and the condensate is established, and thus an external equilibrium stage must be considered[6]. Since the product stream is withdrawn as a vapor stream with the composition y_{D}, x_{D} is replaced with y_{D} (Kister, 1992). Due to the external equilibrium stage, $\dot{G}_1 = \dot{D}$ and

[5] For total condensation, (Kister, 1992) denotes the condenser as stage 0.
[6] Stage 1 is outside the column, stage 2 is the top stage inside the column.

$\dot{L}_0 = 0\,\mathrm{kmol\,h^{-1}}$ is assumed (Kister, 1992). For partial condensation, the intersection between the rectifying section operating line and the diagonal is defined as (Kister, 1992; McCabe and Thiele, 1925):

$$x = y = \frac{\dot{D}}{\dot{G} - \dot{L}} \cdot y_\mathrm{D} = y_\mathrm{D} \tag{2.39}$$

The intersection of the rectifying section operating line with the diagonal is therefore defined as $x = x_\mathrm{D}$ for total condensation and $x = y_\mathrm{D}$ for partial condensation, respectively (Kister, 1992). The intersection of the stripping section operating line with the diagonal can be obtained from similar considerations about the reboiler. Using equations (2.27) and (2.37) with equation (2.26a) gives (Kister, 1992):

$$x = y = \frac{\dot{B}}{\dot{G}' - \dot{L}'} \cdot x_\mathrm{B} \underset{(2.26a)}{=} x_\mathrm{B} \tag{2.40}$$

Combining equations (2.34) and (2.37), the intersection between the feed line and the diagonal is defined as:

$$x = y = x_\mathrm{F} \tag{2.41}$$

Finally, a McCabe-Thiele stage construction can be drawn as shown in figure 2.4.

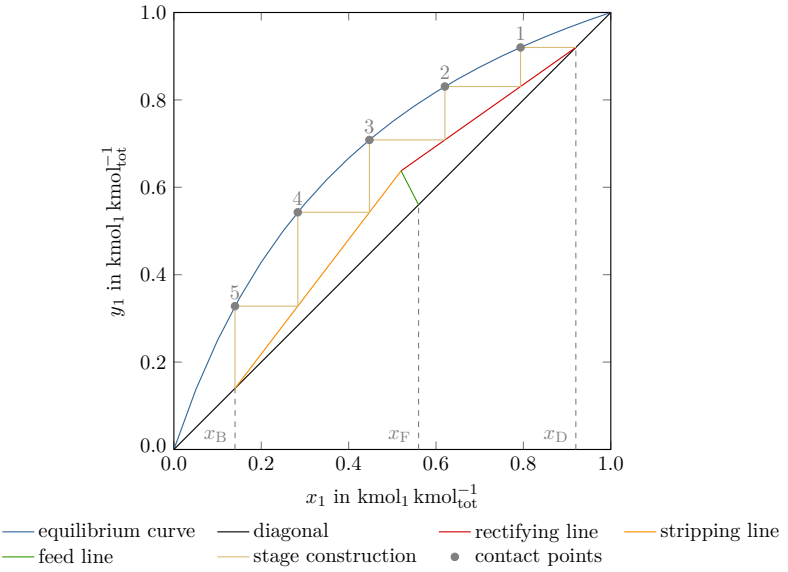

Figure 2.4.: Exemplary McCabe-Thiele stage construction with $x_\mathrm{B} = 0.14\,\mathrm{kmol_1\,kmol_{tot}^{-1}}$, $x_\mathrm{F} = 0.56\,\mathrm{kmol_1\,kmol_{tot}^{-1}}$ and $x_\mathrm{D} = 0.92\,\mathrm{kmol_1\,kmol_{tot}^{-1}}$, $q = 0.66$, $\nu = 2.4$ and $\alpha_{12} = 3.0$

The number of theoretical stages N_{th} is represented by the number of contact points of the stages polyline with the equilibrium curve. For the example given here, the number of theoretical stages is determined as $N_{\mathrm{th}} = 5$.

As thermodynamic equilibrium is established in the reboiler, an extra stage is provided. This needs to be subtracted from the number of theoretical stages N_{th} resulting in the *number of theoretical plates* $N_{\mathrm{th,p}}$:

$$N_{\mathrm{th,p}} = N_{\mathrm{th}} - 1 \tag{2.42}$$

The McCabe-Thiele method can only be used, if the previously mentioned assumptions are fulfilled. In particular, the assumption of constant molar overflow should be critically evaluated. As shown in equation (2.31) it is a vital assumption for defining the component balances and the derivation of the operating lines. As derived from Trouton's rule, the constant molar overflow assumption is based on similar molar enthalpies of vaporization for both mixture components. Although being valid for most organic mixtures, aqueous or more complex mixtures show differing molar enthalpies of vaporization, and thus do not fulfill this assumption (Kister, 1992). In addition, a strong influence of the mixture composition on its boiling point may also result in a varying molar overflow and should therefore be critically evaluated (McCabe and Thiele, 1925). Alternatively, more accurate results are obtained if the enthalpy balance is considered for the stage construction. This method is known as the *Ponchon-Savarit method*, which is based on enthalpy-concentration diagrams instead of equilibrium diagrams (Gmehling, 2003; Kenig and Blagov, 2014; Sattler, 2001).

2.2.1.3. Stage-to-Stage Calculations and MESH Equations

As shown in section 2.2.1.2, the graphical approach by (McCabe and Thiele, 1925) is based on the material/component balances (M), equilibrium data (E) and summation conditions (S) of cascaded equilibrium stages. However, such graphical methods have become less relevant since the late 1950s as (Amundson et al., 1959; Amundson and Pontinen, 1958) started using computers to solve the underlying system of *MESH equations*, which is derived based on an equilibrium stage as illustrated in figure 2.5.

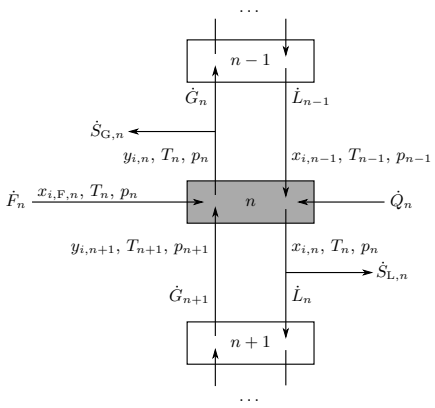

Figure 2.5.: Generalized equilibrium stage to derive MESH equations, based on (Gmehling, 2003; Steffen and da Silva, 2017; Stichlmair et al., 2021)

As a generalized equilibrium stage n is considered, vapor and liquid side streams $\dot{S}_{\mathrm{G},n}$ and $\dot{S}_{\mathrm{L},n}$, a feed stream $\dot{F}_n$ and heat flow $\dot{Q}_n$ are added to the equilibrium stage model introduced in section 2.1.2.

With N_c mixture components ($i = 1 \dots N_\mathrm{c}$) and N_th number of theoretical stages ($n = 1 \dots N_\mathrm{th}$), the resulting MESH equations are:

Material/component balances (M) [$N_\mathrm{th} \cdot N_\mathrm{c}$ equations]:

$$\begin{aligned} 0 = {} & \dot{L}_{n-1} \cdot x_{i,n-1} + \dot{G}_{n+1} \cdot y_{i,n+1} + \dot{F}_n \cdot x_{i,\mathrm{F},n} \\ & - (\dot{L}_n + \dot{S}_{\mathrm{L},n}) \cdot x_{i,n} - (\dot{G}_n + \dot{S}_{\mathrm{G},n}) \cdot y_{i,n} \end{aligned} \tag{2.43a}$$

Equilibrium equations (E) [$N_\mathrm{th} \cdot N_\mathrm{c}$ equations]:

$$\begin{aligned} K_{i,n} \underset{(2.1)}{=} \frac{y_{i,n}}{x_{i,n}} &= f(T_n, p_n, x_{i,n}, y_{i,n}) \\ \iff 0 &= y_{i,n} - K_{i,n} \cdot x_{i,n} \end{aligned} \tag{2.43b}$$

Summation conditions (S) [$2 \cdot N_\mathrm{th}$ equations]:

$$\begin{aligned} \sum_i^{N_c} x_{i,n} - 1 = 0 \\ \sum_i^{N_c} y_{i,n} - 1 = 0 \end{aligned} \tag{2.43c}$$

Heat/enthalpy balances (H) [N_{th} equations]:

$$0 = \dot{L}_{n-1} \cdot h_{\mathrm{L},n-1} + \dot{G}_{n+1} \cdot h_{\mathrm{G},n+1} + \dot{F}_n \cdot h_{\mathrm{F},n} + \dot{Q}_n$$
$$- (\dot{L}_n + \dot{S}_{\mathrm{L},n}) \cdot h_{L,n} - (\dot{G}_n + \dot{S}_{\mathrm{G},n}) \cdot h_{\mathrm{G},n} \tag{2.43d}$$
$$\text{where} \quad h_{\mathrm{L},n} = f(T_n, p_n, x_{i,n}) \quad \text{and} \quad h_{\mathrm{G},n} = f(T_n, p_n, y_{i,n})$$

The resulting system of equations contains $N_{\mathrm{th}} \cdot (2 \cdot N_{\mathrm{c}} + 1)$ equations (Gmehling, 2003). Neglecting the heat/enthalpy balances (H) results in a set of MES equations and is practically identical with the graphical approach of the McCabe-Thiele method (King, 1980). To solve the set of equations defined in equations (2.43a) to (2.43d), several methods were developed in the past; see (King, 1980; Kister, 1992; Seader et al., 2008) for details about calculation procedures, iteration schemes, applicability, characteristics and selection of common methods.

2.2.2. Height Equivalent to a Theoretical Plate (HETP)

Several approaches to estimate the number of theoretical stages N_{th} were introduced in section 2.2.1. While the number of theoretical stages is generally applicable to all common types of mass transfer equipment, the concepts of *number of theoretical stages per meter (NTSM)* and *height equivalent to a theoretical plate (HETP)* are specifically established for packed columns. Therefore, the separation performance of packings is often expressed by NTSM or HETP. Both are defined by the packing height H_{bed} and the number of theoretical stages N_{th} as proposed by (Peters, 1922):

$$\mathrm{HETP} = \frac{H_{\mathrm{bed}}}{N_{\mathrm{th}}} = \frac{1}{\mathrm{NTSM}} \tag{2.44}$$

For experimental results, N_{th} is obtained using the Fenske equation, see section 2.2.1.1, or McCabe-Thiele stage constructions, see section 2.2.1.2.

Alternatively, existing datasets can be used to interpolate HETP. According to (Kister, 1992), this results in very precise estimations, if data of the same or at least a very similar type of packing are used to specifically cover effects poorly described by established mass transfer models[7]. However, for modern types of packings, HETP datasets are often not publicly available, see section 2.3. Alternatively, mass transfer models, see section 2.2.3, can be used to predict HETP based on mixture properties and packing geometry.

Disregarding the evaluation or prediction method, HETP is commonly affected by various factors related to experimental setup and plant operation, which are discussed in the following.

[7] Depending on the specific mass transfer model, established correlations lack a proper estimation of HETP values for special separation problems like viscous distillation; see (Bradtmöller, 2017; Bradtmöller and Scholl, 2015) for details.

Packing geometry / column diameter A higher specific packing surface area results in an increased separation performance and thus lower HETP. This is due to smaller channel sizes and an improved distribution of the increased separation effective surface area (Kister, 1992). According to (Billet, 1979), diameter effects become relevant for column diameters smaller than 300 mm. However, such effects were not observed by e.g. (Meier et al., 1979) or (Valenz et al., 2013) for column diameters of 0.15 m, 0.43 m and 1.22 m or 0.16 m, 0.25 m and 1 m, respectively.

Packing height / bed height For some packings, increased HETP values are observed with increasing bed heights, which is particularly pronounced for smaller packing diameters. This is commonly attributed to uneven concentration profiles due to liquid maldistribution (Zuiderweg et al., 1987). In addition, end effects resulting from liquid dripping off the lower end of the bed or related to the liquid distribution above a packing section may show a larger influence for packed beds with lower heights (Billet, 1989; Kister, 1992). Furthermore, higher beds also provide a higher number of theoretical stages from which a wider concentration spread between top and bottom can generally be achieved. This should be considered for test mixture selection and uncertainties in sample analysis.

Column load / operating regime Despite HETP depends on the column load and the operating regime, a constant HETP is commonly reached in the preloading regime, see section 2.1.3. For structured packings, the effect of liquid load may dominate the effect of vapor load (Kister, 1992). Wetting or, at extremely low liquid loads, underwetting can significantly influence HETP, which is relevant if the liquid viscosity or surface tension depend on the mixture composition.

Vapor and liquid distribution Maldistribution of vapor or liquid has a negative effect on separation performance (reduced effective area due to wetting issues, uneven concentration profile, variations in local $\dot{L}\,\dot{G}^{-1}$ etc.) resulting in a higher HETP.

Reflux ratio Since separation performance is commonly evaluated at total reflux ($\dot{L}\,\dot{G}^{-1} = 1$), the influence of reflux ratio is rarely addressed in the literature. (Kister, 1992) claims that HETP values at total reflux are similar to those obtained at partial reflux based on investigations by (Billet, 1989; Eckert and Walter, 1964; Meier et al., 1979; Morris, 1960; Yuan and Spiegel, 1982). However, (Koshy and Rukovena, 1986) observed significant deviations in HETP for both total and partial reflux. Since the influence of the reflux ratio on separation performance is a core objective of this work, a more detailed discussion is provided in section 2.2.4.

Operating pressure Experimental results by e.g. (Bradtmöller, 2017; Bradtmöller and Scholl, 2015; Čmelíková et al., 2021; Meier et al., 2003; Meier et al., 1979)[8] show a small or even negligible influence of operating pressure on HETP for vacuum and atmospheric pressure.

[8]The original publication by (Meier et al., 2003) was not available through established literature services, but relevant data has been republished by (Düssel and Stichlmair, 2006).

According to (Kister, 1992), this observation can be generalized for vacuum distillation with operating pressures above around 70 mbar(a), but does not apply for vacuum distillation at lower pressures and high pressure distillation with pressures above ca. 14 bar(a). Furthermore, the relative volatility α_{12} may have a strong dependence on operating pressure (Ottenbacher et al., 2011), which can indirectly affect HETP.

Mixture properties (Kister, 1992) claims that HETP has a relatively low dependence on mixture properties for nonaqueous systems. However, investigations by (Böcker and Ronge, 2005; Bradtmöller, 2017; Bradtmöller et al., 2015; Bradtmöller and Scholl, 2015; Manivannan et al., 2020; Tsai et al., 2008; Tsai et al., 2009) indicate a significant dependence on surface tension and viscosity. The importance of relative volatility with respect to test mixture selection was discussed by (Ottenbacher et al., 2011). For multicomponent or complex mixtures, HETP may also be affected by miscibility gaps (two liquid phases) or inert mixture components if the diffusion of key mixture components is hindered (Harrison, 1990).

Uncertainties in VLE Uncertainties in VLE are commonly elaborated in terms of the relative volatility α_{12} and were discussed by e.g. (Coulson and Herington, 1948; Deibele and Brandt, 1985; Kister, 1992); see section 2.3.3 for details.

Concentration range The effect of concentration range was explicitly highlighted by (Ottenbacher et al., 2011; Valenz et al., 2013) and addresses the aforementioned effects of packing geometry, bed height, operating pressure and mixture properties in one single effect. Choosing a suitable concentration range boils down to choosing a suitable test mixture and is important for separation performance measurements.

2.2.3. Non-Equilibrium and Mass Transfer Models

2.2.3.1. Murphree Efficiency

Previously introduced concepts of separation performance are primarily based on equilibrium thermodynamics and the concept of equilibrium stages. However, perfect equilibrium can only be reached in theory, since *rate* effects limit the occurring mass transfer. These effects are considered in *non-equilibrium models* and *mass transfer models*[9].

(Murphree, 1925a; Murphree, 1925b) developed a basic approach to express the deviation between the equilibrium composition y_n^{eq} and actual non-equilibrium composition y_n. For the vapor phase, the *Murphree efficiency* E_{MG}, which can also be interpreted as a pseudo-equilibrium

[9] In addition to mass transfer models, other approaches like *Computational Fluid Dynamics (CFD)* or *Hydrodynamic Analogies (HA)* are commonly used for non-equilibrium modeling. See e.g. (Kenig, 2022; Kenig and Blagov, 2014) for a more detailed overview on column modeling approaches.

(Stichlmair et al., 2021), is defined as (Seader et al., 2008):

$$E_{\mathrm{MG}} = \frac{y_n - y_{n-1}}{y_n^{\mathrm{eq}} - y_{n-1}} \tag{2.45}$$

The Murphree efficiency for the liquid phase E_{ML} can be defined similarly. Inserting E_{MG} and E_{ML} into the equilibrium equation given in equation (2.43b) allows expressing non-equilibrium conditions based on the MESH equations. This approach represents as a very basic, but robust form of a rate-based model (Stichlmair et al., 2021).

2.2.3.2. The Concept of Transfer Units (HTU/NTU)

The concept of transfer units can be derived based on the *two-film theory* as illustrated in figure 2.6. In the boundary envelope with differential height $\mathrm{d}h$, mass transfer from the vapor to the liquid occurs through the planar vapor/liquid interface, resulting in the differential molar flow $\mathrm{d}\dot{n}$. Assuming continuous operation at steady state with perfectly mixed bulk phases, the bulk concentrations y^{b} and x^{b} are constant (Kraume, 2020). Furthermore, there is a laminar film on each side of the vapor/liquid interface. Inside each film, mass can be transferred only by diffusion, which results in the linear concentration gradients in the vicinity of the interface.

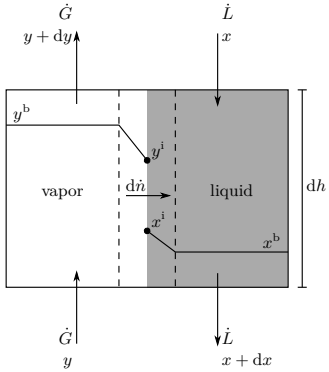

Figure 2.6.: Two-film theory, based on (Kenig and Blagov, 2014; King, 1980; Kraume, 2020)

Due to the thermodynamic equilibrium at the interface (denoted by superscript i), instantaneous mass transfer is assumed[10] (Taylor and Kooijman, 2014). Therefore, mass transfer resistances are present only in the vapor or the liquid film (Schönbucher, 2002).

[10]It should be noted that the profile of molar fractions illustrated in figure 2.6 shows a discontinuity at the phase interface due to the equilibrium condition. Nevertheless, other measures such as partial pressures, concentrations etc. can also be used if the equilibrium condition at the interface is described accordingly. A detailed overview of HTU/NTU for different measures of composition is presented by (Seader and Henley, 2011). A continuous profile is obtained if activities a_i ($a_{\mathrm{G},i} = a_{\mathrm{L},i}$ at equilibrium) are used to represent the driving potential (Sherwood et al., 1975).

The (infinitesimal) molar flow $\mathrm{d}\dot{n}$ through the interface results from the component balance of the illustrated boundary envelope[11]:

$$\mathrm{d}\dot{n} = \dot{G} \cdot y - \dot{G} \cdot (y + \mathrm{d}y) = -\dot{G}\,\mathrm{d}y \tag{2.46a}$$

$$= \dot{L} \cdot (x + \mathrm{d}x) - \dot{L} \cdot x = \dot{L}\,\mathrm{d}x \tag{2.46b}$$

Equations (2.46a) and (2.46b) are valid if the molar flows $\dot{G}$ and $\dot{L}$ are constant. In this case, a constant bulk composition is assumed (assumption of constant molar overflow) which is given for highly diluted mixtures (absorption and stripping) or distillation with equimolar counterdiffusion and a constant molar overflow (Seader and Henley, 2011).

Furthermore, $\mathrm{d}\dot{n}$ is expressed based on the film theory using the mass transfer coefficients of the vapor and liquid film, k_G and k_L, as well as the separation effective specific interfacial area a_eff and the cross-sectional area of the (unpacked) column A_col (Gmehling, 2003)[12]:

$$\mathrm{d}\dot{n} = k_\mathrm{G}\, a_\mathrm{eff}\, (y^\mathrm{b} - y^\mathrm{i})\, A_\mathrm{col}\, \mathrm{d}h \underset{(2.46a)}{=} -\dot{G}\,\mathrm{d}y \tag{2.47a}$$

$$= k_\mathrm{L}\, a_\mathrm{eff}\, (x^\mathrm{i} - x^\mathrm{b})\, A_\mathrm{col}\, \mathrm{d}h \underset{(2.46b)}{=} \dot{L}\,\mathrm{d}x \tag{2.47b}$$

The height of the packed bed H_bed is obtained by integrating equations (2.47a) and (2.47b) (Gmehling, 2003; Kraume, 2020):

$$H_\mathrm{bed} = \int_0^{H_\mathrm{bed}} \mathrm{d}h$$

$$= \underbrace{\frac{\dot{G}}{k_\mathrm{G}\, a_\mathrm{eff}\, A_\mathrm{col}}}_{\mathrm{HTU_G}} \cdot \underbrace{\int_{y_\mathrm{bottom}}^{y_\mathrm{top}} \frac{1}{y^\mathrm{i} - y^\mathrm{b}}\,\mathrm{d}y}_{\mathrm{NTU_G}} = \mathrm{HTU_G} \cdot \mathrm{NTU_G} \tag{2.48a}$$

$$= \underbrace{\frac{\dot{L}}{k_\mathrm{L}\, a_\mathrm{eff}\, A_\mathrm{col}}}_{\mathrm{HTU_L}} \cdot \underbrace{\int_{x_\mathrm{top}}^{x_\mathrm{bottom}} \frac{1}{x^\mathrm{i} - x^\mathrm{b}}\,\mathrm{d}x}_{\mathrm{NTU_L}} = \mathrm{HTU_L} \cdot \mathrm{NTU_L} \tag{2.48b}$$

As highlighted above, equations (2.48a) and (2.48b) also define the *height of a transfer unit (HTU)* and the *number of transfer units (NTU)*, wherein indices G and L denote the vapor and liquid phase, respectively. This approach can be applied without consideration of any specific mass transfer equipment (Stichlmair et al., 2021). It is known as the *concept of transfer units* and was proposed by (Chilton and Colburn, 1935; Colburn, 1939; Colburn, 1941).

To solve equations (2.48a) and (2.48b), the mixture compositions x^i and y^i at the phase

[11] The component balance refers to the light mixture component. However, the according index 1 is omitted in both figure 2.6 and the following equations to improve readability.

[12] Strictly speaking, equations (2.47a) and (2.47b) are extended definitions of the mass transfer coefficients k_G and k_L. Since k_G and k_L should commonly have positive values, the driving forces represented by $\Delta x = x^\mathrm{i} - x^\mathrm{b}$ and $\Delta y = y^\mathrm{b} - y^\mathrm{i}$ need to be chosen accordingly (King, 1980).

interface are required. However, these values are not known a priori. Therefore, equations (2.47a) and (2.47b) are rearranged as (Gmehling, 2003):

$$\frac{y^{\mathrm{i}} - y^{\mathrm{b}}}{x^{\mathrm{i}} - x^{\mathrm{b}}} = -\frac{k_{\mathrm{L}}}{k_{\mathrm{G}}} \underset{(2.48\mathrm{b})}{\overset{(2.48\mathrm{a})}{=}} -\frac{\dot{L}}{\dot{G}} \cdot \frac{\mathrm{HTU_G}}{\mathrm{HTU_L}} \tag{2.49}$$

For small changes in vapor and liquid compositions, such as infinitesimal $\mathrm{d}y$ and $\mathrm{d}x$, the equilibrium curve can be linearly approximated due to its small curvature. In this case, equations (2.46a) and (2.46b) are used to substitute the ratio $\dot{L}\,\dot{G}^{-1}$ with the slope of the equilibrium line[13] m (Katayama and Yoshida, 1968; Kraume, 2020):

$$\frac{\dot{L}}{\dot{G}} = \frac{\mathrm{d}y}{\mathrm{d}x} = m \tag{2.50}$$

Commonly, neither relevant mass transfer resistances nor mixture compositions at the phase interface can be measured individually. Therefore, all occurring mass transfer resistances are fully attributed to either the gas film or the liquid film (overall mass transfer resistance), whereas no mass transfer resistance is assumed for the opposing film. In this case, *overall mass transfer coefficients* k_{oG} and k_{oL} as well as hypothetical equilibrium compositions y^{eq} and x^{eq} are used (Gmehling, 2003):

$$\mathrm{d}\dot{n} = k_{\mathrm{oG}}\, a_{\mathrm{eff}}\, (y^{\mathrm{b}} - y^{\mathrm{eq}})\, A_{\mathrm{col}}\, \mathrm{d}h = -\dot{G}\, \mathrm{d}y \tag{2.51a}$$

$$= k_{\mathrm{oL}}\, a_{\mathrm{eff}}\, (x^{\mathrm{eq}} - x^{\mathrm{b}})\, A_{\mathrm{col}}\, \mathrm{d}h = \dot{L}\, \mathrm{d}x \tag{2.51b}$$

The relation between the molar fractions in the bulk phase (y^{b} and x^{b}), at the interface (y^{i} and x^{i}) and at hypothetical equilibrium (y^{eq} and x^{eq}) is given as (Gmehling, 2003):

$$\begin{aligned} y^{\mathrm{b}} - y^{\mathrm{eq}} &= (y^{\mathrm{b}} - y^{\mathrm{i}}) + (y^{\mathrm{i}} - y^{\mathrm{eq}}) \\ &= (y^{\mathrm{b}} - y^{\mathrm{i}}) + m \cdot (x^{\mathrm{i}} - x^{\mathrm{b}}) \end{aligned} \tag{2.52}$$

Considering countercurrent stripping and thus, a high dilution in both vapor and liquid, equation (2.52) can also be illustrated using an equilibrium diagram (King, 1980)[14] as shown in figure 2.7.

[13] The slope of the equilibrium line m can also be interpreted as the equilibrium constant K^{eq} (Kenig and Blagov, 2014; Kraume, 2020): $y_i = K^{\mathrm{eq}}\, x_i$.

[14] In stripping, component 1 goes from liquid to vapor. However, the balance envelope considered in figure 2.6 assumes component 1 going from vapor to liquid which results in negative driving forces (King, 1980).

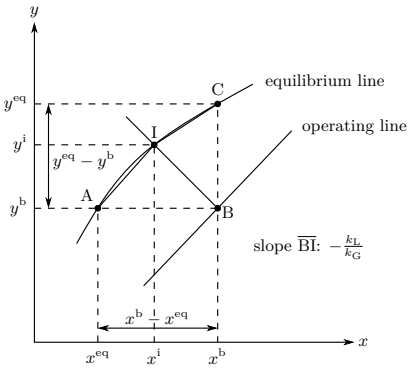

Figure 2.7.: Relation between bulk (superscript b), interface (superscript i) and equilibrium (superscript eq) molar fractions, point B: mixture composition in bulk, point I: mixture composition at interface, based on (Gmehling, 2003; King, 1980; Kraume, 2020; Seader and Henley, 2011)

The overall mass transfer coefficients are defined by combining equations (2.47a), (2.47b), (2.51a) and (2.51b) with equation (2.52) (Gmehling, 2003):

$$\frac{1}{k_{oG}} = \frac{1}{k_G} + \frac{m}{k_L} \tag{2.53a}$$

$$\frac{1}{k_{oL}} = \frac{1}{k_L} + \frac{1}{m\,k_G} \tag{2.53b}$$

To derive equations (2.53a) and (2.53b) based on equation (2.52), the slope of the operating line is assumed to be constant, so that the slope of $\overline{AI}$ equals the slope of $\overline{IC}$. However, as illustrated in figure 2.7, this assumption is invalid for curved equilibrium lines. Therefore, (Seader and Henley, 2011) use different slopes for these sections which results in adapted equations (2.53a) and (2.53b). (Katayama and Yoshida, 1968) suggest considering the slope of $\overline{AC}$, instead of the distinct slopes of $\overline{AI}$ or $\overline{IC}$, and claim that the errors resulting from this procedure are insignificant[15]. In general, deviations due to different definitions of the slope of the operating line m are often considered negligible, since the linear approximation only spans an infinitesimal segment of the equilibrium curve.

Similar to equations (2.48a) and (2.48b), the overall mass transfer coefficients k_{oG} and k_{oL} can be used to estimate the height of the packed bed H_{bed}. This defines HTU_{oG}, NTU_{oG}, HTU_{oL} and NTU_{oL} as shown in equations (2.54a) and (2.54b), respectively (Gmehling, 2003):

$$H_{bed} = \int_0^{H_{bed}} \mathrm{d}h$$

[15]However, (Katayama and Yoshida, 1968) did not provide any numbers to substantiate this statement.

$$= \underbrace{\frac{\dot{G}}{k_{\mathrm{oG}}\, a_{\mathrm{eff}}\, A_{\mathrm{col}}}}_{\mathrm{HTU_{oG}}} \cdot \underbrace{\int_{y_{\mathrm{bottom}}}^{y_{\mathrm{top}}} \frac{1}{y^{\mathrm{eq}} - y^{\mathrm{b}}}\, \mathrm{d}y}_{\mathrm{NTU_{oG}}} = \mathrm{HTU_{oG}} \cdot \mathrm{NTU_{oG}} \tag{2.54a}$$

$$= \underbrace{\frac{\dot{L}}{k_{\mathrm{oL}}\, a_{\mathrm{eff}}\, A_{\mathrm{col}}}}_{\mathrm{HTU_{oL}}} \cdot \underbrace{\int_{x_{\mathrm{top}}}^{x_{\mathrm{bottom}}} \frac{1}{x^{\mathrm{eq}} - x^{\mathrm{b}}}\, \mathrm{d}x}_{\mathrm{NTU_{oL}}} = \mathrm{HTU_{oL}} \cdot \mathrm{NTU_{oL}} \tag{2.54b}$$

$\mathrm{HTU_G}$ and $\mathrm{HTU_L}$ in equations (2.48a) and (2.48b) or $\mathrm{HTU_{oG}}$ and $\mathrm{HTU_{oL}}$ in equations (2.54a) and (2.54b) are commonly considered constant. However, this is not always valid and $\mathrm{HTU_{oG}}$ should not be pulled out of the integral to obtain more precise results for such cases (Sherwood et al., 1975):

$$H_{\mathrm{bed}} = \int_{y_{\mathrm{bottom}}}^{y_{\mathrm{top}}} \mathrm{HTU_{oG}} \cdot \frac{1}{y^{\mathrm{eq}} - y^{\mathrm{b}}}\, \mathrm{d}y \tag{2.55}$$

Furthermore, the *stripping factor* λ is defined as (Edmister, 1957):

$$\lambda = m\, \frac{\dot{G}}{\dot{L}} \tag{2.56}$$

Combining the definitions of $\mathrm{HTU_G}$ and $\mathrm{HTU_L}$, given in equations (2.48a) and (2.48b), with equations (2.53a) and (2.53b) as well as $\mathrm{HTU_{oG}}$ and $\mathrm{HTU_{oL}}$ from equations (2.54a) and (2.54b), allows deriving (Gmehling, 2003):

$$\mathrm{HTU_{oG}} = \mathrm{HTU_G} + m\, \frac{\dot{G}}{\dot{L}}\, \mathrm{HTU_L} \underset{(2.56)}{=} \mathrm{HTU_G} + \lambda\, \mathrm{HTU_L} \tag{2.57a}$$

$$\mathrm{HTU_{oL}} = \frac{\dot{L}}{m\, \dot{G}}\, \mathrm{HTU_G} + \mathrm{HTU_L} \underset{(2.56)}{=} \frac{1}{\lambda}\, \mathrm{HTU_G} + \mathrm{HTU_L} \tag{2.57b}$$

Introspecting equations (2.57a) and (2.57b) as well as equations (2.54a) and (2.54b) shows that the separation effective surface area a_{eff}, the mass transfer coefficients k_{G} and k_{L} as well as the slope of the equilibrium line m are required to estimate the separation effort based on the height of a transfer unit HTU. The parameters a_{eff}, k_{G} and k_{L} are commonly estimated based on mass transfer models, see section 2.2.3.5. The slope of the equilibrium line m for a binary mixture with constant relative volatility α_{12} is given as (Fair et al., 2008):

$$m = \frac{\alpha_{12}}{\left[1 + (\alpha_{12} - 1)\, x_1\right]^2} \tag{2.58}$$

For a mixture with varying relative volatility α_{12}, a geometrically averaged relative volatility $\overline{\alpha}_{12}$ should be considered according to equation (2.4). Depending on the desired calculation accuracy and variations in α_{12} due to temperature and concentration, $\alpha_{12,\mathrm{I}}$ and $\alpha_{12,\mathrm{II}}$ may be considered segmentally along the height of the packed bed. Furthermore, if $\mathrm{HTU_{oG}}$ and $\mathrm{HTU_{oL}}$,

as defined in equations (2.57a) and (2.57b), depend significantly on variations in concentration due to variations in the slope of the equilibrium line, equations (2.54a) and (2.54b) may also be evaluated segmentally (Fair et al., 2008; Olujić et al., 2007; Sherwood et al., 1975).

In addition, (Colburn, 1939) explicitly addressed the influence of variations in operating conditions throughout a distillation column. The slope of the equilibrium curve in the rectifying section is smaller than the slope of the operating line ($\lambda < 1$), whereas the opposite is true in the stripping section ($\lambda > 1$). Therefore, larger $\mathrm{HTU_{oG}}$ are obtained in the stripping section than in the rectifying section of a distillation column. The influence of the stripping factor λ is discussed in section 2.2.3.4 in which HETP and HTU/NTU are compared to each other.

As shown in figure 2.8, the integral for $\mathrm{NTU_{oG}}$ given in equation (2.54a) can also be interpreted graphically. However, to evaluate the corresponding integral, discrete values are commonly integrated numerically or integrated (either analytically or numerically) after a polynomial regression. A pure algebraic solution for $\mathrm{NTU_{oG}}$ is presented in appendix E.1.

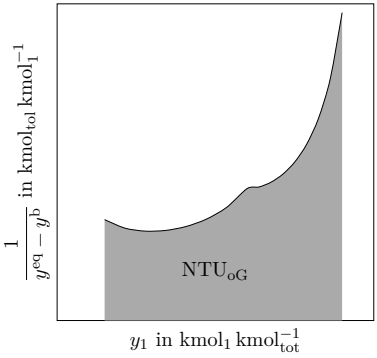

Figure 2.8.: Graphical interpretation of $\mathrm{NTU_{oG}}$, based on (Chilton and Colburn, 1935; Gmehling, 2003; Sherwood et al., 1975)

2.2.3.3. Connecting HETP and HTU/NTU

As already shown in figure 2.2, multistage distillation can be interpreted as a cascade of equilibrium stages and thus, the number of theoretical stages N_{th} is commonly specified as positive integers. Furthermore, HETP is often calculated with the number of theoretical stages N_{th}, see equation (2.44), and is, as the term *height equivalent to a theoretical plate (HETP)* implies, closely related to the concept of theoretical stages. Therefore, HETP can be interpreted as a stepwise (discrete) approach to estimate or specify separation performance (Chilton and Colburn, 1935). In contrast to HETP, the concept of transfer units can be seen as a continuous approach, since the change in concentration along the column height is considered differentially (Chilton and Colburn, 1935; Katayama and Yoshida, 1968). Therefore, (Katayama and Yoshida, 1968) claim HTU to be more theoretically sound than HETP which is also in accordance with

(Graf, 2011).

Despite these fundamentally different approaches, a relation between HETP and $\mathrm{HTU_{oG}}$ can be established by evaluating equivalences in mixture separation on trays and inside a packed section as discussed by (Katayama and Yoshida, 1968; Sherwood et al., 1975). Applying equations (2.46a) and (2.46b) to a packed section with height h, liquid molar fractions x_2 (inlet) and x_3 (outlet) and vapor molar fractions y_3 (outlet) and y_4 (inlet) results in:

$$\dot{G} \cdot (y_4 - y_3) = \dot{L} \cdot (x_3 - x_2) \underset{(2.51a)}{=} k_{\mathrm{oG}}\, a_{\mathrm{eff}}\, (y^{\mathrm{b}} - y^{\mathrm{eq}})\, A_{\mathrm{col}}\, h \tag{2.59a}$$

$$\Longleftrightarrow h = \frac{\dot{G}\,(y_4 - y_3)}{k_{\mathrm{oG}}\, a_{\mathrm{eff}}\, (y^{\mathrm{b}} - y^{\mathrm{eq}})\, A_{\mathrm{col}}} \tag{2.59b}$$

The term $y^{\mathrm{b}} - y^{\mathrm{eq}}$ is unknown, but a suitable approximation can be derived using the logarithmic mean of the driving potential which is applicable if the difference to approximate is linear in the variable defining the driving potential (Sherwood et al., 1975). Applying the logarithmic mean to the term $y^{\mathrm{b}} - y^{\mathrm{eq}}$ results in equation (2.60). Indices A and B refer to the lower and upper end of the packed section.

$$y^{\mathrm{b}} - y^{\mathrm{eq}} = \frac{(y^{\mathrm{b}} - y^{\mathrm{eq}})_{\mathrm{A}} - (y^{\mathrm{b}} - y^{\mathrm{eq}})_{\mathrm{B}}}{\ln\left[\dfrac{(y^{\mathrm{b}} - y^{\mathrm{eq}})_{\mathrm{A}}}{(y^{\mathrm{b}} - y^{\mathrm{eq}})_{\mathrm{B}}}\right]} \tag{2.60}$$

Considering a stage construction covering the equilibrium stages 2, 3 and 4, the terms $(y^{\mathrm{b}} - y^{\mathrm{eq}})_{\mathrm{A}}$ and $(y^{\mathrm{b}} - y^{\mathrm{eq}})_{\mathrm{B}}$ can be determined according to figure 2.7:

$$(y^{\mathrm{b}} - y^{\mathrm{eq}})_{\mathrm{A}} = y_4 - y_3 \tag{2.61a}$$

$$(y^{\mathrm{b}} - y^{\mathrm{eq}})_{\mathrm{B}} = y_3 - y_2 \tag{2.61b}$$

Combining equations (2.61a) and (2.61b) with equations (2.59b) and (2.60) results in (Sherwood et al., 1975):

$$h = \frac{\dot{G}\,(y_4 - y_3)\, \ln\left[\dfrac{y_4 - y_3}{y_3 - y_2}\right]}{k_{\mathrm{oG}}\, a_{\mathrm{eff}}\, A_{\mathrm{col}}\, [(y_4 - y_3) - (y_3 - y_2)]} \tag{2.62}$$

Furthermore, the slope of the equilibrium line as well as the slope of the operating line can be expressed with the liquid and vapor compositions. To simplify rearranging equation (2.62) later, the ratio of the aforementioned slopes is used and the stripping factor λ is recalled from equation (2.56) (Sherwood et al., 1975):

$$\frac{(y_3 - y_2)\,(x_3 - x_2)^{-1}}{(y_4 - y_3)\,(x_3 - x_2)^{-1}} = \frac{\text{slope of equilibrium line}}{\text{slope of operating line}} = \frac{m}{\dot{L}\,\dot{G}^{-1}} \underset{(2.56)}{=} \lambda \tag{2.63}$$

Equation (2.63) is expanded to obtain the following expression (Sherwood et al., 1975):

$$\lambda - 1 = \frac{y_3 - y_2}{y_4 - y_3} - 1 = \frac{(y_3 - y_2) - (y_4 - y_3)}{y_4 - y_3} \tag{2.64}$$

Inserting equations (2.63) and (2.64) into equation (2.62) and factoring out $\mathrm{HTU_{oG}}$ finally results in equation (2.65). As the height h of the considered packed section is equivalent to the height of a theoretical plate in the corresponding section of an arbitrary tray column (as also represented by stage 3 in the corresponding stage construction), h can be replaced with HETP (Sherwood et al., 1975):

$$\mathrm{HETP} = \frac{\dot{G}}{k_{\mathrm{oG}}\, a_{\mathrm{eff}}\, A_{\mathrm{col}}} \frac{\ln \lambda}{\lambda - 1} \underset{(2.54a)}{=} \mathrm{HTU_{oG}} \frac{\ln \lambda}{\lambda - 1} \underset{(2.57a)}{=} (\mathrm{HTU_G} + \lambda\, \mathrm{HTU_L}) \frac{\ln \lambda}{\lambda - 1} \tag{2.65}$$

Equation (2.65) is only valid for $\lambda \neq 1$. However, a simplified approximation can be derived if the logarithmic mean is also satisfied for the driving potential in equation (2.54a) (Sherwood et al., 1975):

$$\mathrm{HETP} = 2\, \mathrm{HTU_{oG}} \frac{1}{\lambda + 1} \underset{(2.57a)}{=} 2\,(\mathrm{HTU_G} + \lambda\, \mathrm{HTU_L}) \frac{1}{\lambda + 1} \tag{2.66}$$

Since equation (2.66) is also valid for $\lambda = 1$, which is given for an operating line parallel to the equilibrium line and total reflux ($\dot{L}\,\dot{G}^{-1} = 1$), it can be shown that $\mathrm{HETP} = \mathrm{HTU_{oG}}$ if $\lambda = 1$ (Kister, 1992; Sherwood et al., 1975). Furthermore, the stripping factor λ is equal to the slope of the equilibrium curve m for total reflux ($\dot{L}\,\dot{G}^{-1} = 1$):

$$\lambda \underset{(2.56)}{=} m \underset{(2.58)}{=} \frac{\alpha_{12}}{[1 + (\alpha_{12} - 1)\, x_1]^2} \tag{2.67}$$

Disregarding whether HETP or HTU/NTU are used to estimate the required height during column design, the total height of the packed bed H_{bed} should be identical, since the separation task is fixed. Therefore, equations (2.44) and (2.54a) are set equal (Fair et al., 2008; King, 1980):

$$H_{\mathrm{bed}} \underset{(2.44)}{=} \mathrm{HETP} \cdot N_{\mathrm{th}} \underset{(2.54a)}{=} \mathrm{HTU_{oG}} \cdot \mathrm{NTU_{oG}} \tag{2.68}$$

Combining equations (2.65) and (2.68) describes the relation between the number of transfer units $\mathrm{NTU_{oG}}$ and the number of theoretical stages N_{th} (Fair et al., 2008; King, 1980):

$$\mathrm{NTU_{oG}} = N_{\mathrm{th}} \frac{\ln \lambda}{\lambda - 1} \tag{2.69}$$

2.2.3.4. HETP vs. HTU/NTU

As already described in section 2.2.3.3, the use of HTU/NTU is often considered as more theoretically sound than HETP (Graf, 2011; Katayama and Yoshida, 1968). (Graf, 2011) states that HETP is often interpreted as a property or parameter solely attributed to the packing. However, according to (Graf, 2011), this is a fundamental misconception, since *separation equipment* (type of packing) and *separation task* (desired product specification) should be strictly differentiated from each other and described by independent measures. With the interpretation that HETP is a packing property, the number of theoretical stages N_{th} describes the separation task. The number of *theoretical stages* should not be interpreted as an independent measure describing the separation task, since assumptions about the mass transfer equipment are implied. However, according to (Graf, 2011), HTU and NTU properly distinguish between the separation equipment and the separation task, respectively.

Contrary to (Graf, 2011; Katayama and Yoshida, 1968), (Kister, 1992) prefers HETP over HTU/NTU, since HETP are generally easier to apply to multicomponent systems, can easily be estimated based on stage-to-stage calculations and simplify direct comparisons with tray columns. Furthermore, (Kister, 1992) does not see an improvement in design accuracy when using HTU/NTU compared to HETP, but rather a significant increase in design complexity. However, (Kister, 1992) admits that HTU provides easier analysis of mass transfer phenomena and can mathematically be converted to HETP. In general, both HETP and HTU/NTU result in equal or very similar column designs (Kister, 1992). This is evident in equation (2.68) where $\mathrm{NTU_{oG}}$ is related to N_{th}.

For a more detailed discussion, the influence of the stripping factor λ, which may considerably change throughout distillation (King, 1980), is elaborated. Commonly, three different cases are considered (Chilton and Colburn, 1935; Duss and Taylor, 2018; Graf, 2011; King, 1980; Koshy and Rukovena, 1986; Seader and Henley, 2011):

1. $\lambda \ll 1$: For high concentrations of the more volatile component, equation (2.58) gives $\lambda \to 1/\alpha_{12}$. Since $\dot{L}\,\dot{G}^{-1} \to 1$ is valid for high reflux ratios, both conditions result in $\lambda \to 1/\alpha_{12}$ and thus, $\lambda \ll 1$. In this case, $\mathrm{HTU_{oG}} < \mathrm{HETP}$ and $\mathrm{NTU_{oG}} > N_{\mathrm{th}}$ is obtained.

2. $\lambda \approx 1$: This condition is obtained for very low reflux ratios in the rectifying section ($x_1 \to 1\,\mathrm{kmol_l\,kmol_{tot}^{-1}}$), very high reflux ratios in the stripping section ($x_1 \to 0\,\mathrm{kmol_l\,kmol_{tot}^{-1}}$) or *symmetric separations*[16]. This case is also relevant for *difficult separations* for which $\alpha_{12} \approx 1$ can be assumed and equation (2.58) results in $m \approx 1$. Due to the narrow operating region between the equilibrium and operating lines, the reflux ratio is close to unity which can be represented as $\dot{L}\,\dot{G}^{-1} \to 1$. Therefore, the stripping factor λ, as defined in equation (2.56), does not vary significantly from unity and its exact value is less important. Finally, $\mathrm{HTU_{oG}} \approx \mathrm{HETP}$ and $\mathrm{NTU_{oG}} \approx N_{\mathrm{th}}$ are obtained disregarding

[16] (Chilton and Colburn, 1935; Koshy and Rukovena, 1986) use this term to describe a separation with product compositions equidistantly spaced around $x_1 = 0.50\,\mathrm{kmol_l\,kmol_{tot}^{-1}}$.

the specific considerations. However, for *easy separations* with $\alpha_{12} \gg 1$, case 1 or case 3 in which λ is an important parameter for separation performance are obtained.

3. $\lambda \gg 1$: According to equation (2.58), a high purity of the bottom product ($x_1 \rightarrow 0\,\mathrm{kmol_l\,kmol_{tot}^{-1}}$) results in $m \rightarrow \alpha_{12}$. Furthermore, if total reflux is approached, $\dot{L}\,\dot{G}^{-1} \rightarrow 1$ is valid and thus, $\lambda \rightarrow \alpha_{12}$ is obtained. In this case, the inverse of case 1 is obtained: $\mathrm{HTU_{oG}} > \mathrm{HETP}$ and $\mathrm{NTU_{oG}} < N_{\mathrm{th}}$.

As mentioned above, the stripping factor λ is approximated with α_{12} for $x_1 \rightarrow 0\,\mathrm{kmol_l\,kmol_{tot}^{-1}}$ (case 3) or with $1/\alpha_{12}$ for $x_1 \rightarrow 1\,\mathrm{kmol_l\,kmol_{tot}^{-1}}$ (case 1). The effects of molar fraction x_1 and relative volatility α_{12} on stripping factor λ were briefly addressed by (Duss and Taylor, 2018) claiming an insignificant difference between α_{12} and λ for $\alpha_{12} < 1.3$. In addition to the previously elaborated cases, (Chilton and Colburn, 1935) explicitly address the effect of diverging and converging equilibrium and operating lines, which are given for ideal mixtures with low relative volatilities and symmetric separations. In such cases, the aforementioned cases 1 and 3 average out each other resulting in $\mathrm{NTU_{oG}} \approx N_{\mathrm{th}}$ (Chilton and Colburn, 1935). This is also valid for most separation performance experiments, since common test mixtures and operating procedures satisfy these conditions (Chilton and Colburn, 1935). However, for many industrial separations, $\mathrm{NTU_{oG}} \neq N_{\mathrm{th}}$ is obtained (Chilton and Colburn, 1935) and thus, $\mathrm{HTU_{oG}} \neq \mathrm{HETP}$, see equation (2.68).

Since HETP is commonly estimated based on equation (2.65) or approximated by equation (2.66), HETP may change, even if $\mathrm{HTU_{oG}}$ does not (King, 1980). Therefore, (King, 1980) suggests calculating HETP for each equilibrium stage. A suitable procedure was proposed by (Sherwood et al., 1975) in which the theoretical stages of the rectifying and stripping section are considered independently of each other. Stages of the rectifying section are drawn from top to bottom, whereas the opposite applies to the stripping section and fractional stages are considered around the feed. The HETP for each stage is then calculated based on equation (2.65) or equation (2.66) and requires $\mathrm{HTU_{oG}}$. Since (Sherwood et al., 1975) suggest using equation (2.57a) to estimate $\mathrm{HTU_{oG}}$, $\mathrm{HTU_G}$ and $\mathrm{HTU_L}$ are needed in addition, but commonly unknown[17]. Finally, the column height is estimated by summing up the height increments along the packed bed with each increment calculated according to equation (2.44).

(Fair et al., 2008) proposed a slightly different procedure where equation (2.69) is used to convert the determined number of theoretical stages N_{th}[18] into the number of transfer units $\mathrm{NTU_{oG}}$. The height of an overall transfer unit $\mathrm{HTU_{oG}}$ is estimated with suitable approximations or mass transfer models; see (Fair et al., 2008) for available approaches. With both $\mathrm{HTU_{oG}}$ and $\mathrm{NTU_{oG}}$ known, equation (2.68) is used to calculate the total column height.

[17] $\mathrm{HTU_{oG}}$ was introduced in section 2.2.3.2, since $\mathrm{HTU_G}$ and $\mathrm{HTU_L}$ are commonly inaccessible. However, (Sherwood et al., 1975) guessed values for $\mathrm{HTU_G}$ and $\mathrm{HTU_L}$ which is an unreasonable approach if the underlying mass transfer phenomena, and thus the resulting heights of transfer units, are widely unknown. Nevertheless, estimating $\mathrm{HTU_{oG}}$ by applying equation (2.54a) to each stage can be a suitable alternative.

[18] (Fair et al., 2008) do not explicitly state how to determine N_{th}. Nevertheless, the established approaches elaborated in section 2.2.1 should be suitable.

2.2.3.5. Delft Mass Transfer Model

As shown in sections 2.2.3.2 and 2.2.3.3, mass transfer coefficients k_G and k_L as well as the separation effective interfacial area a_{eff} are needed to describe separation performance. Many empirical, semi-empirical and predictive mass transfer models to calculate k_G, k_L and a_{eff} have been established in the past and are extensively discussed by several authors, e.g. (Bradtmöller, 2017; Carrillo et al., 2000; Flagiello et al., 2021; Kister, 1992; Olujić and Seibert, 2014; Orlando et al., 2009; Stichlmair et al., 2021; Taylor and Kooijman, 2014; Wang et al., 2005a; Wang et al., 2005b).

Since the *Delft model* was published and cited throughout several contributions, different versions can be found in the literature. (Bradtmöller, 2017) assumes that these variations mainly arose from typing errors and republished a consistent set of equations for the Delft model by (Olujić et al., 2004; Olujić et al., 1999; Olujić et al., 2012) after re-evaluation. The Delft model does not require any empirical factors and relies on packing geometry and operational parameters only. As the predicted separation performance may be too conservative for narrow-boiling systems like chlorobenzene/ethylbenzene (Olujić et al., 2012), (Olujić and Seibert, 2014) published a revised version of the model to improve predicted separation performance for such cases.

Packing and Flow Channel Geometry Considering the geometry of a single flow channel with the width w_c and the height h_c, its corresponding side length s_c is defined as:

$$s_c = \sqrt{\frac{w_c^2}{4} + h_c^2} \tag{2.70}$$

With all channel dimensions known, the specific packing surface area a_p is given by:

$$a_p = 4\,\frac{s_c}{w_c\,h_c} \tag{2.71}$$

The fraction of cross-sectional area occupied by the liquid film flow on the surface of each channel is determined by:

$$\varphi_{c,L} = \frac{2\,s_c}{w_c + 2\,s_c} \tag{2.72}$$

According to (Olujić et al., 2012), $\varphi_{c,L}$ was introduced to consider a potentially enhanced mass transfer due to gas/gas interaction at crossing flow channels. Disregarding the specific packing size, $\varphi_{c,L} \approx 0.59$ is obtained for corrugation fold angles of around 90° (Olujić et al., 2012). However, for narrow-boiling systems, such as chlorobenzene/ethylbenzene (CB/EB), (Olujić et al., 2012) observed an underestimation of the separation performance as $\varphi_{c,L}$ reduces the influence of the turbulent vapor phase mass transfer according to equation (2.90b). Using the test mixture CB/EB to investigate separation performance of a high performance packing, resulted in a 70 % increase in vapor mass transfer coefficients k_G, if $\varphi_{c,L} = 1$ was used instead of $\varphi_{c,L} \approx 0.59$

for data evaluation (Olujić et al., 2012). Therefore, (Olujić et al., 2012) suggested using $\varphi_{c,L} = 1$ to improve agreement between experimental and predicted separation performance in such cases.

The length of a gas flow channel $l_{c,G}$ is estimated using the inclination angle of the packing sheets α_p and the height of a packing element h_p:

$$l_{c,G} = \frac{h_p}{\sin \alpha_p} \tag{2.73}$$

Equation (2.73) can be derived based on geometry considerations disregarding the height of a packing element. However, (Bradtmöller, 2017) suggests using an alternative approach for small-scale columns as the length of a flow channel is rather limited by the diameter of the packing element d_p than by its height:

$$l_{c,G} = \frac{d_p}{\cos \alpha_p} \tag{2.74}$$

Although the flow channels of a corrugated sheet packing are inclined at a packing-specific angle, the liquid film tends to flow at an angle steeper than the channel inclination (Olujić and Seibert, 2014). The resulting effective liquid flow angle α_L is defined as:

$$\alpha_L = \arctan \left[\frac{\cos (90° - \alpha_p)}{\sin (90° - \alpha_p) \cdot \cos \left[\arctan \left(\frac{w_c}{2\, h_c} \right) \right]} \right] \tag{2.75}$$

Liquid and Gas Flow To describe the flow inside a packing channel, the superficial liquid velocity $u_{L,s}$ is calculated using the liquid mass flow m_L, its density ρ_L and the column diameter d_{col}:

$$u_{L,s} = \frac{4 \cdot \dot{m}_L}{\pi \cdot d_{col}^2 \cdot \rho_L} \tag{2.76}$$

Similarly, the superficial gas velocity $u_{G,s}$ is defined as:

$$u_{G,s} \underset{(2.18)}{=} \frac{4 \cdot \dot{m}_G}{\pi \cdot d_{col}^2 \cdot \rho_G} = \frac{f_G}{\rho_G^{0.5}} \tag{2.77}$$

Since both liquid density ρ_L and viscosity η_L can be calculated based on the liquid mixture composition, see appendices C.3.2 and C.6.1, the mean thickness of the liquid film δ_L is estimated according to equation (2.78); g denotes the gravity of Earth ($g = 9.806\,65\,\mathrm{m\,s^{-2}}$):

$$\delta_L = \left(\frac{3\, \eta_L\, u_{L,s}}{\rho_L\, g\, a_p\, \sin \alpha_L} \right)^{\frac{1}{3}} \tag{2.78}$$

Using the channel dimensions h_c, s_c and w_c as well as the mean liquid film thickness δ_L allows

describing the hydraulic diameter of a gas flow channel $d_{\mathrm{h,c,G}}$:

$$d_{\mathrm{h,c,G}} = \frac{\dfrac{\left(w_{\mathrm{c}}\, h_{\mathrm{c}} - 2\,\delta_{\mathrm{L}}\, s_{\mathrm{c}}\right)^2}{w_{\mathrm{c}}\, h_{\mathrm{c}}}}{\left[\left(\dfrac{w_{\mathrm{c}}\, h_{\mathrm{c}} - 2\,\delta_{\mathrm{L}}\, s_{\mathrm{c}}}{2\, h_{\mathrm{c}}}\right)^2 + \left(\dfrac{w_{\mathrm{c}}\, h_{\mathrm{c}} - 2\,\delta_{\mathrm{L}}\, s_{\mathrm{c}}}{w_{\mathrm{c}}}\right)^2\right]^{0.5} + \dfrac{w_{\mathrm{c}}\, h_{\mathrm{c}} - 2\,\delta_{\mathrm{L}}\, s_{\mathrm{c}}}{2\, h_{\mathrm{c}}}} \tag{2.79}$$

Assuming a fully wetted packing surface, the liquid holdup h_{L} is given by:

$$h_{\mathrm{L}} = \delta_{\mathrm{L}}\, a_{\mathrm{p}} \tag{2.80}$$

Superficial gas velocity $u_{\mathrm{G,s}}$, packing void fraction or packing porosity ε_{p} and channel inclination angle α_{p} are used to define the effective gas velocity $u_{\mathrm{G,eff}}$:

$$u_{\mathrm{G,eff}} = \frac{u_{\mathrm{G,s}}}{\left(\varepsilon_{\mathrm{p}} - h_{\mathrm{L}}\right)\, \sin \alpha_{\mathrm{p}}} \tag{2.81}$$

Similarly, the effective liquid velocity $u_{\mathrm{L,eff}}$ is calculated as:

$$u_{\mathrm{L,eff}} = \frac{u_{\mathrm{L,s}}}{\varepsilon_{\mathrm{p}}\, h_{\mathrm{L}}\, \sin \alpha_{\mathrm{L}}} \tag{2.82}$$

The relative gas phase Reynolds number $\mathrm{Re}_{\mathrm{G,rel}}$ is defined with the effective velocities $u_{\mathrm{G,eff}}$ and $u_{\mathrm{L,eff}}$:

$$\mathrm{Re}_{\mathrm{G,rel}} = \frac{\rho_{\mathrm{G}}\, \left(u_{\mathrm{G,eff}} + u_{\mathrm{L,eff}}\right)\, d_{\mathrm{h,c,G}}}{\eta_{\mathrm{G}}} \tag{2.83}$$

Relative Reynolds number $\mathrm{Re}_{\mathrm{G,rel}}$, hydraulic diameter gas flow channel $d_{\mathrm{h,c,G}}$ and mean film thickness δ_{L} allow calculating the gas/liquid friction factor ξ_{GL}:

$$\xi_{\mathrm{GL}} = \left[-2\, \log\left[\frac{\delta_{\mathrm{L}}\, d_{\mathrm{h,c,G}}^{-1}}{3.7} - \frac{5.02}{\mathrm{Re}_{\mathrm{G,rel}}}\, \log\left(\frac{\delta_{\mathrm{L}}\, d_{\mathrm{h,c,G}}^{-1}}{3.7} + \frac{14.5}{\mathrm{Re}_{\mathrm{G,rel}}}\right)\right]\right]^{-2} \tag{2.84}$$

Effective Interfacial Area The separation effective interfacial area is quantified by combining the *Onda correlation* with several correction terms. The correlation by (Onda et al., 1968) can be written as shown in equation (2.85):

$$a_{\mathrm{eff,Onda}} = a_{\mathrm{p}} \left[1 - \exp\left(-1.45\, \left(\frac{\sigma_{\mathrm{p}}}{\sigma_{\mathrm{L}}}\right)^{0.75}\, \mathrm{Re}_{\mathrm{L,s}}^{0.1}\, \mathrm{Fr}_{\mathrm{L,s}}^{-0.05}\, \mathrm{We}_{\mathrm{L,s}}^{0.2}\right)\right] \tag{2.85a}$$

$$\mathrm{Re}_{\mathrm{L,s}} = \frac{\rho_{\mathrm{L}}\, u_{\mathrm{L,s}}}{a_{\mathrm{p}}\, \eta_{\mathrm{L}}} \tag{2.85b}$$

$$\mathrm{Fr}_{\mathrm{L,s}} = \frac{u_{\mathrm{L,s}}^2\, a_{\mathrm{p}}}{g} \tag{2.85c}$$

$$\mathrm{We}_{\mathrm{L,s}} = \frac{\rho_{\mathrm{L}}\, u_{\mathrm{L,s}}^2}{a_{\mathrm{p}}\, \sigma_{\mathrm{L}}} \tag{2.85d}$$

As packing elements may consist of perforated sheets, equation (2.85a) overestimates the effective surface area. To account for the fraction of packing surface area occupied by the perforation holes, Ω_{p} is introduced for correction[19]:

$$a_{\mathrm{eff}} = (1 - \Omega_{\mathrm{p}})\, a_{\mathrm{eff,Onda}} \tag{2.86}$$

To further improve the accuracy of equation (2.86) with respect to experimental results, an empirically determined correction using a specific packing surface area of $250\,\mathrm{m^2\,m^{-3}}$, an inclination angle of 45° and an operating pressure of 1013 mbar(a) as references can be applied (Olujić et al., 2004). Considering all aforementioned corrections, the corrected effective interfacial area $a_{\mathrm{eff,corr}}$ is finally calculated with equation (2.87).

$$a_{\mathrm{eff,corr}} = a_{\mathrm{eff}} \left(\frac{\sin 45^\circ}{\sin \alpha_{\mathrm{L}}} \right)^n \tag{2.87a}$$

$$\begin{aligned} n = {} & \left(1 - \frac{a_{\mathrm{p}}}{250}\right) \left(1 - \frac{\alpha_{\mathrm{L}}}{45^\circ}\right) + \ln\left(\frac{a_{\mathrm{eff,Onda}}}{250}\right) \\ & + \left[0.49 - \left(\frac{1013\,\mathrm{mbar(a)}}{p}\right)^{0.5}\right] \left(1.2 - \frac{\alpha_{\mathrm{L}}}{45^\circ}\right) \end{aligned} \tag{2.87b}$$

Mass Transfer Coefficients The liquid phase mass transfer coefficient k_{L} is estimated based on the liquid diffusion coefficient $D_{\mathrm{L,12}}$, see appendix C.8.1 for details about its calculation, the effective liquid velocity $u_{\mathrm{L,eff}}$ and the hydraulic diameter of a gas flow channel $d_{\mathrm{h,c,G}}$ as shown in equation (2.88). Additionally, (Olujić and Seibert, 2014) introduced a revised calculation for k_{L}, see equation (2.88b), to accommodate for an increased liquid film flow length which is potentially underestimated by the original correlation using the hydraulic diameter $d_{\mathrm{h,c,G}}$ as shown in equation (2.88a).

$$k_{\mathrm{L,original}} = 2 \left(\frac{D_{\mathrm{L,12}}\, u_{\mathrm{L,eff}}}{\pi\, 0.9\, d_{\mathrm{h,c,G}}} \right)^{0.5} \tag{2.88a}$$

$$k_{\mathrm{L,revised}} = 2 \left(\frac{D_{\mathrm{L,12}}\, u_{\mathrm{L,s}}}{\pi\, \varepsilon_{\mathrm{p}}\, h_{\mathrm{L}}\, s_{\mathrm{c}}} \right)^{0.5} \tag{2.88b}$$

For the gas phase mass transfer coefficient k_{G}, laminar and turbulent contributions, $k_{\mathrm{G,lam}}$ and $k_{\mathrm{G,turb}}$, are considered according to equation (2.89). The calculation routine to estimate

[19] The value of Ω_{p} depends on the packing type. (Olujić et al., 2004) suggest $\Omega_{\mathrm{p}} = 0$ for unperforated packings and $\Omega_{\mathrm{p}} = 0.1$ for common types of perforated packings such as *Sulzer Mellapak*.

the vapor phase diffusion coefficient $D_{\mathrm{G},12}$ is documented in appendix C.8.2.

$$k_{\mathrm{G}} = \sqrt{k_{\mathrm{G,lam}}^2 + k_{\mathrm{G,turb}}^2} \tag{2.89a}$$

$$k_{\mathrm{G,lam}} = \frac{\mathrm{Sh}_{\mathrm{G,lam}}\ D_{\mathrm{G},12}}{d_{\mathrm{h,c,G}}} \tag{2.89b}$$

$$k_{\mathrm{G,turb}} = \frac{\mathrm{Sh}_{\mathrm{G,turb}}\ D_{\mathrm{G},12}}{d_{\mathrm{h,c,G}}} \tag{2.89c}$$

Gas phase Sherwood numbers $\mathrm{Sh}_{\mathrm{G,lam}}$ and $\mathrm{Sh}_{\mathrm{G,turb}}$ are defined as[20]:

$$\mathrm{Sh}_{\mathrm{G,lam}} = 0.664\ \mathrm{Sc}_{\mathrm{G}}^{\frac{1}{3}} \left(\mathrm{Re}_{\mathrm{G,rel}}\ \frac{d_{\mathrm{h,c,G}}}{l_{\mathrm{c,G}}}\right)^{0.5} \tag{2.90a}$$

$$\mathrm{Sh}_{\mathrm{G,turb}} = \frac{\mathrm{Re}_{\mathrm{G,rel}}\ \mathrm{Sc}_{\mathrm{G}}\ \dfrac{\xi_{\mathrm{GL}}\,\varphi_{\mathrm{c,L}}}{8}}{1 + 12.7\left(\dfrac{\xi_{\mathrm{GL}}\,\varphi_{\mathrm{c,L}}}{8}\right)^{0.5}\left(\mathrm{Sc}_{\mathrm{G}}^{\frac{2}{3}} - 1\right)} \left[1 + \left(\frac{d_{\mathrm{h,c,G}}}{l_{\mathrm{c,G}}}\right)^{\frac{2}{3}}\right] \tag{2.90b}$$

The gas phase Schmidt number Sc_{G} is calculated according to equation (2.91). For estimating the gas phase density ρ_{G} and gas phase viscosity η_{G} see appendices C.3.3 and C.6.2.

$$\mathrm{Sc}_{\mathrm{G}} = \frac{\eta_{\mathrm{G}}}{\rho_{\mathrm{G}}\, D_{\mathrm{G},12}} \tag{2.91}$$

Separation Performance To finally determine separation effort or to evaluate separation performance, the liquid and vapor phase mass transfer coefficients k_{L} and k_{G} estimated from equations (2.88) and (2.89a) are used to calculate $\mathrm{HTU}_{\mathrm{L}}$ and $\mathrm{HTU}_{\mathrm{G}}$, respectively. For this, $\mathrm{HTU}_{\mathrm{L}}$ and $\mathrm{HTU}_{\mathrm{G}}$ can be expressed as:

$$\mathrm{HTU}_{\mathrm{L}} = \frac{u_{\mathrm{L,s}}}{k_{\mathrm{L}}\, a_{\mathrm{eff,corr}}} \tag{2.92a}$$

$$\mathrm{HTU}_{\mathrm{G}} = \frac{u_{\mathrm{G,s}}}{k_{\mathrm{G}}\, a_{\mathrm{eff,corr}}} \tag{2.92b}$$

While the previously introduced equation (2.57a) allows estimating $\mathrm{HTU}_{\mathrm{oG}}$ based on calculated $\mathrm{HTU}_{\mathrm{L}}$ and $\mathrm{HTU}_{\mathrm{G}}$, equations (2.65) and (2.66) can be used to convert obtained $\mathrm{HTU}_{\mathrm{oG}}$ into HETP.

[20] (Olujić et al., 2004) use a value of 1.27 in the denominator of equation (2.90b), whereas 12.7 is used by (Olujić et al., 1999; Olujić et al., 2012). As 12.7 is used in both the older and the later publication, this value is assumed to be correct and, therefore, also used in this work.

2.2.4. Influence of Reflux Ratio

Since separation performance measurements are commonly conducted at total reflux ($\dot{L}\,\dot{G}^{-1} = 1$), only very limited data about the influence of reflux ratio are available. This seems to be reasonable as experiments with partial reflux ($\dot{L}\,\dot{G}^{-1} \neq 1$) are commonly not focusing on separation performance, but on column hydraulics (Cai, 2014). In such experiments, $\dot{L}\,\dot{G}^{-1} < 1$ and $\dot{L}\,\dot{G}^{-1} > 1$ are used to simulate the operating conditions present in the rectifying section and stripping section, respectively. Other investigations on the influence of reflux ratio have focused on process optimization (Orlando et al., 2009; Shokrkar and Salem, 2008), small-scale process development (Bittorf et al., 2019) or the characterization of *Raschig rings* by empirical correlations (Hands and Whitt, 1951).

As discussed in section 2.2.2, (Kister, 1992) claimed that HETP values of total reflux experiments are similar to those obtained at partial reflux conditions referring to investigations by (Billet, 1989; Eckert and Walter, 1964; Meier et al., 1979; Morris, 1960; Yuan and Spiegel, 1982). However, this claim can only be generalized to a limited extent. (Eckert and Walter, 1964; Morris, 1960) conducted experiments with random packings, (Meier et al., 1979; Yuan and Spiegel, 1982) used structured and gauze packings, (Billet, 1989) discussed data obtained from both random and structured packings[21].

(Meier et al., 1979) presented characterization experiments for packings of type *Sulzer Mellapak 250.Y* (Sulzer Chemtech, Winterthur/Switzerland). Although no detailed results on the influence of the reflux ratio on the achieved separation performance are given, (Meier et al., 1979) stated that an equal number of theoretical stages from total and partial reflux experiments was obtained and thus no influence of reflux ratio was observed. (Yuan and Spiegel, 1982), who worked with *Sulzer gauze*[22] packings, mainly investigated the influence of liquid maldistribution on separation performance. The influence of reflux ratio was addressed indirectly, as the *relative product rate* $\dot{D}\,\dot{G}^{-1}$ was varied for given inlet vapor compositions. The data presented do not indicate a clear influence of the reflux ratio, since both increasing and decreasing numbers of theoretical stages were obtained for an increasing relative product rate. However, (Yuan and Spiegel, 1982) showed that the influence of maldistribution on separation performance is less pronounced at partial reflux conditions. Similarly, (Manning and Cannon, 1957) studied the influence of liquid maldistribution with respect to channeling. Maldistribution was mimicked with an adjusted reflux ratio to generate a liquid bypass in which no mass transfer occurs. Although this approach may be generally comparable to experiments at partial reflux, (Manning and Cannon, 1957) investigated a maldistribution of 1 % which results in a reflux ratio very close to unity and thus, may not be applicable to the investigations presented in this work.

(Eckert and Walter, 1964) conducted experiments on several factors affecting HETP such as liquid distribution, reflux ratio and heat loss with different types of random packings. While

[21] The work by (Morris, 1960) could neither be retrieved through traditional literature services nor from the publisher and was thus not reviewed for this work. The results by (Yuan and Spiegel, 1982) are only available as a considerably shortened publication, the full version was also not available from the publisher.

[22] (Yuan and Spiegel, 1982) did not specify the exact packing type used for their investigations.

the specific characteristics of random packings are only comparable to those of structured packings to a limited extent, certain trends can be generalized for both packing types. The results by (Eckert and Walter, 1964) show significantly increased HETP for increasing reflux ratios, whereas increased HETP were also observed for very low reflux ratios. However, (Eckert and Walter, 1964) state that these variations are within the commonly observed margin for experimental HETP values. Since the liquid load increases with the reflux ratio, both findings can also be explained based on the column load, see section 2.1.3: As the minimum wetting rate may not be reached at very low reflux ratios, underwetting occurs and a low separation performance is obtained. Higher reflux ratios result in higher liquid loads and thus improve separation efficiency.

According to (Graf, 2011), separation performance should be attributed to the separation equipment and thus expressed in terms of HTU. (Pigford and Colburn, 1950) elaborate the effect of reflux ratio on HTU_{oG} based on equation (2.57a). Since the slope of the equilibrium line m is constant for a given concentration x_1, a variation of the reflux ratio, and thus $\dot{G}\,\dot{L}^{-1}$, only changes the relative importance of HTU_G and HTU_L (Pigford and Colburn, 1950). However, as described in section 2.2.3.2, HTU_G and HTU_L are commonly unknown or not accessible independently of each other. Therefore, the final effect of the reflux ratio on HTU_{oG} cannot be generally predicted (Pigford and Colburn, 1950).

2.3. Separation Performance Measurements

2.3.1. Test Mixtures

As separation performance measurements are often evaluated using Fenske's equation, the associated assumptions for this equation need to be fulfilled by the test mixture, see section 2.2.1.1. To limit the uncertainty in the calculated number of stages, (Coulson and Herington, 1948) developed a basic set of requirements for test mixtures. However, (Coulson and Herington, 1948) did not consider operational safety, chemical hazards or substance toxicity which are relevant factors with respect to laboratory standards and regulations. Furthermore, relevant mixture properties such as surface tension or viscosity were not taken into account.

To select a suitable test mixture, a non-exhaustive list of criteria can be obtained by summarizing e.g. (Bradtmöller, 2017; Bradtmöller and Scholl, 2016; Coulson and Herington, 1948; Deibele and Brandt, 1985; Manivannan et al., 2019; Ottenbacher et al., 2011; Schoenmakers and Spiegel, 2014; Spiegel and Duss, 2014; Willingham and Sedlak, 1950):

- VLE is close to ideal (ideal gas law for vapor phase, Raoult's law for liquid phase[23])
- available VLE datasets are thermodynamically consistent[24]

[23] This is especially relevant if Fenske's equation is used for data evaluation, see section 2.2.1.1.

[24] The self-consistency of VLE datasets is discussed by e.g. (Coulson and Herington, 1948; Redlich and Kister, 1948b; Sosa et al., 2019; Wisniak, 1993; Wisniak et al., 2017).

- relative volatility is close to 1.10[25]
- relative volatility is constant over the relevant concentration and temperature range (relative volatility is constant along full column height)
- mixture components have similar boiling points (narrow-boiling mixture)
- there is no heat of mixing[23]
- there is no volume change with mixing
- if $\alpha_{12} \neq$ const., a mixture composition at the left or right concentration end should be used (diluted mixtures[26])
- for azeotropic mixtures, the excess mixture component should have the higher boiling point
- mixture components are readily available with a high purity level (without high-boiling or inert residues) for reasonable prices
- mixture components are fully miscible over the relevant concentration and temperature range
- boiling points of mixture components are between 30 °C and 150 °C
- melting points of mixture components are below 40 °C
- mixture components do not thermally decompose in the relevant temperature range
- racemic components should be avoided
- mixture should not be corrosive or toxic
- negligible influence of mixture composition on surface tension and viscosity in the relevant concentration and temperature range[27]
- mixture composition can be quantified with well-established approaches (e.g. density measurements, refractive index measurements or gas chromatography) to ensure reasonable uncertainties in concentrations and estimated separation performance

[25] (Coulson and Herington, 1948) suggest a relative volatility of around or less than 1.10, but (Deibele and Brandt, 1985) show that the relative uncertainty of the calculated number of theoretical stages dramatically increases for $\alpha_{12} \to 1$. (Bradtmöller, 2017; Bradtmöller and Scholl, 2016) suggest $1.10 \leq \alpha_{12} \leq 2.0$, (Manivannan et al., 2019) propose $1.10 \leq \alpha_{12} \leq 3$. Furthermore, a higher relative volatility may require segmental data evaluation due to significantly changing stripping factors; see section 2.2.3.2.

[26] For diluted mixtures, $\ln \alpha_{12} \approx$ const. can be assumed. However, working with diluted mixtures results in higher requirements for sample analysis to ensure reasonable uncertainties in estimated separation performance.

[27] A varying surface tension or liquid viscosity affects the effective mass transfer area, see section 2.2.3. Special cases, e.g. investigating viscosity dependent separation efficiencies, may require tighter requirements; see (Bradtmöller, 2017; Bradtmöller and Scholl, 2016; Manivannan et al., 2019) for details.

Since a single test mixture fulfilling the above requirements over a wide range of industrially relevant operating conditions can hardly be identified, several test systems have been proposed. Depending on the type of application and the desired investigation (multistage distillation, absorption, desorption, separation performance, mass transfer, pressure drop, liquid holdup, capacity …), these include both organic and aqueous as well as gas/liquid systems.

Binary mixtures of liquids, predominantly used for separation performance measurements, are identified based on the extensive literature review about separation efficiency data for structured metal packings by (Bradtmöller, 2017) as summarized in table 2.2. Although the underlying review is non-exhaustive and only contains publicly available datasets until the year 2015, chlorobenzene/ethylbenzene (CB/EB) and cyclohexane/n-heptane (C6/C7) are identified as the most widely used test mixtures. Using these test mixtures, several experimental results were generated by either research institutions[28] or industrial companies such as packing manufacturers or plant operators. However, most of these datasets are considered confidential and are not publicly available.

Table 2.2.: Common binary test mixtures, data summarized from (Bradtmöller, 2017)

test mixture	abbreviation	reviewed literature references	
cyclohexane/n-heptane	C6/C7	15	46.9 %
chlorobenzene/ethylbenzene	CB/EB	13	40.6 %
p-/*o*-xylene	-	3	9.4 %
trans-/*cis*-decalin	-	1	3.1 %
total		32	100.0 %

Relevant physical properties of the aforementioned binary test mixtures were summarized by e.g. (Billet, 1995; Onken and Arlt, 1990; Ottenbacher et al., 2011) or are available from databanks like *DETHERM* (DECHEMA, Frankfurt/Germany), *Dortmund Data Bank* (DDBST Oldenburg/Germany) or *DIPPR 801 database* (Design Institute for Physical Properties, New York). In addition, a large set of unpublished or confidential data is most likely held by both industrial packing users and packing manufacturers. Regarding publicly available datasets, (Onken and Arlt, 1990) provide an extensive collection of recommended test mixtures. Furthermore, (Ottenbacher et al., 2011) discussed the physical properties of C6/C7, CB/EB and *p*-/*o*-xylene as well as the resulting advantages and disadvantages in their use for separation performance measurements. According to (Ottenbacher et al., 2011; Spiegel and Duss, 2014), CB/EB should be preferred over the other test mixtures due to its nearly ideal VLE, a small dependence of the relative volatility on both mixture concentration and operating pressure as well as its relatively low boiling point.

All the test mixtures listed in table 2.2 and most of the mixtures recommended by (Onken and Arlt, 1990) are binary mixtures of organic solvents with relatively low mixture viscosities

[28] Namely, *Separation Research Program (SRP)* and *Fractionation Research Inc. (FRI)* which conduct separation performance experiments for their members, associated partners or industrial clients.

at distillation operating conditions. Due to recent systematic investigations on the distillation of viscous systems, viscous test mixtures were developed in addition. (Bradtmöller and Scholl, 2016) proposed the mixture 2-Methyl-2-butanol/2-Methyl-1-propanol (MB/MP), whereas (Manivannan et al., 2019) chose cyclopentanol/cyclohexanol (CP/CH). These mixtures allow viscosities of up to $5 \ldots 6\,\mathrm{mPa\,s}$ at operating conditions. Nevertheless, reaching higher viscosities is unlikely for binary mixtures consisting of organic solvents (Böcker and Ronge, 2005; Bradtmöller, 2017; Manivannan et al., 2019). Therefore, (Böcker and Ronge, 2005) enhanced the standardized test mixture CB/EB by adding polybutadiene (PBD) as a viscosity-enhancing polymer. Similarly, adding polyvinylpyrrolidone (PVP) to the viscous mixture MB/MP was proposed by (Gutperl and Scholl, 2018). However, as shown in chapter 3, conducting separation performance measurements with mixtures containing inert or non-volatile components requires an alternative experimental methodology.

2.3.2. Experimental Procedures and Plant Setups

2.3.2.1. General Considerations and Total Reflux

Several authors, e.g. (Billet, 1995; Górak and Schoenmakers, 2014; Kister, 1990; Kister, 1992), have published design and operating recommendations as well as control strategies for industrial distillation plants. However, the approaches established for industrial distillation plants may not be applicable to performance test columns due to their differing modes of operation (Cai, 2014).

The specific procedures and plant setups used for column tests or packing characterization experiments commonly depend on best practices individually defined by each testing facility. A standardized procedure comparable to (VDI 2761 Part 2, 2020), which was established for mass transfer investigations based on ab-/desorption, is not yet available for distillation. The procedures used by *SRP*, *FRI* or packing manufacturers are commonly considered very sound, but are either not published in detail or are not publicly available at all. However, an extensive testing procedure was published by (Starkweather et al., 2014). Furthermore, several authors cite a conference contribution by (Olujić, 2008) which summarized established testing procedures and best practices. However, this literature reference could not be retrieved from any of the cited online sources. Therefore, a brief overview of the core aspects from the reviewed literature is given below.

Bed Height and Diameter Regarding the height of the packed bed, (Cai, 2014) suggested installing an equivalent of $10 \ldots 15$ theoretical stages in total. Since shorter beds show better separation performance due to a decreasing maldistribution, (Ottenbacher et al., 2011) recommended bed heights equivalent to around 20 theoretical stages in total, whereas each single bed should contain $10 \ldots 20$ stages. However, smaller bed heights should generally be preferred for mixtures with high relative volatilities to prevent highly diluted and highly concentrated samples (Starkweather et al., 2014). Since separation performance measurements should be conducted in a similar concentration range to ensure comparable results (Ottenbacher et al., 2011; Valenz

et al., 2013), initial mixture concentration, bed height and test mixture selection are related to each other. Regarding the column dimensions, (Ottenbacher et al., 2011) proposed a diameter of 0.4 m for a packing with a specific surface area of $200\,m^2\,m^{-3}$ and at least a 20-fold hydraulic diameter for smaller packings. This is in accordance with (Billet, 1979) who claimed that wall effects show a significant influence for column diameters of less than 300 mm, but contrary to the findings of (Meier et al., 1979) or (Valenz et al., 2013) in which there was no influence of diameter. (Schoenmakers and Spiegel, 2014) considered a column diameter of 50 mm as sufficient and stated that using smaller columns with diameters of 30 mm or less should be investigated.

Vapor and Liquid Distribution While vapor distribution is considered a minor concern (Ottenbacher et al., 2011), a proper liquid distribution is essential to achieve a representative distillation performance. An extensive review on maldistribution was published by (Spiegel, 2018). However, the capacity of the distributors installed in the column needs to be higher than the maximum capacity of the packing under investigation to prevent any limitations in the vapor or liquid loads. A proper liquid distribution can commonly be achieved with drip point densities of $100 \ldots 150\,m^{-2}$ (Cai, 2014). (Ottenbacher et al., 2011) suggested $150\,m^{-2}$ drip points for a packing of $500\,m^2\,m^{-3}$ to prevent maldistribution. A systematic approach to estimate the required number of drip points based on the packing corrugation geometry was proposed by (Cai et al., 2018). Furthermore, the liquid distributor should be placed directly on top of the packed bed to mitigate liquid entrainment and should not cover more than $25 \ldots 45\,\%$ of the cross-sectional area of the column (Cai, 2014; Ottenbacher et al., 2011), whereas larger open cross-sectional areas may be required for low-pressure test systems due to higher vapor loads. To mitigate end effects at the lower end of the bed, a liquid collector should be installed around one column diameter below the packings (Ottenbacher et al., 2011) and can also be used for liquid sampling (Cai, 2014). Similarly, liquid collection and redistribution may be required, if the packed bed is split into several sections.

Reboiler, Condenser and Auxiliary Equipment The reboiler is considered as one of the most common issues in distillation operation, and thus a proper design according to the required vapor load and operating conditions is required (Cai, 2014). Since the liquid holdup inside the packings changes with the column load, buffer tanks are required to regulate bottom liquid level and reflux flow (Cai, 2014). However, such tanks are usually omitted if the surplus liquid can be collected in the reboiler or the bottom section of the column (Cai, 2014).

Instrumentation The process parameters measured during plant operation commonly include absolute column head pressure, differential pressure along the packed bed, temperatures and flow rates (Cai, 2014). The column head pressure should be measured with suitable accuracy, since it is used for column pressure control. Measuring the pressure drop along the packed bed (or sections thereof) allows identifying the (local) column load regime and flooding in particular (Ottenbacher et al., 2011). However, high accuracy pressure sensors with sufficient

resolution may be required for small bed heights due to their low pressure drops. Furthermore, pressure taps and pressure lines need to be installed properly[29], since pressure measurements are susceptible to fluctuations due to liquid droplets or blockages. Condensate inside the pressure lines should be prevented with an inert gas purge[30]. Temperature measurements around the reboiler and the condenser are essential for closing the energy balances and should be carried out with an accuracy suitable to close the energy balances within reasonable margins. Therefore, (Cai, 2014) suggests calibrating all temperature sensors prior to the installation and to use resistance temperature detectors (RTD) instead of thermocouples (TC), since the latter are commonly less accurate. Furthermore, measuring liquid temperatures should be preferred over measuring vapor temperatures as the latter is more difficult to perform reliably (Cai, 2014). Nevertheless, temperature readings along the column are of less importance, since the according temperature profiles can be sufficiently estimated with computer calculations based on the mixture compositions (Starkweather et al., 2014). However, placing multiple temperature sensors along the column circumference at the same axial position can be helpful to identify potential maldistribution (Ottenbacher et al., 2011) which is especially relevant for columns with larger diameters (Cai, 2014).

Operation and Control Although the full operating region of the installed packing is investigated during separation performance experiments, the minimum load is often considered to be 20 % of the load at the flood point (Cai, 2014). Furthermore, total reflux operation is chosen to avoid composition pinches and uncertainties in the reflux ratio (Cai, 2014). To ensure stable plant operation, column pressure, reboiler level and, if applicable, tank levels are controlled by manipulating reboiler and condenser duties (Cai, 2014). As the influence of a subcooled reflux on the resulting separation performance is commonly considered negligible, the reflux is most often not preheated (Cai, 2014). (Ottenbacher et al., 2011) suggest a maximum subcooling of $5 \ldots 10\,\mathrm{K}$ below the boiling point of the reflux mixture, (Eckert and Walter, 1964) found $3 \ldots 5\,\mathrm{K}$ to be reasonable. However, for highly subcooled reflux streams, (Kister, 1992) recommends providing an additional theoretical stage to ensure proper reflux preheating. Regarding the steady-state operation, (Cai, 2014) distinguishes hydraulic and mass transfer steady state. Hydraulic steady state is characterized by constant pressure drops, liquid holdups and flow velocities. It should be reached $30 \ldots 60\,\mathrm{min}$ after column start-up and can be easily identified based on the pressure drop readings (Cai, 2014). Mass transfer steady state is reached after $2 \ldots 3\,\mathrm{h}$ and characterized by constant concentration and temperature profiles (Cai, 2014). However, temperature readings are usually considered not accurate enough to evaluate steady-state operation, and thus compositional analyses should be carried out to identify mass transfer steady state (Cai, 2014).

[29] Criteria about pressure tap placement and tap geometry are given by (Cai, 2014; Starkweather et al., 2014).
[30] An inert gas purge requires a pressure correction, see (Cai, 2014) for details. Alternative purging strategies are elaborated by (Cai, 2014; Starkweather et al., 2014).

Sampling and Sample Analysis Samples should be taken from suitable locations such as liquid collectors and distributors, reboiler, reflux line, tanks, pump outlets etc. to ensure representative samples (Cai, 2014). Samples from inside the packings can be drawn with bayonet or cross samplers (Cai, 2014), but these approaches are often only applicable to columns with larger diameters due to geometrical restrictions. Representative liquid sampling can be achieved more easily than vapor sampling and should thus be preferred (Cai, 2014; Starkweather et al., 2014). Nevertheless, vapor samples may be taken to obtain additional information about column performance (Cai, 2014; Meier et al., 1979; Starkweather et al., 2014). While (Eckert and Walter, 1964) performed sampling from the reboiler (kettle type reboiler) and the distillate pot, (Meier et al., 1979; Ottenbacher et al., 2011) took liquid samples directly below the packed bed, since liquid from the column bottom may not be representative due to additional mass transfer below the packed bed (end effect). According to (Kister, 1992), the FRI implemented a segmental sampling technique to obtain a concentration profile along the packed bed which is used to quantify the packing performance. Regardless of the specific sampling method, samples are commonly taken in duplicate and analyzed by gas chromatography (Cai, 2014). Sampling lines should be as short as possible to minimize the required purge volume; a diameter of $3 \ldots 6\,\mathrm{mm}$ is considered sufficient for most applications (Cai, 2014).

Balances While the column load can be estimated based on the energy balance of either the condenser or the reboiler, the latter approach is commonly considered more accurate (Cai, 2014). According to (Cai, 2014), both the individual and the overall energy balances should be closed within $\pm 5\,\%$ to allow a systematic error analysis. Therefore, flow and temperature sensors (see above) with an appropriate accuracy are required (Starkweather et al., 2014). To reduce heat losses, suitable column insulation is recommended. (Bradtmöller, 2017; Bradtmöller and Scholl, 2015) used a vacuum jacketed column, whereas the column used by (Eckert and Walter, 1964) was equipped with an electrical trace heating and insulation. However, (Schoenmakers and Spiegel, 2014) highlighted the trade-off between passive and active countermeasures to reduce heat losses (insulation or vacuum jacket vs. trace heating), since a completely heat-neutral operation cannot be reached with either of these methods. Regarding flow measurements of utility streams, (Cai, 2014) suggested using *Coriolis mass flow meters* as their readings are highly accurate and independent of mixture properties (density, temperature, composition etc.). Regarding the mass balance, (Cai, 2014) claimed a maximum deviation of $\pm 2\,\%$ to be acceptable, whereas (Starkweather et al., 2014) specified $\pm 5\,\%$ and $\pm 10\,\%$ for very complex mixtures, respectively.

Data Evaluation Prior to separation performance quantification, recorded raw data should be reduced in order to verify steady-state operation (Cai, 2014). Furthermore, mass and energy balances need to be within the tolerances given above. Multiple measures for separation performance quantification were discussed in section 2.2. However, HETP are commonly used to quantify separation performance for distillation, whereas HTU are preferred for ab-/desorption

(Starkweather et al., 2014). A comparison of both concepts was given in section 2.2.3.4. To improve the accuracy of the estimated separation performance, a stagewise or segmental evaluation can be beneficial. In addition, the influence of an increase in internal reflux due to a subcooled reflux stream or heat losses should be evaluated for both column performance and hydraulics (Cai, 2014; Ottenbacher et al., 2011). Comparing the results obtained from separation performance experiments with those obtained from comparable computer simulations allows identifying experimental errors (Starkweather et al., 2014). Common sources of uncertainties in separation performance estimations are discussed in section 2.3.3.

2.3.2.2. Partial Reflux and Non-Volatile Mixture Components

Investigations with partial reflux were already cited in section 2.2.4. However, except for (Eckert and Walter, 1964), detailed descriptions of the plant setups employed are not provided in the literature references.

To allow experiments with both total and partial reflux, (Eckert and Walter, 1964) split the condensate into a reflux and a distillate stream. Disregarding the specific reflux ratio, the reflux stream was preheated to a temperature of $3 \ldots 5\,\mathrm{K}$ below the boiling point and distributed above the packed bed. In partial reflux operation, surplus distillate was fed into the reboiler reservoir (kettle type reboiler). To quantify the separation performance, liquid samples were taken from the distillate and the reboiler.

Furthermore, (Böcker and Ronge, 2005) investigated the distillation of viscous mixtures. Since the test mixture CB/EB/PBD containing a non-volatile component was used for the investigations, partial reflux operation and an alternative plant setup were required (Böcker and Ronge, 2005). The procedure proposed by (Böcker and Ronge, 2005) is based on a stripping column: The feed stream, which consists of CB/PBD, is distributed above the packing and vaporized EB was fed to the bottom of the column to achieve a countercurrent vapor/liquid flow. As the non-volatile PBD does not participate in the vapor/liquid mass transfer inside the packed bed, an overhead vapor of CB/EB and a bottom product of CB/EB/PBD is obtained (Böcker and Ronge, 2005). To quantify separation performance, the number of theoretical stages was estimated based on McCabe-Thiele stage constructions for which liquid samples were drawn from distillate and bottom product streams.

Regardless of the specific plant concept, experiments with partial reflux may result in concentration pinches between the operating line and equilibrium curve. Furthermore, the internal reflux can be significantly higher than the external reflux if condensation occurs inside the column due to significant heat losses. In such a case, the operating line may even intersect the equilibrium line (Böcker and Ronge, 2005). Therefore, a suitable (external) reflux ratio needs to be chosen to ensure stable plant operation and a robust data evaluation.

2.3.3. Sources of Uncertainties

As shown in section 2.2, separation performance can be quantified in terms of different measures. Nonetheless, HETP values estimated based on the number of theoretical stages are used most often. Recalling Fenske's equation from equation (2.21) allows identifying the mixture compositions x_B and x_D as well as the relative volatility α_{12} as relevant sources of uncertainties.

The influence of the uncertainty associated with α_{12} was discussed by e.g. (Coulson and Herington, 1948; Deibele and Brandt, 1985; Kister, 1992; Peacock, 1967; Zeck, 1990). For $\alpha_{12} = \text{const.}$, (Kister, 1992; Zeck, 1990) state that the effect of uncertainty on the resulting number of theoretical stages may become insignificant, if mixtures with $\alpha_{12} \geq 1.5 \ldots 2.0$ are used. However, since most test mixtures show lower relative volatilities, its associated uncertainty may result in deviations of up to 20 % for the estimated number of theoretical stages (Zeck, 1990). If the relative volatility depends on pressure or mixture composition, such that $\alpha_{12} \neq \text{const.}$, the uncertainties attributed to these parameters should be considered in addition.

Uncertainties in x_B and x_D are related to both sampling procedure and sample analysis. The influence of improper sampling can hardly be quantified as several assumptions and estimates would be required (sample cross-contamination due to improper purge, influence of badly placed sampling tap …). The uncertainty in sample analysis is commonly attributed to both analysis equipment and procedure (accuracy, calibration, robustness of analysis method …) and can, therefore, be quantified based on characteristic parameters of the laboratory procedure or analysis method.

However, the uncertainty in sample or mixture composition is not only relevant to quantify the separation performance but also required to estimate physical properties such as mixture density, surface tension, viscosity or diffusion coefficients which may be used for further data processing and evaluation. In such cases, the used property models as well as corresponding scope and assumptions need to be evaluated carefully (Zeck, 1990).

Since separation performance is often related to the liquid or vapor load, uncertainties of operational parameters, e.g. flow rates, temperatures, total pressure and pressure drops, need also be addressed (Cai, 2014; Starkweather et al., 2014). General considerations about sensor accuracy and precision were discussed in section 2.3.2.1. Uncertainties in operational parameters commonly result from instrumentation and control equipment (pressure and temperature sensors, pumps, valves, controllers …). Information about accuracy and precision of instrumentation or control equipment, which is required for uncertainty quantification, is commonly obtained from the corresponding manufacturer's specifications. However, additional uncertainties due to the electrical or mechanical connections should be considered for some type of sensors (pressure lines, cold junction compensation …). To reduce the related uncertainties, (Cai, 2014; Starkweather et al., 2014) suggest calibrating and checking plant instrumentation on a regular basis. Furthermore, (Cai, 2014; Starkweather et al., 2014) consider an operating state falsely identified as steady state or disruptions to a previously achieved steady state as additional sources of uncertainties. Such cases should be mitigated by optimizing the operational procedure and can be excluded

from further evaluation during data reconciliation. The uncertainty attributed to the reflux ratio is usually not addressed, since most separation performance experiments are conducted at total reflux. However, partial reflux increases the number of parameters to consider for separation performance experiments. Depending on the plant concept used for partial reflux experiments, this may require additional plant equipment of which the attributed uncertainties need to be addressed as well[31].

[31] A detailed elaboration on deviations of reflux ratio and relative volatility with respect to the number of theoretical stages, which is beneficial for column troubleshooting, can be found in (Kister, 1992).

3. Alternative Method for Separation Performance Experiments

3.1. Necessity for an Alternative Approach

Since most industrial multistage distillation processes are operated at partial reflux, total reflux is only relevant for very few applications such as the start-up of batch distillation columns (Edwards, 2013), the repetitive total reflux mode to separate trace components in batch distillation (Edwards, 2013) or the reaction phase in reactive distillation (Lee et al., 2000). Therefore, investigating the separation performance of mass transfer equipment at total reflux, as elaborated in section 2.3, seems contradictory to its industrial relevance, but allows a simplified experimental procedure and reduces associated uncertainties.

Nevertheless, (Wang et al., 2005a) pointed out that established mass transfer correlations are developed based on results from total reflux experiments and suggested consolidating the calculation models with partial reflux measurements. This is especially relevant, since partial reflux operating conditions are required to investigate the separation performance for mixtures with inert or non-volatile components. Applications with such mixtures include:

- viscous distillation with polymer-enhanced mixtures as described by e.g. (Böcker and Ronge, 2005; Bradtmöller, 2017; Gutperl and Scholl, 2018; Gutperl et al., 2022)
- distillation with surfactant-enhanced mixtures to investigate the influence of mixture surface tension on separation performance as discussed by e.g. (Berg, 1988)
- distillation of foaming mixtures which contain suspended particles or anti-foaming agents as investigated by e.g. (Staud et al., 2023)
- recycling of complex feedstocks containing dissolved solids as relevant for e.g. polymer recycling (Peters et al., 2019a; Peters et al., 2019b) or offshore oil and gas production (Schlumberger, 2021)

A method suitable to conduct separation performance experiments for the aforementioned model consolidation and process applications is not known in the literature. Development, characterization and evaluation of a suitable experimental methodology are, therefore, the subjects of this work.

3.2. Research Hypotheses and Objectives

To systematically investigate the separation performance related to the applications given in section 3.1 with respect to the theoretical background and literature review provided in sections 2.2 and 2.3, the following research hypotheses and objectives are defined:

1. A binary liquid mixture with an additional non-volatile component, which does not evaporate, is considered. Although this results in a ternary mixture, the correlations for mixture separation and mass transfer are assumed to remain unaffected as the non-volatile component is highly diluted and fully dissolvable in both liquid mixture components. By assuming equimolar mass transfer from vapor to liquid and vice versa, the concentration of the non-volatile component should, therefore, remain reasonably constant along the entire height of the packed bed.

2. As the non-volatile component does not evaporate, it needs to be constantly fed into the column and distributed above the packed bed. For this, the non-volatile component should be premixed with a suitable liquid stream such as reflux or feed. Furthermore, accumulation of the non-volatile in the bottom section of the column should be prevented by a bottom product purge. This requires partial reflux due to the in- and output streams.

3. The plant concept to be developed should support both partial and total reflux to not only increase operational flexibility but also to enable a reasonable comparability with conventional separation performance measurements at total reflux.

4. A suitable reflux ratio for partial reflux experiments should be chosen so that concentration pinches between the operating and equilibrium lines are prevented and a robust data evaluation is ensured. However, material and component balances may limit the usable reflux ratio due to concentration-dependent mixture properties. In such cases, a reasonable trade-off between data and operational robustness needs to be achieved.

5. The separation performance obtained from experiments with the alternative plant setup may be affected by both mixture-related effects and the operational behavior of the distillation plant. Therefore, plant characterization and evaluation should be performed with a well-known and established binary test mixture satisfying the requirements given in section 2.3.1.

3.3. Distillation Plant

3.3.1. Development

Plant setup development was based on the plant concepts published by (Böcker and Ronge, 2005; Eckert and Walter, 1964), which were briefly described in section 2.3.2.2. Since the reflux stream consists of condensed overhead vapors, the approach used by (Eckert and Walter, 1964)

is widely comparable to the setups commonly used for continuous distillation. However, the remaining distillate stream is not withdrawn as a product stream, but fed into the reboiler reservoir (reboiler reservoir input stream). While no additional buffer tanks are required in this approach, feeding the distillate stream, which is rich in the more volatile component, influences the bottom mixture composition. The setup used by (Eckert and Walter, 1964) is not suitable for partial reflux experiments with mixtures containing a non-volatile component as it is impossible to add this component to the reflux stream. Furthermore, adding a bottom purge stream does not seem to be reasonable as this would counteract storing surplus distillate in the reboiler reservoir.

Contrary to the setup by (Eckert and Walter, 1964), the concept proposed by (Böcker and Ronge, 2005) was especially developed in the context of investigating viscous distillation with polymer-enhanced mixtures. Therefore, this plant concept can directly be used with test mixtures containing non-volatile components. As already described in section 2.3.2.2, (Böcker and Ronge, 2005) used two independent feed streams, which allows varying the slope of the operating line. Although this prevents concentration pinches and ensures a robust data evaluation, large feedstock volumes are required. Assuming operating conditions close to total reflux, a feed mass flow of $20\,\mathrm{kg\,h^{-1}}$, a plant start-up time of 1.5 h and a minimum steady-state operation of 2 h, at least 70 kg of feedstock are required for each input stream. Tanks of similar capacity are needed to collect the product streams. Furthermore, an additional plant is required to recover the feedstock components from the obtained product mixtures. Although (Böcker and Ronge, 2005) claim that this effort is beneficial to achieve a short plant start-up, its is most unlikely to be carried out with the laboratory infrastructure available at non-industrial research facilities. Therefore, a plant concept suitable for separation performance measurements fulfilling the criteria defined in sections 3.1 and 3.2 was developed by adding external recycle streams, see figure 3.1a.

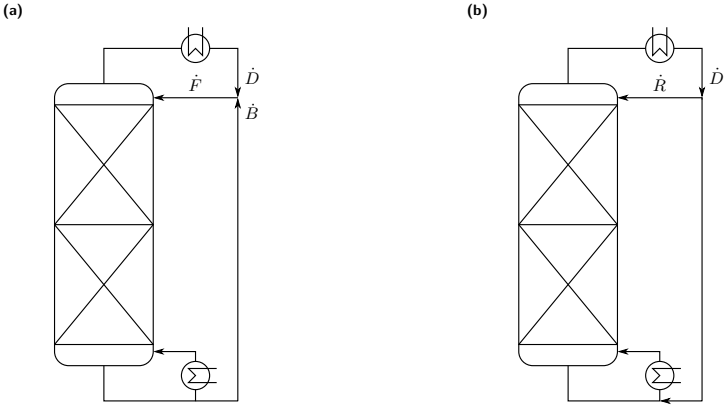

Figure 3.1.: Stream arrangements of plant concepts for separation performance experiments with both total and partial reflux; (a): stream arrangement of plant concept developed for own investigations, based on (Gutperl et al., 2022); (b): stream arrangement of plant concept by (Eckert and Walter, 1964), based on (Eckert and Walter, 1964)

The external recycle streams do not only reduce the required amount of feedstock but also supersede the mixture recovery after each experiment. Comparing the stream arrangement of the developed plant concept as illustrated in figure 3.1a with the stream arrangement by (Eckert and Walter, 1964), which is depicted in figure 3.1b, reveals that both concepts only differ in the flow direction of the reboiler input stream. While (Eckert and Walter, 1964) fed surplus distillate into the reboiler which does not allow using mixtures containing non-volatile components, the concept developed in this work uses a bottom purge to enable the use of such mixtures.

3.3.2. Description

To simplify equipment and instrumentation tagging, the seven functional units listed in table 3.1 were defined. A simplified process flow diagram of the distillation plant is depicted in figure 3.2. A detailed piping and instrumentation diagram can be found in appendix A.1, detailed equipment and instrumentation lists are given in appendix A.2.

Table 3.1.: Functional units of distillation plant

tag	description
100	column head section, overhead vapors and distillate
200	column main section and packed bed
300	column bottom section, reboiler and bottoms purge
400	underfloor weighing for product mass flow quantification
500	recycle tank
600	feedstock tank
700	vacuum generation and distribution

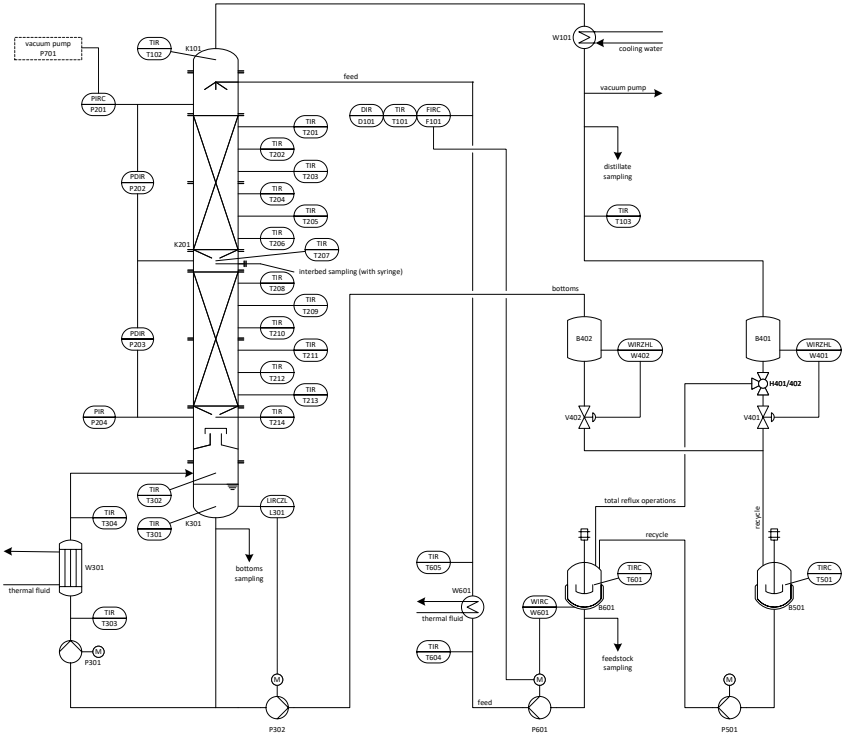

Figure 3.2.: Simplified process flow diagram of distillation plant

Distillation Column (functional units 100, 200 & 300)

The distillation column consists of four borosilicate glass column segments with a nominal diameter of 50 mm (DN50) and a height of 700 mm each. Corrugated metal sheet packings of type *Mellapak M500.Y* (Sulzer Chemtech, Winterthur/Switzerland) with a nominal specific surface area of 500 $m^2\,m^{-3}$ are installed in two separate bed sections with a height of 1224 mm each, resulting in a total bed height of 2448 mm. The packing geometry of the packing elements was characterized in previous research activities, see (Bradtmöller, 2017; Bradtmöller and Scholl, 2015) for details. Geometric dimensions relevant for this work are summarized in table A.1. The column segments are arranged in pairs of two and stacked on top of each other with a column coupling piece in between. While each column segment is equipped with a vacuum jacket and reflective coating to reduce heat losses and internal condensation, the column head section K101 and the column bottom section K301 as well as the coupling piece are single-walled, but equipped with trace heatings and insulation.

To ensure a proper distribution of the liquid feed above the packed bed, a four-point distributor (4970 drip points per m^2, in-house design, see (Gutperl, 2016)) is used. Furthermore, a funnel-like liquid collector and redistributor (single central drip point) is installed in the coupling piece to ensure liquid redistribution between the bed sections. For liquid and vapor distribution inside the packed bed, each packing element is rotated by 90°.

Using the binary test mixture chlorobenzene/ethylbenzene, f-factors of up to $f_G = 3.2\,Pa^{0.5}$ can be realized with a forced circulation shell and tube evaporator equipped with seven tubes of 18×2 mm in diameter and 1400 mm in length (W301). Wire matrix turbulators (full tube length, *hiTRAN Thermal Systems*, Calgavin, Alcester/UK) are inserted into the reboiler tubes to enhance the thermal performance and improve reboiler operation which is beneficial for viscous distillation. Depending on the required heat duty, the evaporator is heated by circulation thermostats WE301 and WE302 with a maximum heat duty of 2 kW_{th} each. The reboiler setup allows varying the gas load based on the heating utility temperature (setpoint for circulation thermostats), the heating utility flow rate (gear pump P302) or the reboiler circulation rate (gear pump P301). Reboiler circulation rate and heating utility mass flow are not measured due to geometrical restrictions which did not allow the installation of suitable mass flow sensors. *Renolin Therm 320* (Fuchs Lubricants, Mannheim/Germany) is used as the thermal fluid for all circulation thermostats. Depending on the operating mode, a two-point controller is used to control the liquid level in the column bottom section based on level switch L301. Surplus liquid is purged with gear pump P302.

Quantification of Product Mass Flows (functional unit 400)

Distillate and bottom product were intermittently collected in trace-heated product tanks B401 and B402, respectively, (in-house design, capacity ca. 3 L) to quantity the product mass flows by underfloor weighing (W401 and W402). To automatically dispose the collected liquid into the recycle tank B501, the solenoid valves V401 and V402 are used.

Feedstock and Recycle Tanks (functional units 500 & 600)

The (initial) feedstock is stored in the heat-jacketed tank B601. Feed mass flows of $2 \ldots 20\,\mathrm{kg\,h^{-1}}$ can be realized by gear pump P601 and are either controlled by Coriolis mass flow meter F101 or controlled based on the total mass of the feedstock tank measured with scale W601. Depending on the operating mode, the recycle streams are collected in the recycle tank B501 during plant start-up. After steady-state operation is reached, collected liquid can cyclically be transferred into feedstock tank B601 using gear pump P501. The annular heat exchanger W601 and a feed line trace heating are used to preheat the feed stream. In- and outlet temperatures of W601 are measured by type T thermocouples. In addition, feed mixture density and temperature are quantified by the Coriolis mass flow meter (D101 & T101).

Vacuum Generation and Distribution (functional unit 700)

Vacuum pump P701 allows vacuum operation with column operating pressures of $p_\mathrm{h} \geq 40\,\mathrm{mbar(a)}$. The additional condenser W701 and cold trap B701 prevent remaining vapors from entering the vacuum pump. Vacuum is distributed to the distillate line, tanks B401 and B402 as well as B501 and B601. Furthermore, nitrogen inertization can be carried out via the ball valve H702.

Column Profiles

The temperature profile along the column is measured with 17 Pt100 class A temperature sensors. Prior installation, all temperature sensors were calibrated, see appendix A.5. Pressures at the column head and bottom sections are quantified by absolute pressure sensors (P201 & P204), differential pressures for each bed were measured with differential pressure sensors (P202 & P203). All pressure lines directly connected to the column are inclined and equipped with small heat exchangers to mitigate condensation droplets inside the pressure lines which may affect the pressure measurements negatively.

Sampling

Each sampling point is equipped with two ball valves to allow liquid sampling during vacuum operation. Liquid samples are directly taken from the distillate (H101 & H102), the column bottom section (H301 & H302), the feedstock tank (H602 & H603) and the recycle tank (H502 & H503). Furthermore, an additional sample can be drawn from the liquid dripping of the liquid collector installed in the column coupling piece using a syringe (inter-bed sampling). However, to reduce the risk of disruptions due to septum ruptures during steady-state operation, inter-bed sampling should only be done occasionally and the septum should be replaced after each experiment.

Data Recording

For an automated plant operation with different operating modes, process control and data recording was implemented in *LabVIEW 2015* (National Instruments Corp., Austin/TX). Recorded process data are saved to CSV files (comma-separated values) and need to be evaluated after the experiment is completed.

While the feed mass flow and weighing values are directly obtained from the devices via their digital interfaces (RS232 or RS485), analog data acquisition is required for all pressure sensors and most of the temperature sensors. To read analog signals, two data recorders, each equipped with two data acquisition modules, are used in parallel which allows data acquisition cycles of around 2 . . . 3 s. Detailed information about the used data recorders and modules are summarized in appendix A.4.

Operating Modes

To investigate the separation performance at both total and partial reflux conditions, two different operating modes are implemented in the plant control software. However, the following operating parameters are set by the operator regardless of the operating mode: operating pressure, thermostat and trace heating temperatures, cycle duty for liquid level controller L301 (typically 50 %), setpoints for variable-frequency drives of reboiler circulation and thermal fluid pumps, setpoint for control voltage of pump P302 (typically 5 V), en-/disable stirrers S501 and S601. The stream ratio $\dot{m}_\mathrm{F}\,\dot{m}_\mathrm{D}^{-1}$ is calculated based on the measured mass flows, but not controlled automatically. Therefore, the reboiler duty needs to be adjusted accordingly by the operator. In partial reflux operating mode, distillate and bottom product streams are, as already elaborated, drawn from the column, collected in the recycle tank B501 and cyclically re-used as feedstock. According to the feed mass flow specified by the user, feed pump P601 is controlled by the Coriolis mass flow meter F101. Furthermore, pump P302 is activated automatically to control the liquid level measured by level switch L301. Solenoid valves V401 and V402 are actuated cyclically to measure the bottoms and distillate mass flows by weighing tanks B401 and B402. Recycle tank B501 is emptied by pump P501 as soon as a liquid level is detected by L501. Since no bottom product is purged from the column bottoms section in total reflux mode, the according liquid level needs to be manually controlled by the operator. Furthermore, valve V401 is constantly kept open and recycle tank B501 is bypassed, such that any distillate is directly collected in the feedstock tank B601. In order to achieve total reflux operation, the feed mass flow is controlled by scale W601, whereas mass flow meter F101 is only used for quantification. In addition to the total and partial reflux operating modes, simulated total reflux can be obtained by setting $\dot{m}_\mathrm{F}\,\dot{m}_\mathrm{D}^{-1} = 1$ in partial reflux mode. Although the underlying column mass balances for conventional total and simulated total reflux are the same, both operating conditions may differ due to the control structures implemented in the plant control system. Therefore, simulated total reflux allows investigating the transition between total reflux and partial reflux operating modes.

Start-Up and Shutdown

To simplify start-up and shutdown, additional plant equipment is installed. Before plant intertization and start-up, remaining liquid needs to be drained from all sampling taps as well as the vacuum pump and vacuum distribution system (H701 & H703). Ball valve H702 allows nitrogen intertization. Furthermore, the column bottom section filling line (V601 & V301) can be used to redirect the feed stream into the reboiler and column bottom section. This is especially useful to prefill the according equipment with feedstock mixture for reboiler preheating and a reduced start-up duration. Since semi-automatic filling is supported by the plant control system, manual start-up preparation tasks can be done in parallel. Similarly, a semi-automated plant shutdown procedure allows emptying the column bottom section. The reboiler thermostats are shut off and the liquid is pumped into the recycle tank B501. The shutdown procedure needs to be stopped manually prior pump P302 runs dry. After all liquid is collected in tank B501, pump P501 can be used to transfer the liquid into the feedstock tank B601.

3.3.3. Operation

3.3.3.1. Operational Characteristics

To discuss the operational characteristics of the proposed plant concept, constant molar overflow and a boiling liquid feed are assumed. Combining the stream arrangement of the proposed plant concept illustrated in figure 3.1a with the nomenclature introduced in figure 2.2 results in:

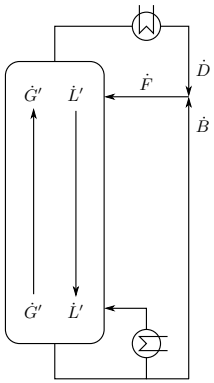

Figure 3.3.: External and internal streams of proposed plant concept

The feed mass flow $\dot{m}_{\mathrm{F}}$ and the slope of the SOL need to be defined for plant operation. While the former is directly available as an operational parameter, the latter is specified indirectly. Recalling its definition from equation (2.29) and applying the streams from figure 3.3 defines

the molar stream ratio $\dot{F}\,\dot{D}^{-1}$:

$$\tan\beta_{\mathrm{SOL}} \underset{(2.29)}{=} \frac{\dot{L}'}{\dot{G}'} \approx \frac{\dot{F}}{\dot{D}} \tag{3.1}$$

The molar feed flow $\dot{F}$ and the molar distillate flow $\dot{D}$ can be calculated from the mass flows $\dot{m}_{\mathrm{F}}$ and $\dot{m}_{\mathrm{D}}$ as well as the molar mass of the according stream:

$$\dot{F} = \frac{\dot{m}_{\mathrm{F}}}{M_{\mathrm{F}}} \tag{3.2a}$$

$$\dot{D} = \frac{\dot{m}_{\mathrm{D}}}{M_{\mathrm{D}}} \tag{3.2b}$$

$$\Longrightarrow \frac{\dot{F}}{\dot{D}} = \frac{\dot{m}_{\mathrm{F}}}{\dot{m}_{\mathrm{D}}}\,\frac{M_{\mathrm{D}}}{M_{\mathrm{F}}} \tag{3.2c}$$

Equation (3.2c) is important for experiment planning and plant operation. According to equation (3.1), $\dot{F}\,\dot{D}^{-1}$ is required for data evaluation. However, the molar stream ratio is not accessible during an experiment as the molar masses M_{F} and M_{D} depend on the according mixture composition. Corresponding molar fractions x_i are unknown during plant operation, since the distillation plant is not equipped with in- or online sample analysis and mixture compositions are determined offline. Therefore, only $\dot{m}_{\mathrm{F}}\,\dot{m}_{\mathrm{D}}^{-1}$ is available for process control. Using $\dot{m}_{\mathrm{F}}\,\dot{m}_{\mathrm{D}}^{-1}$ during plant operation and $\dot{F}\,\dot{D}^{-1}$ for experiment evaluation may result in a notable deviation which can be determined based on equations (3.2c) and (C.1).

Considering a binary mixture results in:

$$\frac{\dot{F}}{\dot{D}} = \frac{\dot{m}_{\mathrm{F}}}{\dot{m}_{\mathrm{D}}}\,\frac{M_{\mathrm{D}}}{M_{\mathrm{F}}} = \frac{\dot{m}_{\mathrm{F}}}{\dot{m}_{\mathrm{D}}} \cdot \frac{x_{\mathrm{D}}\,M_1 + (1-x_{\mathrm{D}})\,M_2}{x_{\mathrm{F}}\,M_1 + (1-x_{\mathrm{F}})\,M_2} = \frac{\dot{m}_{\mathrm{F}}}{\dot{m}_{\mathrm{D}}} \cdot \frac{x_{\mathrm{D}}\,(M_1-M_2) + M_2}{x_{\mathrm{F}}\,(M_1-M_2) + M_2} \tag{3.3}$$

Using equation (3.3) to define two non-linear optimization problems allows estimating the minimum and maximum deviation between $\dot{F}\,\dot{D}^{-1}$ and $\dot{m}_{\mathrm{F}}\,\dot{m}_{\mathrm{D}}^{-1}$ according to equations (3.4) and (3.5):

$$\begin{aligned} \min \quad & \frac{x_{\mathrm{D}}\,(M_1-M_2) + M_2}{x_{\mathrm{F}}\,(M_1-M_2) + M_2} \\ \text{s.t.} \quad & 0 \le x_{\mathrm{D}} \le 1, \\ & 0 \le x_{\mathrm{F}} \le 1 \end{aligned} \tag{3.4}$$

$$\begin{aligned} \max \quad & \frac{x_{\mathrm{D}}\,(M_1-M_2) + M_2}{x_{\mathrm{F}}\,(M_1-M_2) + M_2} \\ \text{s.t.} \quad & 0 \le x_{\mathrm{D}} \le 1, \\ & 0 \le x_{\mathrm{F}} \le 1 \end{aligned} \tag{3.5}$$

Assuming a binary mixture of chlorobenzene and ethylbenzene, equations (3.4) and (3.5) were implemented in *Julia* and solved with the optimizer *Ipopt*[1]. Required molar masses are given in table C.1, interpreted calculation results are summarized in table 3.2.

Table 3.2.: Molar mass ratio $M_\mathrm{D}\,M_\mathrm{F}^{-1}$ as factor of proportionality between stream ratios $\dot{F}\,\dot{D}^{-1}$ and $\dot{m}_\mathrm{F}\,\dot{m}_\mathrm{D}^{-1}$ for binary mixture CB/EB

	unit	minimum	maximum
$M_\mathrm{D}\,M_\mathrm{F}^{-1}$	-	0.94	1.06
at x_D	$\mathrm{kmol_l\,kmol_{tot}^{-1}}$	0.00	1.00
at x_F	$\mathrm{kmol_l\,kmol_{tot}^{-1}}$	1.00	0.00

The resulting deviation can be interpreted as $\pm 6\,\%$. To validate the optimization results, equation (3.3) was solved analytically and equal results were obtained, see figure 3.4. In experimental investigations, however, molar fractions x_D and x_F substantially differ from $x_i = 0\,\mathrm{kmol_l\,kmol_{tot}^{-1}}$ or $x_i = 1\,\mathrm{kmol_l\,kmol_{tot}^{-1}}$. Therefore, smaller deviations are to be expected typically. Similar considerations for a ternary mixture containing a non-volatile component are shown in appendix A.6.2.

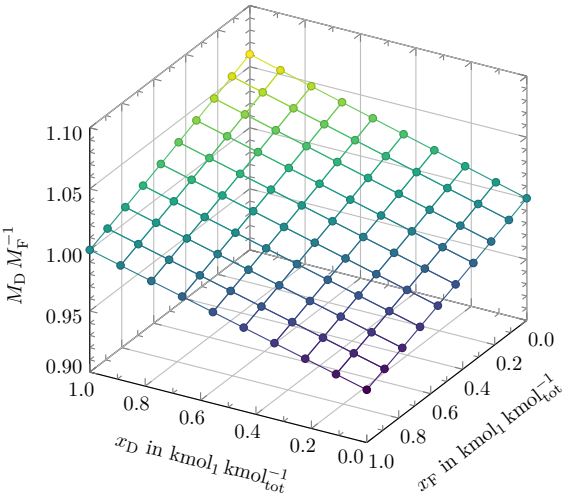

Figure 3.4.: Molar mass ratio $M_\mathrm{D}\,M_\mathrm{F}^{-1}$ in dependence of distillate (x_D) and feed (x_F) molar fractions

For a ternary mixture with a non-volatile component (component 3), the stream ratio defined in equation (3.2c) is restricted by the component balance of the non-volatile mixture component.

[1]The non-linear optimization problems were implemented in *Julia* (Bezanson et al., 2017) using the *JuMP* modeling language (Lubin et al., 2023) and solved with the *Ipopt* optimizer (Wächter and Biegler, 2006). The according code is attached in listing A.1.

Since the non-volatile component does not evaporate and entrainment is neglected, it is only present in the feedstock and the bottom product. Therefore, $w_{3,\mathrm{D}} = 0\,\mathrm{kg_3\,kg_{tot}^{-1}}$ is assumed for its distillate mass fraction. Similar to the overall component balance of a continuous distillation column, see equation (2.30), the component balance for the non-volatile component is defined as:

$$\dot{m}_\mathrm{F} \cdot w_{3,\mathrm{F}} = \dot{m}_\mathrm{D} \cdot w_{3,\mathrm{D}} + \dot{m}_\mathrm{B} \cdot w_{3,\mathrm{B}} \tag{3.6}$$

The bottoms mass fraction of the non-volatile component may be limited by the resulting physical properties of the mixture[2]. For such cases, the minimum stream ratio is derived by inserting $w_{3,\mathrm{B}} = w_{3,\mathrm{B,max}}$ into equation (3.6) (Gutperl et al., 2022):

$$\left(\frac{\dot{m}_\mathrm{F}}{\dot{m}_\mathrm{D}}\right)_{\mathrm{min}} = \frac{w_{3,\mathrm{B,max}}}{w_{3,\mathrm{B,max}} - w_{3,\mathrm{F}}} \tag{3.7}$$

Introspecting equation (3.7) with respect to $w_{3,\mathrm{F}}$ allows deducing operational characteristics regarding total and partial reflux as shown in table 3.3. To improve readability, the according units $[\dot{m}_\mathrm{F}\,\dot{m}_\mathrm{D}^{-1}] = \mathrm{kg_F\,kg_D^{-1}}$ and $[\dot{F}\,\dot{D}^{-1}] = \mathrm{kmol_F\,kmol_D^{-1}}$ are omitted throughout all elaborations presented in this work.

Table 3.3.: Effect of reflux condition on stream ratio $\dot{m}_\mathrm{F}\,\dot{m}_\mathrm{D}^{-1}$ and feed mass fraction of non-volatile component $w_{3,\mathrm{F}}$, $[\dot{m}_\mathrm{F}\,\dot{m}_\mathrm{D}^{-1}] = \mathrm{kg_F\,kg_D^{-1}}$, $[w_{3,\mathrm{F}}] = \mathrm{kg_3\,kg_{tot}^{-1}}$

desired reflux condition	resulting stream ratio	as per equation (3.7) only valid for
partial reflux	$\dot{m}_\mathrm{F}\,\dot{m}_\mathrm{D}^{-1} > 1$	$w_{3,\mathrm{F}} \geq 0$
total reflux	$\dot{m}_\mathrm{F}\,\dot{m}_\mathrm{D}^{-1} = 1$	$w_{3,\mathrm{F}} = 0$

Strictly speaking, partial reflux does not only cover $\dot{m}_\mathrm{F}\,\dot{m}_\mathrm{D}^{-1} > 1$ but also $0 < \dot{m}_\mathrm{F}\,\dot{m}_\mathrm{D}^{-1} < 1$. However, $w_{3,\mathrm{F}}\,w_{3,\mathrm{B,max}}^{-1} < 0$ is required to satisfy equation (3.7) for $0 < \dot{m}_\mathrm{F}\,\dot{m}_\mathrm{D}^{-1} < 1$. In contrast to the concept of (Böcker and Ronge, 2005), see section 2.3.2.2, the proposed plant setup is, therefore, only applicable to reflux conditions of $\dot{m}_\mathrm{F}\,\dot{m}_\mathrm{D}^{-1} \geq 1$.

3.3.3.2. Identifying Steady-State Operation

As discussed in section 2.3.2.1, both hydraulic and mass transfer steady state, which are commonly identified based on compositional analysis, need to be reached for reliable separation performance results. Since the test distillation plant is not equipped with an inline sample analysis, this would require sampling and offline sample analysis during plant start-up. However, the amount of liquid drawn from the test plant should be as small as possible, since the total

[2]For viscous distillation with a polymer-enhanced mixture, the maximum bottoms viscosity may be limited by the reboiler (minimum circulation rate, maximum viscosity for circulation pump, flow regime, reduced heat transfer etc.). However, similar considerations are valid for applications with non-volatile mixture components in general.

reflux experiments were carried out with small feedstocks of around 2.5 kg and disturbances on developing column profiles should be prevented.

Depending on the plant setup and operating conditions, reaching steady state takes several hours. Therefore, a wide range of plant start-up durations can be found in the literature: While (Eckert and Walter, 1964) reported 30 min for their experiments and (Böcker and Ronge, 2005) were able to reach steady state after around 60 min, steady state was reached after several hours in the experiments conducted by (Bradtmöller, 2017). Furthermore, (Schoenmakers and Spiegel, 2014) state that start-up durations of up to 12 h are common for miniplant-scale distillation plants and may be prolonged to several days for setups with small recycle streams.

Since mass transfer steady state does not only result in constant composition profiles, but also constant product compositions, the density measured by the feed Coriolis mass flow meter (instrument tag D101) is related to the composition of the mixture fed to the column. Although the density of the feed mixture varies due to fluctuations in feed temperature and the accuracy of the inline density reading of $\pm\,2\,\mathrm{kg\,m^{-3}}$ (Krohne, 2016) is not sufficient for an inline mixture analysis, the obtained density readings are suitable to identify steady state as shown in figures 3.5 and A.1.

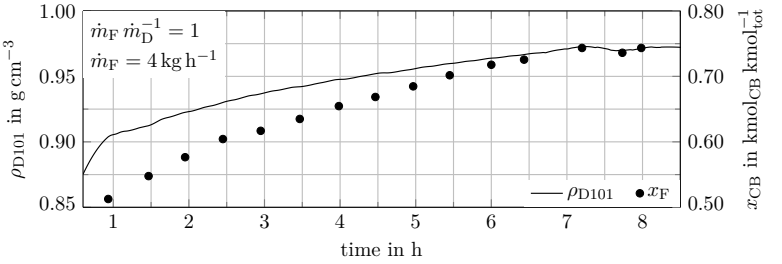

Figure 3.5.: Identifying steady-state plant operation using inline feed density measurements and offline sample analyses, steady state was reached around 7 h after plant start-up, data records were arithmetically averaged every minute and smoothed with a Savitzky-Golay filter using a window size of 42 data points and a second-order filter polynomial, error bars are omitted as the associated uncertainties are negligible, see tables D.5 and D.6 for uncertainties

3.3.4. Experimental Investigations

Limited by plant characteristics and equipment, the separation performance experiments were conducted with the nominal operating conditions shown in table 3.4. Actual operating conditions as well as experiment results are tabulated in appendix F.1.

Table 3.4.: Parameter space of separation performance experiments

process parameter	symbol	unit	nominal value
feed mass flow	$\dot{m}_\mathrm{F}$	$\mathrm{kg\,h^{-1}}$	4; 6; 9; 12; 14
stream ratio	$\dot{m}_\mathrm{F}\,\dot{m}_\mathrm{D}^{-1}$	$\mathrm{kg_F\,kg_D^{-1}}$	1.0; 1.1; 2.0; 3.0
operating mode [a]			total reflux; simulated total reflux, partial reflux
head pressure	p_h	mbar(a)	100
feed temperature	ϑ_F	K	$1 \ldots 3 < \vartheta_\mathrm{F,boil}$
trace heating column head	$\vartheta_\mathrm{tr,h}$	°C	68
trace heating column couplings	$\vartheta_\mathrm{tr,col}$	°C	$70 \ldots 72$
initial feedstock composition	$x_\mathrm{F,initial}$	$\mathrm{kmol_{CB}\,kmol_{tot}^{-1}}$	0.5
mass of feedstock	m_F	kg	$2.7 \ldots 5.6$ [b]

[a] Operating mode is given in experiment designator: simulated total reflux (*5xx*), partial reflux (*6xx*), total reflux (*7xx*).

[b] To ensure stable plant operation, used feedstock mass depends on operating mode.

Since distillation experiments at total and partial reflux were performed, the stream ratio $\dot{m}_\mathrm{F}\,\dot{m}_\mathrm{D}^{-1}$ or $\dot{F}\,\dot{D}^{-1}$ is the most relevant operating parameter. As discussed in sections 2.3.2.1 and 3.3.1, uncertainty in separation performance may increase with higher $\dot{F}\,\dot{D}^{-1}$ due to the additional operating parameter and potential composition pinches between operating line and equilibrium curve. While associated uncertainties heavily depend on the specifications of process sensors and laboratory equipment and can be reduced by selecting suitable devices and laboratory routines, composition pinches can only be mitigated by choosing a lower stream ratio $\dot{F}\,\dot{D}^{-1}$. The relevance of potential concentration pinches with increasing $\dot{F}\,\dot{D}^{-1}$ is illustrated in figure 3.6.

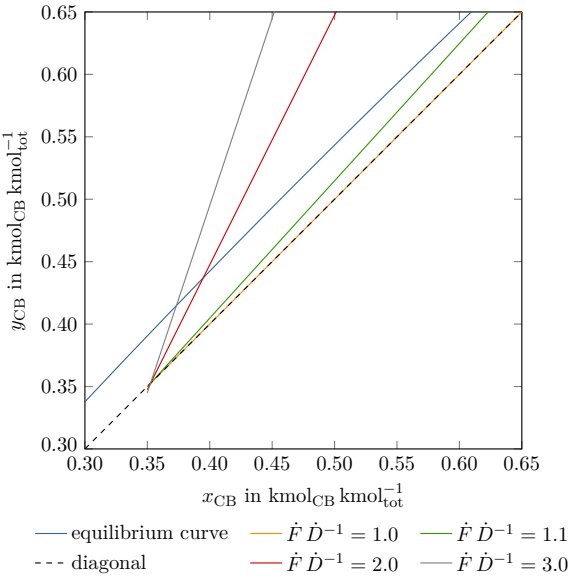

Figure 3.6.: Effect of molar stream ratio $\dot{F}\,\dot{D}^{-1}$ on concentration pinches illustrated in equilibrium diagram, constant bottoms composition with $x_B = 0.35\,kmol_{CB}\,kmol_{tot}^{-1}$ assumed for all cases, mean relative volatility of $\overline{\alpha}_{12} = 1.19$ chosen according to figure C.6

Therefore, most of the partial reflux experiments were conducted with $\dot{m}_F\,\dot{m}_D^{-1} = 1.1$ resulting in a molar stream ratio of $\dot{F}\,\dot{D}^{-1} \approx 1.1$; see table 3.2 for factors of proportionality to expect. Furthermore, experiments with $\dot{F}\,\dot{D}^{-1} \approx 1.0$ were performed at total reflux and simulated total reflux to compare the operating modes and address the transition from total to partial reflux operating conditions.

While all experiments were performed at nominal head pressures of $p_h = 100\,mbar(a)$, the stream ratio $\dot{m}_F\,\dot{m}_D^{-1}$, which affects the slope of the operating line, was changed by either varying the feed mass flow $\dot{m}_F$ or varying the distillate mass flow[3] $\dot{m}_D$. Therefore, liquid load w_L and f-factor f_G were also affected.

To reduce condensation due to a subcooled feed stream, the feed was preheated to approximately $1 \ldots 3\,K$ below its boiling point. As the boiling point of the feed depends on its composition, the exact feed subcooling was determined as part of the experiment evaluation. The trace heating at the column head was set to $68\,°C$ to avoid uncontrolled reflux[4]. Similarly, trace heatings of column couplings and column bottom were set to $70 \ldots 72\,°C$.

Although (Eckert and Walter, 1964) suggest total reflux operation during plant start-up to

[3]While feed mass flow $\dot{m}_F$ can directly be set via the plant control system, distillate mass flow $\dot{m}_D$ can only be set indirectly by changing the reboiler duty.

[4]Boiling points at $p_h = 100\,mbar(a)$: $63\,°C$ (chlorobenzene), $65\,°C$ (equimolar mixture), $67\,°C$ (ethylbenzene).

ensure a complete wetting of the packing surface, the desired nominal operating parameters were directly set upon start-up and, if necessary, only adjusted slightly to mitigate potential disruptions during plant start-up.

An equimolar mixture of CB/EB was used as initial feedstock. Liquid samples were drawn from distillate, bottoms and feedstock around 30 min after steady state was reached. Although possible, no inter-bed samples were drawn to prevent potential septum ruptures and disturbances during steady-state plant operation. Each sampling tap was fully purged prior sampling to prevent cross-contamination. At least three samples, each with a volume of around 5 mL per sample, were taken from each sampling point at intervals of 10 . . . 15 min.

3.4. Sample Analysis

(Onken and Arlt, 1990) suggest using gas chromatography, refractive index or density analysis to determine the composition of the binary mixture CB/EB. While a dedicated analysis method is required for gas chromatography, a refractive index or density analysis is commonly easier to perform. The latter method of analysis is especially suitable as the pure component densities of chlorobenzene and ethylbenzene considerably differ from each other, which allows sufficient determination of the sample composition with readily available laboratory equipment.

Therefore, sample analysis was carried out with a *DMA 4100 M* digital density meter (Anton Paar Germany, Ostfildern/Germany) at a nominal measuring cell temperature of 20 °C. Each sample was analyzed as drawn from the distillation plant. Furthermore, an autosampler *Xsample 530* (Anton Paar Germany, Ostfildern/Germany) was used for automated sample injection and density measurements. Measurement data and device status information were automatically collected and stored in a local databank using the lab execution software *AP Connect* (Anton Paar Germany, Ostfildern/Germany).

Prior to the sample analyses, the density meter was checked according to the device calibration procedure and the manufacturer's recommendations. To determine the composition of the samples drawn from each sampling point, a density/composition calibration curve was determined prior to the plant experiments. While the obtained calibration curve is elaborated in appendix C.3.1, the system calibration procedure and obtained uncertainties associated with the sample analysis are discussed in appendix D.2.2.

3.5. Data Processing and Evaluation

Data processing and evaluation are fully automated using the *Python* programming language (Python, 2022). The underlying procedures, which are described in this section, are exemplarily illustrated based on experiment *604-2*[5]. Software usage and the implemented data evaluation

[5]Experiment designators are formatted as `<experiment number>-<run number>` Therefore, *604-2* represents the first replication (2nd run) of experiment *604*. In addition, operating mode is contained in experiment designators: simulated total reflux (5xx), partial reflux (6xx), total reflux (7xx)

workflow is briefly documented in appendix E.5. Uncertainty quantification for relevant data can be found in appendix D.2, details about the bracket notation used to report quantified uncertainties in this work are given in appendix D.1.4.

3.5.1. Liquid Samples

As elaborated in section 3.3.4, multiple liquid samples were drawn from the distillation plant during steady state. To reduce minor fluctuations during steady state affecting mixture composition as well as density and to ensure representative results, measured sample densities were arithmetically averaged for each sampling point. A representative sample composition was determined for each liquid mixture (distillate, bottoms or feedstock) based on its averaged sample density and subsequently used for further experiment evaluation.

While further information about operating conditions are required for most parts of the data evaluation, the molar mass of each liquid sample is directly calculated based on its composition as shown in appendix C.2. An exemplary evaluation of liquid samples for experiment *604-2* is summarized in table 3.5.

Table 3.5.: Exemplary evaluation of liquid sample compositions for experiment *604-2*, associated combined standard uncertainties rounded to one significant digit, see appendix D.2.2 for details about uncertainties in mixture analysis

sampling point	sample no.	$\rho_{\mathrm{L},i}$	$\overline{\rho_{\mathrm{L},i}}$	x_i	M_i
		$\mathrm{g\,cm^{-3}}$	$\mathrm{g\,cm^{-3}}$	$\mathrm{kmol_{CB}\,kmol_{tot}^{-1}}$	$\mathrm{kg\,kmol^{-1}}$
distillate (D)	1	1.014 90(6)			
	2	1.016 40(6)			
	3	1.015 80(6)	1.0157(8)	0.660(3)	110.39(2)
bottoms (B)	1	0.942 70(6)			
	2	0.942 20(6)			
	3	0.942 50(6)	0.9425(3)	0.353(1)	108.423(7)
feedstock (F)	1	1.006 90(6)			
	2	1.008 10(6)			
	3	1.007 60(6)	1.0075(6)	0.627(2)	110.18(2)

3.5.2. Operating Data and Operating Parameters

As already mentioned in section 3.3.2, all operating parameters and sensor readings were recorded during each experiment and saved to CSV files for later processing. Most relevant sensor readings used for experiment evaluation and calculation of process parameters are listed in table 3.6.

Table 3.6.: Sensor readings and process parameters used for experiment evaluation

sensor tag	process parameter	symbol	unit
F101	feed mass flow [a]	$\dot{m}_\mathrm{F}$	$\mathrm{kg\,h^{-1}}$
P201	head pressure	p_h	mbar(a)
P204	pressure below bed	p_b	mbar(a)
T101	feed temperature	ϑ_F	°C
T102	head temperature	ϑ_h	°C
T214	temperature below bed	ϑ_b	°C
W401	mass of distillate tank B401	m_B401	kg
W402	mass of bottoms tank B402	m_B402	kg

[a] for partial and simulated total reflux operation

Although steady-state operation is generally characterized by constant operating parameters, potential outliers in the recorded data were removed based on the *interquartile range (IQR)*:

$$\mathrm{IQR} = Q_3 - Q_1 = Q_{75\,\%} - Q_{25\,\%} \tag{3.8}$$

Values below $Q_1 - 1.5 \cdot \mathrm{IQR}$ and above $Q_3 + 1.5 \cdot \mathrm{IQR}$ are commonly considered as outliers (Bartolucci et al., 2016). An exemplary comparison of original and IQR-filtered steady-state time series with calculated arithmetic means for experiment *604-2* is given in appendix E.2. After outlier removal, the time series were reduced into a single characteristic value by calculating the corresponding arithmetic mean over a time interval of 30 min prior the first liquid sample was drawn from the distillation plant[6]. The arithmetic mean $\overline{x}$ of an arbitrary parameter x with K readings is defined according to equation (3.9):

$$\overline{x} = \frac{1}{K} \sum^{K} x_k \tag{3.9}$$

While this approach was applicable for continuously recorded process parameters like head pressure, temperatures and feed mass flow, the determination of product mass flows based on the readings recorded from scales W401 and W402 required an alternative evaluation routine. Although the according product mass flows were automatically calculated based on a moving average and recorded by the plant control system during each experiment, later data inspection showed that more precise values are obtained if a linear function, whose slope represents the according mass flow, is fit to the respective time series datasets. For this, *orthogonal*

[6] Strictly speaking, steady-state plant operation implies constant operating conditions and the obtained results should, therefore, not depend on the specific time interval considered for data evaluation. However, to avoid potential disturbances due to liquid sampling, recorded data were evaluated over a time interval of 30 min before the first liquid sample was taken.

distance regression (ODR)[7] was used to incorporate the uncertainties associated with the scale readings. The obtained improvement in mass flow determination was especially useful to reduce deviations in the overall mass balance for experiments with small bottom product mass flows of $\dot{m}_\mathrm{B} \lesssim 1\,\mathrm{kg\,h^{-1}}$, since the plant control system estimated these values as $\dot{m}_\mathrm{B} \approx 0\,\mathrm{kg\,h^{-1}}$.

To calculate the mass flows $\dot{m}_\mathrm{D}$ and $\dot{m}_\mathrm{B}$ by regression, start and end timestamps of each interval during which liquid is collected in the respective product tanks were identified by calculating the difference between two consecutive scale readings. Depending on the number of weighing cycles during the steady-state phase of each experiment, multiple mass flow estimations were performed by regression. Similar to the directly measured operating parameters, potential outliers were removed by IQR and the product mass flows representative for each steady state were finally obtained as the arithmetic averages of the filtered datasets. Identification of weighing cycles and the improvement in mass flow determination associated with the aforementioned regression-based approach are illustrated in figure E.2.

For characteristic operating parameters like liquid load w_L, gas load $u_\mathrm{G,s}$ or f-factor f_G, which depend on pressure, temperature and composition, (Ottenbacher et al., 2011) suggest to use column averaged values of the respective column conditions for the calculations. For total reflux experiments, such averages are readily determined using corresponding operating conditions and mixture compositions above and below the packed bed. While the liquid reflux and overhead vapors are equal in composition for conventional total reflux experiments, the liquid feed entering the column and the vapor leaving the packed bed differ in compositions for the partial reflux experiments conducted in this work. Although gas/liquid interaction above the bed should be negligible, the difference in composition could result in a mass transfer which cannot be quantified easily. This effect can even increase, if the feed is subcooled resulting in an additional partial condensation of the vapors. In such a case, the external feed does not only affect the liquid compositions at the inlet section but also influences gas and liquid loads. Therefore, to define representative mid-bed operating conditions and liquid compositions for the partial reflux experiments performed in this work, the potential mass transfer and partial condensation occurring at the feed inlet section are not considered.

This simplification does not only result in $\dot{L}' = \dot{L} \approx \dot{F}$ and $\dot{G}' = \dot{G} \approx \dot{D}$, as already introduced in equation (3.1), but also allows defining the following mid-bed conditions (index mb):

$$x_\mathrm{mb} = \frac{x_\mathrm{F} + x_\mathrm{B}}{2} \tag{3.10a}$$

$$y_\mathrm{mb} = \frac{y_\mathrm{D} + y_\mathrm{B}}{2} = \frac{x_\mathrm{D} + x_\mathrm{B}}{2} \tag{3.10b}$$

$$\vartheta_\mathrm{mb} = \frac{\vartheta_\mathrm{h} + \vartheta_\mathrm{b}}{2} \qquad \text{and} \qquad T_\mathrm{mb} = \vartheta_\mathrm{mb} + 273.15\,\mathrm{K} \tag{3.10c}$$

[7] Data were fit with `scipy.odr`, which uses an adapted Levenberg-Marquardt least squares algorithm; see (Boggs and Rogers, 1990; Virtanen et al., 2020).

$$p_{\mathrm{mb}} = \frac{p_{\mathrm{h}} + p_{\mathrm{b}}}{2} \tag{3.10d}$$

The liquid load w_{L} is calculated with the column diameter d_{col}, feed molar flow $\dot{F}$, liquid molar mass M_{L} and liquid density ρ_{L}:

$$w_{\mathrm{L}} \underset{(2.19)}{=} \frac{\dot{V}_{\mathrm{L}}}{A_{\mathrm{col}}} = \frac{4}{\pi \cdot d_{\mathrm{col}}^2} \cdot \frac{M_{\mathrm{L}}\,\dot{F}}{\rho_{\mathrm{L}}} \tag{3.11}$$

The required liquid density ρ_{L} is calculated according to appendix C.3.2 using the mid-bed composition x_{mb} and temperature T_{mb}. Liquid molar masses M_{L} and M_{F} are calculated as shown in appendix C.2 using x_{mb} and x_{F}, respectively. The conversion of the recorded feed mass flow $\dot{m}_{\mathrm{F}}$ into its corresponding molar flow $\dot{F}$ was introduced in equation (3.2a).

Similarly, the molar mass M_{G} and density ρ_{G} of the gas phase as well as distillate molar flow $\dot{D}$ are used to calculate the f-factor f_{G} according to equation (3.12). The gas phase density ρ_{G} is approximated with the ideal gas law as shown in appendix C.3.3 using mid-bed composition y_{mb}, mid-bed temperature T_{mb} and mid-bed pressure p_{mb}. For obtaining the molar distillate flow $\dot{D}$ from the recorded mass flow $\dot{m}_{\mathrm{D}}$ see equation (3.2b).

$$f_{\mathrm{G}} \underset{(2.18)}{=} u_{\mathrm{G,s}} \cdot \rho_{\mathrm{G}}^{0.5} = \frac{4}{\pi \cdot d_{\mathrm{col}}^2} \cdot \frac{M_{\mathrm{G}}\,\dot{D}}{\rho_{\mathrm{G}}^{0.5}} \tag{3.12}$$

As already discussed in section 2.1.3, separation performance may vary depending on the operating regime. Therefore, the specific pressure drop Δp_{bed} is calculated in addition to the liquid load w_{L} and f-factor f_{G} to evaluate the operating regime[8]. The specific pressure drop of the packed bed Δp_{bed} is calculated based on the pressure below and above the packings, p_{b} and p_{h}, as shown in equation (3.13). Since the density of the gas phase ρ_{G} is known, the measured pressure drop $\Delta p_{\mathrm{meas}} = p_{\mathrm{b}} - p_{\mathrm{h}}$ is corrected by the hydrostatic pressure of the gas phase as suggested by (Cai, 2014). g denotes the gravity of Earth ($g = 9.806\,65\,\mathrm{m\,s^{-2}}$).

$$\Delta p_{\mathrm{bed}} = \frac{\Delta p_{\mathrm{meas}}}{H_{\mathrm{bed}}} - \rho_{\mathrm{G}}\, g = \frac{p_{\mathrm{b}} - p_{\mathrm{h}}}{H_{\mathrm{bed}}} - \rho_{\mathrm{G}}\, g \tag{3.13}$$

To assess a potentially subcooled feed stream, its boiling point $T_{\mathrm{F,boil}}$ is numerically determined according to appendix C.12. For this, head pressure p_{h} is used, since the feed inlet is located at the top of the column. As the feed temperature T_{F} is known from the recorded plant data, the feed subcooling ΔT_{F} is calculated as:

$$\Delta T_{\mathrm{F}} = T_{\mathrm{F,boil}} - T_{\mathrm{F}} \tag{3.14}$$

With both $T_{\mathrm{F,boil}}$ and T_{F} known, the corresponding enthalpies, h'_{F} and h_{F}, are estimated as

[8] For *Mellapak*-type packings, flooding is commonly defined at a specific pressure drop of $\Delta p_{\mathrm{bed}} = 12\,\mathrm{mbar\,m^{-1}}$ (Lockett et al., 2006).

specific heat capacities, $c_{\mathrm{p,F}} = f(T_{\mathrm{F,boil}}, x_{\mathrm{F}})$ and $c_{\mathrm{p,F}} = f(T_{\mathrm{F}}, x_{\mathrm{F}})$, according to appendices C.4 and C.5. Feed condition q is then calculated using the already introduced equation (2.16).

3.5.3. Material Balances

Both mass and molar balances are evaluated for each experiment. Similar to the molar balance of a continuous distillation, which was introduced in equation (2.12), the mass balance is given as:

$$\dot{m}_{\mathrm{F}} = \dot{m}_{\mathrm{D}} + \dot{m}_{\mathrm{B}} \tag{3.15}$$

As elaborated in section 3.5.2, only mass flows $\dot{m}_{\mathrm{F}}$, $\dot{m}_{\mathrm{D}}$ and $\dot{m}_{\mathrm{B}}$ are directly determined from recorded operating parameters. Nevertheless, corresponding molar flows $\dot{F}$, $\dot{D}$ and $\dot{B}$ can be calculated based on the molar mass M_i of each stream:

$$\dot{F} \underset{(3.2a)}{=} \frac{\dot{m}_{\mathrm{F}}}{M_F} \underset{(C.1)}{=} \frac{\dot{m}_{\mathrm{F}}}{x_{\mathrm{F}} \cdot M_{\mathrm{CB}} + (1 - x_{\mathrm{F}}) \cdot M_{\mathrm{EB}}} \tag{3.16a}$$

$$\dot{D} \underset{(3.2b)}{=} \frac{\dot{m}_{\mathrm{D}}}{M_D} \underset{(C.1)}{=} \frac{\dot{m}_{\mathrm{D}}}{x_{\mathrm{D}} \cdot M_{\mathrm{CB}} + (1 - x_{\mathrm{D}}) \cdot M_{\mathrm{EB}}} \tag{3.16b}$$

$$\dot{B} = \frac{\dot{m}_{\mathrm{B}}}{M_B} \underset{(C.1)}{=} \frac{\dot{m}_{\mathrm{B}}}{x_{\mathrm{B}} \cdot M_{\mathrm{CB}} + (1 - x_{\mathrm{B}}) \cdot M_{\mathrm{EB}}} \tag{3.16c}$$

Disregarding whether the mass or molar balance is considered, both absolute and relative deviations of each balance, ε and δ, were related to the feed flow. The respective deviations of the mass balance are, therefore, calculated according to equation (3.17):

$$\varepsilon = \dot{m}_{\mathrm{F}} - (\dot{m}_{\mathrm{D}} + \dot{m}_{\mathrm{B}}) \tag{3.17a}$$

$$\delta = \frac{\varepsilon}{\dot{m}_{\mathrm{F}}} = \frac{\dot{m}_{\mathrm{F}} - (\dot{m}_{\mathrm{D}} + \dot{m}_{\mathrm{B}})}{\dot{m}_{\mathrm{F}}} = 1 - \frac{\dot{m}_{\mathrm{D}} + \dot{m}_{\mathrm{B}}}{\dot{m}_{\mathrm{F}}} \tag{3.17b}$$

Analogously, equation (3.18) applies for deviations in the molar balance:

$$\varepsilon = \dot{F} - (\dot{D} + \dot{B}) \tag{3.18a}$$

$$\delta = \frac{\varepsilon}{\dot{F}} = \frac{\dot{F} - (\dot{D} + \dot{B})}{\dot{F}} = 1 - \frac{\dot{D} + \dot{B}}{\dot{F}} \tag{3.18b}$$

3.5.4. Separation Performance

3.5.4.1. Using Theoretical Stages

As already discussed in section 2.2, separation performance is most often expressed in terms of HETP values. For this, the number of theoretical stages N_{th} is commonly calculated with

the Fenske equation which is only valid for total reflux operation and relies on distillate and bottoms molar fractions x_D and x_B, respectively.

Since experiments with both finite and infinite reflux ratios need to be evaluated in this work, an alternative approach is chosen for separation performance evaluation. As already defined in equation (2.44), HETP values are calculated based on the height of the packed bed H_bed and the number of theoretical stages N_th, which is obtained from stage constructions according to (McCabe and Thiele, 1925), see section 2.2.1.2. To quantify the uncertainty associated with N_th, Monte Carlo simulations (Monte Carlo methods, MCM) are used due to the iterative calculation scheme inherent to the stage constructions. A brief overview of uncertainty quantification with MCM is given in appendix D.1.2.

Since plant design and operation are comparable to those of a stripping column, bottom product and feedstock compositions, represented by the molar fractions x_B and x_F, are used for the stage constructions. Furthermore, the stripping operating line introduced in equation (2.27) is considered as the only operating line. As elaborated with equation (3.1), the slope of the operating line is approximated with the molar stream ratio $\dot{F}\,\dot{D}^{-1}$. This approximation seems especially feasible, since the constant molar overflow assumption is fulfilled due to similar molar enthalpies of vaporization for chlorobenzene and ethylbenzene, see table C.1. As already shown with equation (3.3), the molar stream ratio $\dot{F}\,\dot{D}^{-1}$ is calculated based on the feed and distillate mass flows, $\dot{m}_\mathrm{F}$ and $\dot{m}_\mathrm{D}$, as well as the according molar masses, M_F and M_D. The calculation of the molar masses is based on the composition of the samples taken from the respective mixtures according to section 3.5.1.

If stripping and equilibrium lines get very close to each other, their positions and progressions are very important for a resilient data evaluation and may result in unprocessable datasets for extreme cases. In such cases, the uncertainty of both experimental data and VLE data becomes decisive. While used VLE datasets were carefully selected and calculated as elaborated in appendices C.12 and C.13, the associated uncertainties could not be assessed, since required information are not stated in the used data sources. Although not further investigated, actual uncertainties associated with the VLE are considered less important as all experiments are evaluated based on the same set of parameters. Therefore, associated uncertainties are considered systematic and should cancel out each other when comparing experimental results. However, the combined standard uncertainty associated with the mid-bed operating pressure $u_\mathrm{c}(p_\mathrm{mb})$, resulting from fluctuations during plant operation and pressure sensor specifications, is propagated through numerical VLE calculation using the aforementioned MCM.

Although the feed subcooling of $1\ldots3\,\mathrm{K}$ in the experiments of this work is commonly considered negligible and a liquid boiling feed is assumed in such cases, significant improvements in experiment evaluation were obtained if feed subcooling was taken into account, inasmuch as a higher number of successful Monte Carlo runs could be achieved. Therefore, feed condition q, see equation (2.16), is calculated for all experiments and used to determine the slope of the feed line. Calculating the required molar enthalpies was already discussed in context of

equation (3.14), used correlations can be found in appendices C.4 and C.5.

To calculate the stage constructions, the liquid molar fraction x_{is} determined from the intersection of the feed line with the stripping line is used. However, depending on the uncertainties associated with the operating conditions and mixture compositions, the intersection point can be located above the equilibrium curve. Although being mathematically consistent, such cases are thermodynamically invalid and excluded from further evaluation based on a constructability check according to appendix E.4. Although performed MCM cover $N_{\mathrm{MC}} = 1 \cdot 10^6$ sets of pseudo-randomly sampled input parameters for each experiment, excluding thermodynamically invalid parameter sets reduces the number of samples used for data evaluation, which in turn affects the reliability of the estimated result distributions used for uncertainty propagation. As the reduced number of underlying samples is especially relevant for edge cases, the success ratio S_{MC} is introduced to quantify the ratio of successful (valid) and total number of Monte Carlo simulations:

$$S_{\mathrm{MC}} = \frac{N_{\mathrm{MC,success}}}{N_{\mathrm{MC}}} \tag{3.19}$$

For parameter sets passing the constructability check, stage constructions are performed top to bottom, starting at x_{is}. The corresponding vapor molar fractions, required to obtain the stage contact points on the equilibrium curve, are calculated by combining Raoult's law with Dalton's law, see equations (2.5) and (2.6), and numerically solving for y_1 as elaborated in appendix C.13. Similarly, for a known y_1, stage contact points on the stripping operating line are obtained by solving for x_1. This iterative approach results the polyline of the stage construction indicating the number of theoretical stages N_{th} used to estimate HETP as already introduced in equation (2.44).

Although N_{th} is commonly determined and interpreted as an integer number, a fractional stage at the bottom of the column is considered for the calculations of this work. The interpretation of such fractional stage is illustrated in figure 3.7:

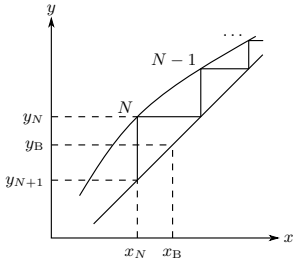

Figure 3.7.: Fractional equilibrium stage to determine $N_{\mathrm{th,dec}}$

Since the molar fraction of the more volatile component in the liquid stream exiting the last stage x_N is smaller than the experimentally achieved bottoms composition x_{B}, only a fractional

part of the last equilibrium stage is considered. Assuming N_{th} theoretical stages are obtained from a McCabe-Thiele stage construction, $N_{\mathrm{th,dec}}$ is calculated according to equation (3.20):

$$N_{\mathrm{th,dec}} = N_{\mathrm{th}} - 1 + \frac{y_N - y_{\mathrm{B}}}{y_N - y_{N+1}} = N_{\mathrm{th}} - 1 + \frac{y_N - x_{\mathrm{B}}}{y_N - x_N} \tag{3.20}$$

This approach is similar to the one presented by (Sherwood et al., 1975) in which fractional stages are taken into account around the feed inlet. It is used to not only increase the robustness of the obtained results, but also to emphasize the continuous characteristic of packed bed columns. Since HETP values are consistently calculated with the corresponding decimal number of theoretical stages, an explicit distinction between the integer and decimal number of theoretical stages should commonly not be required for further results discussion. However, in cases in which integer and decimal number of theoretical stages need to be distinguished explicitly, the according values are denoted by N_{th} and $N_{\mathrm{th,dec}}$, respectively.

Figure 3.7 also allows illustrating the driving forces available for mixture separation. Considering an arbitrary stage n, the liquid and vapor driving concentration potential of this stage, Δx_n and Δy_n, are defined as:

$$\Delta x_n = x_{n-1} - x_n \tag{3.21a}$$

$$\Delta y_n = y_{n-1} - y_n \tag{3.21b}$$

Depending on the progression of equilibrium curve and stripping operating line, the driving potentials Δx_n and Δy_n may substantially differ between individual stages (small vs. large stages). Therefore, corresponding values are aggregated into overall liquid and vapor driving potentials, Δx_{drv} and Δy_{drv}, based on the corresponding arithmetic averages along a stage construction with N stages:

$$\Delta x_{\mathrm{drv}} = \frac{1}{N} \sum^{N} \Delta x_n = \frac{\Delta x_{\mathrm{sep}}}{N_{\mathrm{th}}} = \frac{x_{\mathrm{F}} - x_{\mathrm{B}}}{N_{\mathrm{th}}} \tag{3.22a}$$

$$\Delta y_{\mathrm{drv}} = \frac{1}{N} \sum^{N} \Delta y_n = \frac{\Delta y_{\mathrm{sep}}}{N_{\mathrm{th}}} = \frac{y^{\mathrm{eq}}(x_{\mathrm{F}}) - y^{\mathrm{eq}}(x_{\mathrm{B}})}{N_{\mathrm{th}}} \tag{3.22b}$$

The McCabe-Thiele stage construction created for experiment *604-2* is shown in figure 3.8. Even for a small molar stream ratio of $\dot{F}\,\dot{D}^{-1} = 1.1$, the relevance of concentration pinches between stripping operating line and equilibrium curve gets noticeable, since small stages are obtained in the upper part of the column.

In addition, the relevance of a fractional equilibrium stage at the bottom of the column is apparent as the bottoms concentration represented by x_{B} is only marginally lower than the molar fraction of the liquid stream leaving stage 12 ($x_{\mathrm{B}} \approx x_{12}$). This is even more obvious, if $N_{\mathrm{th,dec}}$ is considered instead of N_{th}. Obtained results for N_{th}, $N_{\mathrm{th,dec}}$ and corresponding HETP

are exemplarily summarized in table 3.7.

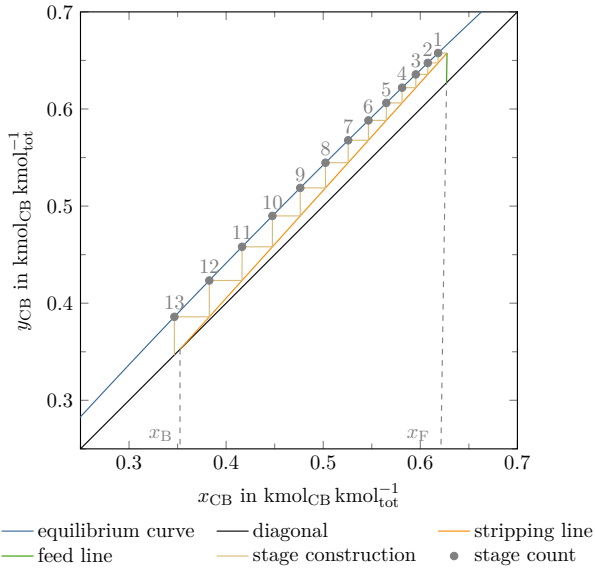

Figure 3.8.: Exemplary McCabe-Thiele stage construction for experiment *604-2*, uncertainties and ensemble of solutions obtained from Monte Carlo simulations not illustrated to improve readability

Table 3.7.: Number of theoretical stages N_{th} and HETP determined based on McCabe-Thiele stage constructions for experiment *604-2*, uncertainty quantification integrated into data evaluation workflow according to appendix D.2.1 and table E.3

experiment evaluation	N_{th}	HETP
	-	m
without fractional stage	13.37(62)	0.1831(87)
with fractional stage	12.89(56)	0.1900(83)

3.5.4.2. Using the Delft Mass Transfer Model

In addition to the HETP obtained from equilibrium stage constructions, HETP values are predicted using mass transfer correlations. For this, HTU_{oG} is calculated with the Delft model, see section 2.2.3.5. To be consistent with the separation performance evaluation based on equilibrium stages, mixture separation is considered between the composition of the feed mixture and the bottom product. Therefore, the mid-bed vapor composition y_{mb}, temperature T_{mb} and pressure p_{mb}, as defined in equations (3.10b) to (3.10d), are used throughout the calculation

of required physical properties. However, in contrast to equation (3.10a), the effect of feed subcooling is considered for mid-bed liquid composition and thus, the liquid molar fraction at the intersection between feed line and stripping line x_{is} is used to define the representative mid-bed liquid molar fraction $x_{\mathrm{mb,is}}$:

$$x_{\mathrm{mb,is}} = \frac{x_{\mathrm{is}} + x_{\mathrm{B}}}{2} \tag{3.23}$$

To determine the height of a liquid side transfer unit $\mathrm{HTU_L}$ based on equation (2.92a), both the original and the revised correlation are used to calculate mass transfer coefficients $k_{\mathrm{L,original}}$ and $k_{\mathrm{L,revised}}$, see equation (2.88). Similarly, the height of a gas side transfer unit $\mathrm{HTU_G}$ is calculated according to equation (2.92a) using mass transfer coefficients $k_{\mathrm{G,original}}$ and $k_{\mathrm{G,revised}}$ to potentially obtain a better agreement between the predicted and measured separation performance. Correlations for mass transfer coefficients used in data evaluation are given in table 3.8:

Table 3.8.: Delft mass transfer correlations used for data evaluation, see section 2.2.3.5 for details

phase	mass transfer coefficient calculated with	
	original correlation	revised correlation
liquid	$k_{\mathrm{L,original}}$: equation (2.88a)	$k_{\mathrm{L,revised}}$: equation (2.88b)
vapor	$k_{\mathrm{G,original}}$: equation (2.89a) with $\varphi_{\mathrm{c,L}}$ according to equation (2.72)	$k_{\mathrm{G,revised}}$: equation (2.89a) with $\varphi_{\mathrm{c,L}} = 1$

Using equation (2.57a), $\mathrm{HTU_L}$ and $\mathrm{HTU_G}$ are combined into $\mathrm{HTU_{oG}}$, which in turn is converted into HETP according to equation (2.65). The stripping factor λ, required for equations (2.57a), (2.65) and (2.66), is obtained from combining equation (2.56) with the molar stream ratio $\dot{F}\,\dot{D}^{-1}$:

$$\lambda \underset{(2.56)}{=} m\,\frac{\dot{G}}{\dot{L}} \underset{(3.1)}{=} m\,\frac{\dot{D}}{\dot{F}} \tag{3.24}$$

To determine the slope of the equilibrium curve m, equation (2.58) is used with the mid-bed composition $x_{\mathrm{mb,is}}$:

$$m = \frac{\overline{\alpha}_{12}}{\left[1 + (\overline{\alpha}_{12} - 1)\,x_{\mathrm{mb,is}}\right]^2} \tag{3.25}$$

Inserting x_{B} and x_{is} into equation (2.4) allows calculating the geometrically averaged relative volatility $\overline{\alpha}_{12}$ required for equation (3.25):

$$\overline{\alpha}_{12} = \sqrt{\alpha_{12}(x_{\mathrm{B}}) \cdot \alpha_{12}(x_{\mathrm{is}})} \tag{3.26}$$

Relative volatilities $\alpha_{12}(x_{\mathrm{B}})$ and $\alpha_{12}(x_{\mathrm{is}})$ are calculated according to equation (2.7). Required

vapor pressures p_1^0 and p_2^0 are numerically estimated based on mid-bed pressure p_{mb} as well as mixture compositions x_{B} and x_{is} according to appendix C.12.

As already mentioned, HETP is obtained from $\mathrm{HTU_{oG}}$ using equation (2.65), which is only mathematically valid for $\lambda \neq 1$. For such cases, an approximation mathematically valid for $\lambda = 1$ was introduced in equation (2.66). As indicated by the ratio HETP $\mathrm{HTU_{oG}^{-1}}$ and illustrated in figure 3.9, resulting deviations are expected to be small for $\lambda \to 1$. However, as $m = 1$ is hardly achieved in total reflux experiments due to variations in mixture composition or operating conditions, an exact value of $\lambda = 1$ seems very unlikely. Therefore, the HETP approximation given in equation (2.66) is less important for experiment evaluation and thus, not used in this work.

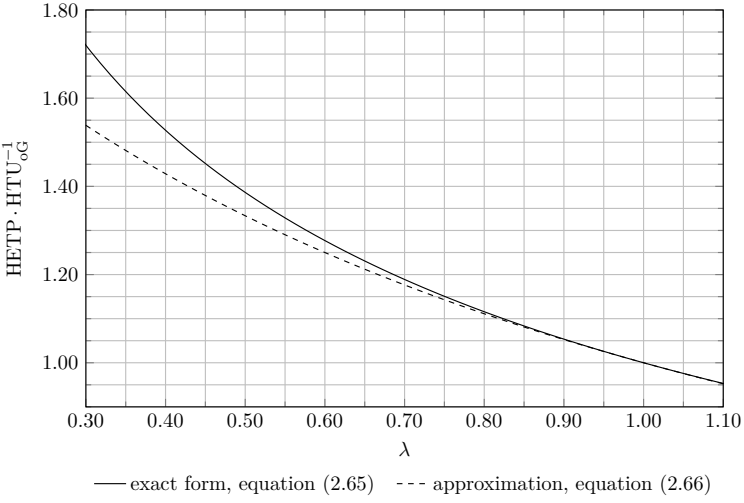

Figure 3.9.: Comparison of equations to calculate HETP from $\mathrm{HTU_{oG}}$, exact form: $\mathrm{HETP} \cdot \mathrm{HTU_{oG}^{-1}} = \ln(\lambda)\,(\lambda-1)^{-1}$, approximation: $\mathrm{HETP} \cdot \mathrm{HTU_{oG}^{-1}} = 2\,(\lambda+1)^{-1}$

3.5.4.3. Comparing Theoretical Stages and Transfer Units

As described in sections 2.2.1 and 2.2.2, expressing separation performance in terms of the number of theoretical stages N_{th} or the height equivalent to a theoretical plate HETP is strongly linked to the concept of equilibrium stages. To achieve vapor-liquid equilibrium between the outlet streams of each stage, relevant mass transfer phenomena are neglected and an instantaneous mass transfer is assumed. Contrary, mass transfer is considered in the concept of transfer units wherein mass transfer correlations are used to describe relevant mass transfer-phenomena occurring in both the vapor and the liquid phase. Due to their conceptual difference, both approaches are sometimes considered independent of each other. Nonetheless, as evaluating

separation performance of existing separation equipment should result in equal or at least very similar results, both concepts can be linked to each other as elaborated in sections 2.2.3.3 and 2.2.3.4.

Using equation (2.65), $\mathrm{HTU_{oG}}$ determined with the Delft model are converted into HETP and compared to the corresponding results obtained from the McCabe-Thiele stage constructions. A similar comparison is carried out based on equation (2.69), which links $\mathrm{NTU_{oG}}$ and N_{th}. In addition to converting N_{th} into $\mathrm{NTU_{oG}}$ with equation (2.69), $\mathrm{NTU_{oG}}$ is also calculated by integration according to equation (2.54a). The respective graphical representation of $\mathrm{NTU_{oG}}$ was already introduced in figure 2.8. Since both VLE and stripping operating line are given as discrete data points, $\mathrm{NTU_{oG}}$ is determined by numeric integration using the composite trapezoidal rule[9]. Using the obtained $\mathrm{HTU_{oG}}$ and $\mathrm{NTU_{oG}}$, the height of the packed bed H_{bed}, required to perform the mixture separation achieved in each experiment, is predicted according to equation (2.68) and compared with the height of the packed bed installed in the distillation column of the experimental setup.

In addition, HETP and $\mathrm{HTU_{oG}}$ as well as N_{th} and $\mathrm{NTU_{oG}}$ are directly compared to each other. For this, the case study of varying stripping factors λ is recalled from section 2.2.3.4. Since (Duss and Taylor, 2018; Koshy and Rukovena, 1986) originally defined these cases for total reflux experiments ($\lambda = m\,\dot{G}\,\dot{L}^{-1}$, $\dot{L}\,\dot{G}^{-1} = 1 \Longrightarrow \lambda = m$, see equation (2.56)), a variation of λ solely originates from a change in the slope of the equilibrium curve m, which itself results from changes in liquid composition or operating pressure. Furthermore, as separation performance experiments are commonly conducted under total reflux conditions using a narrow-boiling binary mixture with an equimolar mid-bed liquid composition, a *difficult symmetric separation* is used to investigate separation performance experimentally[10]. Depending on the operating and mixture conditions, such separations can be represented by $\lambda \approx 1$ (case 2 defined in section 2.2.3.4). Therefore, $\mathrm{HTU_{oG}} \approx \mathrm{HETP}$ and $\mathrm{NTU_{oG}} \approx N_{\mathrm{th}}$ is commonly obtained for separation performance experiments at total reflux, which does not allow addressing the applicability of HETP vs. $\mathrm{HTU_{oG}}$ and $\mathrm{NTU_{oG}}$.

However, for partial reflux experiments, the slope of the operating line offers an additional degree of freedom, which in turn allows varying the stripping factor λ without changing the slope of the equilibrium curve m and, depending on the operating conditions, does not necessarily result $\mathrm{HTU_{oG}} \approx \mathrm{HETP}$ and $\mathrm{NTU_{oG}} \approx N_{\mathrm{th}}$. Due to the used plant setup, the experiments conducted in this work, only cover operating conditions with $\lambda \leq 1$, which is represented by the cases 1 and 2 elaborated in section 2.2.3.4. Although this can be considered as a data bias in experimental results, obtained data are used to discuss HETP vs. $\mathrm{HTU_{oG}}$ and $\mathrm{NTU_{oG}}$, as the relationship enabling this particular comparison is unique to partial reflux experiments.

[9] Numeric integration is performed with `numpy.trapz`; see (Harris et al., 2020). An approach for algebraic integration is given in appendix E.1.

[10] The terms *symmetric separation* and *difficult separation* were introduced in section 2.2.3.4.

4. Results and Discussion

In contrast to conventional separation performance experiments conducted at total reflux, additional effects inherent to the characteristics of the proposed plant setup need to be considered for the experiments of this work. This is especially relevant for the results obtained from partial reflux experiments, since the slope of the operating line offers an additional degree of freedom and thus, increases the number of uncertainty components to consider. Therefore, plant operating conditions and their associated uncertainties will be addressed in the first section of this chapter, while separation performance is discussed in the second section. Finally, a method evaluation highlighting potential improvements for the developed plant concept, its apparative realization and the data processing procedures based on the identified plant characteristics and the discussed results is provided in the third section of this chapter.

As already highlighted in section 3.5, relevant uncertainties are quantified based on appendix D.2 and the data evaluation workflow summarized in table E.3. Although uncertainties are consistently propagated, quantifying individual uncertainty contributions does require not only individual uncertainty components, but also corresponding sensitivity coefficients, which are not available based on the implementation used in this work[1]. Therefore, uncertainties associated with the experimental results are discussed without addressing individual uncertainty contributions.

4.1. Plant Operation

4.1.1. Molar Stream Ratio as an Additional Degree of Freedom

The external feed stream required for partial reflux offers an additional degree of freedom, which is expressed in terms of the molar stream ratio $\dot{F}\,\dot{D}^{-1}$ representing the slope of the operating line, see equation (3.1). However, varying the slope of the operating line may cause a substantial source of uncertainty which is discussed in the following.

The combined standard uncertainty associated with the molar stream ratio is denoted by $u_c(\dot{F}\,\dot{D}^{-1})$ and illustrated in figure 4.1. In accordance with expectations, the smallest uncertainty is obtained for $\dot{F}\,\dot{D}^{-1} = 1.0$ in total reflux operating mode. The determination and control of feed mass flow are directly coupled to the distillate mass flow in this operating mode. Therefore, this observation is related to the underlying control loops of the plant control system, inasmuch

[1] Individual uncertainty contributions are accessible using the *uncertainties* package, see (Lebigot, 2017) for details, but not explicitly exported in this work.

as $\dot{F}\,\dot{D}^{-1} = 1.0$ is strictly enforced by controlling the feed flow based on the liquid level of feedstock tank B601 and measuring the resulting mass flow with flow meter F101, which reduces the number of uncertainty contributions affecting the molar stream ratio $\dot{F}\,\dot{D}^{-1}$.

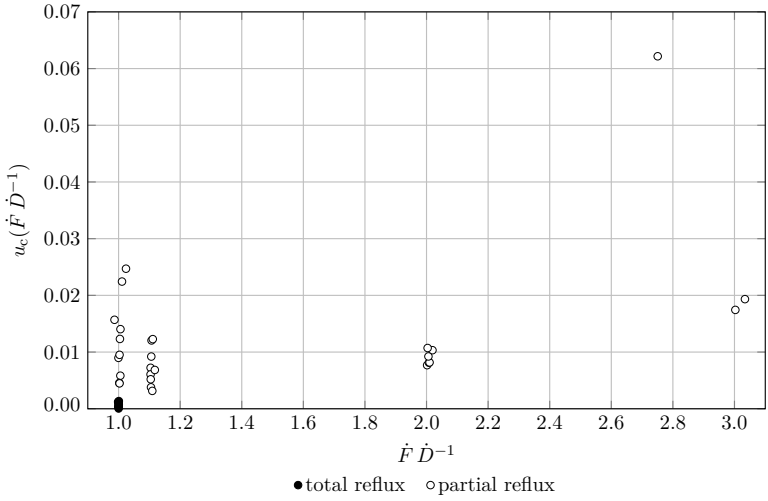

Figure 4.1.: Combined standard uncertainty associated with molar stream ratio $\dot{F}\,\dot{D}^{-1}$

For partial reflux operation, the range of associated combined standard uncertainty increases. Although the largest spread in uncertainties is observed for simulated total reflux ($\dot{F}\,\dot{D}^{-1} = 1.0$), its spread decreases with increasing $\dot{F}\,\dot{D}^{-1}$. However, this trend may be biased due to the low number of experiments performed for $\dot{F}\,\dot{D}^{-1} = 2.8$ ($N = 1$) and $\dot{F}\,\dot{D}^{-1} = 3.0$ ($N = 2$).

While the molar stream ratio $\dot{F}\,\dot{D}^{-1}$ is essential for experiment evaluation, it is not accessible during plant operation and calculated using the corresponding mass flows, $\dot{m}_\mathrm{F}$ and $\dot{m}_\mathrm{D}$, as well as liquid mixture compositions, x_F and x_D, according to equation (3.2c). Furthermore, equation (3.2c) links the molar stream ratio $\dot{F}\,\dot{D}^{-1}$ to the stream ratio $\dot{m}_\mathrm{F}\,\dot{m}_\mathrm{D}^{-1}$ using the ratio of the molar masses of distillate and feed streams $M_\mathrm{D}\,M_\mathrm{F}^{-1}$. In this context, a maximum deviation between $\dot{m}_\mathrm{F}\,\dot{m}_\mathrm{D}^{-1}$ and $\dot{F}\,\dot{D}^{-1}$ of $\pm 6\,\%$ ($M_\mathrm{D}\,M_\mathrm{F}^{-1} = 0.94 \ldots 1.06$) was derived in section 3.3.3.1. However, deviations of less than $\pm 6\,\%$ are expected, since liquid molar fractions x_D and x_F substantially differ from $x_i = 0\,\mathrm{kmol_{CB}\,kmol_{tot}^{-1}}$ or $x_i = 1\,\mathrm{kmol_{CB}\,kmol_{tot}^{-1}}$ for separation performance experiments. The results obtained from the conducted separation performance experiments consolidate this assumption, inasmuch as a maximum value of $M_\mathrm{D}\,M_\mathrm{F}^{-1} = 1.0029(57)$ was determined for experiment *627-2*.

4.1.2. Column Load and Operating Regime

Regardless of the specific operating mode, liquid load w_L and f-factor f_G are linked to each other by the corresponding column-internal flows and a suitable stream ratio. Therefore, both measures can be considered equivalent such that any liquid-vapor ratio, e.g. $\dot{m}_F\,\dot{m}_D^{-1}$, $\dot{F}\,\dot{D}^{-1}$ or $w_L\,f_G^{-1}$, can be used to describe plant operation. In this work, column load and plant operation are described based on the f-factor f_G and the molar stream ratio $\dot{F}\,\dot{D}^{-1}$ to ensure a consistent presentation of results and comparability with literature references. However, f_G and $\dot{F}\,\dot{D}^{-1}$ can be converted into the aforementioned measures using the corresponding mass or molar flows as well as mid-bed temperatures and compositions as shown in appendix A.8.

The relation between liquid load w_L and f-factor f_G is depicted in figure 4.2. Corresponding combined standard uncertainties, $u_c(w_L)$ and $u_c(f_G)$, are illustrated in figures F.2a and F.2b, respectively.

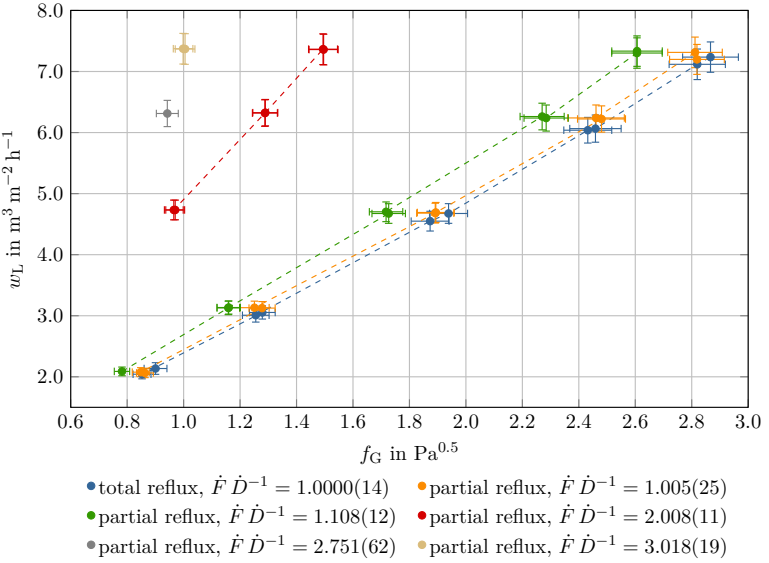

Figure 4.2.: Relation between liquid load w_L and f-factor f_G in dependence of molar stream ratio $\dot{F}\,\dot{D}^{-1}$, indicated uncertainties are combined standard uncertainties $u_c(\cdot)$

The data shown in figure 4.2 indicate an approximately linear relation between liquid load w_L and f-factor f_G. As can be seen, the slope increases with higher molar stream ratio $\dot{F}\,\dot{D}^{-1}$. This observation is similar to trends reported by (Cai, 2014) who published data points illustrating the relation between capacity factor[2] and liquid load w_L for total and partial reflux.

Since separation performance is substantially affected by the operating regime in which

[2]Capacity factor C_G: $C_G = f_G\,(\rho_L - \rho_G)^{-1}$, see (Cai, 2014) for details.

experimental investigations are carried out, the specific pressure drop Δp_{bed} is evaluated. As briefly discussed in section 3.5.2, the flood point of *Mellapak*-type packings is commonly defined at a specific pressure drop of $\Delta p_{\mathrm{bed}} = 12\,\mathrm{mbar\,m^{-1}}$. Furthermore, (Cai, 2014) states that 20 % of the load at the flood point is commonly considered as the minimum liquid load. Using these limits results in an operating window of $\Delta p_{\mathrm{bed}} \approx 2.4 \ldots 12\,\mathrm{mbar\,m^{-1}}$. As shown in figure 4.3, all experiments were approximately conducted within this range, inasmuch as $\Delta p_{\mathrm{bed}} = 1.42(80)\,\mathrm{mbar\,m^{-1}}$ and $\Delta p_{\mathrm{bed}} = 12.16(80)\,\mathrm{mbar\,m^{-1}}$ are obtained as minimum and maximum specific pressure drop, respectively. Furthermore, recorded data do not show the abrupt increase in specific pressure drop characteristic for reaching the flood point. This is especially confirmed as (Bradtmöller, 2017) achieved flooding at $f_{\mathrm{G}} \approx 3.2\,\mathrm{Pa}^{0.5}$ with a similar plant setup at total reflux. The specific pressure drops of all experiments are tabulated in table F.2.

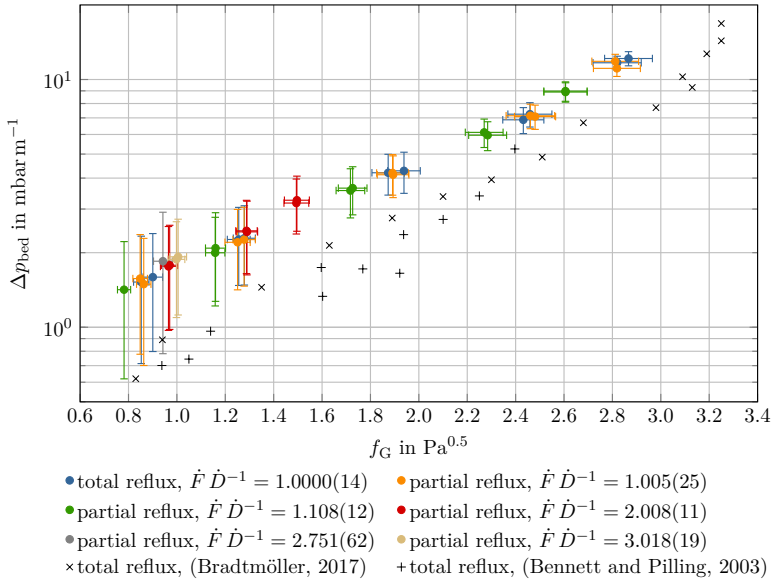

Figure 4.3.: Specific pressure drop Δp_{bed} in dependence of f-factor f_{G} and molar stream ratio $\dot{F}\,\dot{D}^{-1}$, literature data for $d_{\mathrm{col}} = 50\,\mathrm{mm}$ (Bradtmöller, 2017) and $d_{\mathrm{col}} = 1\,\mathrm{m}$ (Bennett and Pilling, 2003), indicated uncertainties are combined standard uncertainties $u_{\mathrm{c}}(\cdot)$

4.1.3. Material Balances

To assess plant control loops and plant operating modes, the mass balance of each experiment is assessed during data evaluation. The mixture compositions obtained from sample analyses allow deriving the molar balance corresponding to each mass balance according to section 3.5.3. Deviations in both mass and molar balances are expressed in absolute as well as in relative

numbers, see figures F.3 and F.4. Obtained results are summarized in table 4.1. Although a maximum deviation of up to 20 % occurred for three experiments with molar stream ratios of $\dot{F}\,\dot{D}^{-1} = 1.1$, $\dot{F}\,\dot{D}^{-1} = 2.0$ and $\dot{F}\,\dot{D}^{-1} = 3.0$, more than 75 % of all experiments conducted in this work satisfy the maximum deviation ranges proposed by (Cai, 2014; Starkweather et al., 2014).

Table 4.1.: Deviations in mass balance

deviation within	reference	satisfied by number of experiments	
±20 %	-	38	100.0 %
±5 %	(Starkweather et al., 2014)	35	92.1 %
±2 %	(Cai, 2014)	30	78.9 %

Furthermore, the deviations illustrated in figure F.3 do not indicate any systematic relation with respect to column load or molar stream ratio. Therefore, the used plant instrumentation and implemented plant control loops are considered appropriate to perform separation performance experiments with both total and partial reflux.

However, in total reflux operating mode, the feed stream is controlled by the weight of the feedstock tank B601 and recorded by the flow meter F101. Therefore, $\dot{m}_\mathrm{F} \stackrel{!}{=} \dot{m}_\mathrm{D}$ and $\dot{m}_\mathrm{B} \stackrel{!}{=} 0\,\mathrm{kg\,h^{-1}}$ are assumed for data evaluation resulting in $\varepsilon = 0\,\mathrm{kg\,h^{-1}}$ for the total reflux experiments.

In addition to mass balances, the molar balances illustrated in figure F.4 are considered to address the consistency of molar in- and output streams, since they affect the molar stream ratio $\dot{F}\,\dot{D}^{-1}$. Similar to the observed deviations in mass balance, no systematic relation between the operating conditions and the occurring deviation in molar balance was identified. This observation is consolidated by the uncertainties associated with the in- and output streams illustrated in figure F.1 from which no correlation is apparent.

It is worth noting that the molar balances are also affected by the mixture composition of each stream. As uncertainty quantification for mixture analysis shows small uncertainties, see section 3.5.1, the effect of respective uncertainties on molar balances is considered less important and thus, not explicitly addressed in this work. However, compositions of in- and output streams are illustrated in figures F.5 and F.6.

4.1.4. Mid-Bed Conditions

As suggested by (Ottenbacher et al., 2011) and elaborated in section 3.5.2, separation performance is evaluated based on representative mid-bed pressures, temperatures and compositions. These mid-bed operating conditions are calculated according to equation (3.10) and discussed in the following sections. Mid-bed operating pressures p_mb and mid-bed temperatures ϑ_mb as well as their associated combined standard uncertainties $u_\mathrm{c}(p_\mathrm{mb})$ and $u_\mathrm{c}(\vartheta_\mathrm{mb})$ are tabulated in

table F.2.

4.1.4.1. Pressures, Temperatures and Feed Subcooling

As shown in figure 4.4a, a slight increase in mid-bed operating pressure p_{mb} is observed for increasing f-factors f_{G}. According to equation (3.10d), mid-bed operating pressure is obtained as the arithmetic average of head pressure p_{h} and the pressure below the packed bed p_{b}. Since a setpoint of $p_{\mathrm{h}} = 100\,\mathrm{mbar(a)}$ is used for all experiments and kept constant by the plant control system, variations in p_{mb} solely result from varying pressures p_{b}, which originate from variations in mixture composition below the packed bed and the fluiddynamics inside the bed. A comparison of head and bottom pressures, p_{h} and p_{b}, is given in figure F.11.

The progression of the mid-bed operating temperature ϑ_{mb}, which is illustrated in figure 4.4b, is similar to the plot obtained for mid-bed pressure p_{mb}. Underlying values and associated combined standard uncertainties are listed in table F.2. Analogous to the mid-bed operating pressure, the mid-bed operating temperature is calculated as the arithmetic average of head and bottom temperatures, ϑ_{h} and ϑ_{b}, see equation (3.10c). Neglecting potential heat transfer originating from the trace heating at the column head, neither ϑ_{h} nor ϑ_{b} are controlled. Therefore, the mid-bed temperature ϑ_{mb} is directly affected by ϑ_{h} and ϑ_{b}, which are shown in figure F.13.

Since head and bottoms temperatures, ϑ_{h} and ϑ_{b}, are addressed for the mid-bed operating temperature ϑ_{mb}, it is convenient to discuss the feed subcooling in this context. The feed subcooling ΔT_{F} is calculated according to equation (3.14). Feed inlet temperatures ϑ_{F} and feed boiling points $\vartheta_{\mathrm{F,boil}}$ are illustrated in figure F.12, resulting feed subcoolings are shown in figure 4.5. Obtained values are within the range $\Delta T_{\mathrm{F}} = 0.13(67) \ldots 2.83(67)\,\mathrm{K}$, such that a maximum difference between the corresponding liquid molar fractions of $x_{\mathrm{is}} - x_{\mathrm{F}} = 0.0008(13)\,\mathrm{kmol_{CB}\,kmol_{tot}^{-1}}$ is obtained. As the associated combined standard uncertainties of $x_{\mathrm{is}} - x_{\mathrm{F}}$ are consistently larger than the nominal values, the calculated differences in feed composition due to feed subcooling are assumed to be negligible[3].

[3] Although assumed negligible, considering feed subcooling in terms of the feed condition q improved the robustness of the separation performance based on Monte Carlo methods.

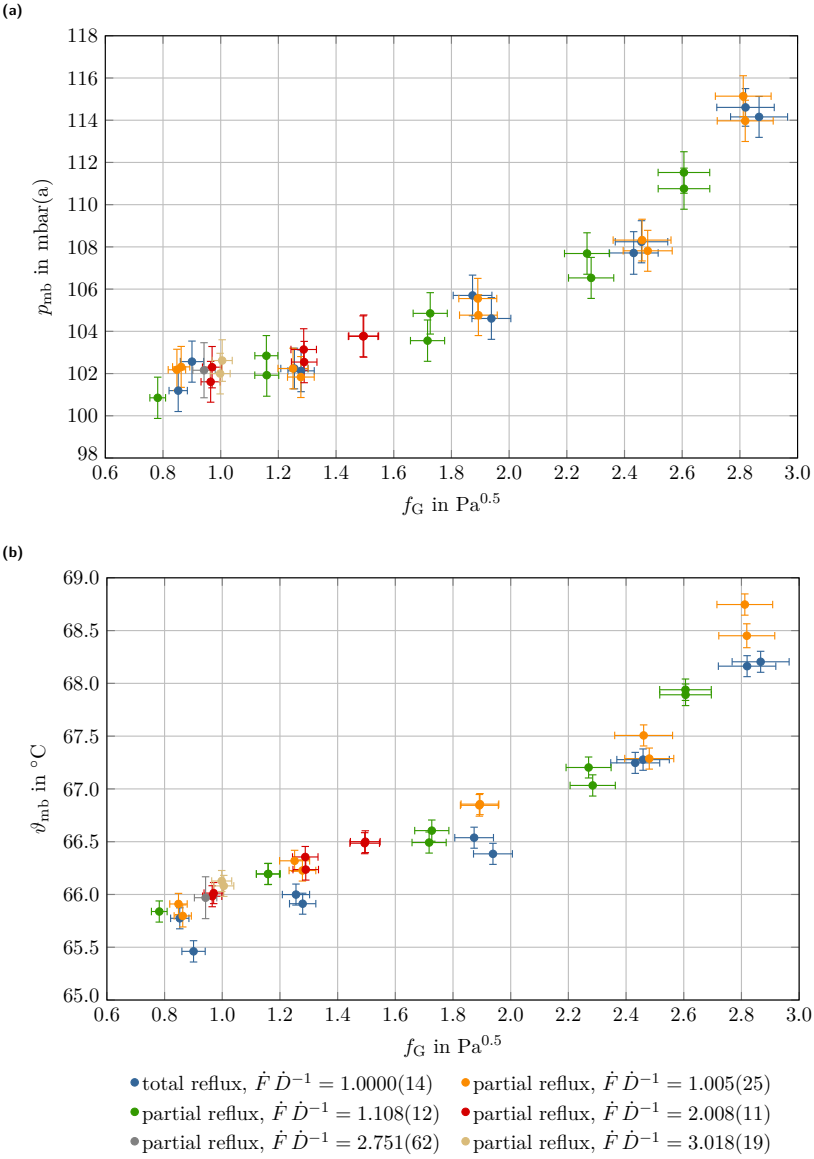

Figure 4.4.: Mid-bed operating pressure p_{mb} (a) and temperature ϑ_{mb} (b) in dependence of f-factor f_G and molar stream ratio $\dot{F}\,\dot{D}^{-1}$, indicated uncertainties are combined standard uncertainties $u_c(\cdot)$

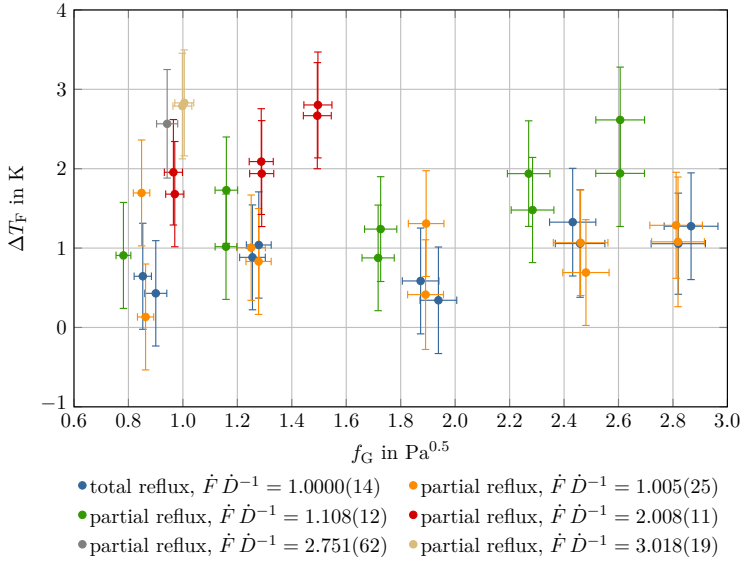

Figure 4.5.: Feed subcooling ΔT_F in dependence of f-factor f_G and molar stream ratio $\dot{F}\,\dot{D}^{-1}$, indicated uncertainties are combined standard uncertainties $u_c(\cdot)$

4.1.4.2. Mid-Bed and Feedstock Compositions

Separation performance measures heavily depend on the obtained mixture separation and the corresponding concentration spread between two representative sampling points. However, the positions of sampling points are strongly related to the used plant setup. As highlighted, the plant setup used in this work comprises a product recycle which is used as the feedstock mixture. The feed inlet is positioned above the packed bed substituting the conventional reflux stream, see figure 3.3. In contrast to the conventional plant setup, the composition of distillate and feed/reflux streams are thus not equal to each other. As a result, mid-bed liquid and vapor compositions, x_{mb} and y_{mb}, also differ from each other ($x_{mb} \neq y_{mb}$). Suitable definitions for both x_{mb} and y_{mb} were addressed with equations (3.10a) and (3.10b). Due to the negligible difference between the composition of the feed inlet mixture x_F and the calculated mixture composition at the intersection x_{is} elaborated in section 4.1.4.1, $x_F \approx x_{is}$ and $x_{mb} \approx x_{mb,is}$ is deduced. Therefore, further discussions focus on x_{mb} and y_{mb}, only. Achieved compositions of feed and product streams are shown in figures F.5 and F.6.

To achieve a symmetric separation problem, equimolar mid-bed fractions ($x_{mb} = y_{mb} = 0.5\,\mathrm{kmol_{CB}\,kmol_{tot}^{-1}}$) are commonly recommended for conventional separation performance experiments. For this, the initial composition of the mixture used for the separation performance experiments needs to be chosen appropriately. In contrast to the conventional approach, an

equimolar initial feedstock mixture was used in this work. As the feedstock composition changes until separation steady state is reached, $x_{\mathrm{mb}} \neq 0.5\,\mathrm{kmol_{CB}\,kmol_{tot}^{-1}}$ and $y_{\mathrm{mb}} \neq 0.5\,\mathrm{kmol_{CB}\,kmol_{tot}^{-1}}$ are achieved in steady state. The specific values depend on the occurring separation performance which itself is affected by the molar stream ratio $\dot{F}\,\dot{D}^{-1}$. Although the molar stream ratio was varied within the range $\dot{F}\,\dot{D}^{-1} = 1.0 \ldots 3.0$, obtained mid-bed liquid compositions x_{mb} and vapor compositions y_{mb} are mostly within the range $0.45 \ldots 0.62\,\mathrm{kmol_{CB}\,kmol_{tot}^{-1}}$, see figure F.9.

Compared to partial reflux operation, consistently higher mid-bed molar fractions x_{mb} and y_{mb} are achieved in total reflux experiments. The higher mid-bed compositions originate from the missing bottoms recycle resulting in $x_{\mathrm{F}} = x_{\mathrm{D}}$ and thus, $x_{\mathrm{mb}} = y_{\mathrm{mb}}$. In contrast, $x_{\mathrm{F}} < x_{\mathrm{D}}$ is obtained for partial reflux as the bottoms recycle added to the distillate stream is rich in less volatile component lowering the concentration of the more volatile component in the resulting feed mixture. The parity plot given in figure 4.6 consolidates this observation.

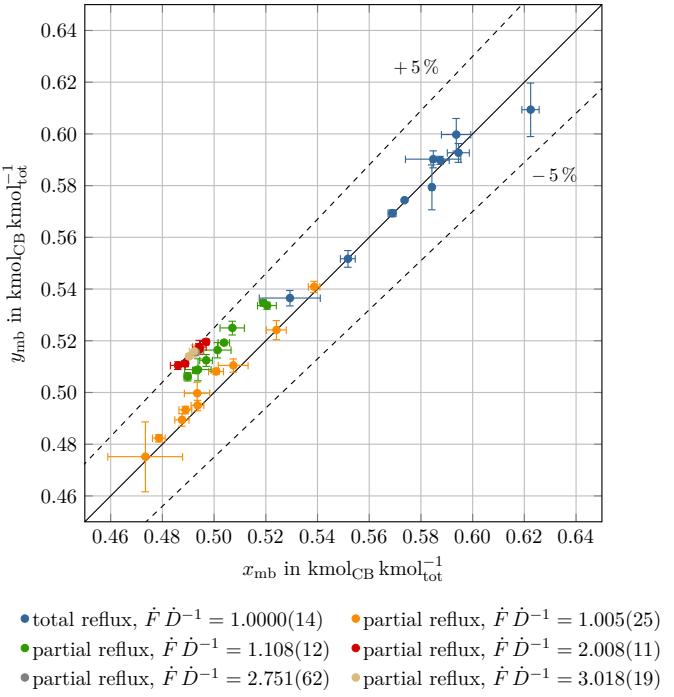

Figure 4.6.: Parity plot of molar fractions of chlorobenzene in liquid stream (x_{mb}) and vapor stream (y_{mb}) at mid-bed position, indicated uncertainties are combined standard uncertainties $u_c(\cdot)$

Furthermore, figure 4.6 shows higher mid-bed vapor compositions for increasing molar stream ratios $\dot{F}\,\dot{D}^{-1}$. In particular, the illustrated data indicate a linear relation between x_{mb} and y_{mb},

which can also be derived from equations (3.10a) and (3.10b): $y_{\mathrm{mb}} = x_{\mathrm{mb}} + 0.5 \cdot (x_{\mathrm{D}} - x_{\mathrm{F}})$. While the slope of the linear function is equal to unity and constant for all experiments, the y-intercept depends on the concentration spread between distillate and feed $(x_{\mathrm{D}} - x_{\mathrm{F}})$. Both x_{D} and x_{F} depend on the achieved separation performance and thus, are affected by the molar stream ratio $\dot{F}\,\dot{D}^{-1}$.

All vapor mid-bed compositions y_{mb} presented in figure 4.6 are within a margin of $\pm\,5\,\%$ with respect to the corresponding liquid composition x_{mb}. However, data points below the parity line are not feasible, since mixture compositions must satisfy $x_{\mathrm{B}} < x_{\mathrm{F}} \leq x_{\mathrm{D}}$. Except for the experiment with $x_{\mathrm{mb}} = 0.6224(33)\,\mathrm{kmol_{CB}\,kmol_{tot}^{-1}}$, this is valid for all experiments within the indicated combined standard uncertainties $u_{\mathrm{c}}(x_{\mathrm{mb}})$ and $u_{\mathrm{c}}(y_{\mathrm{mb}})$.

4.2. Separation Performance

4.2.1. Using Theoretical Stages

4.2.1.1. Data Evaluation with Monte Carlo Methods

As presented in section 3.5.4.1, McCabe-Thiele stage constructions were used to determine the number of theoretical stages N_{th} for each experiment. Since this approach generally involves numeric and iterative calculation routines, uncertainties are propagated with Monte Carlo methods (MCM). Although mathematically consistent, thermodynamically invalid combinations of parameters may be drawn from the underlying probability distributions and passed to the McCabe-Thiele stage construction routine. To restrict data evaluation on thermodynamically valid parameter sets, invalid sets are excluded from further data processing as elaborated in section 3.5.4.1 and appendix E.4. To quantify the fraction of successful/valid stage constructions, the success ratio S_{MC} was introduced in equation (3.19). Evaluating S_{MC} for each experiment, allows identifying two edge cases: While $S_{\mathrm{MC}} = 100\,\%$ represents experiments for which all McCabe-Thiele constructions created with random samples from the respective parameter distributions are valid, $S_{\mathrm{MC}} \approx 0\,\%$ indicates that almost all the generated sets of parameters passed to the McCabe-Thiele stage construction routine result in invalid stage constructions. Such cases are consistently obtained for parameter combinations in which the intersection between stripping line and feed line is located above the equilibrium curve, see figure 4.7. Illustrations of the MCM solution space for each experiment are given in appendix F.2.4, corresponding success ratios S_{MC} can be found in table F.4.

As discussed in section 3.5.4.1, a low success ratio S_{MC} results in a substantially reduced number of samples used for uncertainty propagation. Furthermore, the probability distributions of the input parameters used for the McCabe-Thiele stage constructions depend on the operating conditions. Therefore, as shown in figure 4.8, the number of successful stage constructions is also related to the operating conditions. For all f-factors f_{G} investigated in this work, success ratios of $S_{\mathrm{MC}} > 99\,\%$ are obtained for molar stream ratios of $\dot{F}\,\dot{D}^{-1} \leq 1.1$.

In contrast, all experiments with $\dot{F}\,\dot{D}^{-1} > 1.1$ show substantially lower success ratios of

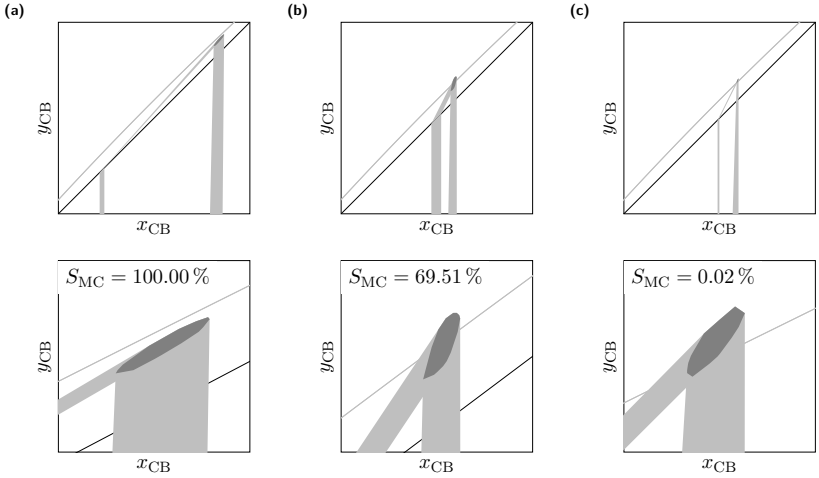

Figure 4.7.: Constructability of McCabe-Thiele stage constructions, exemplary illustration for experiments *604-2* (a), *626-1* (b) and *628-1* (c); filled areas: convex hulls containing solutions space of MCM; lightgray: equilibrium curves, bottoms compositions, stripping lines and feed lines; darkgray: intersections of feed lines with stripping lines; top: McCabe-Thiele diagram within $0.25 \ldots 0.7\,\mathrm{kmol_{CB}\,kmol_{tot}^{-1}}$; bottom: zoomed view to highlight intersections of feed lines with stripping lines; S_{MC}: success ratio for MCM

$S_{MC} < 83\,\%$. The largest spread in S_{MC} between replicates[4] is identified for $\dot{F}\,\dot{D}^{-1} = 2.0$ at $f_G \approx 1.3\,\mathrm{Pa}^{0.5}$ and $\dot{F}\,\dot{D}^{-1} = 3.0$. Although not exhaustively investigated due to a limited accessibility of intermediate values used in MCM, it is assumed that the large spread in success ratio S_{MC} is related to the pseudo-random samples drawn from the probability distributions of the operating parameters, since respective experiments do not substantially vary in feed and bottoms compositions, x_F and x_B, see figures F.5 and F.6, as well as head pressures p_h, see figure F.11. While figure 4.5 indicates a slightly higher feed subcooling ΔT_F compared to the other experiments, for which similar success ratios are obtained throughout conducted replicates, the feed subcooling ΔT_F of the respective replicates are within their associated combined standard uncertainties and resulting liquid compositions at the intersection x_{is} are also similar, see figure F.5. Since substantial variations in the input parameters for the McCabe-Thiele stage constructions are very unlikely, the only effect which cannot be directly evaluated is the generation of random samples passed to the MCM. The large spreads in success ratio S_{MC} for the experiments with $\dot{F}\,\dot{D}^{-1} = 2.0$ at $f_G \approx 1.3\,\mathrm{Pa}^{0.5}$ and $\dot{F}\,\dot{D}^{-1} = 3.0$ are, therefore, considered indicating a high sensitivity with respect to the pseudo-random sampling for the respective combination of operating parameters.

[4]Except for $\dot{F}\,\dot{D}^{-1} = 2.8$, each experiment was replicated once ($N = 2$).

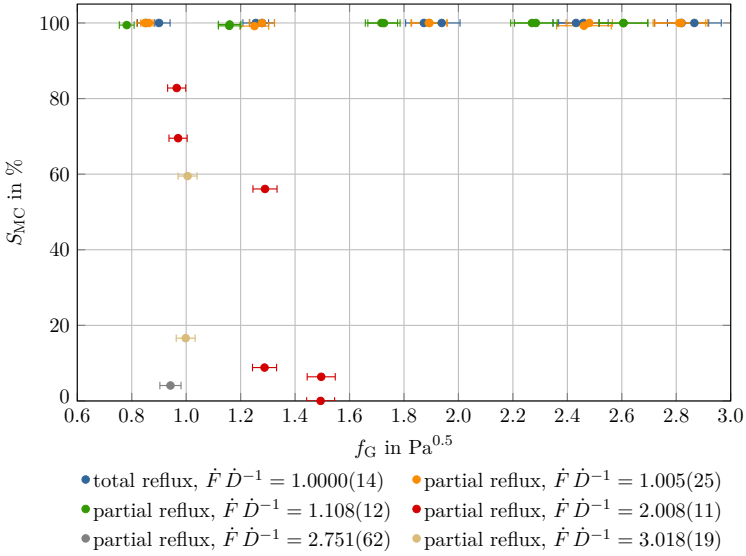

Figure 4.8.: Success ratio S_{MC} of McCabe-Thiele stage constructions created during Monte Carlo simulations in dependence of f-factor f_G and molar stream ratio $\dot{F}\,\dot{D}^{-1}$, indicated uncertainties are combined standard uncertainties $u_c(\cdot)$

4.2.1.2. Considering Fractional Equilibrium Stages

Considerations for a fractional equilibrium stage at the end of a stage polyline were introduced with equation (3.20) and figure 3.7. This approach is supported by table 3.7 providing an exemplary comparison of the number of theoretical stages N_{th} and $N_{th,dec}$ for experiment *604-2*. Both N_{th} and $N_{th,dec}$ as well as their associated combined standard uncertainties $u_c(N_{th})$ and $u_c(N_{th,dec})$ are aggregated from the distributions of the respective values determined by MCM. As illustrated in figure 4.9, considering fractional stages results in smoother density distribution functions, which in turn affects both its arithmetic mean and the standard deviation of the mean[5]. This improvement in experiment evaluation and uncertainty quantification is especially relevant for experiments with a low success ratio for which estimation and associated combined standard uncertainties are calculated based on a smaller number of valid samples.

As shown in the parity plot given in figure 4.10, considering a fractional stage at the end of the calculated stage constructions consistently results a lower number of theoretical stages. Although this observation can readily be deduced from equation (3.20), figure 4.10 indicates that the resulting differences between N_{th} and $N_{th,dec}$ are smaller than $-10\,\%$ for most cases.

[5] As described in appendix D.1, the *arithmetic mean* of a distribution is used to determine an *estimation* of a measurand and the *standard deviation of the mean* is interpreted as its associated combined standard uncertainty.

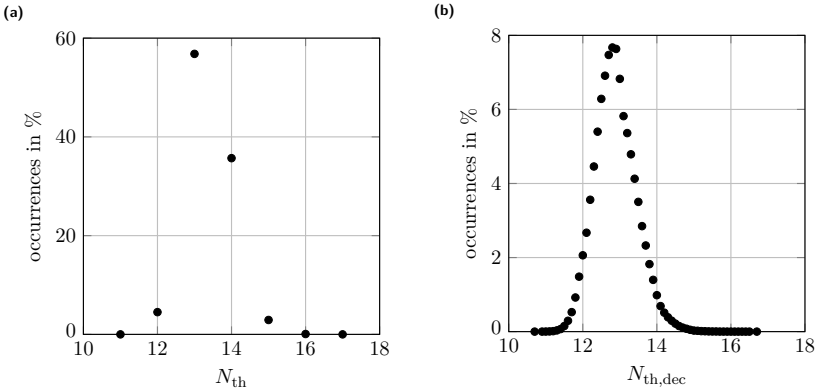

Figure 4.9.: Distribution of number of theoretical stages obtained from MCM without (a) and with (b) considering fractional stages, exemplary illustration for experiment *604-2*, N_{th}: number of theoretical stages without considering fractional stages, $N_{\mathrm{th,dec}}$: number of theoretical stages with considering fractional stages

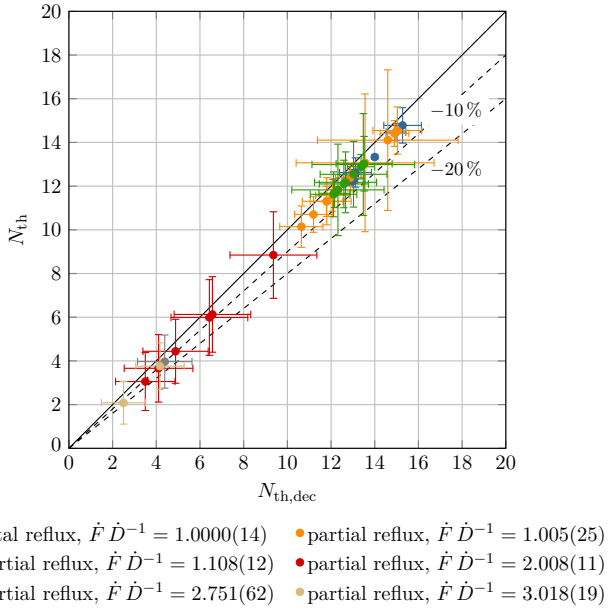

Figure 4.10.: Parity plot of number of theoretical stages obtained with and without considering fractional stages, N_{th}: number of theoretical stages without considering fractional stages, $N_{\mathrm{th,dec}}$: number of theoretical stages with considering fractional stages, indicated uncertainties are combined standard uncertainties $u_{\mathrm{c}}(\cdot)$

However, the difference between N_{th} and $N_{\mathrm{th,dec}}$ increases with a decreasing number of theoretical stages and deviations of around $-20\,\%$ are obtained for experiments with $N_{\mathrm{th}} \leq 4$. Therefore, considering fractional stages allows reducing systematic deviations in separation performance estimation. This is especially relevant for experiments in which a low number of theoretical stages is obtained from the McCabe-Thiele stage constructions.

Since fractional stages are consistently used in the further discussion of results, $N_{\mathrm{th,dec}}$ and N_{th} are not explicitly distinguished in the following sections.

4.2.1.3. Number of Theoretical Stages and HETP

To express the experimentally determined separation performance in terms of HETP values, the height of the packed bed H_{bed} and the number of theoretical stages N_{th} are used according to equation (2.44). Furthermore, a fractional stage is considered in the McCabe-Thiele stage constructions used to determine N_{th}[6]. Since all experiments of this work are conducted with an identical bed height, H_{bed} can be interpreted as the constant of proportionality for the inverse proportionality between N_{th} and HETP. Therefore, general trends in separation efficiency presented in this section are initially discussed based on the number of theoretical stages N_{th}.

As elaborated in section 3.3.2, the alternative plant setup used in this work supports both total and partial reflux operation. According to the research hypotheses and objectives, this is to allow a reasonable comparability with conventional separation performance experiments. In particular, the transition from total to partial reflux operation with respect to separation performance is addressed with simulated total reflux experiments.

An exemplary comparison of McCabe-Thiele stage constructions from experiments with similar column loads at total reflux, simulated total reflux and partial reflux is given in figure 4.11. While total and simulated total reflux experiments slightly vary in mid-bed liquid molar fractions x_{mb}, both the concentration spreads achieved by mixture separation Δx_{sep} ($\Delta x_{\mathrm{sep}} = x_{\mathrm{is}} - x_{\mathrm{B}}$) and the resulting number of theoretical stages N_{th} are similar. However, a substantially smaller concentration spread and a smaller number of theoretical stages are obtained for the exemplary partial reflux experiment with a molar stream ratio of $\dot{F}\,\dot{D}^{-1} = 2.0$.

Although subject to further discussions, these observations indicate a good comparability between total and simulated total reflux experiments and consolidate the conclusion deduced from the material balances, see section 4.1.3.

To generalize the exemplary comparison provided in figure 4.11, the number of theoretical stages as well as liquid mid-bed concentrations x_{mb} and concentration spreads Δx_{sep} of all experiments are discussed as a function of operating parameters. As shown in figure 4.12, the number of theoretical stages N_{th} obtained for total and simulated total reflux experiments ($\dot{F}\,\dot{D}^{-1} = 1.0$) are very similar and not affected by the f-factor for $f_{\mathrm{G}} < 2.4\,\mathrm{Pa}^{0.5}$. A similar observation applies for the partial reflux ratio experiments with a molar stream ratio of

[6] Although the symbol $N_{\mathrm{th,dec}}$ was introduced for cases in which fractional stages are explicitly considered, N_{th} is consistently used throughout further discussions which is in accordance with sections 3.5.4.1 and 4.2.1.2.

(a)

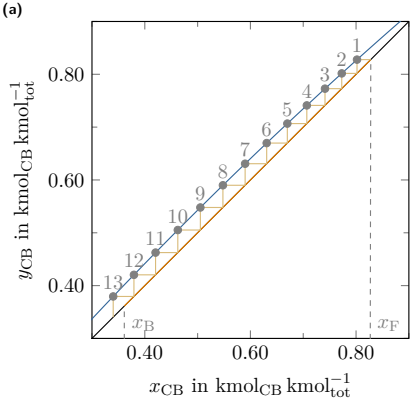

total reflux (experiment *702-2*)

	unit	value
$\dot{F}\,\dot{D}^{-1}$	-	0.999 79(54)
w_L	$m^3\,m^{-2}\,h^{-1}$	4.67(16)
f_G	$Pa^{0.5}$	1.939(67)
x_{mb}	$kmol_{CB}\,kmol_{tot}^{-1}$	0.5945(43)
Δx_{sep}	$kmol_{CB}\,kmol_{tot}^{-1}$	0.4667(85)
N_{th}	-	12.47(28)
S_{MC}	%	100.00

(b)

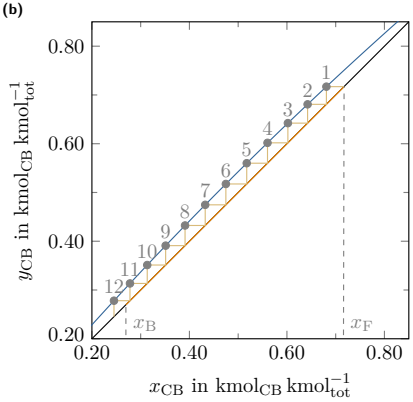

simulated total reflux (experiment *502-1*)

	unit	value
$\dot{F}\,\dot{D}^{-1}$	-	0.9996(90)
w_L	$m^3\,m^{-2}\,h^{-1}$	4.68(16)
f_G	$Pa^{0.5}$	1.891(66)
x_{mb}	$kmol_{CB}\,kmol_{tot}^{-1}$	0.4935(49)
Δx_{sep}	$kmol_{CB}\,kmol_{tot}^{-1}$	0.4475(98)
N_{th}	-	11.30(69)
S_{MC}	%	100.00

(c)

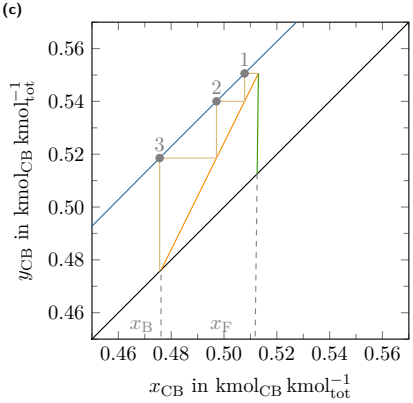

partial reflux (experiment *626-2*)

	unit	value
$\dot{F}\,\dot{D}^{-1}$	-	2.019(10)
w_L	$m^3\,m^{-2}\,h^{-1}$	4.73(16)
f_G	$Pa^{0.5}$	0.965(33)
x_{mb}	$kmol_{CB}\,kmol_{tot}^{-1}$	0.4944(26)
Δx_{sep}	$kmol_{CB}\,kmol_{tot}^{-1}$	0.0369(53)
N_{th}	-	3.1(1.3)
S_{MC}	%	82.79

Figure 4.11.: Exemplary McCabe-Thiele stage constructions for experiments with similar column loads at total (a), simulated total (b) and partial reflux (c), tabulated results are aggregated from MCM

$\dot{F}\,\dot{D}^{-1} = 1.1$, as a constant value of $N_{\mathrm{th}} \approx 12.5$ can be identified within indicated combined standard uncertainties. Despite not investigated due to a limited reboiler duty, an increasing trend in N_{th} similar to the data for $\dot{F}\,\dot{D}^{-1} = 1.0$ is expected for f-factors of $f_{\mathrm{G}} > 2.6\,\mathrm{Pa}^{0.5}$.

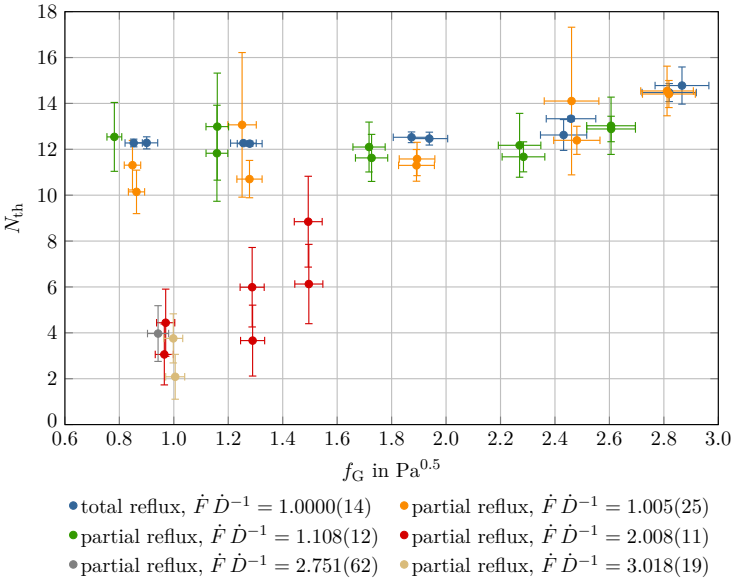

Figure 4.12.: Number of theoretical stages N_{th} in dependence of f-factor f_{G} and molar stream ratio $\dot{F}\,\dot{D}^{-1}$, indicated uncertainties are combined standard uncertainties $u_{\mathrm{c}}(\cdot)$

However, a considerably smaller number of theoretical stages is obtained for experiments with $\dot{F}\,\dot{D}^{-1} > 1.1$. In particular, the number of theoretical stages decreased to about 15 . . . 75 % of the value determined for experiments with $\dot{F}\,\dot{D}^{-1} \leq 1.1$. A similar trend was indicated by figure 4.10, giving a range of $N_{\mathrm{th}} = 2.08(98) \ldots 8.8(2.0)$ for $\dot{F}\,\dot{D}^{-1} > 1.1$ and $N_{\mathrm{th}} = 10.14(95) \ldots 14.78(81)$ for $\dot{F}\,\dot{D}^{-1} \leq 1.1$.

Since the molar stream ratio $\dot{F}\,\dot{D}^{-1}$ affects the slope of the stripping line, see equation (3.1), and a higher number of theoretical stages would generally result from a more inclined stripping line, the decrease in the number of theoretical stages with higher molar stream ratios $\dot{F}\,\dot{D}^{-1}$ might seem contradictory. This conclusion is only valid, if constant feed and bottoms compositions, x_{F} and x_{B}, are assumed. However, as shown in figure 4.11, higher molar stream ratios result in lower concentration spreads Δx_{sep}. Since this effect dominates, an overall decrease of the number of theoretical stages occurs for increasing $\dot{F}\,\dot{D}^{-1}$.

The effects and relations highlighted above show that several parameters need to be considered to consistently discuss separation performance in terms of the number of theoretical stages N_{th}:

- Molar stream ratio $\dot{F}\,\dot{D}^{-1}$: Describes plant operation with respect to column load, slope of the stripping line and deviation from total reflux operation.
- f-factor f_{G}: Describes column load; also used in evaluation of conventional separation performance measurements.
- Mid-bed compositions x_{mb}: Describes the "position" of the separation and thus, the "position" of the corresponding stage construction (symmetric separations are commonly preferred, see section 2.2.3.4).
- Concentration spread Δx_{sep}: Describes the change in composition achieved by mixture separation ($\Delta x_{\mathrm{sep}} = x_{\mathrm{is}} - x_{\mathrm{B}}$).
- Driving force Δx_{drv}: Describes the mean difference between input and equilibrium compositions of each stage along the full McCabe-Thiele stage construction which results in $\Delta x_{\mathrm{drv}} = \Delta x_{\mathrm{sep}}\, N_{\mathrm{th}}^{-1}$, see equation (3.22a).

The molar stream ratio $\dot{F}\,\dot{D}^{-1}$ and the f-factor f_{G} are varied as independent variables as part of the parameter studies, introduced in table 3.4. Mid-bed compositions x_{mb}, concentration spreads Δx_{sep} and the number of theoretical stages N_{th} are considered as dependent variables. While the mid-bed compositions x_{mb} obtained from total reflux experiments are consistently higher than those from partial reflux experiments, no substantial deviation between simulated total and partial reflux experiments is observed, see figure F.9a. Therefore, as illustrated in figure 4.13, N_{th} is considered to be independent of the mid-bed composition x_{mb} for the experiments performed in this work[7].

[7] As elaborated in section 2.2.3.4, a dependence of N_{th} on x_{mb} is expected for mixture separation in the concentration edges ($x_{\mathrm{mb}} \ll 0.5\,\mathrm{kmol_{CB}\,kmol_{tot}^{-1}}$ or $x_{\mathrm{mb}} \gg 0.5\,\mathrm{kmol_{CB}\,kmol_{tot}^{-1}}$), which are not covered by the experiments of this work.

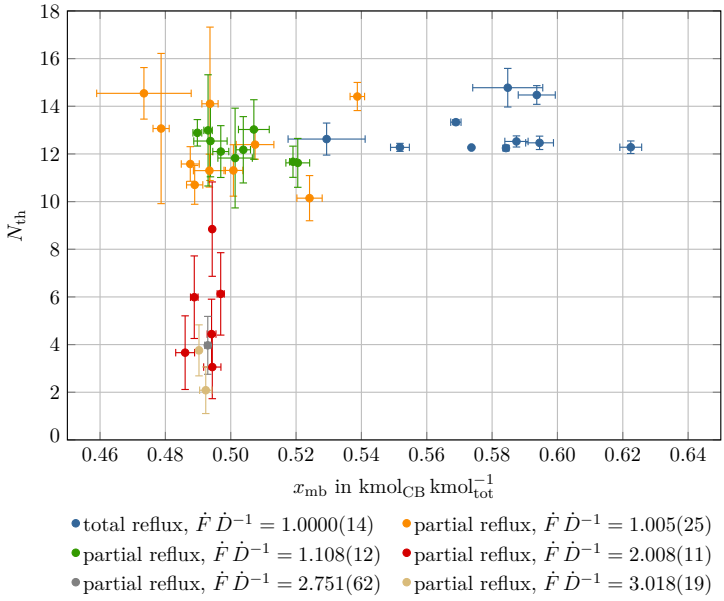

Figure 4.13.: Number of theoretical stages N_{th} in dependence of mid-bed liquid molar fraction x_{mb} and molar stream ratio $\dot{F}\,\dot{D}^{-1}$, indicated uncertainties are combined standard uncertainties $u_{\mathrm{c}}(\cdot)$

The exemplary comparison of McCabe-Thiele stage constructions depicted in figure 4.11 indicated a substantial reduction of concentration spread Δx_{sep} for an increasing molar stream ratio $\dot{F}\,\dot{D}^{-1}$. As shown in figure 4.14, this trend is consistent throughout all experiments resulting in three distinct clusters of results:

1. $\dot{F}\,\dot{D}^{-1} = 1.0$: Only slight variations in N_{th} and Δx_{sep} are observed for total and simulated total reflux experiments. Data indicate a linear trend in N_{th} with increasing Δx_{sep}. $\dot{F}\,\dot{D}^{-1} = 1.0$ represents the smallest slope of the stripping operating line investigated in the experiments which is equal to the diagonal line. Therefore, large driving forces result for the upper equilibrium stages which does not only improve mixture separation, but also results in high concentration spreads.

2. $\dot{F}\,\dot{D}^{-1} = 1.1$: Neither N_{th} nor Δx_{sep} vary substantially which results in a narrow cluster of values. Obtained results overlap within the indicated combined standard uncertainties.

3. $\dot{F}\,\dot{D}^{-1} \geq 2.0$: While only small variations in Δx_{sep} are observed, N_{th} vary by a factor of up to 4.5 which indicates a pronounced sensitivity. This supports the assumption of Δx_{sep} dominating the effect of $\dot{F}\,\dot{D}^{-1}$ on the resulting number of theoretical stages.

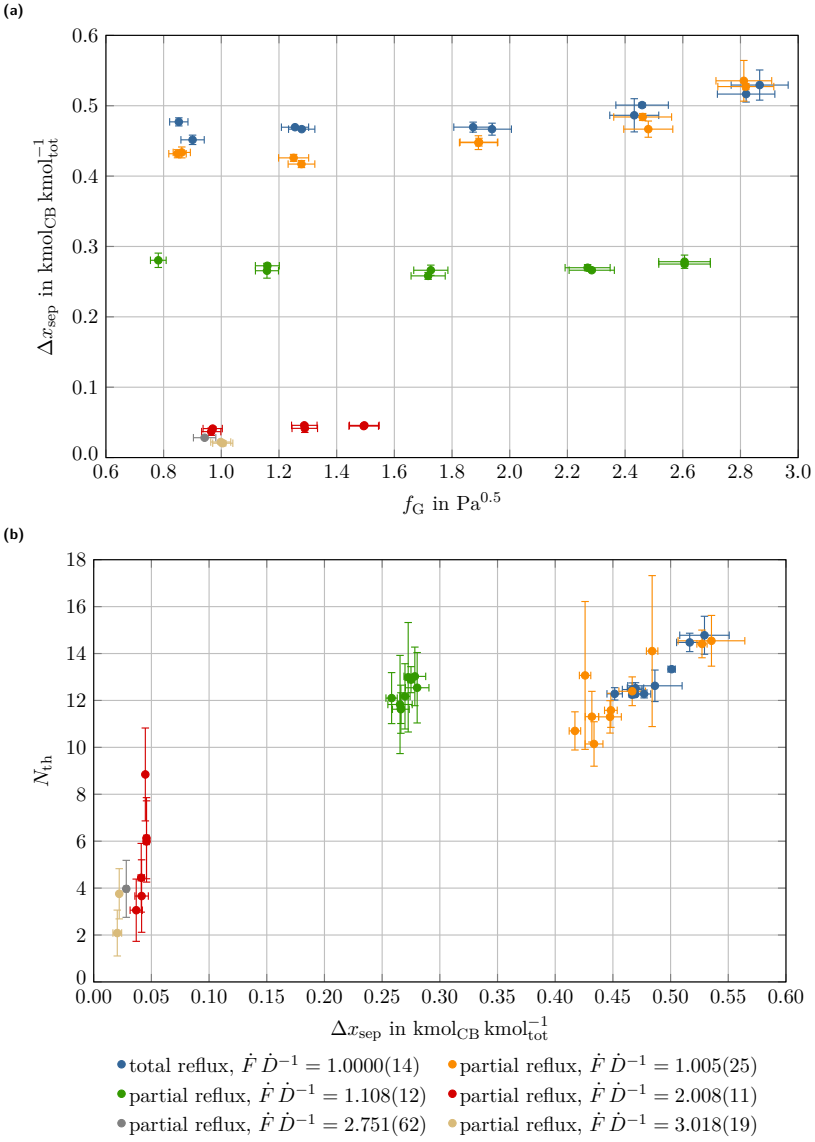

Figure 4.14.: Concentration spread Δx_{sep} in dependence of f-factor f_{G} and molar stream ratio $\dot{F}\,\dot{D}^{-1}$ (a), and number of theoretical stages N_{th} in dependence of concentration spread Δx_{sep} and molar stream ratio $\dot{F}\,\dot{D}^{-1}$ (b), indicated uncertainties are combined standard uncertainties $u_{\mathrm{c}}(\cdot)$

For each cluster, the concentration spreads Δx_{sep} and the number of theoretical stages N_{th} are aggregated as arithmetic averages as summarized in table 4.2. In addition, arithmetic averages for the driving concentration potentials Δx_{drv} illustrated in figure F.10 are calculated. Since $\Delta x_{\mathrm{drv}} = \Delta x_{\mathrm{sep}} N_{\mathrm{th}}^{-1}$, see equation (3.22a), obtained trends are similar to those of Δx_{sep} already illustrated in figure 4.14b, but inversely proportional to N_{th}.

Table 4.2.: Arithmetic averages of concentration spread Δx_{sep}, number of theoretical stages N_{th} and driving concentration potential per stage Δx_{sep}, indicated uncertainties are combined standard uncertainties $u_{\mathrm{c}}(\cdot)$

cluster with	$\overline{\Delta x_{\mathrm{sep}}}$	$\overline{N_{\mathrm{th}}}$	$\overline{\Delta x_{\mathrm{drv}}}$
	$\mathrm{kmol_{CB}\,kmol_{tot}^{-1}}$	-	$\mathrm{kmol_{CB}\,kmol_{tot}^{-1}}$
$\dot{F}\,\dot{D}^{-1} = 1.0$	0.4726(26)	12.64(26)	0.037 39(80)
$\dot{F}\,\dot{D}^{-1} = 1.1$	0.2699(23)	12.32(48)	0.021 92(87)
$\dot{F}\,\dot{D}^{-1} \geq 2.0$	0.0356(11)	4.66(49)	0.007 65(84)

The discussed results show a substantial dependence of the number of theoretical stages N_{th} on f-factor f_{G} and molar stream ratio $\dot{F}\,\dot{D}^{-1}$. A consistent comparison of N_{th}, and thus separation performance, is easily possible if one of the mentioned operating parameters is kept constant ($f_{\mathrm{G}} = \text{const.}$ with $\dot{F}\,\dot{D}^{-1} \neq \text{const.}$ or $f_{\mathrm{G}} \neq \text{const.}$ with $\dot{F}\,\dot{D}^{-1} = \text{const.}$). Assuming that conventional separation performance experiments with $\dot{F}\,\dot{D}^{-1} = 1$ can be interpreted as $\dot{F}\,\dot{D}^{-1} = \text{const.}$ allows applying already established data evaluation and interpretation routines if generalized accordingly.

However, considering variations in both f-factor f_{G} and molar stream ratio $\dot{F}\,\dot{D}^{-1}$ requires a suitable adjustment, normalization or conversion of the results. This is especially relevant, if the obtained number of theoretical stages N_{th}, or the separation efficiency in general, should be compared with separation performance determined from conventional separation performance experiments. Although experiments conducted in this work cover parameter studies for both f_{G} and $\dot{F}\,\dot{D}^{-1}$, obtained experimental results do not allow deriving a suitable correlation to correct for effects caused by these parameters due to a lack of data in relevant regions of result space[8] as illustrated in figure 4.15.

[8]The set of outcomes or results is commonly called *sample space*. However, the term *result space* is used here to explicitly distinguish the set of results from the set of input samples.

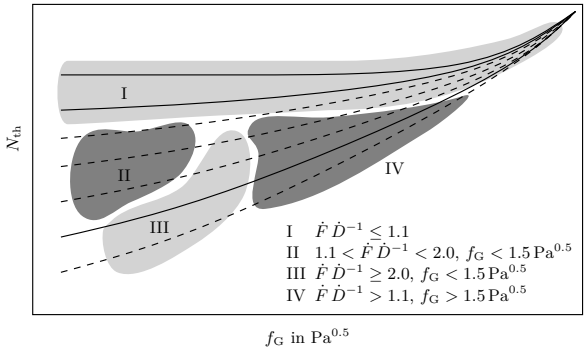

Figure 4.15.: Illustration of missing data in result space of number of theoretical stages N_{th}; lightgray: regions investigated in this work, highlighted hulls contain results abstracted from figure 4.12; darkgray: no results available in this work, regions not investigated; solid lines: curves proposed based on experimental results; dashed lines: assumed curves indicating set of functions

Compared to the number of theoretical stages N_{th}, the HETP values presented in figure 4.16 show inverse trends due to the inverse proportionality given by $\mathrm{HETP} = H_{\mathrm{bed}}\, N_{\mathrm{th}}^{-1}$. Therefore, the affecting factors discussed for the number of theoretical stages N_{th} apply accordingly.

Corresponding to the small number of theoretical stages N_{th}, high HETP values are obtained for $\dot{F}\,\dot{D}^{-1} \geq 2.0$. A detailed evaluation of the HETP values determined for $\dot{F}\,\dot{D}^{-1} \leq 1.1$ indicates similar trends between corresponding datasets, see figure 4.16. Due to the combined standard uncertainty associated with each value, determined values can be considered constant for f-factors of $f_{\mathrm{G}} \leq 2.3\,\mathrm{Pa}^{0.5}$, and a decrease in HETP is observed for higher f-factors which is common for miniplant-scale columns and primarily caused by wall effects. Using a very similar plant setup, (Bradtmöller, 2017) obtained a comparable decrease in HETP for f-factors of $f_{\mathrm{G}} \geq 2.5\,\mathrm{Pa}^{0.5}$ and attributed this observation to an increased stagnation of liquid between packing elements and column wall when reaching the loading point at $f_{\mathrm{G}} \approx 2\,\mathrm{Pa}^{0.5}$ and transitioning to the flood point at $f_{\mathrm{G}} \approx 3.2\,\mathrm{Pa}^{0.5}$.

The separation performance achieved under total reflux operating conditions is consistently higher than the results by (Bennett and Pilling, 2003; Bradtmöller, 2017). In particular, the HETP values by (Bradtmöller, 2017) are around 10 % higher than the values of this work. Although the plant setup of this work is very similar that used by (Bradtmöller, 2017), the used procedures differ in liquid sampling and the evaluation of operating conditions, which may explain the observed systematic offset.

As indicated by the error bars given in figure 4.16a, HETP values calculated for experiments with $\dot{F}\,\dot{D}^{-1} \geq 2.0$ are associated with considerably large uncertainties of $u_{\mathrm{c}} = 0.06 \ldots 0.55\,\mathrm{m}$ which primarily originate[9] from the combined standard uncertainty associated with the number of theoretical stages $u_{\mathrm{c}}(N_{\mathrm{th}})$.

[9]The effect of the combined standard uncertainty $u_{\mathrm{c}}(H_{\mathrm{bed}})$ is neglected as all experiments were conducted with the same bed height resulting in $u_{\mathrm{c}}(H_{\mathrm{bed}}) = \mathrm{const}$.

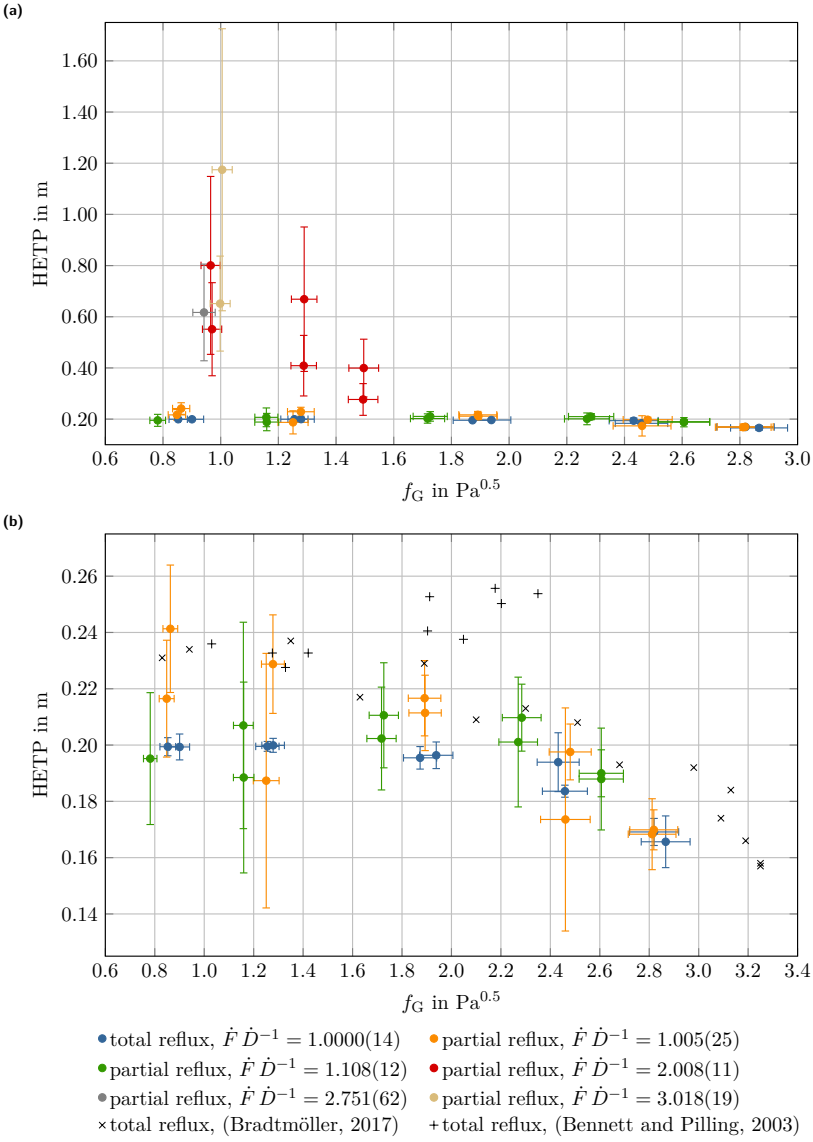

Figure 4.16.: HETP determined from McCabe-Thiele stage constructions in dependence of f-factor f_G and molar stream ratio $\dot{F}\,\dot{D}^{-1}$; (a): overview for all investigated molar stream ratios $\dot{F}\,\dot{D}^{-1}$; (b): zoomed view for $1.0 \leq \dot{F}\,\dot{D}^{-1} \leq 1.1$; literature data for $d_{col} = 50\,mm$ (Bradtmöller, 2017) and $d_{col} = 1\,m$ (Bennett and Pilling, 2003); indicated uncertainties are combined standard uncertainties $u_c(\cdot)$

The combined standard uncertainties $u_c(N_{th})$ illustrated in figure 4.17 do not indicate any obvious correlation with f-factor f_G or molar stream ratio $\dot{F}\,\dot{D}^{-1}$. However, to calculate the combined standard uncertainty $u_c(\mathrm{HETP})$, not only the uncertainties associated with the number of theoretical stages and the bed height, $u_c(N_{th})$ and $u_c(H_{bed})$, but also the corresponding sensitivity coefficients c_i, see equations (D.8) and (D.10), are required. While a higher number of theoretical stages results in a small sensitivity coefficient, the inverse applies for a small number of theoretical stages. Therefore, small combined standard uncertainties $u_c(\mathrm{HETP})$ are obtained for small HETP values.

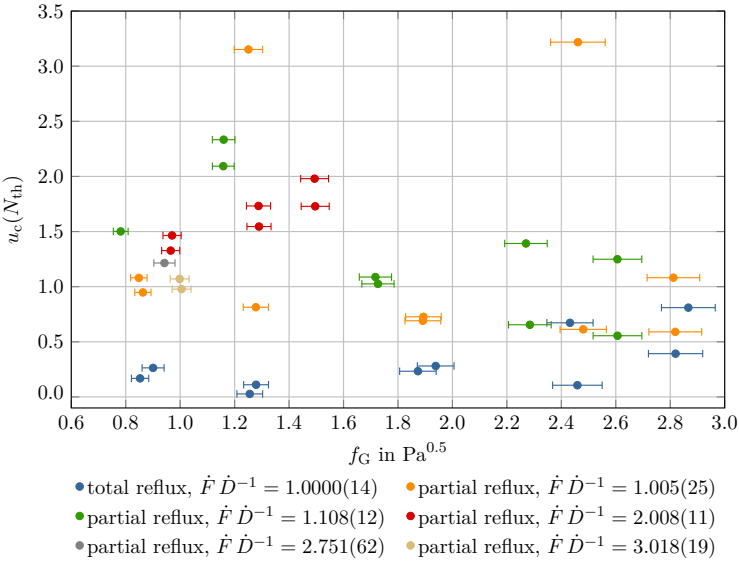

Figure 4.17.: Combined standard uncertainty associated with number of theoretical stages N_{th} in dependence of f-factor f_G and molar stream ratio $\dot{F}\,\dot{D}^{-1}$, indicated uncertainties are combined standard uncertainties $u_c(\cdot)$

4.2.2. Delft Mass Transfer Model

In addition to the HETP values calculated using the number of theoretical stages obtained from McCabe-Thiele stage constructions, HETP values are also estimated based on the Delft mass transfer model according to section 3.5.4.2. As the separation effective surface area $a_{eff,corr}$ and mass transfer coefficients, k_L and k_G, provide fundamental information about vapor-liquid interaction, their corresponding values are discussed first.

Since the corrected separation effective surface area $a_{eff,corr}$ is affected by the fluiddynamics inside the packed bed, corresponding values depend on the operating conditions. The effects of f-factor f_G and molar stream ratio $\dot{F}\,\dot{D}^{-1}$ on $a_{eff,corr}$ are illustrated in figure 4.18.

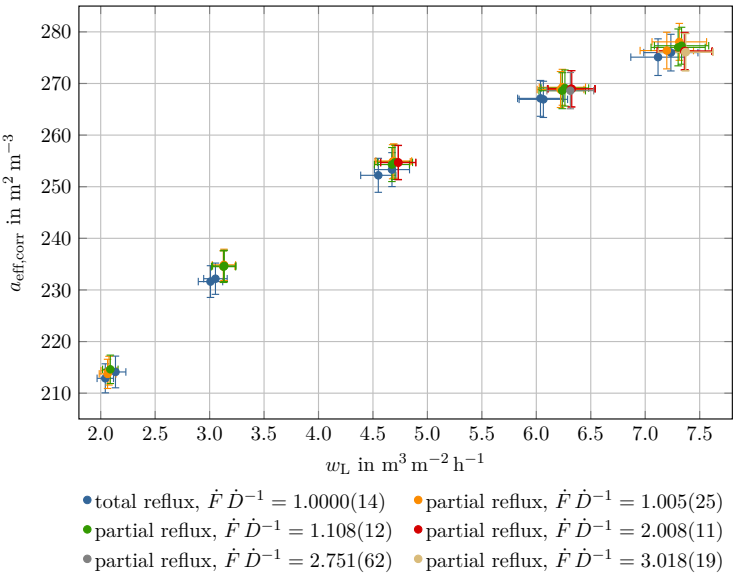

Figure 4.18.: Separation effective surface area $a_{\mathrm{eff,corr}}$ determined with Delft model in dependence of liquid load w_{L} and molar stream ratio $\dot{F}\,\dot{D}^{-1}$, indicated uncertainties are combined standard uncertainties $u_{\mathrm{c}}(\cdot)$

Obtained results indicate the expected increase of the corrected separation effective surface area $a_{\mathrm{eff,corr}}$ with liquid load w_{L} and are within the range $a_{\mathrm{eff,corr}} \approx 213(3) \ldots 278(4)\,\mathrm{m^2\,m^{-3}}$. This equals $41 \ldots 55\,\%$ of the calculated specific area of the installed packing elements ($a_{\mathrm{p}} = 508(5)\,\mathrm{m^2\,m^{-3}}$, see equation (2.71) and table A.1) indicating that only a fraction of the installed surface area is used for mixture separation. Nonetheless, the estimated separation effective areas are in good agreement with $a_{\mathrm{eff,corr}} \approx 200 \ldots 280\,\mathrm{m^2\,m^{-3}}$ as reported by (Bradtmöller, 2017) for a similar plant setup and operating conditions. Furthermore, clusters of data points with small variations for each liquid load w_{L} can be identified. Investigating equation (2.87) shows that $a_{\mathrm{eff,corr}}$ only depends on packing geometry and the separation effective surface area $a_{\mathrm{eff,Onda}}$ estimated with the Onda correlation. As the molar stream ratio $\dot{F}\,\dot{D}^{-1}$ and liquid load w_{L} fully define plant operation with respect to the material balance, and since $a_{\mathrm{eff,Onda}}$ is calculated based on the superficial liquid and gas velocities, $u_{\mathrm{L,s}}$ and $u_{\mathrm{G,s}}$, as well as physical properties of liquid and gas phase, see equation (2.85a), variations within each cluster are caused by variations in the mixture composition resulting from the achieved mixture separation.

Liquid and vapor phase mass transfer coefficients, k_{L} and k_{G}, illustrated in figure 4.19 are calculated with the original and revised correlations of the Delft model according to table 3.8.

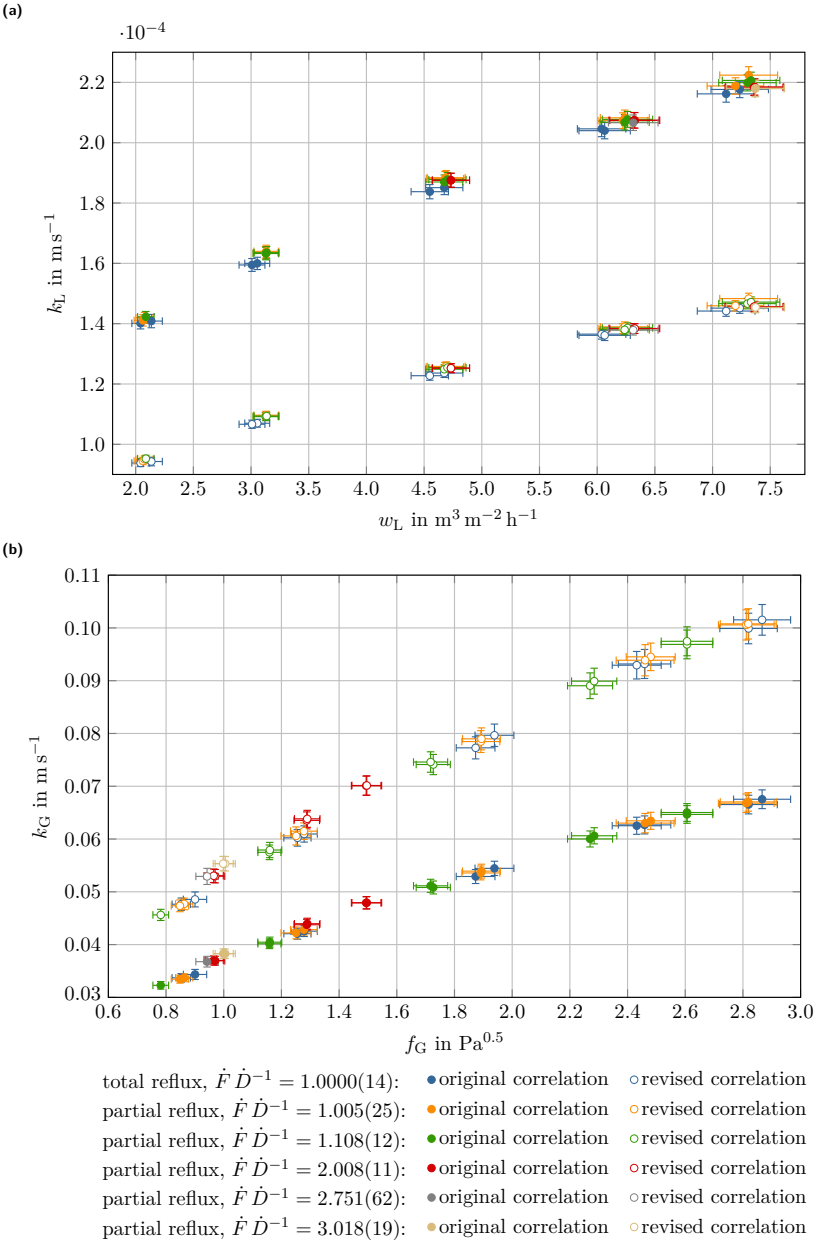

Figure 4.19.: Liquid phase mass transfer coefficient k_L in dependence of liquid load w_L and molar stream ratio $\dot{F}\,\dot{D}^{-1}$ (a), and vapor phase mass transfer coefficient k_G in dependence of f-factor f_G and molar stream ratio $\dot{F}\,\dot{D}^{-1}$ (b), values determined with original and revised correlations of Delft model, indicated uncertainties are combined standard uncertainties $u_c(\cdot)$

Disregarding the specific correlations, both liquid and vapor phase mass transfer coefficients increase with the column load due to higher superficial velocities which promote the vapor-liquid interaction at the phase interface and thus, improve mass transfer. Estimated liquid mass transfer coefficients are within the ranges of $k_{\mathrm{L,original}} = (1.401(19) \ldots 2.224(28)) \cdot 10^{-4}\,\mathrm{m\,s^{-1}}$ and $k_{\mathrm{L,revised}} = (0.938(12) \ldots 1.483(18)) \cdot 10^{-4}\,\mathrm{m\,s^{-1}}$. Noting the non-linear relation between liquid phase mass transfer coefficients k_{L} and the liquid load w_{L}, the increase of $k_{\mathrm{L,original}}$ and $k_{\mathrm{L,revised}}$ over w_{L} is equivalent to around 58 % each. However, using the revised correlation results in reduced liquid mass transfer coefficients of around 67 % of the values predicted with the original correlation due to the increased liquid flow path length considered in the revised correlation, see equations (2.88a) and (2.88b). $k_{\mathrm{L,original}}$ and $k_{\mathrm{L,revised}}$ estimated in this work are close to the range of $k_{\mathrm{L,revised}} \approx (0.9 \ldots 1.3) \cdot 10^{-4}\,\mathrm{m\,s^{-1}}$ reported by (Bradtmöller, 2017) for a similar plant setup and operating conditions and the ranges of $k_{\mathrm{L,original}} \approx (1.2 \ldots 2.2) \cdot 10^{-4}\,\mathrm{m\,s^{-1}}$ and $k_{\mathrm{L,revised}} \approx (0.8 \ldots 1.2) \cdot 10^{-4}\,\mathrm{m\,s^{-1}}$ reported by (Olujić and Seibert, 2014) using a different type of packing and column diameter, but same test mixture and operating pressure[10].

While the revised Delft model predicts lower liquid mass transfer coefficients, an increase in vapor phase mass transfer coefficients is observed as illustrated in figure 4.19b. Estimated gas phase mass transfer coefficients are within $k_{\mathrm{G,original}} = 0.032\,28(72) \ldots 0.0675(18)\,\mathrm{m\,s^{-1}}$ and $k_{\mathrm{G,revised}} = 0.0456(11) \ldots 0.1015(29)\,\mathrm{m\,s^{-1}}$. The effect of f-factor f_{G} on $k_{\mathrm{G,original}}$ and $k_{\mathrm{G,revised}}$ corresponds to an 2.09 times and 2.22 times increase, respectively. Using $\varphi_{\mathrm{c,L}} = 1$ in the revised calculation approach results in a higher contribution of the turbulent gas mass transfer coefficient $k_{\mathrm{G,turb}}$ and thus, increases the resulting vapor phase mass transfer coefficient $k_{\mathrm{G,revised}}$ by 41 . . . 50 %. In contrast to $k_{\mathrm{G,original}}$, the non-linearity between k_{G} and f_{G} is less pronounced for $k_{\mathrm{G,revised}}$. Although not strictly resulting from the underlying correlations, an approximately linear relation between k_{G} and f_{G} is often reported in the literature, see e.g. (Bradtmöller, 2017; Olujić et al., 2012; Olujić and Seibert, 2014). Despite this discrepancy with the literature, which is particularly pronounced for $k_{\mathrm{G,original}}$, predicted vapor phase mass transfer coefficients are comparable to $k_{\mathrm{G,original}} \approx 0.020 \ldots 0.064\,\mathrm{m\,s^{-1}}$ and $k_{\mathrm{G,revised}} \approx 0.035 \ldots 0.120\,\mathrm{m\,s^{-1}}$ reported by (Olujić et al., 2012)[11] as well as $k_{\mathrm{G,original}} \approx 0.030 \ldots 0.068\,\mathrm{m\,s^{-1}}$ reported by (Bradtmöller, 2017).

Using the presented liquid and vapor phase mass transfer coefficients, $k_{\mathrm{L,original}}$ and $k_{\mathrm{L,revised}}$ as well as $k_{\mathrm{G,original}}$ and $k_{\mathrm{G,revised}}$, $\mathrm{HTU_L}$ and $\mathrm{HTU_G}$ are calculated according to equations (2.92a) and (2.92b). Since estimated values $\mathrm{HTU_L}$ and $\mathrm{HTU_G}$, and thus also HETP, depend on whether the corresponding mass transfer coefficients are calculated with the original or the revised correlations of the Delft model, the index notation given in table 4.3 is introduced to distinguish respective results.

[10] (Olujić and Seibert, 2014) investigated the separation performance of packing *Montz-Pak B1–500* (Julius Montz, Hilden/Germany) with a nominal specific surface area of $a_{\mathrm{p}} = 500\,\mathrm{m^2\,m^{-3}}$ at $p = 0.1\,\mathrm{bar(a)}$, a column diameter of $d_{\mathrm{col}} = 0.59\,\mathrm{m}$ and a bed height of $H_{\mathrm{bed}} = 3.43\,\mathrm{m}$.

[11] (Olujić et al., 2012) investigated the separation performance of high performance packing *Montz-Pak B1–500MN* (Julius Montz, Hilden/Germany) with a nominal specific surface area of $a_{\mathrm{p}} = 500\,\mathrm{m^2\,m^{-3}}$ at $p = 0.1\,\mathrm{bar(a)}$, a column diameter of $d_{\mathrm{col}} = 0.588\,\mathrm{m}$ and a bed height of $H_{\mathrm{bed}} = 3.49\,\mathrm{m}$.

Table 4.3.: Index notation for separation performance predicted with Delft model, see table 3.8 for correlations used to calculate mass transfer coefficients k_L and k_G

index	k_L	k_G
1	$k_{L,original}$	$k_{G,original}$
2	$k_{L,original}$	$k_{G,revised}$
3	$k_{L,revised}$	$k_{G,original}$
4	$k_{L,revised}$	$k_{G,revised}$

HETP values calculated from HTU_{oG} and stripping factor λ are illustrated in figure 4.20. Since HTU_{oG} and HETP are proportional to each other with $\ln\lambda\,(\lambda-1)^{-1}$ as the corresponding factor of proportionality, see equation (2.65), HTU_{oG} are not explicitly discussed here; respective values can be found in figure F.18.

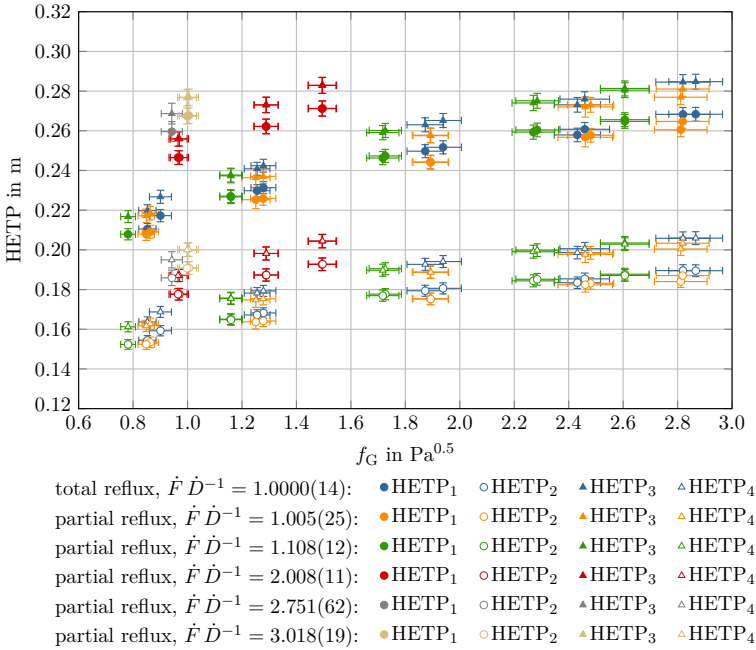

Figure 4.20.: HETP predicted with Delft model in dependence of f-factor f_G and molar stream ratio $\dot{F}\,\dot{D}^{-1}$, see table 4.3 for index notation of HETP, indicated uncertainties are combined standard uncertainties $u_c(\cdot)$

Although uncertainties are transparently propagated with the *uncertainties* package according

to appendix D.2.1, initially calculated combined standard uncertainties associated with the HETP values of $\dot{F}\,\dot{D}^{-1} = 1.0$ seem unreasonably large, see figure F.19. The respective uncertainties are particularly surprising, since total reflux operation is commonly used to reduce potential uncertainty contributions, see section 2.3.3. Detailed inspection of calculated uncertainties indicated that the largest uncertainty contributions originate from stripping factor λ, bottoms composition x_B and distillate composition x_D. However, as shown in figures F.6 and F.15, uncertainties associated with these parameters are reasonable and should not cause such large combined standard uncertainties. Although not exhaustively evaluated, it is assumed that the unreasonable uncertainty contributions result from correlations between input parameters and high sensitivity coefficients. However, correlated parameters commonly result in second- or higher-order uncertainty components which are commonly much smaller than the first order contributions of uncorrelated inputs. Therefore, combined standard uncertainties u_c(HETP) indicated in figure 4.20 were recalculated without considering potential correlations in input parameters as part of the data post-processing routine.

Independent of the used mass transfer correlations, an increase of $\mathrm{HTU_{oG}}$, and thus HETP, is observed for an increasing f-factor f_G. As increasing f-factors f_G cause higher superficial gas and liquid velocities, $u_\mathrm{G,s}$ and $u_\mathrm{L,s}$, the height of the corresponding transfer units, $\mathrm{HTU_G}$ and $\mathrm{HTU_L}$, also increase according to equations (2.92a) and (2.92b). This finally results in larger $\mathrm{HTU_{oG}}$ as per equation (2.57a). Using the original correlation to calculate the liquid phase mass transfer coefficient and the revised correlation for the gas phase mass transfer coefficient ($\mathrm{HETP_2}$: $k_\mathrm{L,original}$ and $k_\mathrm{G,revised}$) consistently predicts the smallest HETP and thus, the highest separation performance. In contrast, the lowest separation performance is predicted with $k_\mathrm{L,revised}$ and $k_\mathrm{G,original}$ in terms of $\mathrm{HETP_3}$. While the predicted values are similar within each series of HETP for molar stream ratios of $\dot{F}\,\dot{D}^{-1} \leq 1.1$, slightly increased HETP values are predicted for $\dot{F}\,\dot{D}^{-1} \geq 2.0$. In particular, $\mathrm{HETP_2} = 0.1523(24) \ldots 0.1896(30)\,\mathrm{m}$ and $\mathrm{HETP_3} = 0.2168(30) \ldots 0.2848(38)\,\mathrm{m}$ are obtained for $\dot{F}\,\dot{D}^{-1} \leq 1.1$, whereas $\mathrm{HETP_2} = 0.1777(29) \ldots 0.1928(32)\,\mathrm{m}$ and $\mathrm{HETP_3} = 0.2559(37) \ldots 0.2830(40)\,\mathrm{m}$ are predicted for $\dot{F}\,\dot{D}^{-1} \geq 2.0$.

The observed effects of $k_\mathrm{L,original}$ and $k_\mathrm{L,revised}$ as well as $k_\mathrm{G,original}$ and $k_\mathrm{G,revised}$ on HETP are in accordance with (Olujić et al., 2012; Olujić and Seibert, 2014). As elaborated, an increased flow path length is considered for $k_\mathrm{L,revised}$ which, in comparison to $k_\mathrm{L,original}$, results in a reduced liquid mass transfer coefficient and thus, causes a higher $\mathrm{HTU_L}$. In contrast to $\mathrm{HTU_L}$, smaller $\mathrm{HTU_G}$ are obtained with the revised calculation approach. Since $\varphi_\mathrm{c,L} = 1$ is used instead of $\varphi_\mathrm{c,L} \approx 0.59$, the gas phase mass transfer coefficient $k_\mathrm{G,revised}$ is larger than $k_\mathrm{G,original}$, which in turn lowers $\mathrm{HTU_G}$. Therefore, $\mathrm{HETP_2} < \mathrm{HETP_3}$ is obtained according to equation (2.65). Underlying $\mathrm{HTU_L}$ and $\mathrm{HTU_G}$ are illustrated in figures F.16 and F.17.

For increasing molar stream ratios $\dot{F}\,\dot{D}^{-1}$, a gradually increasing HETP, representing a decrease in separation performance, is observed. As shown in table 4.4, the cause of the reduced separation performance, which is especially observed for $\dot{F}\,\dot{D}^{-1} \geq 2.0$, can be derived by relating

the discussed observations to the corresponding terms of equation (2.65).

Table 4.4.: Chain of causations for the effect of molar stream ratio $\dot{F}\,\dot{D}^{-1}$ on HETP

$\dot{F}\,\dot{D}^{-1}$	λ	$\ln\lambda\,(\lambda-1)^{-1}$	$\mathrm{HTU_G}$	$\mathrm{HTU_L}$	$\mathrm{HTU_{oG}}$	HETP
↑	↓	↑	↓	↑	↓	↑

4.2.3. Comparison of Theoretical Stages and Transfer Units

Since HETP values are determined based on both equilibrium- and rate-based approaches, the respective results allow a direct comparison of both approaches. Further elaborations cover the number of transfer units $\mathrm{NTU_{oG}}$ to determine the height of the packed bed H_{bed} using the height of a transfer unit $\mathrm{HTU_{oG}}$ predicted with the Delft model. In addition, the comparability of HETP and $\mathrm{HTU_{oG}}$ is addressed.

To distinguish HETP values calculated from the number of theoretical stages from those predicted with the Delft model, the symbols $\mathrm{HETP_{stages}}$ and $\mathrm{HETP_{Delft}}$ are introduced. Furthermore, depending on whether the original or revised correlations are used to estimate liquid and gas phase mass transfer coefficients, $\mathrm{HETP_{Delft}}$ is annotated with index 1, 2, 3 or 4 according to table 4.3. A comparison of experimental and predicted HETP values is given in figure 4.21.

Disregarding the specific mass transfer correlations, the rate-based model overestimates separation performance for molar stream ratios of $\dot{F}\,\dot{D}^{-1} \geq 2.0$ considerably, as experimental HETP values are up to 6.2 times the predicted values. While $\mathrm{HETP_{Delft,1}}$ shows the smallest deviation between predicted and experimental HETP values for $\dot{F}\,\dot{D}^{-1} \geq 2.0$ with a factor of up to 4.2, the HETP values are considerably overestimated for $\dot{F}\,\dot{D}^{-1} \leq 1.1$. Considering $\dot{F}\,\dot{D}^{-1} \leq 1.1$, the smallest deviation between $\mathrm{HETP_{Delft}}$ and $\mathrm{HETP_{stages}}$ is obtained with $\mathrm{HETP_{Delft,4}}$. Corresponding predictions are mostly within a margin of $\pm\,25\,\%$. This observation is in good agreement with the $\pm\,20\ldots30\,\%$ margin reported by (Schultes, 2013) who evaluated the prediction quality of several mass transfer models with respect to industrial applications. In addition, (Schultes, 2013) reported that experimental and predicted separation performance differ by a margin of $\pm\,80\ldots90\,\%$ for some edge cases. Although not explicitly stated in the literature, it is assumed that these margins refer to conventional separation performance experiments with total reflux.

Nonetheless, the differences between predicted and experimental separation performances observed for $\dot{F}\,\dot{D}^{-1} \geq 2.0$ even exceed the extended margin of $\pm\,80\ldots90\,\%$ by a factor of approximately 3.4 and are not sufficiently covered by the effects already illustrated in table 4.4. This may indicate a systematic error in data evaluation or a limited applicability of the Delft mass transfer model for the partial reflux experiments conducted in this work. Since both partial and total reflux experiments are evaluated with identical calculation routines and reasonable results are obtained for $\dot{F}\,\dot{D}^{-1} \leq 1.1$, a systematic error is unlikely. However, a limited applicability of the Delft model for partial reflux experiments may result from the data

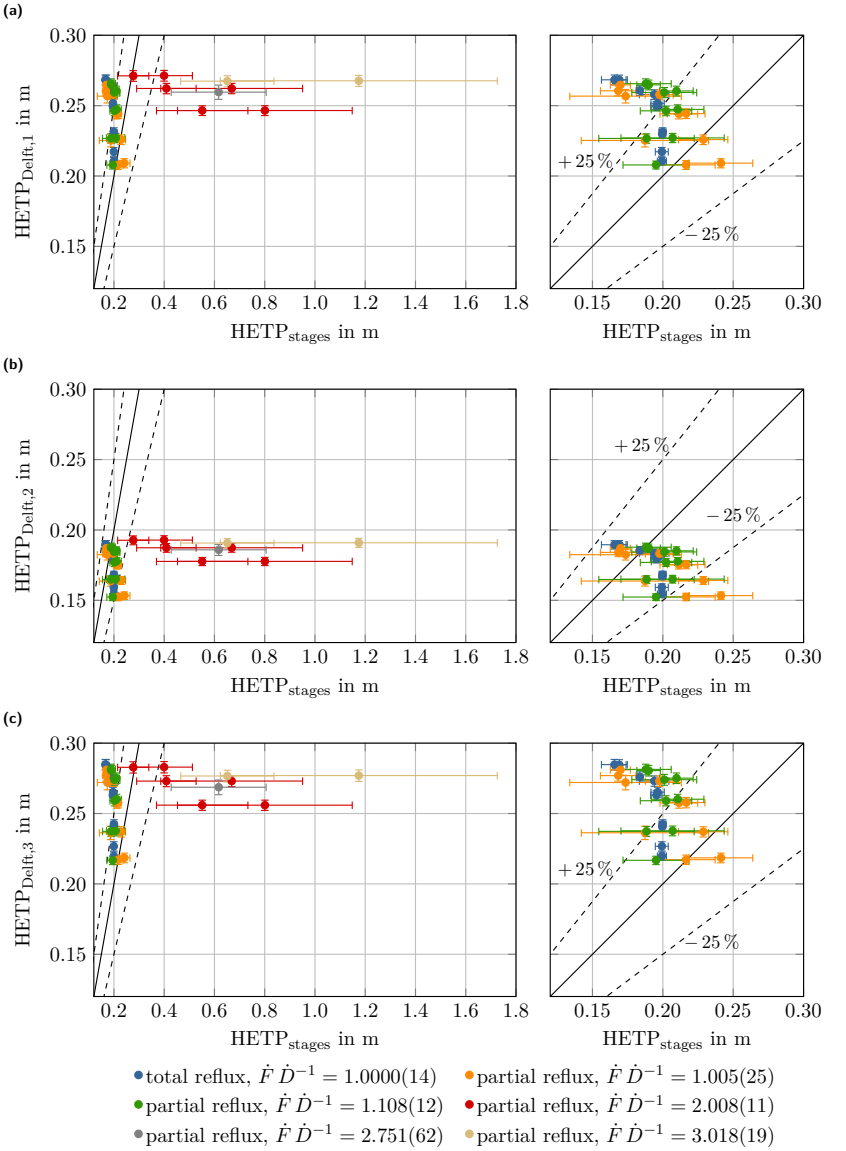

Figure 4.21.: Parity plot of experimental ($\mathrm{HETP_{stages}}$) and predicted ($\mathrm{HETP_{Delft}}$) separation performance, left: overview for all investigated molar stream ratios $\dot{F}\,\dot{D}^{-1}$, right: zoomed view for $1.0 \leq \dot{F}\,\dot{D}^{-1} \leq 1.1$, see table 4.3 for index notation of $\mathrm{HETP_{Delft}}$, indicated uncertainties are combined standard uncertainties $u_\mathrm{c}(\cdot)$

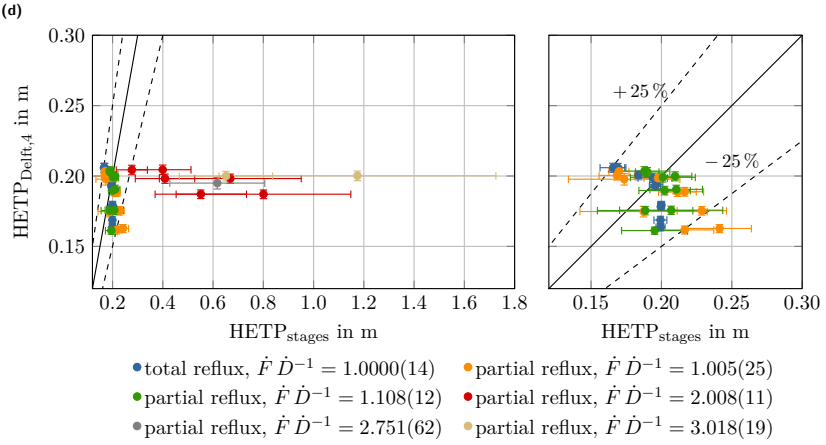

Figure 4.21.: Parity plot of experimental ($\mathrm{HETP}_{\mathrm{stages}}$) and predicted ($\mathrm{HETP}_{\mathrm{Delft}}$) separation performance, left: overview for all investigated molar stream ratios $\dot{F}\,\dot{D}^{-1}$, right: zoomed view for $1.0 \leq \dot{F}\,\dot{D}^{-1} \leq 1.1$, see table 4.3 for index notation of $\mathrm{HETP}_{\mathrm{Delft}}$, indicated uncertainties are combined standard uncertainties $u_{\mathrm{c}}(\cdot)$ (continued)

sets used for model development, since the model was originally validated against separation performance experiments conducted with *Montz*-type packings at total reflux (Olujić et al., 1999). Although later model improvements presented by (Olujić et al., 2004; Olujić et al., 2007; Olujić et al., 2012; Olujić and Seibert, 2014) comprise substantial adaptations to increase the prediction accuracy and applicability for other packing types, partial reflux operation has not been addressed. Nevertheless, this should not be considered as a drawback specific to the Delft model. Since separation performance is commonly quantified based on total reflux experiments, available data are strongly biased towards total reflux operation. Therefore, this operating mode is not commonly considered in model development or validation and thus, corresponding separation performance at partial reflux is presumably overestimated by most of the well-established mass transfer models.

Furthermore, the observed discrepancy may also be related to the characteristic operational behavior of total and partial reflux experiments. As discussed, the molar stream ratio affects the column-internal streams and thus, the superficial liquid and gas velocities, $u_{\mathrm{L,s}}$ and $u_{\mathrm{G,s}}$. In the Delft model, see section 2.2.3.5, such effects are considered with respect to the fluiddynamics and mass transfer coefficients. However, total and partial reflux experiments characteristically differ from each other with respect to the column loads. While the liquid and gas flows are equivalent to each other in total reflux experiments ($\dot{F}\,\dot{D}^{-1} = 1$), partial reflux operating conditions ($\dot{F}\,\dot{D}^{-1} \neq 1$) allow a variety of values for the stream ratio. Due to this additional degree of freedom, the superficial liquid and gas velocities, $u_{\mathrm{L,s}}$ and $u_{\mathrm{G,s}}$, can vary over a wide range, which may not be represented in the data used for model development and validation.

Although rarely discussed in the literature, this interpretation of the obtained results is in line with (Wang et al., 2005a) claiming that conventional separation performance experiments at total reflux conditions do not allow assessing the effects of gas and liquid loads on separation performance independently of each other.

The last part of the result discussion focuses on predicting the height of the packed bed H_{bed} required to achieve the observed mixture separations. For this, the height of a transfer unit $\mathrm{HTU_{oG}}$ and the number of transfer units $\mathrm{NTU_{oG}}$ are required according to equation (2.68). As highlighted, none of the used sets of mass transfer correlations allows predicting $\mathrm{HTU_{oG}}$ within a reasonable margin over the full range of experiments. However, as discussed in the context of figure 4.21, using the revised correlations for liquid and vapor mass transfer coefficients (index 4) results the most suitable prediction of separation performance for $\dot{F}\,\dot{D}^{-1} \leq 1.1$. Therefore, the corresponding height of a transfer unit $\mathrm{HTU_{oG,4}}$ is used for further discussions. The number of transfer units $\mathrm{NTU_{oG}}$ is calculated using the definite integral given in equation (2.54a) or the number of theoretical stages N_{th} and the stripping factor λ according to equation (2.69). Obtained results are denoted by $\mathrm{NTU_{oG,integration}}$ and $\mathrm{NTU_{oG,stages}}$, respectively.

To ensure a consistent propagation of uncertainties, the integration for $\mathrm{NTU_{oG,integration}}$ was performed as part of the MCM used to estimate the number of theoretical stages N_{th} with McCabe-Thiele stage constructions. As described in section 3.5.4.1 and appendix E.4, thermodynamically invalid combinations of input parameters were excluded from further processing. As this reduces the number of samples contained in the resulting distribution and affects its corresponding standard deviation, potential correlations between the combined standard uncertainty $u_{\mathrm{c}}(\mathrm{NTU_{oG,integration}})$, MCM success ratio S_{MC} and molar stream ratio $\dot{F}\,\dot{D}^{-1}$ are investigated based on figure 4.22. Illustrated data indicate a strong relation between the combined standard uncertainty $u_{\mathrm{c}}(\mathrm{NTU_{oG,integration}})$, success ratio S_{MC} and molar stream ratio $\dot{F}\,\dot{D}^{-1}$, inasmuch as $u_{\mathrm{c}}(\mathrm{NTU_{oG,integration}})$ increases for a decreasing number of successful Monte Carlo simulations and reasonable uncertainties are exclusively obtained for $\dot{F}\,\dot{D}^{-1} = 1.0$ with $S_{\mathrm{MC}} \approx 100\,\%$.

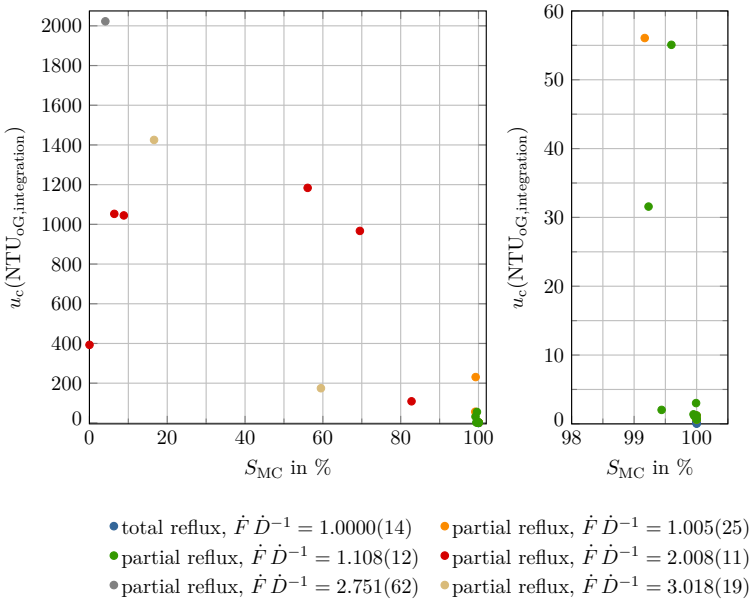

Figure 4.22.: Combined standard uncertainty associated with $\mathrm{NTU_{oG,integration}}$ in dependence of MCM success ratio S_{MC} and molar stream ratio $\dot{F}\,\dot{D}^{-1}$, left: overview for all investigated molar stream ratios $\dot{F}\,\dot{D}^{-1}$, right: zoomed view for $S_{\mathrm{MC}} \approx 100\,\%$

To achieve a clear indication about the applicability of equilibrium- and rate-based evaluation approaches, corresponding results should be strictly separated. In general, $\mathrm{NTU_{oG}}$ is defined by the concept of transfer units, which does not consider equilibrium stages. However, calculating $\mathrm{NTU_{oG,stages}}$ according to equation (2.69) depends on N_{th} and thus, is related to the McCabe-Thiele stage constructions. In contrast, using the integral for $\mathrm{NTU_{oG,integration}}$ defined in equation (2.54a) allows determining $\mathrm{NTU_{oG}}$ independently of equilibrium stages. Calculating $\mathrm{NTU_{oG,integration}}$ requires the bulk concentration of the vapor phase, which is commonly described by the equations of the operating lines and VLE data, see figure 2.7 and appendix E.1. Disregarding whether $\mathrm{NTU_{oG}}$ is calculated by integration ($\mathrm{NTU_{oG,integration}}$) or based on the number of theoretical stages ($\mathrm{NTU_{oG,stages}}$), obtained results should generally be similar to each other. As shown in figure 4.23, this is given for molar stream ratios of $\dot{F}\,\dot{D}^{-1} \leq 1.1$, such that obtained results are within a margin of $\pm\,5\,\%$. In contrast, $\mathrm{NTU_{oG,integration}}$ and $\mathrm{NTU_{oG,stages}}$ differ by a factor of up to 9.6 for $\dot{F}\,\dot{D}^{-1} \geq 2.0$.

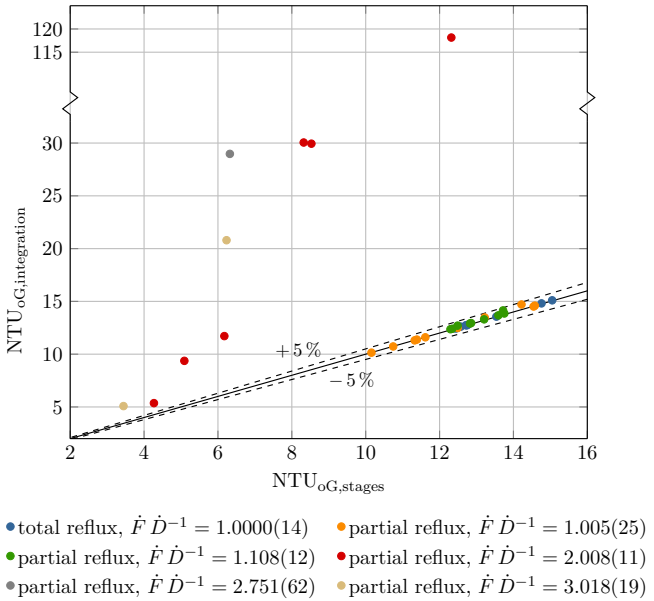

Figure 4.23.: Parity plot of $\mathrm{NTU_{oG,integration}}$ and $\mathrm{NTU_{oG,stages}}$, error bars indicating combined standard uncertainties $u_c(\cdot)$ are omitted to improve readability

To identify the reasons causing the substantial differences observed for $\dot{F}\,\dot{D}^{-1} \geq 2.0$, relevant equations, related assumptions and simplifications were reviewed from the original literature published by (Chilton and Colburn, 1935; Colburn, 1939; Colburn, 1941; Peters, 1922). Since no assumptions or restrictions regarding total or partial reflux conditions were found in the literature references, equations (2.54a) and (2.69) are considered to be valid for both operating modes. As discussed by (Chilton and Colburn, 1935), a substantial difference between $\mathrm{NTU_{oG,integration}}$ and N_{th}, and thus also $\mathrm{NTU_{oG,stages}}$, may occur for certain operating conditions for which $\mathrm{NTU_{oG,integration}}$ provides a more resilient or conservative column design. As shown in figure 4.23, $\mathrm{NTU_{oG,integration}} \gtrsim \mathrm{NTU_{oG,stages}}$ is obtained for all experiments conducted in this work. Although using $\mathrm{NTU_{oG,integration}}$ instead of $\mathrm{NTU_{oG,stages}}$ certainly results in a conservative column design, a design margin this large seems unreasonable.

The relation between transfer units and equilibrium stages is often discussed as a function of stripping factor λ. Since $\dot{F}\,\dot{D}^{-1} = 1$ applies for total reflux, the stripping factor λ is equal to the slope of the equilibrium curve m and variations in the stripping factor are solely attributed to the molar fraction x_1, see equation (2.67). However, partial reflux experiments allow investigating the effect of stripping factor λ at a constant molar fraction x_1 as the molar stream ratio $\dot{F}\,\dot{D}^{-1}$ can be varied. To ensure that the stripping factor λ is primarily affected by $\dot{F}\,\dot{D}^{-1}$, potential

variations of the slope of the operating line m need to be addressed based on the mean relative volatility $\overline{\alpha}_{12}$ and the mid-bed liquid molar fraction x_{mb}. As illustrated in figure F.9a, constant mid-bed liquid molar fractions x_{mb} can be assumed for all partial reflux experiments of this work. Potential effects caused by variations in relative volatility $\overline{\alpha}_{12}$ can also be considered negligible, since similar concentration spreads Δx_{sep} are observed for each molar stream ratio $\dot{F}\,\dot{D}^{-1}$, see figure 4.14, and the dependence of relative volatility α_{12} on liquid molar fraction x_1 is small for the test mixture used in the experiments, see figure C.6. Furthermore, to address the comparability of equilibrium- and rate-based approaches based on the effect of stripping factor λ, the general cases $\lambda \ll 1$, $\lambda \approx 1$ and $\lambda \gg 1$ were introduced in section 2.2.3.4. Although partial reflux experiments with $\dot{F}\,\dot{D}^{-1} \neq 1$, or $\dot{L}\,\dot{G}^{-1} \neq 1$ in general, would enable a systematic comparison of the aforementioned cases, only $\lambda \ll 1$ and $\lambda \approx 1$ are addressed in this work due to the characteristics inherent to the used plant setup.

As shown in figure 4.24a, the experiments were performed with stripping factors of $\lambda = 0.3282(21) \ldots 0.9997(67)$. Associated combined standard uncertainties are smaller than the marker size for most of the data points and explicitly illustrated in figure F.15. While potentially biased due to the smaller number of experiments, calculated values indicate less variation in λ for increasing molar stream ratios $\dot{F}\,\dot{D}^{-1}$. As a similar trend is observed for the f-factor f_{G} and liquid load w_{L}, see figure 4.2, this observation can be attributed to the control loops of the plant control system allowing a slightly more stable plant operation for $\dot{F}\,\dot{D}^{-1} \geq 1.1$. Although the stripping factor λ is commonly discussed for comparability of equilibrium- and rate-based approaches, the nonlinear term $\ln(\lambda)\,(\lambda - 1)^{-1}$ illustrated in figure 4.24b seems to be more relevant since it can be interpreted as a factor of proportionality between HETP and $\mathrm{HTU}_{\mathrm{oG}}$, see equation (2.65), as well as between $\mathrm{NTU}_{\mathrm{oG}}$ and N_{th}, see equation (2.69).

Putting the results discussed in this section into perspective indicates a good agreement between equilibrium- and rate-based approaches for total reflux operating conditions ($\dot{F}\,\dot{D}^{-1} = 1.0$). As elaborated in section 2.2.3.4, this behavior is not only commonly known in the literature, but can also be derived from equations (2.65) and (2.69) if symmetric mixture separations are investigated. Therefore, both approaches are often considered interchangeable and discussions about which approach should be preferred over the other arise. According to the experimental results obtained for $\dot{F}\,\dot{D}^{-1} = 1.1$, both approaches describe the achieved separation performance in good agreement with each other for a small deviation from total reflux conditions. However, obtained data indicate substantial deviations between the experimentally determined and predicted separation performance for higher molar stream ratios of $\dot{F}\,\dot{D}^{-1} \geq 2.0$. As discussed, these differences are most likely due to the model not covering partial reflux operating conditions. Furthermore, large deviations between $\mathrm{NTU}_{\mathrm{oG,integration}}$ and N_{th} are observed for partial reflux operation. Therefore, the applicability of $\mathrm{NTU}_{\mathrm{oG}}$ and N_{th} as well as suitable extensions for established mass transfer models with respect to partial reflux operation should be addressed in future activities.

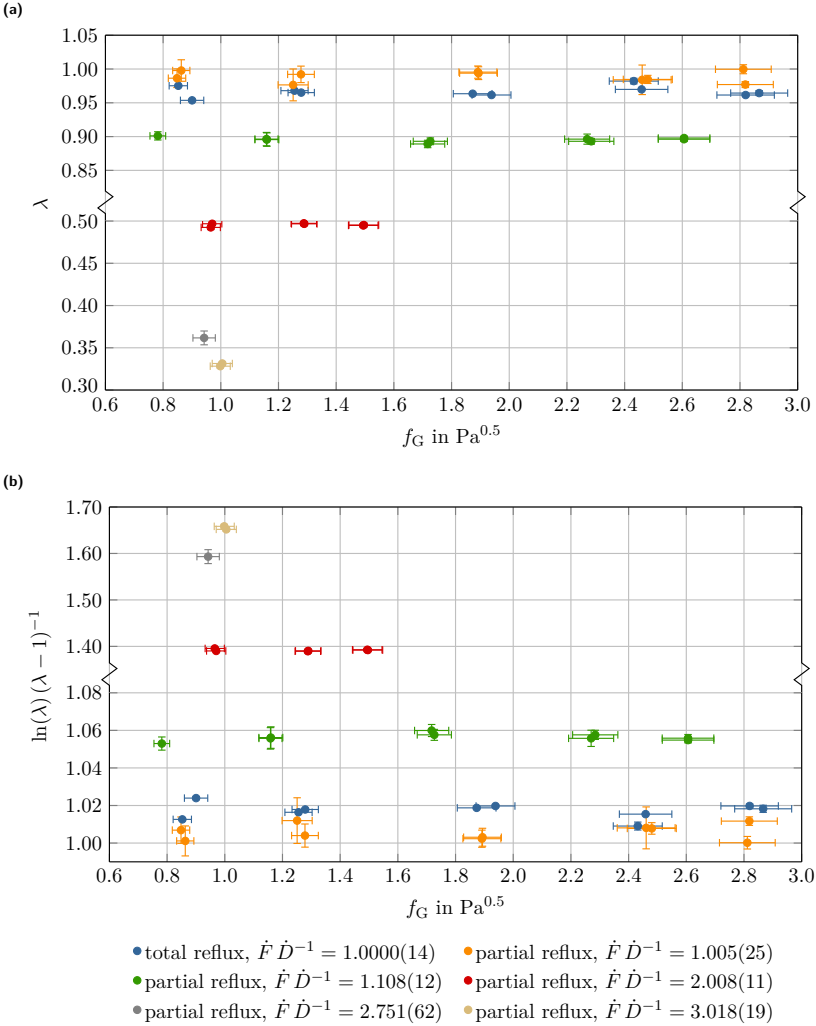

Figure 4.24.: Stripping factor λ (a) and ratio $\ln(\lambda)\,(\lambda-1)^{-1}$ (b) in dependence of f-factor f_G and molar stream ratio $\dot{F}\,\dot{D}^{-1}$, indicated uncertainties are combined standard uncertainties $u_c(\cdot)$

4.3. Method Evaluation and Future Improvements

In addition to the general applicability of the method developed and used in this work, the following method components described in chapter 3 are evaluated in this section:

1. plant concept
2. apparative realization of plant concept and experimental method
3. data processing

For this, not only the best practices for separation performance presented in section 2.3, the experimental results discussed in sections 4.1 and 4.2, and the identified plant characteristics, but also results from separation performance experiments at elevated viscosities by (Gutperl et al., 2022) are used.

4.3.1. General Applicability

Experimental results show substantially reduced HETP values for increasing molar stream ratios $\dot{F}\,\dot{D}^{-1}$. Therefore, disregarding the specific apparative realization of the plant concept proposed in section 3.3.1, separation performance should only be compared for a single constant molar stream ratio. This is especially relevant, if mixtures containing non-volatile components are used in separation performance experiments, since the material balance of the non-volatile component limits the range of suitable molar stream ratios $\dot{F}\,\dot{D}^{-1}$ as shown in section 3.3.3.1. Although choosing a high $\dot{F}\,\dot{D}^{-1}$ allows higher concentrations of the non-volatile component, the obtained results indicate substantially decreased success ratios S_{MC} for increasing $\dot{F}\,\dot{D}^{-1}$, see figure 4.8. As claimed in the research hypotheses and experienced during the experimental investigations, this results in a trade-off between stable plant operation, robust data evaluation and the maximum allowed concentration of the non-volatile mixture component. In particular, the range of $\dot{F}\,\dot{D}^{-1} = 1.0 \ldots 2.0$ seems suitable for separation performance experiments using the standardized test mixture CB/EB and symmetric mixture separations. Molar stream ratios of $\dot{F}\,\dot{D}^{-1} > 2.0$ result in a less robust plant operation and thus, limit data evaluation. If the proposed plant setup is used to assess the separation performance of viscous mixtures as shown by (Gutperl et al., 2022), it is, therefore, advised to conduct baseline experiments without non-volatile mixture components prior to the actual separation performance experiments at elevated viscosities to distinguish the reduction in separation performance related to $\dot{F}\,\dot{D}^{-1} > 1$ from the reduction caused by the increased mixture viscosity.

4.3.2. Plant Concept

While the proposed plant concept was successfully realized with the setup presented in section 3.3 and thus, successfully used to conduct separation performance experiments at both total and partial reflux conditions, its operational flexibility and the range of potential use cases can

be extended by implementing some adaptations. Although the bottom product and distillate recycles substantially reduce the required amount of feedstock mixture compared to the approach used by (Böcker and Ronge, 2005), they also link the corresponding mass flows, $\dot{m}_{\mathrm{B}}$ and $\dot{m}_{\mathrm{D}}$, to the feed mass flow $\dot{m}_{\mathrm{F}}$ due to the underlying mass and component balances. As discussed in section 3.3.3.1, this results in $\dot{m}_{\mathrm{F}}\,\dot{m}_{\mathrm{D}}^{-1} \geq 1$. However, partial reflux operating conditions also include the operational region of $\dot{m}_{\mathrm{F}}\,\dot{m}_{\mathrm{D}}^{-1} < 1$, which is commonly used for hydraulic investigations, see (Cai, 2014), and cannot be realized with the plant concept proposed in this work. Although decoupling the in- and output streams generally allows $\dot{m}_{\mathrm{F}}\,\dot{m}_{\mathrm{D}}^{-1} < 1$, this would result in the approach presented by (Böcker and Ronge, 2005) and thus, also entail the drawbacks inherent to this setup. Nonetheless, the operating region of $\dot{m}_{\mathrm{F}}\,\dot{m}_{\mathrm{D}}^{-1} < 1$ can also be realized with $\dot{m}_{\mathrm{B}} < 0\,\mathrm{kg\,h^{-1}}$. This case would be similar to the plant concept used by (Eckert and Walter, 1964), see figure 3.1b, inasmuch as surplus distillate is fed into to bottom section of the column with a bottom input stream. Therefore, adapting the plant concept proposed in this work to support not only $\dot{m}_{\mathrm{B}} \geq 0\,\mathrm{kg\,h^{-1}}$, but also $\dot{m}_{\mathrm{B}} < 0\,\mathrm{kg\,h^{-1}}$ would allow a more flexible plant operation with both total ($\dot{F}\,\dot{D}^{-1} = 1$) and partial reflux ($\dot{F}\,\dot{D}^{-1} \neq 1$). Combining this adaptation with a variable feed inlet position, would result in a universal plant concept suitable to address various aspects of separation performance measurements and packing characterization, e.g. feed inlet position, reflux ratio, feedstock composition, column hydraulics etc.

4.3.3. Plant Setup and Experimental Method

In addition to the general improvements regarding the proposed plant concept, the experimental investigations also allowed identifying improvements specific to the distillation plant used for the separation performance experiments.

As discussed in section 3.3.3.2, plant start-up and reaching steady state took up to 7 h. Although (Schoenmakers and Spiegel, 2014) state that start-up times of around 12 h are quite common for miniplant-scale distillation columns, the plant start-up time can substantially be reduced by removing product recycle tank B501. This not only decreases the total liquid hold-up volume of the distillation plant, but also increases mixing between the feedstock and the product recycle mixture. While this apparative adaptation can easily be realized by connecting valve V402 with the feedstock tank B601, it was not carried out during the parameter studies conducted in this work to prevent potentially caused side-effects on comparability of plant operation and experimental results.

Furthermore, presented results indicate that the uncertainty associated with the molar stream ratio is especially relevant for partial reflux experiments with $\dot{F}\,\dot{D}^{-1} \geq 2.0$, see e.g. figure 4.7 and appendix F.2.4. Although the overall mass balance is satisfied within the margins suggested in the literature for most of the experiments conducted in this work, see table 4.1, the gravimetric estimation of distillate and bottoms mass flows based on scales W401 and W402 as well as tanks B401 and B402 should be replaced by suitable Coriolis mass flow meters. This would not only further reduce the total liquid hold-up of the distillation plant and thus, increase the mixing of

the product recycles with the feedstock, but also improve measurement accuracy and simplify data evaluation. Similarly, scale W601, which is used to measure the feedstock mass, should be replaced by a liquid level sensor.

In addition to the improvements for measuring the in- and output mass flows of the distillation plant with respect to operating conditions and material balance, the energy balances should be assessed. In particular, flow meters and temperature sensors should be retrofitted to reboiler W301, feed preheater W601 as well as condensers W101 and W701 to evaluate the corresponding heat duties; see (Cai, 2014) for information about the accuracies of corresponding sensors. However, upgrading the heat-jacketed tanks B501 and B601 with similar instrumentation does not seem feasible, as it was already suggested to remove the first and the heat duty of the second could easily be compensated by using heat exchanger W301 instead of the heated jacket of the tank. Furthermore, heat flux sensors could be applied to the column head, column segments and column coupling pieces to evaluate a heat-neutral plant operation and to assess the heat duty of the trace-heatings installed at the column head as well as the column coupling pieces.

As mentioned in section 3.3.4 and apparent from figure 4.3, plant operation at partial reflux conditions is limited by the maximum reboiler duty. Since figure 4.3 indicates operational reserves with respect to specific pressure drop, and thus column loads, thermostats WE301 and WE302 should either be replaced by a more powerful device or steam should be used a heating utility, since higher gas loads are required to extend the investigated parameter space. This is especially useful to fill the missing data regions highlighted in figure 4.15 which in turn should allow deriving a data-driven model to describe the relation between separation performance and partial reflux operating conditions. In particular, separation performance experiments with molar stream ratios of $1.1 < \dot{F}\,\dot{D}^{-1} < 2.0$ at f-factors of $f_\mathrm{G} < 1.5\,\mathrm{Pa}^{0.5}$ and $\dot{F}\,\dot{D}^{-1} > 1.1$ at $f_\mathrm{G} > 1.5\,\mathrm{Pa}^{0.5}$ are suggested based on figures 4.12 and 4.15.

To monitor plant operation at higher column loads and to detect flooding, differential pressure sensors P202 and P203 as well as corresponding pressure lines should be used. Although all pressure lines have been checked and re-done during plant commissioning, obtained sensor readings remained unreasonable. Therefore, as shown in equation (3.13) and table 3.6, specific pressure drops Δp_bed were calculated based on absolute pressure sensors P201 and P204. However, using differential sensors P202 and P203 would not only allow measuring the individual pressure drop of the upper and lower section of the packed bed, but should generally result in more accurate readings due to the more suitable measuring ranges of the respective sensors. To further decrease the uncertainty associated with the sensor readings and to check for potential sensor malfunction, it is suggested to re-calibrate all pressure sensors. Although not explicitly observed during the experiments, adding a nitrogen purge gas seal as described by (Cai, 2014; Starkweather et al., 2014) is recommended to prevent condensate in the pressure lines and increase the reliability of the pressure readings.

Additional adaptations can be made with respect to liquid sampling and sample analysis. Since the estimation of separation performance focuses on the installed packings, liquid samples

should be taken from the liquid trickling out of the packed bed rather than from the liquid in the column bottom section. Although rarely used in this work, the septum based sampling tap for inter-bed sampling should be replaced by a ball valve lock to prevent leaks caused by potential septum ruptures and increase operational stability. Furthermore, smaller sampling taps are recommended to achieve smaller sampling purge volumes and thus, reduce the total liquid volume drawn from the column as well as disturbances in steady-state plant operation. This is especially relevant for the total reflux experiments in which small feedstock volumes were used. In addition, vacuum sampling is suggested to not only simplify liquid sampling substantially, but also allow drawing samples from the gas phase. Disregarding the specific sampling approach, sample analysis should be performed with gas chromatography instead of density measurements. Although (Onken and Arlt, 1990) consider density or refractive index measurements suitable for the test mixture CB/EB, the effect of impurities cannot be addressed with such analyses. As elaborated in appendix D.2.2, mixture effects caused by impurities were neglected in this work. However, depending on the specification of the used chemicals and the type of impurities present in the test mixture, related effects may not be negligible. Furthermore, the density measurements used in this work require a rather large sample volume of about 5 mL due to the used autosampler. Performing mixture analysis with gas chromatography instead would not only allow detecting mixture impurities and reduce uncertainties, but also reduce the required sample volume substantially which in turn mitigates disturbances on steady-state operation and mixture separation caused by sampling.

Although being not suitable for mixture analysis with respect to separation performance evaluation, feed and distillate lines should be equipped with inline refractive index or inline density measurements. Since respective sensor signals correlate with mixture composition, trends in mixture composition can be monitored during plant operation to detect mass transfer steady state, see section 2.3.2.1. If the measured refractive index or density is calibrated against mixture composition, liquid molar fractions of feed and distillate stream, x_F and x_D, could be estimated continuously. This would not only allow calculating the molar stream ratio $\dot{F}\,\dot{D}^{-1}$ during plant operation, but also enable a direct control of $\dot{F}\,\dot{D}^{-1}$ instead of $\dot{m}_\mathrm{F}\,\dot{m}_\mathrm{D}^{-1}$ which reduces the deviation between desired and achieved operating conditions.

Operational reliability should considerably be increased by improving the hard- and software of the used plant control system to reduce sporadically occurring device communication errors and system crashes. Using robust soft- and hardware would also allow increasing plant automation and enable an unattended operation, so that the supervision related to plant start-up and steady-state operation is reduced. This seems especially feasible as plant start-up can take up to 7 h, whereas separation performance evaluation in steady state only takes around $0.75 \ldots 1.50$ h. In addition, extending the plant control system with a data interface would allow performing online data evaluation, automated design of experiments or experiment planning and co-simulations.

With the proposed improvements for the plant control system and the increased degree of automation resulting from the respective adaptations, the experimental effort related to a more

refined experimental approach becomes feasible. This is especially useful, if variations in mid-bed composition should be reduced by additional experiments to determine the steady-state feedstock composition resulting from the initially unknown separation performance. Since variations in mixture composition between different experiments could be mitigated based on this approach, this would also allow investigating the effect of mixture composition on separation performance systematically.

In conclusion, various aspects should be addressed to further increase operational stability and reduce uncertainty contributions as well as experimental effort, so that both usability and applicability can be substantially improved, resulting in even more robust experimental results and insights.

4.3.4. Data Processing and Evaluation

Since data processing is inherently coupled with the obtained results, the used approaches cannot be assessed independently of the results, and no reference values are available for an objective comparison. Therefore, potential improvements are derived based on the general characteristics of the data processing routines.

As elaborated in section 3.5.4.1, the separation performance is evaluated in terms of HETP values, which are estimated based on the number of theoretical stages N_{th} obtained from McCabe-Thiele stage constructions. As this approach does not consider the energy/enthalpy balances, only material, equilibrium and summation equations are covered (MES vs. MESH equations, see section 2.2.1.3). However, to improve data evaluation with respect to temperature profiles according to (Starkweather et al., 2014), see section 2.3.2.1, and to account for heat losses, the enthalpy equations should be considered. This would also allow assessing the column-internal streams stage- or segment-wise, so that segment-wise mass transfer coefficients can be calculated, if the set of MESH equations is extended with a rate-based calculation approach as illustrated by e.g. (Kister, 1992; Seader et al., 2008). In addition, solving the MESH equations in matrix notation should increase calculation performance, since optimized solvers can be used instead of the manual iteration scheme implemented in the current data evaluation routine.

Disregarding whether the MES or MESH equations are solved, choosing a more efficient iteration scheme is especially beneficial for the uncertainty propagation based on Monte Carlo methods. Although runtimes were substantially reduced by parallelized calculations, see figure E.3, using an even higher CPU count to further increase parallelization seems unfeasible. Therefore, future performance optimizations should address more efficient data types, optimized data structures and compilers. The current implementations can be improved by substantial refactoring as well as the extensive use of *NumPy* data types and functions, resulting in decreased execution times with the *Numba* Just-In-Time Compiler; see (Lam et al., 2015) for details. Depending on the results of code inspection, review and refactoring as well as the identified performance bottlenecks, a complete re-write in a more performant programming language like *Julia*, see (Bezanson et al., 2017), may be appropriate. Furthermore, the limited flexibility of

the current data evaluation caused by its monolithic architecture and the stringent data flow within the evaluation routines, can be reduced by switching to a data pipeline design pattern as independent parts of data processing (sample analyses, operational parameters, equilibrium-based and rate-based separation performance) are separated from each other. This does not only allow executing these routines independently of each other, but also mitigates evaluating the same experiment multiple times upon changes or errors in downstream data processing. Regardless of these implementation and workflow details, future changes should include a sensitivity analysis to determine the uncertainty contribution of each uncertainty component, so that individual sensitivity coefficients as well as primary uncertainty contributions can be identified and specifically addressed by improving the plant setup with respect to instrumentation and equipment. Since this also results in an increased amount of data, the data structures used to export and store results need to be adapted accordingly.

5. Conclusion and Outlook

To investigate distillative separation performance with both total and partial reflux operating conditions, an alternative plant concept was developed in this work. Such setup is required to conduct separation performance measurements with mixtures containing non-volatile components, e.g. polymer-enhanced test mixtures to assess the effect of mixture viscosity on separation performance as discussed by (Böcker and Ronge, 2005; Gutperl et al., 2022). In contrast to the experimental approach presented by (Böcker and Ronge, 2005), the alternative concept proposed in this work comprises product recycles to eliminate external mixture re-processing and to reduce the required amount of feedstock. However, as the feed stream containing the non-volatile mixture component needs to be distributed along the entire height of the packed bed, the feed inlet is located above the packed bed similar to a stripping column. Due to the product recycles, the column internal flows are related to the feed and distillate stream. This characteristic relation is described by the molar stream ratio $\dot{F}\,\dot{D}^{-1}$, which also defines the slope of the operating line and thus, is representative for the reflux condition (total reflux: $\dot{F}\,\dot{D}^{-1} = 1$, partial reflux: $\dot{F}\,\dot{D}^{-1} > 1$). As the molar stream ratio is limited by mass and component balances, suitable values depend on the maximum concentration of the non-volatile component in the bottom product.

The developed plant concept was realized using a miniplant-scale distillation column with a nominal diameter of 50 mm equipped with corrugated metal sheet packings of type *Mellapak M500.Y* (Sulzer Chemtech, Winterthur/Switzerland) and a total bed height of 2448 mm. After plant commissioning, systematic investigations on operational behavior as well as separation performance at total and partial reflux were successfully performed with the well-established standardized test mixture chlorobenzene/ethylbenzene at a constant head pressure of 100 mbar(a). To address the transition from conventional separation performance experiments with total reflux to experiments with partial reflux, a simulated total reflux operating mode was implemented in addition to the total and partial reflux operating modes. The separation performance achieved in total and simulated total operating modes are not only in good agreement with each other, but also in good agreement with observations by (Bradtmöller, 2017) using a very similar plant setup at total reflux.

Separation performance was quantified with HETP values determined based on the number of theoretical stages obtained from McCabe-Thiele stage constructions. To account for the stream arrangement of the used plant setup, separation performance was evaluated using the concentration spread between feed mixture and bottom product. Furthermore, a fractional equilibrium stage at the end of the stage polyline was considered to obtain more robust results.

Uncertainties associated with mixture compositions and operating conditions were consistently propagated through data processing and evaluation using the law of propagation of uncertainty. Since this approach is not suitable for the stage constructions due to its inherently iterative calculation scheme, Monte Carlo methods were used to propagate uncertainties alternatively. However, propagating unconstrained uncertainty distributions can result in thermodynamically invalid parameter combinations. Respective cases were excluded from further evaluation by a validity/constructability check. To evaluate the number of valid/successful stage constructions performed as part of the Monte Carlo simulations, the success ratio S_{MC} was introduced. Since the number of successful constructions affects the uncertainty distributions of the obtained results, corresponding values were discussed with respect to not only operating conditions, but also success ratio. Preheating the feed stream allowed a consistent feed subcooling of around $1 \ldots 3\,\mathrm{K}$. Considering the feed condition in the stage constructions resulted in slightly inclined feed lines and small deviations between the measured feed composition and the calculated composition at the operating line intersection. Although the effect of feed subcooling on separation performance is thus negligible, a considerable increase in the Monte Carlo success ratio was achieved. The experimental HETP values for experiments with molar stream ratios of $\dot{F}\,\dot{D}^{-1} = 1.1$ are very similar to those obtained for $\dot{F}\,\dot{D}^{-1} = 1.0$ and mostly within the associated combined standard uncertainties. In particular, HETP values of $0.1656(92) \ldots 0.211(19)\,\mathrm{m}$ were determined for $\dot{F}\,\dot{D}^{-1} \leq 1.1$ and are in good agreement with results reported by (Bradtmöller, 2017). However, for an increased deviation from total reflux conditions, a substantially reduced separation performance was observed in the experiments of this work, since HETP values of $0.277(62) \ldots 1.17(55)\,\mathrm{m}$ are obtained for $\dot{F}\,\dot{D}^{-1} \geq 2.0$ due to smaller driving forces.

In addition to the HETP values determined with McCabe-Thiele stage constructions, the Delft model was used to predict HETP based on mass transfer coefficients. For this, both the original and the revised set of mass transfer correlations were considered. Comparing the separation performance predicted based on the revised correlations for both liquid and vapor mass transfer coefficients with the experimental HETP values results in a difference of $\pm 25\,\%$ for $\dot{F}\,\dot{D}^{-1} \leq 1.1$. Since predicted and observed separation performance commonly differ by about $\pm 20 \ldots 30\,\%$ (Schultes, 2013), obtained results indicate a good prediction for the respective molar stream ratios. However, for higher molar stream ratios of $\dot{F}\,\dot{D}^{-1} \geq 2.0$, experimental and predicted HETP values substantially differ from each other and exceed the margin reported by (Schultes, 2013) by a factor of approximately 3.4. This difference most likely originates from the experimental datasets used to develop and validate the Delft model, inasmuch as the model does not cover partial reflux experiments. Although not further investigated in this work, such differences between the experimental and predicted separation performance are to be expected for most of the established mass transfer models, since separation performance at partial reflux conditions is rarely covered by the established mass transfer models. Furthermore, the equilibrium- and rate-based approaches were compared based on the obtained HETP and N_{th} as well as $\mathrm{HTU_{oG}}$ and $\mathrm{NTU_{oG}}$. As the term $\ln(\lambda)\,(\lambda - 1)^{-1}$ can be interpreted

as a factor of proportionality between $\mathrm{HTU_{oG}}$ and HETP as well as between $\mathrm{NTU_{oG}}$ and N_{th}, it was used to compare the corresponding separation performance measures. While $\ln(\lambda)\,(\lambda-1)^{-1} = 0.9536(16)\ldots0.9011(61)$ is obtained for molar stream ratios of $\dot{F}\,\dot{D}^{-1} \leq 1.1$, a range of $\ln(\lambda)\,(\lambda-1)^{-1} = 0.4925(26)\ldots0.3314(19)$ is determined for $\dot{F}\,\dot{D}^{-1} \geq 2.0$. Therefore, HETP $\approx \mathrm{HTU_{oG}}$ and $N_{\mathrm{th}} \approx \mathrm{NTU_{oG}}$ result for $\dot{F}\,\dot{D}^{-1} \leq 1.1$. Similarly, HETP $< \mathrm{HTU_{oG}}$ and $N_{\mathrm{th}} > \mathrm{NTU_{oG}}$ are deduced for $\dot{F}\,\dot{D}^{-1} \geq 2.0$. As indicated by the results, the differences between HETP and $\mathrm{HTU_{oG}}$ as well as N_{th} and $\mathrm{NTU_{oG}}$ are negligible for total reflux experiments. Therefore, separation performance determined by equilibrium- or rate-based approaches are commonly considered equal. Although both observations are already known in the literature and can also easily be derived from the underlying equations, discussions about whether the one or the other should be preferred arise. Although the experimental results of this work indicate a pronounced dependence of separation performance on reflux condition, obtained data did not allow deriving a correlation to describe the underlying relation. Furthermore, adapting the established mass transfer models for partial reflux operation may increase their prediction quality. In addition, experimental results should be compared to alternative modelling approaches like the concept of Hydrodynamic Analogies, which (Bolenz et al., 2021) extended to partial reflux operating conditions.

Future activities should thus cover systematic investigations of partial reflux operating conditions to extend the results of this work. In particular, experiments with molar stream ratios of $1.1 < \dot{F}\,\dot{D}^{-1} < 2.0$ at f-factors of $f_{\mathrm{G}} < 1.5\,\mathrm{Pa}^{0.5}$ and $\dot{F}\,\dot{D}^{-1} > 1.1$ at $f_{\mathrm{G}} > 1.5\,\mathrm{Pa}^{0.5}$ are recommended to address the currently empty regions in the result space. To achieve such operating conditions and to increase operational stability as well as to reduce associated combined standard uncertainties, extensive improvements for the methodology developed in this work were presented. These include suitable adaptations of the proposed plant concept, the used experimental setup and the data evaluation routines. Potential improvements on the plant concept mainly focus on partial reflux operating conditions with $\dot{F}\,\dot{D}^{-1} < 1.0$, so that the alternative plant concept becomes applicable to the full operating range ($\dot{F}\,\dot{D}^{-1} < 1.0$, $\dot{F}\,\dot{D}^{-1} = 1.0$ and $\dot{F}\,\dot{D}^{-1} > 1.0$). Improvements suggested for the plant setup are to reduce the total liquid hold-up of the distillation plant, the plant start-up duration and the combined standard uncertainties associated with the recorded operating parameters. To achieve higher reboiler duties and, thus, allow higher column loads and molar stream ratios, replacing the thermostat of the reboiler is suggested. Furthermore, improved liquid sampling and sample analysis procedures to decrease systematic deviations and uncertainties affecting the separation performance evaluation were described. Future improvements on data evaluation routines should not only include a sensitivity analysis to identify the most important uncertainty contributions, but also focus on reducing the corresponding execution times.

By implementing the presented improvements, the quality of future results is expected to be improved considerably. It is worth noting that reliable benchmark or reference experiments with well-known test mixtures under variation of mixture composition and reflux condition are a

mandatory prerequisite for future separation performance experiments with non-volatile mixture components, since the effects of reflux condition and mixture properties (e.g. composition, increased viscosity etc.) on separation performance are superimposed and thus, can only be indirectly assessed during experiment evaluation. Using this adapted procedure, the experimental results presented by (Gutperl et al., 2022) could not only be extended with further experiments, but also re-evaluated to systematically address viscous distillation with polymer-enhanced test mixtures.

Recalling the considerably reduced separation performance for increased molar stream ratios of $\dot{F}\,\dot{D}^{-1} \geq 2.0$, and the fact that none of the evaluated measures allows expressing separation performance universally for both total and partial reflux conditions, raises the following question: What is separation performance for partial reflux conditions after all?

A. Distillation Plant

A.1. Piping and Instrumentation Diagram

intentionally left blank

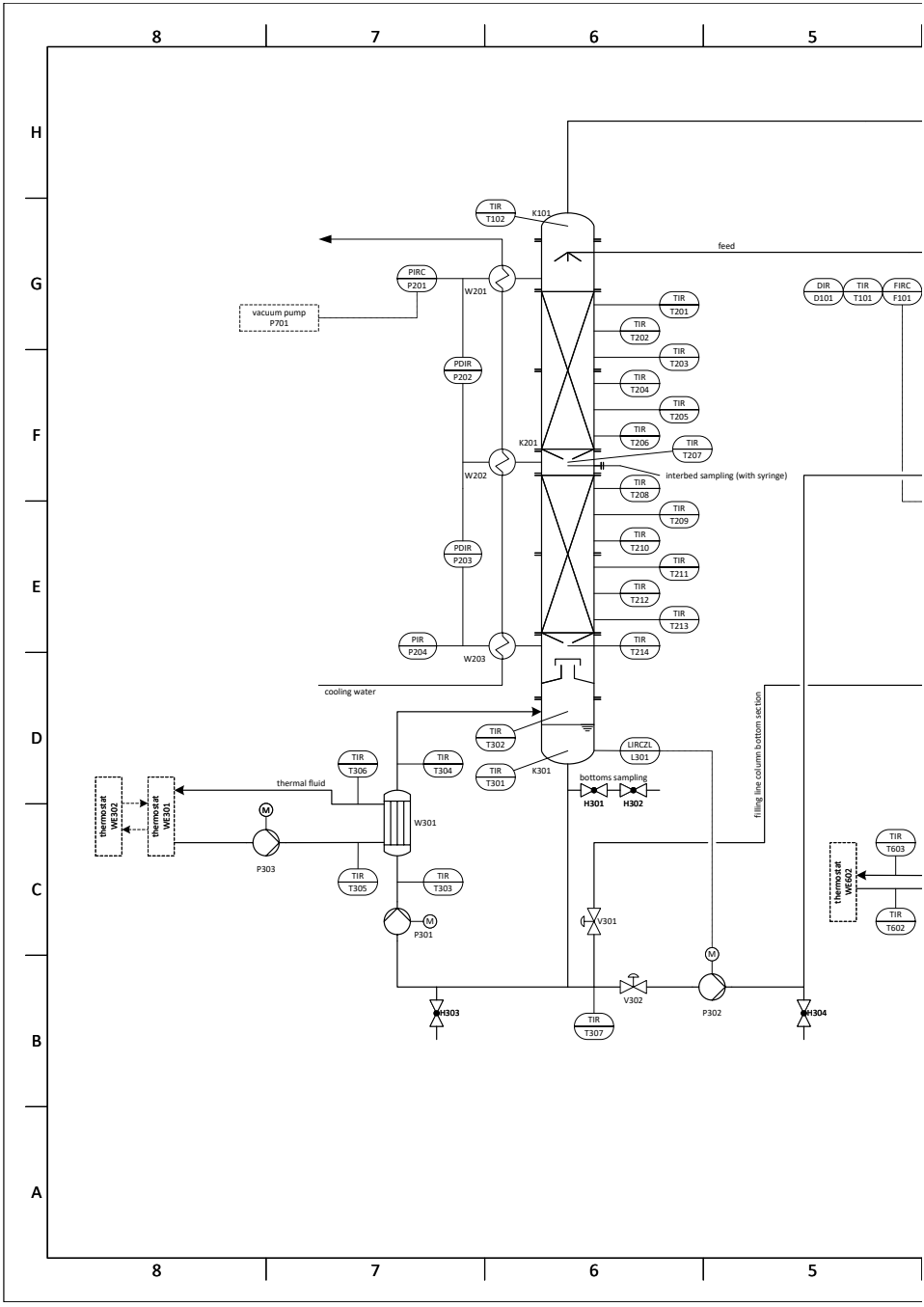
8
7
6
5
H
G
F
E
D
C
B
A
TIR T102
K101
feed
PIRC P201
W201
vacuum pump P701
DIR D101
TIR T101
FIRC F101
TIR T201
TIR T202
TIR T203
TIR T204
TIR T205
TIR T206
TIR T207
PDIR P202
K201
W202
interbed sampling (with syringe)
TIR T208
TIR T209
TIR T210
TIR T211
TIR T212
TIR T213
PDIR P203
PIR P204
W203
TIR T214
cooling water
TIR T302
LIRCZL L301
TIR T306
TIR T304
TIR T301
K301
bottoms sampling
H301
H302
thermal fluid
thermostat WE303
thermostat WE301
W301
filling line column bottom section
P303
TIR T305
TIR T303
TIR T603
thermostat WE602
TIR T602
P301
V301
V302
P302
H303
H304
TIR T307

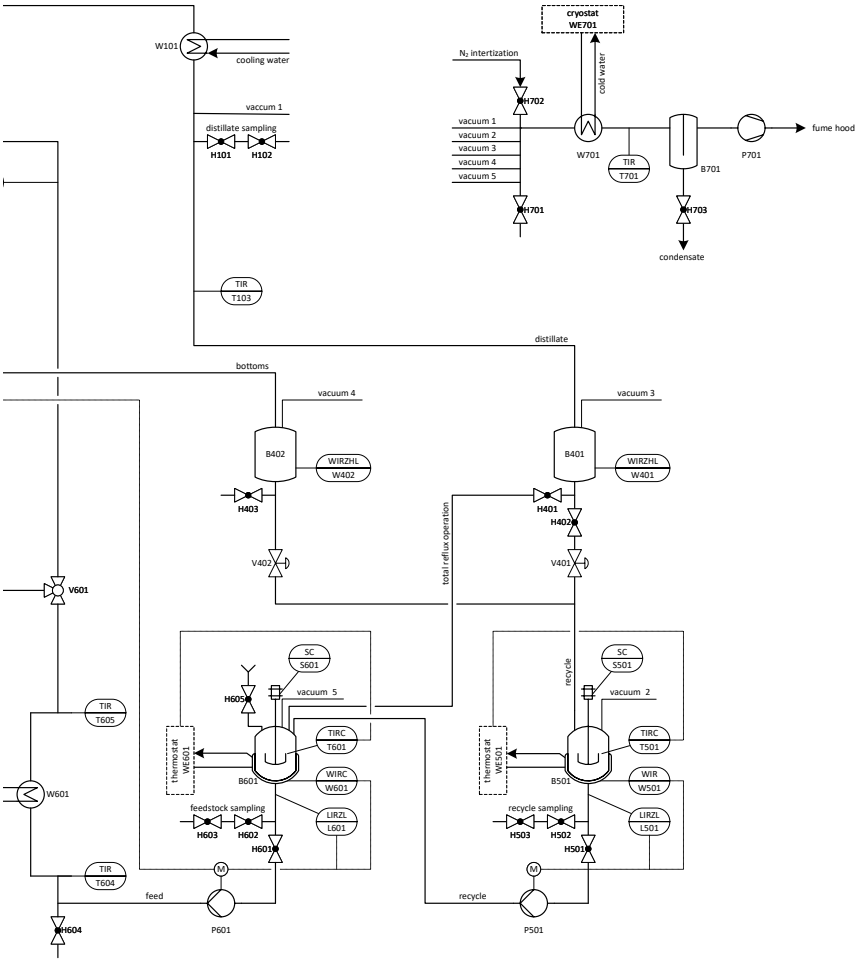

Technische Universität Braunschweig

ICTV

Institute for Chemical and Thermal Process Engineering
Technische Universität Braunschweig

Sven Gutperl

 # SCHO 842/12-3

Test distillation plant
for separation performance measurements with non-volatile mixture components

REVISION	DESCRIPTION	DATE	PERSON
24	removed B101, H103, V501, V601 & H604; fixed WE501	2023-04-24	sgut
23	B501: vacuum, T301: TIR, W401/W402: WIRZHL, W501: WIR	2023-04-17	sgut

PAPER SIZE	DRAWING NO.	REV.
A3	842/12-3_20230413	24

PAGE 1 of 1

A.2. Equipment, Sensors and Instrumentation

intentionally left blank

Table A.1.: Column and packing specifications, geometry data by (Bradtmöller, 2017), assigned tolerances as per (DIN ISO 2768-1, 1991)

parameter	symbol	unit	nominal value	tolerance class	tolerance	standard uncertainty
distillation column						
diameter	d_{col}	mm	51	very coarse	± 1.5	0.87
packing elements						
element height	h_{p}	mm	102	very coarse	± 1.5	0.87
element diameter	d_{p}	mm	41	fine	± 0.15	0.087
channel width	w_{c}	mm	9.8	medium	± 0.2	0.12
channel height	h_{c}	mm	6.6	medium	± 0.2	0.12
channel angle	α_{p}	$^\circ$	45	medium	± 0.3	0.17
void fraction	ε_{p}	-	0.975[a]	-	-	-
fraction of surface area occupied by holes	Ω_{p}	-	0.1 [b]	-	-	-
surface tension	σ_{p}	$\mathrm{N\,m^{-1}}$	0.075[c]	-	-	-

[a] value by (Schmit et al., 2004) used in this work.
(Olujić, 2014) proposes $\varepsilon_{\mathrm{p}} = 1 - 0.5\, a_{\mathrm{p}}\, \delta_{\mathrm{p}}$; a_{p}: specific packing surface area, see equation (2.71); δ_{p}: sheet thickness

[b] (Olujić et al., 2004)

[c] (Stichlmair et al., 2021)

Table A.2.: Equipment of distillation plant

tag	category	description	model	manufacturer
B401	tank	underfloor weighing distillate mass flow	-	*in-house*
B402	tank	underfloor weighing bottoms mass flow	-	*in-house*
B501	tank	recycle tank	4VJ, 30 L	DeDietrich, Mainz/Germany
B601	tank	feedstock tank	4VJ, 30 L	DeDietrich, Mainz/Germany
B701	tank	cold trap	M-CT85/04	QVF, Mainz/Germany
H101	ball valve	sampling distillate	PED15	QVF, Mainz/Germany
H102	ball valve	sampling distillate	SK31941	QVF, Mainz/Germany
H301	ball valve	sampling column bottom section	PVD15	QVF, Mainz/Germany
H302	ball valve	sampling column bottom section	SK31941	QVF, Mainz/Germany
H303	ball valve	drain column bottom section	PVA15/16	QVF, Mainz/Germany
H304	ball valve	drain bottoms line	BVA-12M	Hy-Lok D, Oyten/Germany
H401	ball valve	distillate tank total reflux	BVA-12M	Hy-Lok D, Oyten/Germany
H402	ball valve	distillate tank partial reflux	BVA-12M	Hy-Lok D, Oyten/Germany
H403	ball valve	drain bottoms tank	BVA-12M	Hy-Lok D, Oyten/Germany
H501	ball valve	recycle tank	BVA-12M	Hy-Lok D, Oyten/Germany
H502	ball valve	sampling recycle	BVA-12M	Hy-Lok D, Oyten/Germany
H503	ball valve	sampling recycle	BVA-12M	Hy-Lok D, Oyten/Germany
H601	ball valve	feedstock tank	BVA-12M	Hy-Lok D, Oyten/Germany
H602	ball valve	sampling feedstock	BVA-12M	Hy-Lok D, Oyten/Germany
H603	ball valve	sampling feedstock	BVA-12M	Hy-Lok D, Oyten/Germany
H604	ball valve	drain feed line	BVA-12M	Hy-Lok D, Oyten/Germany

Table A.2.: Equipment of distillation plant (continued)

tag	category	description	model	manufacturer
H605	ball valve	filling funnel feedstock tank	BVA-12M	Hy-Lok D, Oyten/Germany
H701	ball valve	drain vacuum distributor	PVL15	QVF, Mainz/Germany
H702	ball valve	nitrogen intertization	Minibinox 2641	Effebi, Bovezzo/Italy
H703	ball valve	drain cold trap	*integrated in B701*	
K101	column	head section	*unknown*	QVF, Mainz/Germany
K201	column	main section and packed bed	SK32185	QVF, Mainz/Germany
		column coupling piece	SK32192	QVF, Mainz/Germany
K301	column	bottom section	SK32255	QVF, Mainz/Germany
P301	pump	reboiler circulation	VGS 1300.05	Verder, Haan/Deutschland
P302	pump	bottom purge	BVP Z-1830P	Cole-Parmer, Wertheim/Germany
P303	pump	reboiler heating utility	VGS 330.07	Verder, Haan/Deutschland
P501	pump	recycle transfer	*unknown*	Verder, Haan/Deutschland
P601	pump	feed	3030-045-DM-2	Scherzinger Pumpen, Furtwangen/Germany
P701	pump	vacuum	PC 3004 Vario	Vacuubrand, Wertheim/Germany
S501	stirrer	recycle	RW 20.n	IKA-Werke, Staufen/Germany
S601	stirrer	feedstock	RW 20 digital	IKA-Werke, Staufen/Germany
V301	actuated valve	filling line column bottom section	DG2D3129015/OS	END-Armaturen, Bad Oeynhausen/Germany
V302	actuated valve	bottoms purge line	DG2D3129015/OS	END-Armaturen, Bad Oeynhausen/Germany
V401	actuated valve	underfloor weighing distillate mass flow	DG2D3129015/OS	END-Armaturen, Bad Oeynhausen/Germany
V402	actuated valve	underfloor weighing bottoms mass flow	DG2D3129015/OS	END-Armaturen, Bad Oeynhausen/Germany
V601	actuated valve	feed line / filling line column bottom	DG3D3115015/A-OS	END-Armaturen, Bad Oeynhausen/Germany

Table A.2.: Equipment of distillation plant (continued)

tag	category	description	model	manufacturer
W101	heat exchanger	column head condenser	HEC150/7	QVF, Mainz/Germany
W201	heat exchanger	pressure line column	-	*in-house*
W202	heat exchanger	pressure line column	*not specified*	
W203	heat exchanger	pressure line column	*not specified*	
W301	heat exchanger	reboiler	-	*in-house*
W601	heat exchanger	feed stream preheater	-	*in-house*
W701	heat exchanger	vacuum distribution	HEC40/2	QVF, Mainz/Germany
WE301	thermostat	reboiler	Phoenix II P1-B5	Thermo Haake, Karlsruhe/Germany
WE302	thermostat	reboiler	Phoenix II P1-B5	Thermo Haake, Karlsruhe/Germany
WE501	thermostat	recycle tank	HD	Julabo, Seelbach/Germany
WE601	thermostat	feedstock tank	ME	Julabo, Seelbach/Germany
WE602	thermostat	feed stream preheater	MA	Julabo, Seelbach/Germany
WE701	cryostat	condenser vacuum distribution	CC-405	Peter Huber Kältemaschinenbau, Offenburg/Germany

Table A.3.: Sensors and instrumentation, dif: differential, abs: absolute, TC: thermocouple

tag	type	description	model	manufacturer
D101	density	*density measurement integrated in F101*		
F101	mass flow	Coriolis feed flow	Optimass 3400-S03/MFC 400 C	Krohne Messtechnik, Duisburg/Germany
L301	liquid level (switch)	column bottom	KN5121	ifm electronic, Essen/Germany
L501	liquid level (switch)	recycle tank	KI5311	ifm electronic, Essen/Germany
L601	liquid level (switch)	feedstock tank	KI5311	ifm electronic, Essen/Germany
P201	pressure (abs.)	column head	Cerabar-S PMC71	Endress+Hauser, Reinach/Switzerland
P202	pressure (dif.)	upper packed bed	DIF34	VEGA Grieshaber, Schiltach/Germany
P203	pressure (dif.)	lower packed bed	DIF34	VEGA Grieshaber, Schiltach/Germany
P204	pressure (abs.)	column bottom	Cerabar-S PMC71	Endress+Hauser, Reinach/Switzerland
T101	Pt500	*temperature sensor integrated in F101*		
T102	Pt100, class A	column head	WT WV82.L	Temperaturmesstechnik Geraberg, Martinroda/Germany
T103	Pt100, class A	distillate	WT WV82.L	Temperaturmesstechnik Geraberg, Martinroda/Germany
T201	Pt100, class A	column profile	WT WV82.L	Temperaturmesstechnik Geraberg, Martinroda/Germany
T202	Pt100, class A	column profile	WT WV82.L	Temperaturmesstechnik Geraberg, Martinroda/Germany
T203	Pt100, class A	column profile	WT WV82.L	Temperaturmesstechnik Geraberg, Martinroda/Germany
T204	Pt100, class A	column profile	WT WV82.L	Temperaturmesstechnik Geraberg, Martinroda/Germany

Table A.3.: Sensors and instrumentation, dif: differential, abs: absolute, TC: thermocouple (continued)

tag	type	description	model	manufacturer
T205	Pt100, class A	column profile	WT WV82.L	Temperaturmesstechnik Geraberg, Martinroda/Germany
T206	Pt100, class A	column profile	WT WV82.L	Temperaturmesstechnik Geraberg, Martinroda/Germany
T207	Pt100, class A	column profile	WT WV82.L	Temperaturmesstechnik Geraberg, Martinroda/Germany
T208	Pt100, class A	column profile	WT WV82.L	Temperaturmesstechnik Geraberg, Martinroda/Germany
T209	Pt100, class A	column profile	WT WV82.L	Temperaturmesstechnik Geraberg, Martinroda/Germany
T210	Pt100, class A	column profile	WT WV82.L	Temperaturmesstechnik Geraberg, Martinroda/Germany
T211	Pt100, class A	column profile	WT WV82.L	Temperaturmesstechnik Geraberg, Martinroda/Germany
T212	Pt100, class A	column profile	WT WV82.L	Temperaturmesstechnik Geraberg, Martinroda/Germany
T213	Pt100, class A	column profile	WT WV82.L	Temperaturmesstechnik Geraberg, Martinroda/Germany
T214	Pt100, class A	column profile	WT WV82.L	Temperaturmesstechnik Geraberg, Martinroda/Germany
T301	Pt100, class A	column bottom liquid	WT WV82.L	Temperaturmesstechnik Geraberg, Martinroda/Germany
T302	Pt100, class A	column bottom gas	WT WV82.L	Temperaturmesstechnik Geraberg, Martinroda/Germany

Table A.3.: Sensors and instrumentation, dif: differential, abs: absolute, TC: thermocouple (continued)

tag	type	description	model	manufacturer
T303	TC type K, class 1	reboiler product in	405-269	TC Mess- und Regeltechnik, Mönchengladbach/Germany
T304	TC type K, class 1	reboiler product out	405-269	TC Mess- und Regeltechnik, Mönchengladbach/Germany
T305	TC type K, class 1	reboiler heating in	405-269	TC Mess- und Regeltechnik, Mönchengladbach/Germany
T306	TC type K, class 1	reboiler heating out	405-269	TC Mess- und Regeltechnik, Mönchengladbach/Germany
T307	TC type T, class 1	bottoms purge line	MMT-11022-100-1	Therma Thermofühler, Lindlar/Germany
T501	Pt100, class A	recycle tank	MRW-46080-700-500-Pt100-A	Therma Thermofühler, Lindlar/Germany
T601	Pt100, class A	feedstock tank	MRW-46080-700-500-Pt100-A	Therma Thermofühler, Lindlar/Germany
T602	TC type T, class 1	feed preheater heating in	MMT-11022-100-1	Therma Thermofühler, Lindlar/Germany
T603	TC type T, class 1	feed preheater heating out	MMT-11022-100-1	Therma Thermofühler, Lindlar/Germany
T604	TC type T, class 1	feed preheater product in	MMT-11022-100-1	Therma Thermofühler, Lindlar/Germany
T605	TC type T, class 1	feed preheater product out	MMT-11022-100-1	Therma Thermofühler, Lindlar/Germany
T701	Pt100, class A	vacuum distribution	WT WV82.L	Temperaturmesstechnik Geraberg, Martinroda/Germany

Table A.3.: Sensors and instrumentation, dif: differential, abs: absolute, TC: thermocouple (continued)

tag	type	description	model	manufacturer
W401	scale	underfloor weighing distillate mass flow	FKB 16K0.1	Kern & Sohn, Balingen/Germany
W402	scale	underfloor weighing bottoms mass flow	Combics 1 CW1P1-30ED-I	Sartorius, Göttingen/Germany
W501	scale	recycle tank	DS100K0.5	Kern & Sohn, Balingen/Germany
	(weighing terminal)		IT1	SysTec Systemtechnik & Industrieautomation, Bergheim/Germany
W601	scale	feedstock tank	DS100K0.5	Kern & Sohn, Balingen/Germany
	(weighing terminal)		IT1	SysTec Systemtechnik & Industrieautomation, Bergheim/Germany

A.3. Sensor Measuring Ranges and Accuracies

Table A.4.: Sensor measuring ranges and accuracies, accuracies of temperature sensors given in relevant temperature range only, $[\vartheta] = {}^{\circ}\mathrm{C}$, $[\dot{m}] = \mathrm{kg\,h^{-1}}$, $[p] = \mathrm{bar(a)}$ or $[p] = \mathrm{mbar}$

tag	measuring range	accuracy	literature reference
D101	$400 \ldots 3000\,\mathrm{kg\,m^{-3}}$	$\pm 2\,\mathrm{kg\,m^{-3}}$	(Krohne, 2016)
F101	$0 \ldots 130\,\mathrm{kg\,h^{-1}}$	$\pm(0.001 \cdot \dot{m} + 0.007\,41\,\mathrm{kg\,h^{-1}})$ [a]	(Krohne, 2016)
P201	$0 \ldots 2\,\mathrm{bar(a)}$ [b]	$\pm 1.5\,\mathrm{mbar(a)}$ [c]	(E+H, 2004)
P202	$5 \ldots 25\,\mathrm{mbar}$ [d]	$\pm 0.025\,\mathrm{mbar}$ [e]	(VEGA, 2014)
P203	$5 \ldots 25\,\mathrm{mbar}$ [d]	$\pm 0.025\,\mathrm{mbar}$ [e]	(VEGA, 2014)
P204	$0 \ldots 2\,\mathrm{bar(a)}$ [b]	$\pm 1.5\,\mathrm{mbar(a)}$ [c]	(E+H, 2004)
T101	$-40 \ldots 150\,^{\circ}\mathrm{C}$	$\pm 1\,\mathrm{K}$	(Krohne, 2016)
T102	$-50 \ldots 250\,^{\circ}\mathrm{C}$	$\pm(0.15\,\mathrm{K} + 0.002 \cdot \lvert\vartheta\rvert)$	(DIN EN 60751, 2009)
T103	$-50 \ldots 250\,^{\circ}\mathrm{C}$	$\pm(0.15\,\mathrm{K} + 0.002 \cdot \lvert\vartheta\rvert)$	(DIN EN 60751, 2009)
T201	$-50 \ldots 250\,^{\circ}\mathrm{C}$	$\pm(0.15\,\mathrm{K} + 0.002 \cdot \lvert\vartheta\rvert)$	(DIN EN 60751, 2009)
T202	$-50 \ldots 250\,^{\circ}\mathrm{C}$	$\pm(0.15\,\mathrm{K} + 0.002 \cdot \lvert\vartheta\rvert)$	(DIN EN 60751, 2009)
T203	$-50 \ldots 250\,^{\circ}\mathrm{C}$	$\pm(0.15\,\mathrm{K} + 0.002 \cdot \lvert\vartheta\rvert)$	(DIN EN 60751, 2009)
T204	$-50 \ldots 250\,^{\circ}\mathrm{C}$	$\pm(0.15\,\mathrm{K} + 0.002 \cdot \lvert\vartheta\rvert)$	(DIN EN 60751, 2009)
T205	$-50 \ldots 250\,^{\circ}\mathrm{C}$	$\pm(0.15\,\mathrm{K} + 0.002 \cdot \lvert\vartheta\rvert)$	(DIN EN 60751, 2009)
T206	$-50 \ldots 250\,^{\circ}\mathrm{C}$	$\pm(0.15\,\mathrm{K} + 0.002 \cdot \lvert\vartheta\rvert)$	(DIN EN 60751, 2009)
T207	$-50 \ldots 250\,^{\circ}\mathrm{C}$	$\pm(0.15\,\mathrm{K} + 0.002 \cdot \lvert\vartheta\rvert)$	(DIN EN 60751, 2009)
T208	$-50 \ldots 250\,^{\circ}\mathrm{C}$	$\pm(0.15\,\mathrm{K} + 0.002 \cdot \lvert\vartheta\rvert)$	(DIN EN 60751, 2009)
T209	$-50 \ldots 250\,^{\circ}\mathrm{C}$	$\pm(0.15\,\mathrm{K} + 0.002 \cdot \lvert\vartheta\rvert)$	(DIN EN 60751, 2009)
T210	$-50 \ldots 250\,^{\circ}\mathrm{C}$	$\pm(0.15\,\mathrm{K} + 0.002 \cdot \lvert\vartheta\rvert)$	(DIN EN 60751, 2009)
T211	$-50 \ldots 250\,^{\circ}\mathrm{C}$	$\pm(0.15\,\mathrm{K} + 0.002 \cdot \lvert\vartheta\rvert)$	(DIN EN 60751, 2009)
T212	$-50 \ldots 250\,^{\circ}\mathrm{C}$	$\pm(0.15\,\mathrm{K} + 0.002 \cdot \lvert\vartheta\rvert)$	(DIN EN 60751, 2009)
T213	$-50 \ldots 250\,^{\circ}\mathrm{C}$	$\pm(0.15\,\mathrm{K} + 0.002 \cdot \lvert\vartheta\rvert)$	(DIN EN 60751, 2009)
T214	$-50 \ldots 250\,^{\circ}\mathrm{C}$	$\pm(0.15\,\mathrm{K} + 0.002 \cdot \lvert\vartheta\rvert)$	(DIN EN 60751, 2009)
T301	$-50 \ldots 250\,^{\circ}\mathrm{C}$	$\pm(0.15\,\mathrm{K} + 0.002 \cdot \lvert\vartheta\rvert)$	(DIN EN 60751, 2009)
T302	$-50 \ldots 250\,^{\circ}\mathrm{C}$	$\pm(0.15\,\mathrm{K} + 0.002 \cdot \lvert\vartheta\rvert)$	(DIN EN 60751, 2009)
T303	$-40 \ldots 375\,^{\circ}\mathrm{C}$	$\pm 1.5\,\mathrm{K}$	(DIN EN 60584-1, 2014)
T304	$-40 \ldots 375\,^{\circ}\mathrm{C}$	$\pm 1.5\,\mathrm{K}$	(DIN EN 60584-1, 2014)
T305	$-40 \ldots 375\,^{\circ}\mathrm{C}$	$\pm 1.5\,\mathrm{K}$	(DIN EN 60584-1, 2014)
T306	$-40 \ldots 375\,^{\circ}\mathrm{C}$	$\pm 1.5\,\mathrm{K}$	(DIN EN 60584-1, 2014)

Table A.4.: Sensor measuring ranges and accuracies, accuracies of temperature sensors given in relevant temperature range only, $[\vartheta] = {}^\circ\mathrm{C}$, $[\dot{m}] = \mathrm{kg\,h^{-1}}$, $[p] = \mathrm{bar(a)}$ or $[p] = \mathrm{mbar}$ (continued)

tag	measuring range	accuracy	literature reference
T307	$-40 \ldots 125\,^\circ\mathrm{C}$	$\pm 0.5\,\mathrm{K}$	(DIN EN 60584-1, 2014)
T501	$-50 \ldots 250\,^\circ\mathrm{C}$	$\pm(0.15\,\mathrm{K} + 0.002 \cdot \lvert\vartheta\rvert)$	(DIN EN 60751, 2009)
T601	$-50 \ldots 250\,^\circ\mathrm{C}$	$\pm(0.15\,\mathrm{K} + 0.002 \cdot \lvert\vartheta\rvert)$	(DIN EN 60751, 2009)
T602	$-40 \ldots 125\,^\circ\mathrm{C}$	$\pm 0.5\,\mathrm{K}$	(DIN EN 60584-1, 2014)
T603	$-40 \ldots 125\,^\circ\mathrm{C}$	$\pm 0.5\,\mathrm{K}$	(DIN EN 60584-1, 2014)
T604	$-40 \ldots 125\,^\circ\mathrm{C}$	$\pm 0.5\,\mathrm{K}$	(DIN EN 60584-1, 2014)
T605	$-40 \ldots 125\,^\circ\mathrm{C}$	$\pm 0.5\,\mathrm{K}$	(DIN EN 60584-1, 2014)
T701	$-50 \ldots 250\,^\circ\mathrm{C}$	$\pm(0.15\,\mathrm{K} + 0.002 \cdot \lvert\vartheta\rvert)$	(DIN EN 60751, 2009)
W401	$\leq 16\,\mathrm{kg}$	readability: 0.1 g	(Kern & Sohn, 2021)
		reproducibility: 0.1 g	(Kern & Sohn, 2021)
		linearity: ±0.31 g	(Kern & Sohn, 2021)
W402	$\leq 30\,\mathrm{kg}$	readability: 1.0 g	(Sartorius, 2014)
		reproducibility: *not specified*	
		linearity: *not specified*	
W501	$\leq 100\,\mathrm{kg}$	readability: 0.5 g	(Kern & Sohn, 2021)
		reproducibility: 0.5 g	(Kern & Sohn, 2021)
		linearity: ±1.5 g	(Kern & Sohn, 2021)
W601	$\leq 100\,\mathrm{kg}$	readability: 0.5 g	(Kern & Sohn, 2021)
		reproducibility: 0.5 g	(Kern & Sohn, 2021)
		linearity: ±1.5 g	(Kern & Sohn, 2021)

[a] zero stability: $0.000057 \cdot \dot{m}_{\mathrm{nominal}} = 0.000057 \cdot 130\,\mathrm{kg\,h^{-1}} = 0.007\,41\,\mathrm{kg\,h^{-1}}$

[b] measuring span: $0 \ldots 1.5\,\mathrm{bar(a)}$, nominal range: $0 \ldots 2\,\mathrm{bar(a)}$

[c] specified as: $\pm 0.001 \cdot p_{\mathrm{span}} = \pm 0.001 \cdot 1.5\,\mathrm{bar(a)} = 1.5\,\mathrm{mbar(a)}$; including reproducibility, linearity and hysteresis; long-term stability and temperature-induced drift are not considered; see literature reference for detailed specifications

[d] measuring span: $5 \ldots 25\,\mathrm{mbar}$, nominal range: $-25 \ldots 25\,\mathrm{mbar}$

[e] specified as: $\pm 0.001 \cdot p_{\mathrm{nominal}} = \pm 0.001 \cdot 25\,\mathrm{mbar} = 0.025\,\mathrm{mbar}$; including reproducibility and hysteresis; linearity, long-term stability and temperature-induced drift are not considered; see literature reference for detailed specifications

A.4. Data Acquisition

To read analog signals of pressure sensors and temperature sensors, two data recorders (*34970A Data Acquisition Unit*, Keysight Technologies, Santa Rosa/CA) with two multiplexer modules each (*34901A 20-Channel Multiplexer*, Keysight Technologies, Santa Rosa/CA) were used. The accuracy specifications of the channel configuration used for data acquisition are summarized in table A.5 and include all relevant components attributed to signal processing, signal conversion and, in case of thermocouples, cold junction compensation (Keysight Technologies, 2020).

Table A.5.: Accuracies of data acquisition modules used for analog sensor signals, specifications as per (Keysight Technologies, 2020)

channel configuration	used range	accuracy
resistance thermometer	n/a	$\pm 0.06\,\mathrm{K}$
thermocouple type T	n/a	$\pm 1.0\,\mathrm{K}$
current measurement (DC)	$100.0000\,\mathrm{mA}$	$\pm(0.0001 \cdot I_{\mathrm{reading}} + 0.004\,\mathrm{mA})$

A.5. Temperature Sensor Calibration

To reduce deviations and uncertainties in temperature sensor readings, used temperature sensors were calibrated against a reference sensor (*ISOTECH 930-14-61/P795*, Dostmann electronic, Wertheim/Germany) prior installation[1]. Deviations of the reference sensor with respect to an external reference standard are listed in table A.6. However, the deviations of the reference sensor to the external reference standard were neglected to simplify calculations according to GUM annex H.3 (BIPM et al., 2008a).

Table A.6.: Temperature readings of reference temperature sensor as per calibration certificate

test temperature	indicated temperature	deviation	expanded standard uncertainty ($k = 2$)
°C	°C	K	K
200.000	199.90	−0.10	0.05
150.000	149.950	−0.050	0.03
100.000	99.983	−0.017	0.03
50.000	49.997	−0.003	0.03
0.000	−0.019	−0.019	0.03

[1]Sensor T101 was not calibrated as it is integrated in the Coriolis mass flow meter F101. Furthermore, sensors T604 and T605 were retrofitted after plant commissioning and thus, are also not covered by the calibration.

The calibration was performed in two batches over a nominal temperature range of 40 . . . 130 °C covering all relevant operating conditions. Starting with 40 °C, the temperature was increased with increments of 10 K, whereby each temperature level was held stationary for 10 min.

Recorded reference and calibration sensor readings were arithmetically averaged over each stationary temperature level. The according values used to derive a linear calibration curve for each temperature sensor are summarized in tables A.7 and A.8. The standard deviation of the calculated averages, which can be interpreted as the standard uncertainty, see appendix D, of each temperature reading, are not considered. Calibrations were calculated with the *GUM Tree Calculator* (Hall, 2022) which supports uncertainty quantification for linear calibrations according to GUM annex H.3 (BIPM et al., 2008a).

Estimated linear regression parameters are listed in table A.9. Evaluating the regressions of all temperature sensors over the full temperature range showed a maximum standard uncertainty of 0.14 K.

Table A.7.: Temperature readings of sensor calibration, first calibration batch

	temperature in °C									
level	40	50	60	70	80	90	100	110	120	130
reference	39.648	49.822	59.848	69.843	79.784	89.691	99.675	109.692	119.690	129.679
T102	39.709	49.934	59.965	69.981	79.934	89.855	99.833	109.831	119.802	129.787
T103	39.742	49.956	59.993	70.005	79.949	89.840	99.812	109.810	119.792	129.787
T104	39.680	49.898	59.951	69.942	79.883	89.774	99.738	109.735	119.747	129.759
T202	39.764	49.795	59.771	69.704	79.535	89.324	99.240	109.268	119.246	129.106
T301	39.735	49.964	60.009	70.026	79.975	89.862	99.834	109.832	119.813	129.813
T302	39.712	49.954	59.994	70.005	79.949	89.839	99.812	109.826	119.820	129.803
T303	39.753	49.965	60.018	70.016	79.964	89.863	99.830	109.833	119.846	129.855
T303	39.733	49.704	59.594	69.510	79.398	89.308	99.334	109.555	119.777	129.954
T304	39.705	49.714	59.609	69.528	79.460	89.418	99.446	109.555	119.686	129.845
T305	39.351	49.506	59.469	69.450	79.335	89.166	99.127	109.207	119.190	129.159
T306	39.307	49.442	59.451	69.433	79.270	89.176	99.190	109.161	119.065	128.990
T307	39.042	49.111	58.979	68.823	78.612	88.384	98.228	108.083	117.871	127.681
T501	39.610	49.747	59.733	69.692	79.539	89.357	99.283	109.297	119.276	129.242
T601	39.621	49.770	59.772	69.746	79.632	89.476	99.421	109.429	119.410	129.385
T602	38.961	49.017	58.881	68.722	78.475	88.186	97.972	107.570	117.215	126.932
T603	39.146	49.201	59.046	68.885	78.633	88.401	98.231	108.176	118.089	127.994
T701	39.676	49.900	59.930	69.943	79.889	89.799	99.771	109.764	119.727	129.708

Table A.8.: Temperature readings of sensor calibration, second calibration batch

	temperature in °C									
level	40	50	60	70	80	90	100	110	120	130
reference	40.019	49.999	59.999	69.995	79.996	89.999	99.994	109.993	119.995	129.995
T204	39.909	49.921	59.960	69.973	79.937	89.812	99.785	109.776	119.770	129.754
T205	39.910	49.923	59.959	69.973	79.937	89.813	99.785	109.776	119.772	129.755
T206	39.910	49.925	59.958	69.972	79.938	89.817	99.784	109.774	119.773	129.754
T207	39.912	49.926	59.957	69.974	79.938	89.819	99.783	109.774	119.774	129.753
T208	39.914	49.926	59.960	69.971	79.939	89.818	99.783	109.773	119.775	129.752
T209	39.901	49.908	59.949	69.964	79.926	89.799	99.774	109.766	119.764	129.749
T210	39.902	49.909	59.950	69.963	79.927	89.803	99.773	109.768	119.765	129.749
T211	39.902	49.912	59.951	69.961	79.928	89.805	99.771	109.767	119.766	129.748
T212	39.903	49.911	59.951	69.959	79.928	89.807	99.771	109.767	119.764	129.747
T213	39.902	49.913	59.952	69.957	79.928	89.809	99.772	109.765	119.765	129.748
T214	39.905	49.914	59.958	69.949	79.927	89.811	99.771	109.766	119.764	129.747

Table A.9.: Results of temperature sensor calibration, SSR: sum of squared residuals, r: correlation coefficient, $\vartheta_{\mathrm{meas}}$: measured temperature, ϑ_{ref}: reference temperature

sensor	slope	y-intercept	SSR	$r(\vartheta_{\mathrm{meas}}, \vartheta_{\mathrm{ref}})$
T102	0.999 63(33)	−0.094(30)	0.007 26	−0.95
T103	1.000 19(28)	−0.147(25)	0.005 31	−0.95
T201	1.000 07(29)	−0.080(26)	0.005 39	−0.95
T202	1.007 24(53)	−0.350(48)	0.018 55	−0.95
T203	0.999 68(25)	−0.130(22)	0.003 96	−0.95
T204	0.999 49(13)	−0.069(12)	0.001 10	−0.95
T205	1.003 61(52)	−0.198(46)	0.017 58	−0.95
T206	0.999 30(12)	−0.047(11)	0.000 93	−0.95
T207	0.999 63(17)	−0.093(15)	0.001 86	−0.95
T208	0.999 57(18)	−0.150(16)	0.002 21	−0.95
T209	0.997 54(13)	−0.084(12)	0.001 13	−0.95
T210	0.998 70(11)	−0.0763(95)	0.000 74	−0.95
T211	0.999 17(10)	−0.0922(90)	0.000 66	−0.95
T212	1.0037(11)	−0.243(95)	0.073 50	−0.95
T213	0.999 22(20)	−0.099(18)	0.002 64	−0.95
T214	0.999 73(19)	−0.079(17)	0.002 34	−0.95
T301	0.999 94(36)	−0.144(32)	0.008 54	−0.95
T302	0.999 77(32)	−0.115(29)	0.006 83	−0.95
T303	0.9977(26)	0.34(23)	0.440 47	−0.95
T304	0.9984(19)	0.27(17)	0.231 57	−0.95
T305	1.002 65(48)	0.218(43)	0.015 00	−0.95

Table A.9.: Results of temperature sensor calibration, SSR: sum of squared residuals, r: correlation coefficient, $\vartheta_{\mathrm{meas}}$: measured temperature, ϑ_{ref}: reference temperature (continued)

sensor	slope	y-intercept	SSR	$r(\vartheta_{\mathrm{meas}}, \vartheta_{\mathrm{ref}})$
T306	1.003 49(40)	0.194(35)	0.010 32	−0.95
T307	1.015 65(37)	−0.051(32)	0.008 55	−0.95
T501	1.004 98(40)	−0.161(36)	0.010 40	−0.95
T601	1.003 32(23)	−0.110(21)	0.003 55	−0.95
T602	1.0235(16)	−0.41(14)	0.167 95	−0.95
T603	1.013 94(68)	−0.008(60)	0.029 70	−0.95
T701	1.000 20(36)	−0.090(32)	0.008 57	−0.95

A.6. Stream Ratio

A.6.1. Binary Mixture

The optimization problems defined in equations (3.4) and (3.5) were solved with the following code:

Listing A.1: Non-linear optimization problem to estimate deviation in stream ratio for binary mixture CB/EB

```
using JuMP
using Ipopt

model = Model(Ipopt.Optimizer)

set_attribute(model, "max_cpu_time", 60.0)
set_attribute(model, "print_level", 0)

@NLparameter(model, M_CB == 112.56)
@NLparameter(model, M_EB == 106.17)

@variable(model, 0 <= x_D <= 1)
@variable(model, 0 <= x_F <= 1)

# (un)comment according line to solve 'Min' or 'Max' optimization problem
@NLobjective(model, Min, (x_D * M_CB + (1-x_D) * M_EB) / (x_F * M_CB + (1-x_F) * M_EB))
@NLobjective(model, Max, (x_D * M_CB + (1-x_D) * M_EB) / (x_F * M_CB + (1-x_F) * M_EB))

optimize!(model)

println(model)

println("objective value: ", objective_value(model))
println("x_D: ", value(x_D))
println("x_F: ", value(x_F))
```

A.6.2. Ternary Mixture with Non-Volatile Component

As discussed and validated in section 3.3.3.1, two optimization problems can be defined to estimate the deviation between the stream ratios $\dot{F}\,\dot{D}^{-1}$ and $\dot{m}_\mathrm{F}\,\dot{m}_\mathrm{D}^{-1}$.

Since the non-volatile component (component 3) does not evaporate and entrainment is neglected, $x_{3,\mathrm{D}} = 0\,\mathrm{kmol_3\,kmol_{tot}^{-1}}$ is assumed. Extending equation (3.3) results in:

$$\frac{\dot{F}}{\dot{D}} = \frac{\dot{m}_\mathrm{F}}{\dot{m}_\mathrm{D}}\,\frac{M_\mathrm{D}}{M_\mathrm{F}} = \frac{\dot{m}_\mathrm{F}}{\dot{m}_\mathrm{D}} \cdot \frac{x_{1,\mathrm{D}}\,M_1 + (1 - x_{1,\mathrm{D}})\,M_2}{x_{1,\mathrm{F}}\,M_1 + x_{2,\mathrm{F}}\,M_2 + x_{3,\mathrm{F}}\,M_3} \tag{A.1}$$

Investigating viscous distillation with the test mixture CB/EB/PBD, (Gutperl et al., 2022) reached mixture viscosities of 20 mPa s with polymer feed mass fractions of $w_{3,\mathrm{F}} \approx 2.6 \cdot 10^{-2}\,\mathrm{kg_3\,kg_{tot}^{-1}}$. Assuming a molar mass of $M_3 \approx 200\,000\,\mathrm{kg\,kmol^{-1}}$ and an equimolar mixture of the volatile components, the according polymer mass fraction is $x_{3,\mathrm{F}} \approx 1.46 \cdot 10^{-5}\,\mathrm{kmol_3\,kmol_{tot}^{-1}}$. Therefore, the optimization problems are:

$$\begin{aligned}
\min \quad & \frac{x_{1,\mathrm{D}}\,M_1 + (1 - x_{1,\mathrm{D}})\,M_2}{x_{1,\mathrm{F}}\,M_1 + x_{2,\mathrm{F}}\,M_2 + x_{3,\mathrm{F}}\,M_3} \\
\text{s.t.} \quad & 0 \le x_{1,\mathrm{D}} \le 1, \\
& 0 \le x_{1,\mathrm{F}} \le 1, \\
& 0 \le x_{2,\mathrm{F}} \le 1, \\
& 0 \le x_{3,\mathrm{F}} \le 1.46 \cdot 10^{-5}, \\
& x_{1,\mathrm{F}} + x_{2,\mathrm{F}} + x_{3,\mathrm{F}} = 1
\end{aligned} \tag{A.2}$$

$$\begin{aligned}
\max \quad & \frac{x_{1,\mathrm{D}}\,M_1 + (1 - x_{1,\mathrm{D}})\,M_2}{x_{1,\mathrm{F}}\,M_1 + x_{2,\mathrm{F}}\,M_2 + x_{3,\mathrm{F}}\,M_3} \\
\text{s.t.} \quad & 0 \le x_{1,\mathrm{D}} \le 1, \\
& 0 \le x_{1,\mathrm{F}} \le 1, \\
& 0 \le x_{2,\mathrm{F}} \le 1, \\
& 0 \le x_{3,\mathrm{F}} \le 1.46 \cdot 10^{-5}, \\
& x_{1,\mathrm{F}} + x_{2,\mathrm{F}} + x_{3,\mathrm{F}} = 1
\end{aligned} \tag{A.3}$$

The optimization problems defined in equations (A.2) and (A.3) were implemented in *Julia* (Bezanson et al., 2017) using the *JuMP* (Lubin et al., 2023) modeling language and solved with the optimizer *Ipopt* (Wächter and Biegler, 2006). Obtained results are summarized in table A.10. The corresponding code is given in listing A.2.

Table A.10.: Molar mass ratio $M_\mathrm{D}\,M_\mathrm{F}^{-1}$ as factor of proportionality between stream ratios $\dot{F}\,\dot{D}^{-1}$ and $\dot{m}_\mathrm{F}\,\dot{m}_\mathrm{D}^{-1}$ for ternary mixture CB/EB/PBD

	unit	minimum	maximum
$M_\mathrm{D}\,M_\mathrm{F}^{-1}$	-	0.92	1.06
at $x_{1,\mathrm{D}}$	$\mathrm{kmol_1\,kmol_{tot}^{-1}}$	0.00	1.00
at $x_{1,\mathrm{F}}$	$\mathrm{kmol_1\,kmol_{tot}^{-1}}$	0.9993	0.00
at $x_{2,\mathrm{F}}$	$\mathrm{kmol_2\,kmol_{tot}^{-1}}$	$7.08 \cdot 10^{-4}$	1.00
at $x_{3,\mathrm{F}}$	$\mathrm{kmol_3\,kmol_{tot}^{-1}}$	$1.46 \cdot 10^{-5}$	0.00

In contrast to the experiments with the binary mixture CB/EB, an asymmetric deviation is obtained for CB/EB/PBD. While the maximum deviation of $+6\,\%$ remains the same, a lower limit of $-8\,\%$ is obtained due to the influence of the polymer. However, as discussed in section 3.3.3.1, smaller deviations should typically be obtained during experimental investigations, since the molar fractions x_i substantially differ from $x_i = 0\,\mathrm{kmol_1\,kmol_{tot}^{-1}}$ or $x_i = 1\,\mathrm{kmol_1\,kmol_{tot}^{-1}}$.

Listing A.2: Non-linear optimization problem to estimate deviation in stream ratio for ternary mixture CB/EB/PBD

```
using JuMP
using Ipopt

model = Model(Ipopt.Optimizer)

set_attribute(model, "max_cpu_time", 60.0)
set_attribute(model, "print_level", 0)

@NLparameter(model, M_1 == 112.56)
@NLparameter(model, M_2 == 106.17)
@NLparameter(model, M_3 == 200000)

@variable(model, 0 <= x_1D <= 1)
@variable(model, 0 <= x_1F <= 1)
@variable(model, 0 <= x_2F <= 1)
@variable(model, 0 <= x_3F <= 1.46e-5)

@NLconstraint(model, x_1F + x_2F + x_3F == 1)

# (un)comment according line to solve 'Min' or 'Max' optimization problem
@NLobjective(model, Min, ( x_1D * M_1 + (1-x_1D) * M_2 ) / ( x_1F * M_1 + x_2F * M_2 + x_3F * M_3 ) )
@NLobjective(model, Max, ( x_1D * M_1 + (1-x_1D) * M_2 ) / ( x_1F * M_1 + x_2F * M_2 + x_3F * M_3 ) )

optimize!(model)

```

```
println(model)

println("objective value: ", objective_value(model))
println("x_1D: ", value(x_1D))
println("x_1F: ", value(x_1F))
println("x_2F: ", value(x_2F))
println("x_3F: ", value(x_3F))
```

A.7. Identifying Steady-State Operation

As discussed in section 3.3.3.2, steady-state plant operation was identified using the inline density measurement of the feed mixture (sensor D101) which allowed to reduce the number of drawn liquid samples considerably. The suitability of this approach was tested for three different feed mass flows of $4\,\mathrm{kg\,h^{-1}}$, $9\,\mathrm{kg\,h^{-1}}$ and $14\,\mathrm{kg\,h^{-1}}$ during the first plant experiments in which liquid samples were taken from the feedstock tank during plant start-up. Sample composition was determined as described in section 3.4 and compared to the readings from sensor D101. The obtained trends are shown in figure A.1.

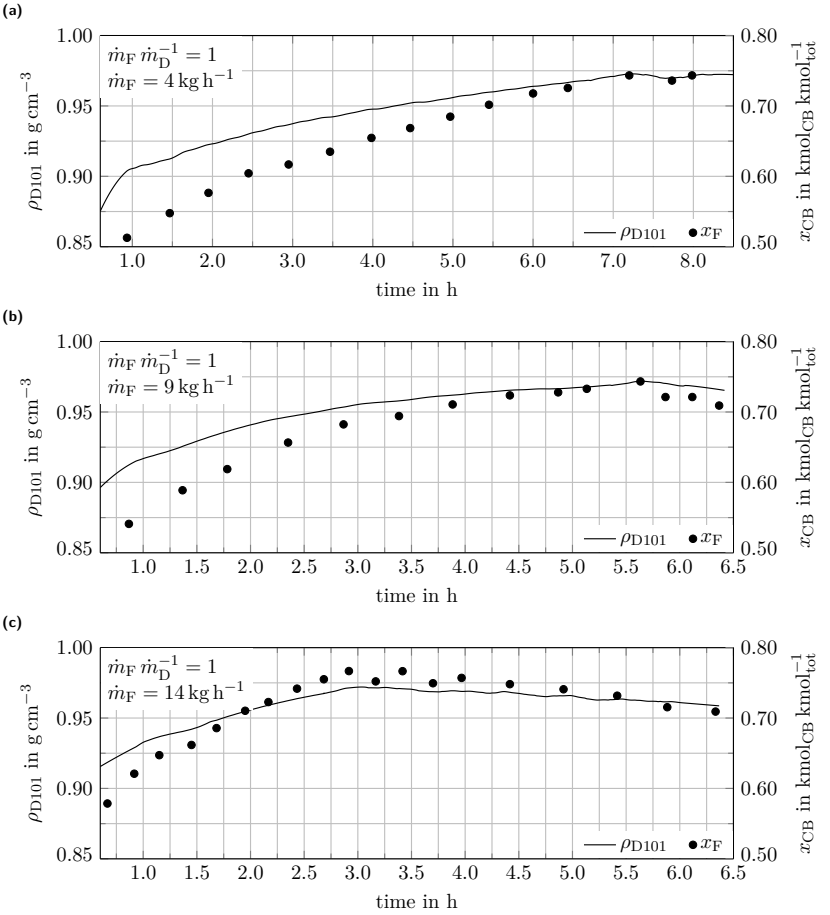

Figure A.1.: Identifying steady-state plant operation using inline feed density measurements and offline sample analyses; (a): low feed mass flow, steady state was reached around 7 h after plant start-up; (b): medium feed mass flow, steady state was reached around 5.5 h after plant start-up; (c): high feed mass flow, steady state was reached around 4.5 h after plant start-up; data records were arithmetically averaged every minute and smoothed with a Savitzky-Golay filter using a window size of 42 data points and a second-order filter polynomial, error bars are omitted as the associated uncertainties seem negligible, see tables D.5 and D.6 for uncertainties

A.8. Relations between Stream and Column Load Ratios

As mentioned in section 4.1.2, plant operation can be fully described with any liquid-vapor ratio, such as $\dot{m}_\mathrm{F}\,\dot{m}_\mathrm{D}^{-1}$, $\dot{F}\,\dot{D}^{-1}$ or $w_\mathrm{L}\,f_\mathrm{G}^{-1}$, and any liquid or vapor column load. Since the molar stream ratio $\dot{F}\,\dot{D}^{-1}$ represents the slope of the operating line for the McCabe-Thiele stage constructions, see equation (3.1), it is used throughout data evaluation and discussion. However, to illustrate the equivalence of the aforementioned ratios, corresponding relations are derived in this section.

The relation between the molar stream ratio $\dot{F}\,\dot{D}^{-1}$ and the stream ratio $\dot{m}_\mathrm{F}\,\dot{m}_\mathrm{D}^{-1}$ was introduced in equation (3.2c):

$$\frac{\dot{F}}{\dot{D}} = \frac{\dot{m}_\mathrm{F}}{\dot{m}_\mathrm{D}}\,\frac{M_\mathrm{D}}{M_\mathrm{F}} \tag{3.2c}$$

The relation between $\dot{m}_\mathrm{F}\,\dot{m}_\mathrm{D}^{-1}$ and $\dot{F}\,\dot{D}^{-1}$ given in equation (3.2c) is illustrated in figure A.2.

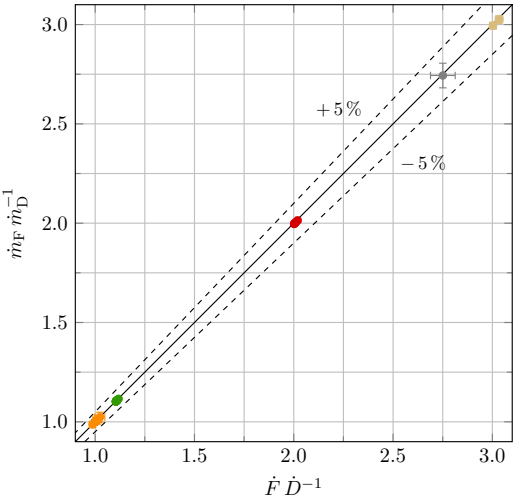

- total reflux, $\dot{F}\,\dot{D}^{-1} = 1.0000(14)$
- partial reflux, $\dot{F}\,\dot{D}^{-1} = 1.005(25)$
- partial reflux, $\dot{F}\,\dot{D}^{-1} = 1.108(12)$
- partial reflux, $\dot{F}\,\dot{D}^{-1} = 2.008(11)$
- partial reflux, $\dot{F}\,\dot{D}^{-1} = 2.751(62)$
- partial reflux, $\dot{F}\,\dot{D}^{-1} = 3.018(19)$

Figure A.2.: Relation between stream ratio $\dot{m}_\mathrm{F}\,\dot{m}_\mathrm{D}^{-1}$ and molar stream ratio $\dot{F}\,\dot{D}^{-1}$, indicated uncertainties are combined standard uncertainties $u_\mathrm{c}(\cdot)$

The liquid load w_L is recalled from equation (2.19). Substituting the liquid volumetric flow rate results in:

$$w_L \underset{(2.19)}{=} \frac{\dot{V}_L}{A_{col}} = \frac{\dot{m}_L}{\rho_L A_{col}} \tag{A.4}$$

Analogously, the f-factor f_G is expressed as:

$$f_G \underset{(2.18)}{=} u_{G,s} \cdot \rho_G^{0.5} = \frac{\dot{m}_G}{\rho_G A_{col}} \cdot \rho_G^{0.5} = \frac{\dot{m}_G}{\rho_G^{0.5} A_{col}} \tag{A.5}$$

Combining $\dot{m}_L = \dot{m}_F$ and $\dot{m}_G = \dot{m}_D$ with equations (A.4) and (A.5) allows deriving:

$$\frac{w_L}{f_G} = \frac{\dot{m}_F}{\dot{m}_D} \frac{\rho_G^{0.5}}{\rho_L} \underset{(3.2c)}{=} \frac{\dot{F}}{\dot{D}} \frac{M_F}{M_D} \frac{\rho_G^{0.5}}{\rho_L} \tag{A.6}$$

The relation between $w_L f_G^{-1}$ and $\dot{F}\,\dot{D}^{-1}$ is illustrated in figure A.3.

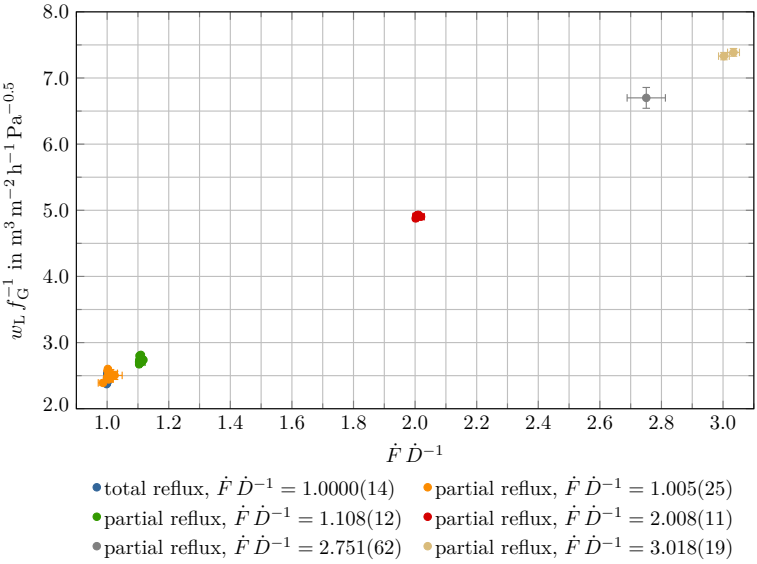

Figure A.3.: Relation between column load ratio $w_L\, f_G^{-1}$ and molar stream ratio $\dot{F}\,\dot{D}^{-1}$, indicated uncertainties are combined standard uncertainties $u_c(\cdot)$

The required molar masses M_i are estimated according to appendix C.2. To calculate the mixture densities, mid-bed conditions are used. The mid-bed temperature T_{mb} is defined in equation (3.10c). The liquid density ρ_L is calculated as shown in appendix C.3.2 using the mid-bed liquid molar fraction x_{mb} from equation (3.10a). Similarly, the mid-bed vapor

molar fraction y_{mb}, see equation (3.10b), is used to estimate the gas density ρ_{G} according to appendix C.3.3.

B. Chemicals

Chlorobenzene and ethylbenzene were supplied by Acros Organics, Geel/Belgium, and used without any further purification. For each lot, a certificate of analysis was retrieved from the supplier, see (Acros Organics, 2022). The purities of the chemicals used for the experimental investigations are listed in table B.1.

Table B.1.: Chemicals used for separation performance experiments, purities as per certificate of analysis (gas chromatography), water content (coulometric) only specified for ethylbenzene

substance	product code	lot number	purity in %	water content in %
chlorobenzene	146410250	A0406480	99.9	n/a
		A0396779	99.9	n/a
		A0412581	99.9	n/a
ethylbenzene	118080251	A0402315	99.9	0.0028
		A0417984	99.91	0.0025
		A0415069	99.92	0.004
		A0424549	99.91	0.0025

As potential impurities are not specified in the certificates of analysis, resulting affects on physical properties as well as sample analysis and experiment evaluation cannot be assessed reliably. Therefore, potential impurities were neglected, and the chemicals were assumed to be pure substances.

In addition to the chemicals used for the separation performance experiments, the density meter used for sample analysis was checked with toluene and water according to the manufacturer's recommendations, see appendix D.2.2. The respective chemicals are summarized in table B.2.

Table B.2.: Chemicals used to check density meter

substance	supplier	product code	lot number	purity in %
toluene	Fisher Scientific [a]	T/2306/17	2180112	99.98
ultrapure water	*in-house*	-	-	n/a
ultrapure water (reference)	Anton Paar [b]	96044	7487	n/a

[a] Fisher Scientific, Loughborough/UK

[b] Anton Paar Germany, Ostfildern/Germany

C. Pure Component and Mixture Properties

C.1. Tabulated Properties

The physical properties of the pure components chlorobenzene and ethylbenzene used for the calculations in this work are summarized in table C.1.

Table C.1.: Physical properties of chlorobenzene and ethylbenzene

property	unit	chlorobenzene	ethylbenzene	remark
M_i	$\mathrm{kg\,kmol^{-1}}$	112.56 [a]	106.17 [a]	
$\Delta h_{\mathrm{vap},i}$	$\mathrm{kJ\,mol^{-1}}$	40.97 [b]	42.24 [c]	at 25 °C
$\rho_{\mathrm{L},i}$	$\mathrm{g\,cm^{-3}}$	1.1058 [b]	0.867 [c]	at 20 °C
	$\mathrm{kg\,m^{-3}}$	1106.4 [d]	866.9 [d]	at 20 °C
$\vartheta_{\mathrm{boil,n},i}$	°C	131.6 [b]	136.2 [c]	at 1.013 25 bar(a)

[a] (Ottenbacher et al., 2011)

[b] (National Center for Biotechnology Information, 2021a)

[c] (National Center for Biotechnology Information, 2021b)

[d] own measurements

C.2. Molar Mass

The molar mass of a mixture M_{mix} is calculated based the (liquid) molar fractions x_i and the molar mass M_i of mixture component i:

$$M_{\mathrm{mix}} = \sum x_i \cdot M_i \underset{\substack{\text{binary}\\\text{mixture}}}{=} x_1 \cdot M_1 + x_2 \cdot M_2 = x_1 \cdot M_1 + (1 - x_1) \cdot M_2 \tag{C.1}$$

The molar masses of chlorobenzene and ethylbenzene are given in table C.1. Uncertainty quantification is provided in appendix D.2.3.

C.3. Density

C.3.1. Calibration Curve for Sample Analysis

To quantify the composition of a given liquid mixture sample, a density calibration curve for the binary mixture CB/EB was determined using a third-order polynomial. Compositions of prepared samples are represented by liquid mass fractions w_{CB} and the resulting molar fractions x_{CB} according to equation (C.2). Required molar masses, M_{CB} and M_{EB}, can be found in table C.1.

$$w_{\mathrm{CB}} = \frac{m_{\mathrm{CB}}}{m_{\mathrm{CB}} + m_{\mathrm{EB}}} \tag{C.2a}$$

$$x_{\mathrm{CB}} = \frac{w_{\mathrm{CB}} \cdot M_{\mathrm{CB}}^{-1}}{w_{\mathrm{CB}} \cdot M_{\mathrm{CB}}^{-1} + (1 - w_{\mathrm{CB}}) \cdot M_{\mathrm{EB}}^{-1}} \tag{C.2b}$$

Mass and molar fractions, obtained density readings and corresponding arithmetic averages are given in table C.3; uncertainty analysis is performed in appendix D.2.2. The density calibration curve estimated from the liquid density measurements is shown in figure C.1.

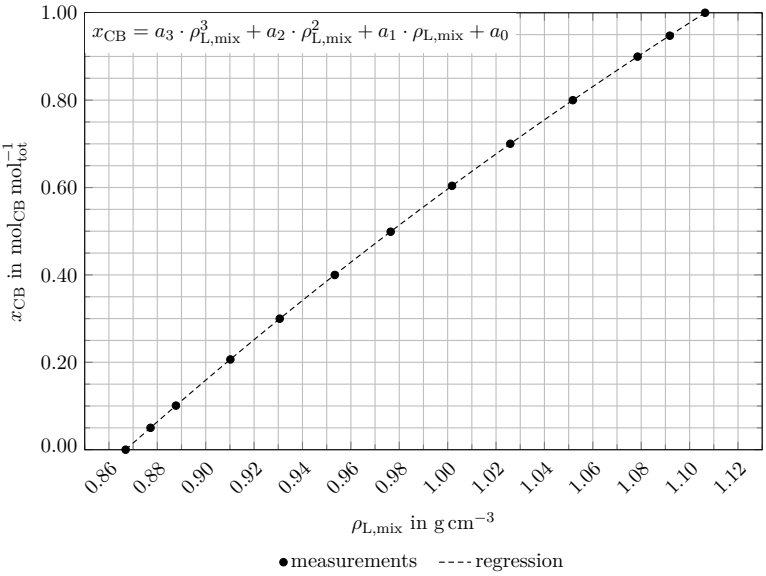

Figure C.1.: Density calibration curve for binary mixture CB/EB at $\vartheta = 20.000(22)\,^{\circ}\mathrm{C}$, data given in table C.3, error bars are omitted as they are smaller than the marker size

Although associated uncertainties are very small and thus, not indicated with error bars, data

are fit using an *orthogonal distance regression (ODR)*[1], which allows considering uncertainties in both dependent and independent variables. To evaluate the goodness of fit, the coefficient of determination R^2 and the absolute deviation ε are calculated according to equation (C.3). The regression parameters and the respective values for the goodness of fit are summarized in table C.2.

$$R^2 = 1 - \frac{\mathrm{Var}(x_{\mathrm{CB,exp}} - x_{\mathrm{CB,pred}})}{\mathrm{Var}(x_{\mathrm{CB,exp}})} \tag{C.3a}$$

$$\varepsilon = \pm\,|x_{\mathrm{CB,exp}} - x_{\mathrm{CB,pred}}| \tag{C.3b}$$

Table C.2.: Regression results for density calibration curve $x_{\mathrm{CB}} = a_3 \cdot \rho_{\mathrm{L,mix}}^3 + a_2 \cdot \rho_{\mathrm{L,mix}}^2 + a_1 \cdot \rho_{\mathrm{L,mix}} + a_0$

parameter	value	unit	remark
a_3	1.845 84		regression parameter
a_2	−8.379 34		regression parameter
a_1	15.292 95		regression parameter
a_0	−8.162 91		regression parameter
R^2	0.9999		coefficient of determination
$\varepsilon_{\mathrm{max}}$	±0.000 36(36)	$\mathrm{mol_{CB}\,mol_{tot}^{-1}}$	maximum absolute deviation
$\varepsilon_{\mathrm{min}}$	±0.000 03(24)	$\mathrm{mol_{CB}\,mol_{tot}^{-1}}$	minimum absolute deviation
$\bar{\varepsilon}$	±0.000 15(21)	$\mathrm{mol_{CB}\,mol_{tot}^{-1}}$	mean absolute deviation

[1]Data were fit with `scipy.odr`, which uses an adapted Levenberg-Marquardt least squares algorithm; see (Boggs and Rogers, 1990; Virtanen et al., 2020).

Table C.3.: Liquid mixture densities for binary mixture CB/EB, m_i: mass of component i in prepared sample, w_i: mass fraction of component i, x_i: molar fraction of component i, $\rho_{\mathrm{L,mix}}$: measured liquid density, $\overline{\rho_{\mathrm{L,mix}}}$: arithmetic average of measured liquid densities

no.	m_{CB}	m_{EB}	w_{CB}	x_{CB}	$\rho_{\mathrm{L,mix}}$	$\overline{\rho_{\mathrm{L,mix}}}$
	g	g	$\mathrm{g_{CB}\,g_{tot}^{-1}}$	$\mathrm{mol_{CB}\,mol_{tot}^{-1}}$	$\mathrm{g\,cm^{-3}}$	$\mathrm{g\,cm^{-3}}$
1.1	0.0000(1)	25.0000(1)	0.000 000(5)	0.000 000(5)	0.866 90(6)	
1.2	⋮	⋮	⋮	⋮	⋮	
1.3	⋮	⋮	⋮	⋮	⋮	
1.4	⋮	⋮	⋮	⋮	⋮	0.866 90(6)
2.1	1.3245(1)	23.6951(1)	0.052 938(5)	0.050 084(5)	0.877 20(6)	
2.2	⋮	⋮	⋮	⋮	⋮	
2.3	⋮	⋮	⋮	⋮	⋮	
2.4	⋮	⋮	⋮	⋮	⋮	0.877 20(6)
3.1	2.6603(1)	22.3599(1)	0.106 326(5)	0.100 899(5)	0.887 70(6)	
3.2	⋮	⋮	⋮	⋮	⋮	
3.3	⋮	⋮	⋮	⋮	⋮	
3.4	⋮	⋮	⋮	⋮	⋮	0.887 70(6)
4.1	5.4605(1)	19.7915(1)	0.216 240(4)	0.206 499(4)	0.910 20(6)	
4.2	⋮	⋮	⋮	⋮	⋮	
4.3	⋮	⋮	⋮	⋮	⋮	
4.4	⋮	⋮	⋮	⋮	⋮	0.910 20(6)

Table C.3.: Liquid mixture densities for binary mixture CB/EB, m_i: mass of component i in prepared sample, w_i: mass fraction of component i, x_i: molar fraction of component i, $\rho_{\mathrm{L,mix}}$: measured liquid density, $\overline{\rho_{\mathrm{L,mix}}}$: arithmetic average of measured liquid densities (continued)

no.	m_{CB}	m_{EB}	w_{CB}	x_{CB}	$\rho_{\mathrm{L,mix}}$	$\overline{\rho_{\mathrm{L,mix}}}$
	g	g	$\mathrm{g_{CB}\,g_{tot}^{-1}}$	$\mathrm{mol_{CB}\,mol_{tot}^{-1}}$	$\mathrm{g\,cm^{-3}}$	$\mathrm{g\,cm^{-3}}$
5.1	7.8158(1)	17.2107(1)	0.312 301(4)	0.299 889(4)	0.930 60(6)	
5.2	⋮	⋮	⋮	⋮	⋮	
5.3	⋮	⋮	⋮	⋮	⋮	
5.4	⋮	⋮	⋮	⋮	⋮	0.930 60(6)
6.1	10.3484(1)	14.6499(1)	0.413 964(4)	0.399 860(4)	0.953 30(6)	
6.2	⋮	⋮	⋮	⋮	0.953 40(6)	
6.3	⋮	⋮	⋮	⋮	0.953 30(6)	
6.4	⋮	⋮	⋮	⋮	0.953 40(6)	0.953 35(8)
7.1	12.8755(1)	12.2003(1)	0.513 463(4)	0.498 855(4)	0.976 50(6)	
7.2	⋮	⋮	⋮	⋮	0.976 10(6)	
7.3	⋮	⋮	⋮	⋮	0.975 90(6)	
7.4	⋮	⋮	⋮	⋮	0.977 30(6)	0.9765(6)
8.1	15.6023(1)	9.6533(1)	0.617 776(4)	0.603 884(4)	1.001 80(6)	
8.2	⋮	⋮	⋮	⋮	⋮	
8.3	⋮	⋮	⋮	⋮	⋮	
8.4	⋮	⋮	⋮	⋮	⋮	1.001 80(6)

Table C.3.: Liquid mixture densities for binary mixture CB/EB, m_i: mass of component i in prepared sample, w_i: mass fraction of component i, x_i: molar fraction of component i, $\rho_{\mathrm{L,mix}}$: measured liquid density, $\overline{\rho_{\mathrm{L,mix}}}$: arithmetic average of measured liquid densities (continued)

no.	m_{CB} / g	m_{EB} / g	w_{CB} / $\mathrm{g_{CB}\,g_{tot}^{-1}}$	x_{CB} / $\mathrm{mol_{CB}\,mol_{tot}^{-1}}$	$\rho_{\mathrm{L,mix}}$ / $\mathrm{g\,cm^{-3}}$	$\overline{\rho_{\mathrm{L,mix}}}$ / $\mathrm{g\,cm^{-3}}$
9.1	17.8421(1)	7.2063(1)	0.712 305(4)	0.700 181(4)	1.025 90(6)	
9.2	⋮	⋮	⋮	⋮	⋮	
9.3	⋮	⋮	⋮	⋮	⋮	
9.4	⋮	⋮	⋮	⋮	⋮	1.025 90(6)
10.1	20.3358(1)	4.7980(1)	0.809 102(4)	0.799 911(5)	1.051 70(6)	
10.2	⋮	⋮	⋮	⋮	⋮	
10.3	⋮	⋮	⋮	⋮	⋮	
10.4	⋮	⋮	⋮	⋮	1.051 80(6)	1.051 73(8)
11.1	22.6524(1)	2.3850(1)	0.904 743(5)	0.899 585(5)	1.078 50(6)	
11.2	⋮	⋮	⋮	⋮	⋮	
11.3	⋮	⋮	⋮	⋮	⋮	
11.4	⋮	⋮	⋮	⋮	⋮	1.078 50(6)
12.1	23.8181(1)	1.2444(1)	0.950 348(5)	0.947 517(5)	1.091 80(6)	
12.2	⋮	⋮	⋮	⋮	⋮	
12.3	⋮	⋮	⋮	⋮	⋮	
12.4	⋮	⋮	⋮	⋮	⋮	1.091 80(6)

Table C.3.: Liquid mixture densities for binary mixture CB/EB, m_i: mass of component i in prepared sample, w_i: mass fraction of component i, x_i: molar fraction of component i, $\rho_{\mathrm{L,mix}}$: measured liquid density, $\overline{\rho_{\mathrm{L,mix}}}$: arithmetic average of measured liquid densities (continued)

no.	m_{CB}	m_{EB}	w_{CB}	x_{CB}	$\rho_{\mathrm{L,mix}}$	$\overline{\rho_{\mathrm{L,mix}}}$
	g	g	$\mathrm{g_{CB}\,g_{tot}^{-1}}$	$\mathrm{mol_{CB}\,mol_{tot}^{-1}}$	$\mathrm{g\,cm^{-3}}$	$\mathrm{g\,cm^{-3}}$
13.1	25.0000(1)	0.0000(1)	1.000 000(5)	1.000 000(6)	1.106 40(6)	
13.2	⋮	⋮	⋮	⋮	⋮	
13.3	⋮	⋮	⋮	⋮	⋮	
13.4	⋮	⋮	⋮	⋮	⋮	1.106 40(6)

C.3.2. Liquid

The liquid mixture density $\rho_{\mathrm{L,mix}}$ is calculated based on the mixing rule given in equation (C.4) as described by (Ottenbacher et al., 2011). For this, the liquid density of the pure components $\rho_{\mathrm{L},i}$, the molar masses M_i and the molar fractions representing the mixture composition $x_{\mathrm{L},i}$ are used. A potentially occurring excess volume V^{E} is not taken into account as it is considered negligible, see appendix C.9.

$$\rho_{\mathrm{L,mix}} = \left(\sum_i x_i \cdot M_i\right)\left(\sum_i \frac{x_i \cdot M_i}{\rho_{\mathrm{L},i}}\right)^{-1} \tag{C.4}$$

Based on (Ottenbacher et al., 2011), the temperature dependence of the pure substance density $\rho_{\mathrm{L},i}$ is estimated by:

$$\frac{\rho_{\mathrm{L},i}}{\mathrm{kg\,m^{-3}}} = \frac{a_i}{b_i^{1+\left(1-\frac{T}{c_i}\right)^{d_i}}} \cdot M_i \tag{C.5}$$

While the required molar masses M_i of the pure mixture components are given in table C.1, the parameters a_i, b_i, c_i and d_i can be found in table C.4.

Table C.4.: Parameters to estimate liquid densities of chlorobenzene and ethylbenzene (Ottenbacher et al., 2011)

parameter	a_i	b_i	c_i	d_i
chlorobenzene	0.836 842 794	0.262 187 917	632.35	0.28
ethylbenzene	0.687 265 03	0.259 576 28	616.988 54	0.28

C.3.3. Vapor

The vapor or gas phase density ρ_{G} is approximated using the ideal gas law as shown in equation (C.6). The average molar mass of the gas phase M_{G} is calculated with the mixing rule already defined in equation (C.1). Furthermore, pressure p, temperature T as well as the ideal gas constant R ($R = 8.314\,\mathrm{kJ\,kmol^{-1}\,K^{-1}}$) are used.

$$\rho_{\mathrm{G}} = \frac{M_{\mathrm{G}} \cdot p}{R \cdot T} \tag{C.6}$$

C.4. Heat Capacity

The specific heat capacities of the pure liquid substances $c_{\mathrm{p,L},i}$ are calculated based on equation (C.7) as well as the parameters a_i, b_i, c_i and d_i as proposed by (Ottenbacher et al., 2011).

Relevant values are tabulated in table C.5; Molar masses M_i are given in table C.1.

$$\frac{c_{\mathrm{p,L},i}}{\mathrm{J\,kg^{-1}\,K^{-1}}} = \frac{a_i + b_i \cdot T + c_i \cdot T^2 + d_i \cdot T^3 + e \cdot T^4}{M_i} \tag{C.7}$$

Table C.5.: Parameters to estimate heat capacities of chlorobenzene and ethylbenzene (Ottenbacher et al., 2011)

parameter	a_i	b_i	c_i	d_i	e_i
chlorobenzene	105 510.79	186.739 52	−0.117 412 271	0	0
ethylbenzene	81 337.50	359.996 918	−0.031 926 29	0	0

Using the specific heat capacities $c_{\mathrm{p,L},i}$ and molar masses of the pure substances M_i, the specific heat capacity of a mixture with known molar fractions x_i is estimated using the mixing rule given in equation (C.8) as described by (Ottenbacher et al., 2011). The molar mass of the mixture M_{mix} is calculated with equation (C.1).

$$c_{\mathrm{p,L,mix}} = \frac{\sum_i x_i \cdot c_{\mathrm{p,L},i} \cdot M_i}{M_{\mathrm{mix}}} \tag{C.8}$$

C.5. Enthalpy of Vaporization

The estimation of enthalpy of vaporization for both chlorobenzene and ethylbenzene is based on (Ottenbacher et al., 2011). Required parameter sets a_i, b_i, c_i, d_i and e_i listed in table C.6 are applied to equation (C.9). The molar masses of the pure components M_i are given in table C.1.

$$\frac{\Delta h_{\mathrm{vap},i}}{\mathrm{J\,kg^{-1}}} = \frac{a_i \cdot \left(1 - \frac{T}{f_i}\right)^{b_i + c_i \cdot \frac{T}{f_i} + d_i \cdot \left(\frac{T}{f_i}\right)^2 + e_i \cdot \left(\frac{T}{f_i}\right)^3}}{M_i} \tag{C.9}$$

Table C.6.: Parameters to estimate enthalpies of vaporization of chlorobenzene and ethylbenzene (Ottenbacher et al., 2011)

parameter	a_i	b_i	c_i	d_i	e_i	f_i [a]
chlorobenzene	49 363 572	0.245 007 304	0.119 781 836	0	0	632.35
ethylbenzene	65 095 179	1.032 892 17	−0.952 264 5	0.347 883 14	0	617.1

[a] $f_i = T_{\mathrm{c},i}$ ($T_{\mathrm{c},i}$: critical temperature of component i)

With known enthalpies of vaporization $\Delta h_{\mathrm{vap},i}$ and known liquid molar fractions x_i, the corresponding mixture property is determined using equation (C.10) as proposed by (Ottenbacher

et al., 2011). To calculate the mixture molar mass M_{mix}, equation (C.1) is used.

$$\Delta h_{\mathrm{vap,mix}} = \frac{\sum_i x_i \cdot \Delta h_{\mathrm{vap},i} \cdot M_i}{M_{\mathrm{mix}}} \tag{C.10}$$

C.6. Dynamic Viscosity

C.6.1. Liquid

Pure substance liquid viscosities $\eta_{\mathrm{L},i}$ are calculated using equation (C.11). Required parameters a_i, b_i, c_i, d_i and e_i by (Ottenbacher et al., 2011) are summarized in table C.7. T denotes the temperature.

$$\frac{\eta_{\mathrm{L},i}}{\mathrm{Pa\,s}} = \exp\left(a_i + \frac{b_i}{T} + c_i \cdot \ln T + d_i \cdot T^{e_i}\right) \tag{C.11}$$

Table C.7.: Parameters to estimate liquid viscosities of chlorobenzene and ethylbenzene (Ottenbacher et al., 2011)

parameter	a_i	b_i	c_i	d_i	e_i
chlorobenzene	0.157 72	540.5	−1.6075	0	0
ethylbenzene	−120.914 387	4167.044 39	18.986 634 8	$-2.8880 \cdot 10^{-2}$	1

The mixture liquid viscosity $\eta_{\mathrm{L,mix}}$ is estimated according to equation (C.12), which is based on a mixing rule presented by (Ottenbacher et al., 2011). x_i denotes the liquid molar fraction of mixture component i.

$$\eta_{\mathrm{L,mix}} = \exp\left(\sum_i x_i \cdot \ln \eta_{\mathrm{L},i}\right) \tag{C.12}$$

C.6.2. Vapor

Based on the approach proposed by (Ottenbacher et al., 2011), vapor or gas viscosities of the pure substances $\eta_{\mathrm{G},i}$ are estimated according to equation (C.13). Required parameters a_i, b_i, c_i and d_i are given in table C.8. T denotes the temperature.

$$\frac{\eta_{\mathrm{G},i}}{\mathrm{Pa\,s}} = \frac{a_i \cdot T^{b_i}}{1 + c_i \cdot T^{-1} + d_i \cdot T^{-2}} \tag{C.13}$$

Table C.8.: Parameters to estimate vapor viscosities of chlorobenzene and ethylbenzene (Ottenbacher et al., 2011)

parameter	a_i	b_i	c_i	d_i
chlorobenzene	$1.065 \cdot 10^{-7}$	0.7942	94.7	0
ethylbenzene	$4.2231 \cdot 10^{-7}$	0.581 54	239.21	0

Using the viscosities of the pure components $\eta_{\mathrm{G},i}$, the vapor viscosity $\eta_{\mathrm{G,mix}}$ of the binary mixture with known composition, represented by the molar fractions y_1 and y_2, is calculated with equation (C.14) as proposed by (Ottenbacher et al., 2011). Molar masses of the pure components M_i can be found in table C.1.

$$\eta_{\mathrm{G,mix}} = \frac{y_1 \cdot \eta_{\mathrm{G},1}}{(y_1 + y_2 \cdot \Psi_{12})} + \frac{y_2 \cdot \eta_{\mathrm{G},2}}{y_1 \cdot \Psi_{21} + y_2} \tag{C.14a}$$

$$\Psi_{ij} = \left[1 + \left(\frac{\eta_{\mathrm{G},i}}{\eta_{\mathrm{G},j}}\right)^{0.5} \cdot \left(\frac{M_j}{M_i}\right)^{0.25}\right]^2 \cdot \left[8 \cdot \left(1 + \frac{M_i}{M_j}\right)\right]^{-0.5} \tag{C.14b}$$

$$i = \{1, 2\} \qquad j = \{1, 2\} \qquad i \neq j \tag{C.14c}$$

C.7. Surface Tension

As surface tension is only defined for liquids, no distinction between liquid and vapor is made. To calculate the surface tension of the pure liquids, equation (C.15) is used according to (Ottenbacher et al., 2011). Values for parameters a_i, b_i, c_i, d_i, e_i and f_i are given in table C.9. T denotes the substance temperature.

$$\frac{\sigma_{\mathrm{L},i}}{\mathrm{N\,m^{-1}}} = a_i \cdot \left(1 - \frac{T}{f_i}\right)^{b_i + c_i \cdot \frac{T}{f_i} + d_i \cdot \left(\frac{T}{f_i}\right)^2 + e_i \cdot \left(\frac{T}{f_i}\right)^3} \tag{C.15}$$

Table C.9.: Parameters to estimate surface tensions of chlorobenzene and ethylbenzene (Ottenbacher et al., 2011)

parameter	a_i	b_i	c_i	d_i	e_i	f_i [a]
chlorobenzene	0.0727	1.242	0	0	0	632.35
ethylbenzene	0.065 774 72	1.267 19	0	0	0	617.2

[a] $f_i = T_{\mathrm{c},i}$ ($T_{\mathrm{c},i}$: critical temperature of component i)

For a liquid mixture with known molar fractions x_i, the corresponding surface tension is estimated based on equation (C.16) as shown by (Ottenbacher et al., 2011). Required molar masses M_i of the pure substances are tabulated in table C.1. $\rho_{\mathrm{L},i}$ denotes the liquid density of

mixture component i and is calculated according to equation (C.5).

$$\frac{\sigma_{\mathrm{L,mix}}}{\mathrm{N\,m^{-1}}} = \left[\left(\sum_i x_i \cdot \frac{M_i^2}{\rho_{\mathrm{L},i}} \cdot \sigma_{\mathrm{L},i}^{0.25} \right) \cdot \left(\sum_i x_i \cdot \frac{M_i^2}{\rho_{\mathrm{L},i}} \right)^{-1} \right]^4 \tag{C.16}$$

C.8. Diffusion Coefficient

C.8.1. Liquid

Estimation of liquid diffusion coefficients is based on (Poling et al., 2001). In particular, the empirical approach proposed by (Wilke and Chang, 1955) is used to approximate mutual diffusion coefficients $D^{\circ}_{\mathrm{L},12}$ and $D^{\circ}_{\mathrm{L},21}$. To correct potential mixture effects, the *Vignes correlation*, see (Poling et al., 2001; Vignes, 1966), which shows good fits between calculated and experimental diffusion coefficients for ideal or nearly ideal mixtures (Dullien, 1971; Poling et al., 2001), is applied to obtain the corrected liquid diffusion coefficient $D_{\mathrm{L},12}$.

As the approach proposed by (Wilke and Chang, 1955), see equation (C.17), is based on an empirical correlation, required physical properties need to be provided in suitable units. Considering a binary mixture with components i and j ($i = \{1,2\}$; $j = \{1,2\}$; $i \neq j$), $V_{\mathrm{m},i}$ denotes the molar volume of component i in $\mathrm{cm^3\,mol^{-1}}$ at its normal boiling point $T_{\mathrm{boil,n},i}$ according to equation (C.18) ($T_{\mathrm{boil,n},i} = \vartheta_{\mathrm{boil,n},i} + 273.15\,\mathrm{K}$, for $\vartheta_{\mathrm{boil,n},i}$ see table C.1), the molar masses M_i and M_j in $\mathrm{g\,mol^{-1}}$ are given in table C.1. The viscosity η_j is in mPa s and calculated according to equation (C.11). Temperature T is in K. For the dimensionless association factors, $\phi_i = 1$ and $\phi_j = 1$ are assumed which is valid for unassociated solvents (Poling et al., 2001; Wilke and Chang, 1955) and should, therefore, be also applicable for chlorobenzene and ethylbenzene (Bradtmöller, 2017). Contrary to (Poling et al., 2001), a factor of 10^{-15} instead of 10^{-8} is used to ensure consistent units[2].

$$\frac{D^{\circ}_{\mathrm{L},ij}}{\mathrm{m^2\,s^{-1}}} = \frac{7.4 \cdot 10^{-15}\,(\phi\, M_j)^{0.5}\, T}{\eta_j\, V_{\mathrm{m},i}^{0.6}} \tag{C.17}$$

The molar volume $V_{\mathrm{m},i}$ of each mixture component depends on its molar mass M_i and density $\rho_{\mathrm{L},i}$. While molar masses are given in table C.1, densities $\rho_{\mathrm{L},i}$ are calculated with equation (C.5) using the normal boiling points also listed in the aforementioned table. A factor of 1000 is applied for conversion of units[3].

$$\frac{V_{\mathrm{m},i}}{\mathrm{cm^3\,mol}} = \frac{1000\, M_i}{\rho_{\mathrm{L},i}} \tag{C.18}$$

[2] A factor of 10^3 is used in the denominator to convert η_j from Pa s into mPa s. As the equation published by (Poling et al., 2001) gives D°_{ij} in $\mathrm{cm^2\,s^{-1}}$, an additional conversion factor of 10^{-4} is introduced to obtain $\mathrm{m^2\,s^{-1}}$. Considering both unit conversions and the factor of 10^{-8} in the equation presented by (Poling et al., 2001) results in an overall factor of 10^{-15}.

[3] As liquid densities $\rho_{\mathrm{L},i}$ obtained from equation (C.5) are given in $\mathrm{kg\,m^{-3}}$, a factor of 10^{-3} is needed in the denominator to convert into $\mathrm{g\,cm^{-3}}$.

With calculated mutual diffusion coefficients D_{12}° and D_{21}°, the Vignes correlation is used to correct for concentration effects as shown in equation (C.19). Mixture composition is considered based on the liquid molar fractions x_1 and x_2. The thermodynamic correction factor Ψ_{corr} is estimated using the NRTL model, see appendix C.11.

$$D_{\text{L},12} = \left[(D_{\text{L},12}^{\circ})^{x_2} \, (D_{\text{L},21}^{\circ})^{x_1} \right] \Psi_{\text{corr}} \tag{C.19a}$$

$$\Psi_{\text{corr}} = 1 - 2\,x_1\,x_2\,\frac{\tau_{12}\,G_{21}^2}{(x_1 + x_2\,G_{21})^3} + \frac{\tau_{21}\,G_{12}^2}{(x_2 + x_1\,G_{12})^3} \tag{C.19b}$$

C.8.2. Vapor

Vapor or gas phase diffusion coefficients are calculated using the method proposed by (Fuller et al., 1969; Fuller and Giddings, 1965; Fuller et al., 1966), see also (Poling et al., 2001):

$$\frac{D_{\text{G},12}}{\text{m}^2\,\text{s}^{-1}} = \frac{(0.00143\,T^{1.75})}{10\,p\,M_{12}^{0.5}\left(\Sigma_{\nu,1}^{\frac{1}{3}} + \Sigma_{\nu,2}^{\frac{1}{3}}\right)^2} \tag{C.20a}$$

$$M_{12} = \frac{2}{M_1^{-1} + M_2^{-1}} \tag{C.20b}$$

In contrast to the form published by (Poling et al., 2001), the factor of 10 in the denominator of equation (C.20a) is required to ensure consistent units[4]. Pressure p needs to be provided in mbar(a), temperature T in K. Molar masses M_1 and M_2 are listed in table C.1. Diffusion volumes $\Sigma_{\nu,1}$ and $\Sigma_{\nu,2}$ given in table C.10 were calculated using equation (C.21) and table C.11.

Table C.10.: Diffusion volumes of chlorobenzene and ethylbenzene, calculated according to equation (C.21) and table C.11

substance	chemical formula	ν_{C}	ν_{H}	ν_{Cl}	diffusion volume Σ_i
chlorobenzene	C_6H_5Cl	6	5	1	127.95
ethylbenzene	C_8H_{10}	8	10	0	150.3

$$\Sigma_{\nu,\text{i}} = \sum_j \nu_j \cdot \Sigma_j \tag{C.21}$$

[4] A factor of 10^{-3} is used in the denominator to convert p from mbar(a) into bar(a). As the equation published by (Poling et al., 2001) gives $D_{\text{G},ij}$ in $\text{cm}^2\,\text{s}^{-1}$, an additional conversion factor of 10^{-4} is introduced to obtain $\text{m}^2\,\text{s}^{-1}$. Considering both conversions results in an overall factor of 10 in the denominator.

Table C.11.: Diffusion volume increments of carbon, hydrogen and chlorine atoms (Poling et al., 2001)

atom	symbol	volume increment
carbon	C	15.9
hydrogen	H	2.31
chlorine	Cl	21.0

C.9. Excess Volume and Redlich-Kister Parameters

Although the excess volume of the binary mixture CB/EB is commonly not considered in separation performance measurements, see e.g. (Bradtmöller, 2017; Ottenbacher et al., 2011), the effect of neglecting this mixture property is rarely addressed. Therefore, the excess volume of CB/EB was investigated based on the density calibration measurements, see table C.3.

The excess volume V^{E} for each sample is calculated based on the arithmetically averaged mixture density for which a rearranged mixing rule was applied as shown in equation (C.22) (Mahajan and Mirgane, 2013; Stec et al., 2014). The required molar masses and pure component liquid densities are given in table C.1.

$$V^{\mathrm{E}} = \frac{x_{\mathrm{CB}} \cdot M_{\mathrm{CB}} + x_{\mathrm{EB}} \cdot M_{\mathrm{EB}}}{\rho_{\mathrm{L,mix}}} - \frac{x_{\mathrm{CB}} \cdot M_{\mathrm{CB}}}{\rho_{\mathrm{L,CB}}} - \frac{x_{\mathrm{EB}} \cdot M_{\mathrm{EB}}}{\rho_{\mathrm{L,EB}}} \tag{C.22}$$

As proposed by (Redlich and Kister, 1948a), a second-order expansion series is used to correlate calculated molar excess volumes to the composition of the liquid binary mixture sample (Gmehling et al., 2019):

$$V^{\mathrm{E}} = (1 - x_{\mathrm{CB}})\, x_{\mathrm{CB}} \cdot (A + B\,(2\,x_{\mathrm{CB}} - 1) + C\,(2\,x_{\mathrm{CB}} - 1)^2) \tag{C.23}$$

To determine the Redlich-Kister parameters A, B and C from equation (C.23) considering the uncertainties associated with the sample compositions and density readings, calculated excess volume V^{E} are fit using an *orthogonal distance regression (ODR)*[5]. The excess volume V^{E} for each sample composition and the corresponding prediction based on equation (C.23) are illustrated in figure C.2. The associated uncertainties are addressed in appendix D.2.4. To evaluate the goodness of fit, the coefficient of determination R^2 and the absolute deviation ε were calculated according to equation (C.24). Determined Redlich-Kister parameters and respective values for goodness of fit are summarized in table C.12.

$$R^2 = 1 - \frac{\mathrm{Var}(V^{\mathrm{E}}_{\mathrm{exp}} - V^{\mathrm{E}}_{\mathrm{pred}})}{\mathrm{Var}(V^{\mathrm{E}}_{\mathrm{exp}})} \tag{C.24a}$$

[5]Data were fit with `scipy.odr`, which uses an adapted Levenberg-Marquardt least squares algorithm; see (Boggs and Rogers, 1990; Virtanen et al., 2020).

$$\varepsilon = \pm\,|V^{\mathrm{E}}_{\mathrm{exp}} - V^{\mathrm{E}}_{\mathrm{pred}}| \tag{C.24b}$$

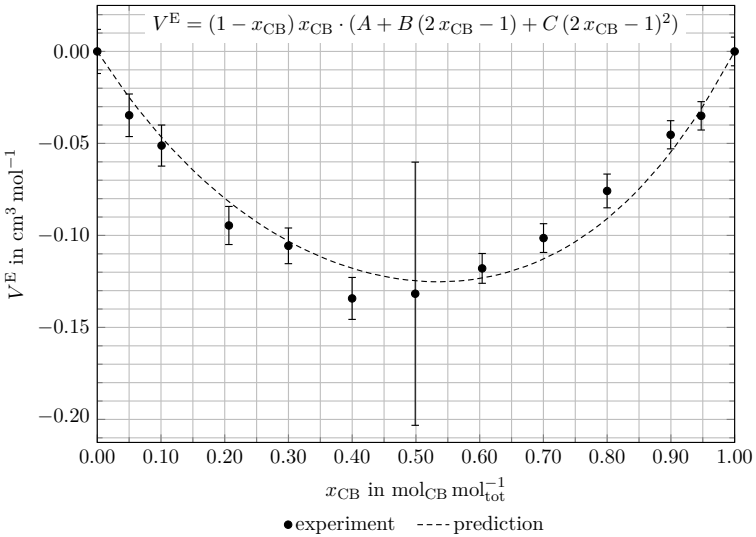

Figure C.2.: Excess volume V^{E} of binary mixture CB/EB in dependence of liquid molar fraction x_{CB}, sample compositions according to table C.3, error bars of sample composition omitted as they are smaller than the marker size, large error bar at $x_{\mathrm{CB}} = 0.5\,\mathrm{mol_{CB}\,mol_{tot}^{-1}}$ results from averaging density readings with deviations in the least significant digit

Table C.12.: Redlich-Kister parameters and goodness of fit for binary mixture CB/EB

parameter	value	unit	remark
A	−0.512 28	$\mathrm{cm^3\,mol^{-1}}$	Redlich-Kister parameter
B	−0.061 74	$\mathrm{cm^3\,mol^{-1}}$	Redlich-Kister parameter
C	−0.055 77	$\mathrm{cm^3\,mol^{-1}}$	Redlich-Kister parameter
R^2	0.9581	-	coefficient of determination
$\varepsilon_{\mathrm{max}}$	±0.0153(92)	$\mathrm{cm^3\,mol^{-1}}$	maximum absolute deviation
$\varepsilon_{\mathrm{min}}$	±0.000(12)	$\mathrm{cm^3\,mol^{-1}}$	minimum absolute deviation
$\overline{\varepsilon}$	±0.0076(61)	$\mathrm{cm^3\,mol^{-1}}$	mean absolute deviation

Since the Redlich-Kister parameters are known, the excess volume can be calculated for any mixture composition, see equation (C.23). Therefore, rearranging equation (C.22) for $\rho_{\mathrm{L,mix}}$

allows estimating the relative deviation δ between predicted liquid mixture densities $\rho_{\mathrm{L,pred}}$ and values obtained from the sample analyses $\rho_{\mathrm{L,exp}}$ according to equation (C.25). Obtained results are illustrated in figure C.3.

$$\delta = \frac{\rho_{\mathrm{L,pred}} - \rho_{\mathrm{L,exp}}}{\rho_{\mathrm{L,exp}}} \tag{C.25}$$

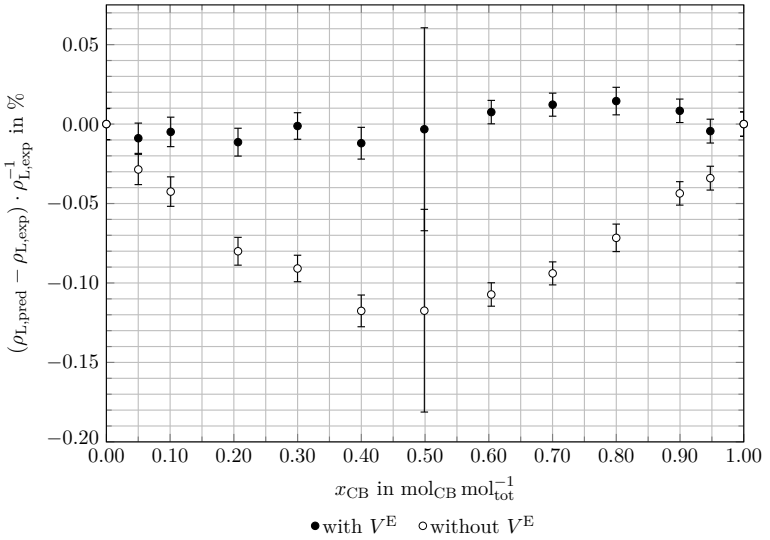

Figure C.3.: Relative deviations between experimental ($\rho_{\mathrm{L,exp}}$) and predicted ($\rho_{\mathrm{L,pred}}$) liquid densities of binary mixture CB/EB when considering or neglecting excess volume V^{E}

As shown in figure C.3, neglecting excess volume V^{E} results in negative relative deviations for all mixture compositions. As $\rho_{\mathrm{L,pred}} \leq \rho_{\mathrm{L,exp}}$, the mixture density is underestimated and a maximum relative deviation of around $\delta \approx -0.12\,\%$ is obtained. In contrast, considering the occurring excess volume reduces the relative deviation to $|\delta| \approx 0.014\,\%$. Although this is roughly equivalent to an order of magnitude, the overall effect of not considering the excess volume is negligible due to the small relative deviations.

C.10. Vapor Pressure

Many literature sources, e.g. (Liley et al., 2008; Onken and Arlt, 1990; Ottenbacher et al., 2011; Poling et al., 2001), and databank entries, e.g. CHEMCAD (Chemstations, Austin/TX), ChemSep (ChemSep Consortium, Potsdam/NY) or NIST Chemistry Webbook (NIST, 2023a; NIST, 2023b), are available to calculate the vapor pressure of the pure mixture components

chlorobenzene and ethylbenzene.

Although all the aforementioned data sources are considered reliable, datasets from (Ottenbacher et al., 2011) and CHEMCAD (CHEMCAD 7.1.0 Systems Components Databank, part of CHEMCAD 7.1.5) were reviewed prior to experiment evaluation. While both use the DIPPR equation to estimate the vapor pressure of the pure mixture components, see equation (C.26), the corresponding datasets vary in their parameter values. The values published by (Ottenbacher et al., 2011), which were finally used for experiment evaluation, are given in table C.13.

$$p_i^0 = \exp\left(a_i + \frac{b_i}{T} + c_i \ln T + d_i T^{e_i}\right) \tag{C.26}$$

Table C.13.: Parameters to estimate vapor pressures of chlorobenzene and ethylbenzene (Ottenbacher et al., 2011)

parameter	a_i	b_i	c_i	d_i	e_i
chlorobenzene	76.082 903	−7186.8780	−7.851 896 9	$5.010\,977\,8 \cdot 10^{-9}$	3
ethylbenzene	−304.342 52	−10 407.9980	−121.851 04	588.662 06	0.1

C.11. NRTL Equations and Parameters

For a binary mixture, the NRTL model proposed by (Renon and Prausnitz, 1968) consists of the following equations (Gmehling and Kleiber, 2014; Gmehling et al., 2019):

$$\ln \gamma_1 = x_2^2 \left[\tau_{21} \left(\frac{G_{21}}{x_1 + x_2\, G_{21}}\right)^2 + \frac{\tau_{12}\, G_{12}}{(x_2 + x_1\, G_{12})^2}\right] \tag{C.27a}$$

$$\ln \gamma_2 = x_1^2 \left[\tau_{12} \left(\frac{G_{12}}{x_2 + x_1\, G_{12}}\right)^2 + \frac{\tau_{21}\, G_{21}}{(x_1 + x_2\, G_{21})^2}\right] \tag{C.27b}$$

$$\tau_{ij} = \frac{\Delta g_{ij}}{T} \tag{C.27c}$$

$$G_{ij} = \exp\left(-\alpha_{ij}\, \tau_{ij}\right) \tag{C.27d}$$

$$\alpha_{ij} = \alpha_{ji} = \alpha_{12} = \alpha_{21} \tag{C.27e}$$

The NRTL model comprises three model parameters Δg_{12}, Δg_{21} and α_{12} to describe the VLE of a binary mixture. Values for the model parameters used in this work are from the databanks provided by the flowsheet simulators CHEMCAD (CHEMCAD 7.1.0 Systems Components Databank, part of CHEMCAD 7.1.5) and ChemSep (ChemSep 8.1 Pure Component Data, part of ChemSep 8.25).

C.12. Boiling Point and Activity Coefficients

As mentioned in section 2.3.1, the binary mixture CB/EB is commonly considered ideal (Onken and Arlt, 1990; Ottenbacher et al., 2011). To check this assumption, the activity coefficients γ_{CB} and γ_{EB} were evaluated over the complete concentration range of $x_{\mathrm{CB}} = 0 \ldots 1\,\mathrm{kmol_{CB}\,kmol_{tot}^{-1}}$.

Total pressure p_{tot}, molar fractions x_i, activity coefficients γ_i and boiling point T_{boil} are related to each other by:

$$\begin{aligned} p_{\mathrm{tot}} &= p_{\mathrm{CB}} + p_{\mathrm{EB}} \\ &= x_{\mathrm{CB}} \cdot p^0_{\mathrm{CB}}(T_{\mathrm{boil}}) \cdot \gamma_{\mathrm{CB}}(x_{\mathrm{CB}}, T_{\mathrm{boil}}) + x_{\mathrm{EB}} \cdot p^0_{\mathrm{EB}}(T_{\mathrm{boil}}) \cdot \gamma_{\mathrm{EB}}(x_{\mathrm{EB}}, T_{\mathrm{boil}}) \end{aligned} \tag{C.28}$$

As shown in equation (C.28), which is derived from Raoult's and Dalton's laws, see equations (2.5) and (2.6), vapor pressures p_i^0 and activity coefficients γ_i depend on the boiling point T_{boil}. Since the respective dependencies on temperature were introduced in equations (C.26) and (C.27), T_{boil} can be determined numerically for any given p_{tot} and x_i.

Using the DIPPR equation and the corresponding parameters proposed by (Ottenbacher et al., 2011) to estimate the required vapor pressures p_i^0, see equation (C.26) and table C.13, activity coefficients were calculated according to equation (C.27), obtained results are illustrated in figure C.4.

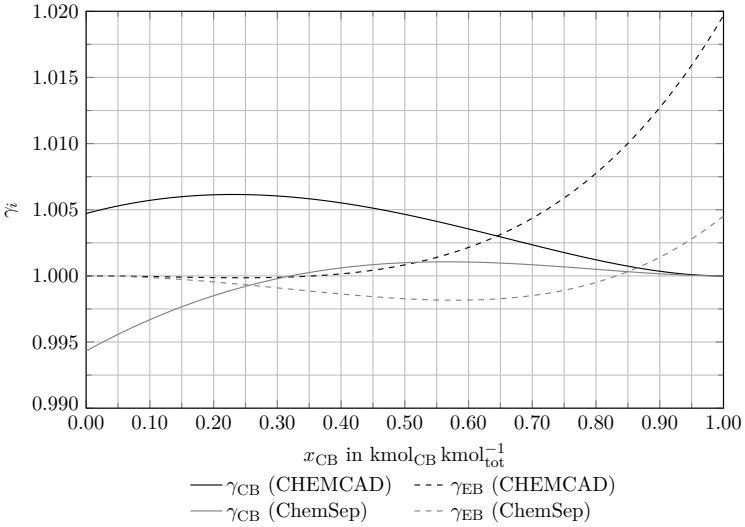

Figure C.4.: Activity coefficients for binary mixture CB/EB at $p_{\mathrm{tot}} = 100\,\mathrm{mbar(a)}$ in dependence of liquid molar fraction x_{CB}, DIPPR parameters for vapor pressure correlation from (Ottenbacher et al., 2011), NRTL parameters from the CHEMCAD (CHEMCAD 7.1.0 Systems Components Databank, part of CHEMCAD 7.1.5) and ChemSep (ChemSep 8.1 Pure Component Data, part of ChemSep 8.25) databanks, see appendices C.10 and C.11 for details

Minimum and maximum values $\gamma_{i,\min}$ and $\gamma_{i,\max}$ as well as their arithmetic averages $\overline{\gamma_i}$ are summarized in table C.14. Since calculated activity coefficients are very close to unity, the assumption of ideal behavior is fulfilled and $\gamma_i = 1$ is used throughout this work.

Table C.14.: Ranges of calculated activity coefficients γ_i for binary mixture CB/EB, DIPPR parameters for vapor pressure correlation from (Ottenbacher et al., 2011), NRTL parameters from the CHEMCAD and ChemSep databanks, see appendices C.10 and C.11 for details

parameter	chlorobenzene		ethylbenzene	
	Ottenbacher et al., 2011 with		Ottenbacher et al., 2011 with	
	CHEMCAD [a]	ChemSep [b]	CHEMCAD [a]	ChemSep [b]
$\gamma_{i,\min}$	1.0000	0.9943	0.9999	0.9982
$\gamma_{i,\max}$	1.0062	1.0011	1.0197	1.0045
$\overline{\gamma_i}$	1.0038	0.9996	1.0037	0.9995

[a] CHEMCAD 7.1.0 Systems Components Databank (part of CHEMCAD 7.1.5)

[b] ChemSep 8.1 Pure Component Data (part of ChemSep 8.25)

C.13. VLE and Relative Volatility

As discussed in the context of equation (C.28), the boiling point of a binary mixture T_{boil} can be numerically estimated using the liquid molar mass fraction x_1 and the total pressure p_{tot}. In addition, considering i substances and j phases, equations (C.29a) to (C.29c) are fulfilled at equilibrium[6] (Seader and Henley, 2011):

$$T_i^{(1)} = T_i^{(2)} = T_i^{(3)} = \cdots = T_i^{(j)} \tag{C.29a}$$

$$p_i^{(1)} = p_i^{(2)} = p_i^{(3)} = \cdots = p_i^{(j)} \tag{C.29b}$$

$$\mu_i^{(1)} = \mu_i^{(2)} = \mu_i^{(3)} = \cdots = \mu_i^{(j)} \tag{C.29c}$$

Since boiling point T_{boil} and vapor pressure p_1^0 corresponding to a given liquid molar fraction x_1 are known, the partial pressure p_1 can be obtained from Raoult's law, see equation (2.5). This in turn allows calculating the vapor molar fraction y_1 from Dalton's law, see equation (2.6), and finally results in the VLE data as well as relative volatility α_{12} for a (binary) mixture according to equation (2.7).

Assuming ideal mixture behavior ($\gamma_i = 1$), this approach was used to calculate the VLE of CB/EB at $p_{\text{tot}} = 100\,\text{mbar(a)}$ using the DIPPR parameters published by (Ottenbacher et al., 2011) and parameters from the CHEMCAD databank. The resulting VLE datasets are illustrated in figure C.5 and were used to determine separation performance based on

[6] equation (C.29c) can also be expressed in terms of the fugacity f (Seader and Henley, 2011): $f_i^{(1)} = f_i^{(2)} = f_i^{(3)} = \cdots = f_i^{(j)}$.

McCabe-Thiele stage constructions.

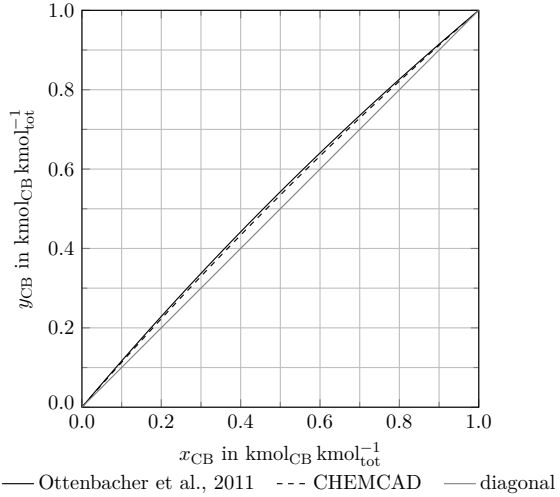

Figure C.5.: VLE data for binary mixture CB/EB at $p_{tot} = 100\,mbar(a)$, underlying vapor pressures calculated based on DIPPR parameters from (Ottenbacher et al., 2011) and the CHEMCAD 7.1.0 Systems Components Databank (part of CHEMCAD 7.1.5), see appendix C.10

As only very small deviations between the VLE datasets are apparent, the influence of data selection on determined calculation performance is assumed to be negligible. Therefore, calculated separation efficiencies should be comparable disregarding which VLE dataset was used for data evaluation. To support this assumption, relative deviations δ between both VLE were calculated according to equation (C.30)[7] and summarized in table C.15.

$$\delta = \frac{y_{CB,lit} - y_{CB,CC}}{y_{CB,CC}} \tag{C.30}$$

Table C.15.: Relative deviations in VLE for binary mixture CB/EB at $p_{tot} = 100\,mbar(a)$, underlying vapor pressures calculated based on DIPPR parameters from (Ottenbacher et al., 2011) and the CHEMCAD 7.1.0 Systems Components Databank (part of CHEMCAD 7.1.5), see appendix C.10

parameter	δ_{max}	δ_{min}	$\overline{\delta}$
value	$3.34 \cdot 10^{-2}$	$1.42 \cdot 10^{-14}$	$1.58 \cdot 10^{-2}$

[7] lit: (Ottenbacher et al., 2011), CC: CHEMCAD 7.1.0 Systems Components Databank (part of CHEMCAD 7.1.5)

Albeit McCabe-Thiele stage constructions are primarily used in this work to evaluate separation performance, the relative volatility α_{12} is required if the number of theoretical stages N_{th} is calculated with Fenske's equation, see section 2.2.1.1, or the slope of the operating line m, see equation (3.25), is estimated.

Assuming ideal behavior for the binary mixture CB/EB ($\gamma_i = 1$), the relative volatility α_{12} is calculated according to equation (2.7) for liquid molar fractions x_{CB} and $x_{\mathrm{EB}} = 1 - x_{\mathrm{CB}}$. According to section 2.1.1, an averaged relative volatility $\overline{\alpha}_{12}$ is obtained based on the geometric mean. While only two representative values $\alpha_{12,\mathrm{I}}$ and $\alpha_{12,\mathrm{II}}$ are considered in equation (2.4), the averaged $\overline{\alpha}_{12}$ given in figure C.6 were calculated according to equation (C.31) using $N = 101$ data points.

$$\overline{\alpha}_{12} = \exp\left(\frac{1}{N}\sum_{i=1}^{N}\ln\overline{\alpha}_{12,i}\right) \tag{C.31}$$

The obtained results illustrated in figure C.6 indicate a small dependence on mixture composition. Furthermore, the relative volatilities calculated with vapor pressure DIPPR parameters by (Ottenbacher et al., 2011) are consistently higher than the results determined with the CHEMCAD parameters.

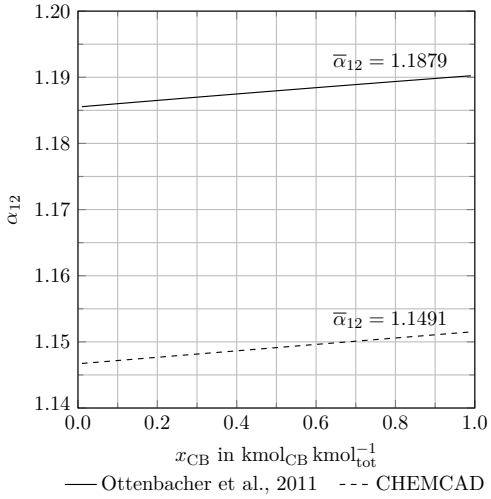

Figure C.6.: Relative volatilities α_{12} for binary mixture CB/EB at $p_{\mathrm{tot}} = 100\,\mathrm{mbar(a)}$ in dependence of liquid molar fraction x_{CB}, underlying vapor pressures calculated based on DIPPR parameters from (Ottenbacher et al., 2011) and the CHEMCAD 7.1.0 Systems Components Databank (part of CHEMCAD 7.1.5), see appendix C.10

Applying equation (C.30) to the calculated relative volatilities allows deriving relative deviations δ as summarized in table C.16. However, since the offset between both curves is almost

constant, minimum, maximum and arithmetically averaged relative deviations are very similar.

To ensure comparability with literature results, the VLE used for experiment evaluation is described using the parameters published by (Ottenbacher et al., 2011).

Table C.16.: Relative deviations in relative volatilities for binary mixture CB/EB at $p_{\mathrm{tot}} = 100\,\mathrm{mbar(a)}$, underlying vapor pressures calculated based on DIPPR parameters from (Ottenbacher et al., 2011) and the CHEMCAD 7.1.0 Systems Components Databank (part of CHEMCAD 7.1.5), see appendix C.10

parameter	$\delta_{\max}$	$\delta_{\min}$	$\overline{\delta}$
value	$3.38 \cdot 10^{-2}$	$3.36 \cdot 10^{-2}$	$3.38 \cdot 10^{-2}$

D. Deviations and Uncertainties

D.1. Brief Introduction to Uncertainty Quantification

Deviations and uncertainties inevitably occur for every measurement and have to be assessed for a proper data evaluation. For this purpose, several approaches have been developed in recent years and discussed in the literature. Two approaches are commonly used (Deldossi and Zappa, 2009):

1. ISO 5725 (Parts 1 . . . 6)

2. Guide to the expression of Uncertainty in Measurement (GUM[1])

Both methods differ in their core concepts, assumptions and prerequisites, which in turn may limit their applicability and was discussed by (Deldossi and Zappa, 2009) in detail: For the approach defined in ISO 5725 a design of experiments (DoE) with a statistical model for each measurand and directly measurable measurands is required; uncertainties resulting from multiple input parameters are calculated based on analysis of variance (ANOVA). GUM in contrast also allows indirect measurands and empirical uncertainty assessment; uncertainties of multiple inputs are combined based on the law of propagation of uncertainty. However, the method as per ISO 5725 can generally being considered as more accurate (Deldossi and Zappa, 2009).

Since experimental measurements (sensor readings for process conditions, density measurements for sample analysis …) and data evaluation (calculation of operational parameters and sample composition, evaluation of separation performance …) in this work largely comprise indirect measurands, the GUM is used for uncertainty quantification.

D.1.1. Core Concepts of GUM

Any measurand Y can be determined based on N inputs X_i using a generic mathematical model f (BIPM et al., 2008a; BIPM et al., 2009):

$$Y = f(X_1, X_2, \ldots, X_\mathrm{N}) \tag{D.1}$$

[1] Although being often referred to as *The GUM*, it comprises several documents: (BIPM et al., 2008a; BIPM et al., 2008b; BIPM et al., 2009; BIPM et al., 2011; BIPM et al., 2012a; BIPM et al., 2012b; BIPM et al., 2020).

Despite the mathematical formulation, the model equation is not required to be known and can also be estimated empirically. Furthermore, all input parameters may also be considered as measurands and hence depend on other quantities. Since no measurand is directly measurable, equation (D.1) is expressed with estimates for input variables x_i and the output y:

$$y = f(x_1, x_2, \ldots, x_\mathrm{N}) \tag{D.2}$$

Estimates for each input quantity x_i can either be obtained by K repeated measurements or by a single observation. In case of K repetitions, the arithmetic mean is used to determine an appropriate estimate $\overline{x}_i$:

$$\overline{x}_i = \frac{1}{K} \sum_{k=1}^{K} x_{i,k} \tag{D.3}$$

Due to randomness, each of the $x_{i,k}$ varies in value. The standard deviation of the resulting probability distribution $s(x_\mathrm{i,k})$ is given as:

$$s(x_{i,k}) = \sqrt{\frac{1}{K-1} \sum_{k=1}^{K} (x_{i,k} - \overline{x}_i)^2} \tag{D.4}$$

Considering the standard deviation of each repeated measurement $s(x_{i,k})$ and the total number of repetitions K, the standard deviation of the arithmetic mean $s(\overline{x}_i)$, which also defines its standard uncertainty $u(\overline{x}_i)$, can be calculated as:

$$s(\overline{x}_i) = u(\overline{x}_i) = \frac{s(x_\mathrm{i,k})}{\sqrt{K}} \tag{D.5}$$

While evaluating uncertainties based on the statistical analysis of repeated observations is called *Type A evaluation of uncertainty*, uncertainty quantification for single observations or measurements is called *Type B evaluation of uncertainty* (BIPM et al., 2008a). For the latter, various sources of information, such as technical specifications, calibration certificates or experiences from previous measurements are used to estimate suitable probability density functions (PDF), which allow calculating the related standard uncertainty. As most of the Type B uncertainties to be approximated in this work originate from substance impurities, chemical analysis (density measurements, mixture compositions …) or deviations in process sensor readings (temperature, pressure, mass flow …), rectangular (or uniform) distributions are assumed according to (BIPM et al., 2008a; Coskun and Oosterhuis, 2020; Ellison and Williams, 2012; Prohaska et al., 2022). In such cases, the uncertainty can either be estimated based on the upper and the lower limits of the distribution, a_+ and a_-, or the semi-range (or half-width) a:

$$u(x_i) = \frac{a_+ - a_-}{2\sqrt{3}} = \frac{a}{\sqrt{3}} \tag{D.6}$$

If the uncertainty of each input variable $u(x_i)$ is known, the combined uncertainty of the output $u_c(y)$ can be estimated with the law of propagation of uncertainty:

$$u_c(y) = \left[\sum_{i=1}^{N} \left(\frac{\partial f}{\partial x_i} \right)^2 \cdot u(x_i)^2 \; + \; 2 \sum_{i=1}^{N-1} \sum_{j=i+1}^{N} \frac{\partial f}{\partial x_i} \frac{\partial f}{\partial x_j} \, u(x_i) \, u(x_j) \, r(x_i, x_j) \right]^{\frac{1}{2}} \tag{D.7}$$

The first term accounts for the uncertainty contribution of each input variable. The partial derivative represents the sensitivity coefficient:

$$c_i = \frac{\partial f}{\partial x_i} \tag{D.8}$$

Correlations between input variables are represented by the second term of equation (D.7) using the correlation coefficient $r(x_i, x_j)$:

$$r(x_i, x_j) = \frac{u(x_i, x_j)}{u(x_i) \, u(x_j)} \tag{D.9}$$

$r(x_i, x_j) = 0$ is valid for uncorrelated inputs. In such cases, a change in one input does not affect any other input variable, and equation (D.7) simplifies to:

$$u_c(y) = \left[\sum_{i=1}^{N} (c_i \cdot u(x_i))^2 \right]^{\frac{1}{2}} \underset{\text{(D.8)}}{=} \left[\sum_{i=1}^{N} \left(\frac{\partial f}{\partial x_i} \cdot u(x_i) \right)^2 \right]^{\frac{1}{2}} \tag{D.10}$$

Equation (D.10) is based on a first-order Taylor series expansion of the model function f defined in equations (D.1) and (D.2). Neglecting higher order terms in the series expansion can result in a poor model approximation, which is especially relevant if significant nonlinearities are present. This is considered as a drawback of the GUM approach (Deldossi and Zappa, 2009).

Based on the standard uncertainty $u_c(y)$, the expanded uncertainty $U(y)$ can be calculated with the coverage factor k (BIPM et al., 2008a):

$$U(y) = k \cdot u_c(y) \tag{D.11}$$

The coverage factor k is chosen depending on the desired coverage probability and resulting probability distribution. Assuming a normal distribution, a coverage factor of $k = 1$ represents an interval with a coverage probability of around 68 %, $k = 2$ represents a probability of ca. 95 % and approximately 99 % are obtained for $k = 3$ (BIPM et al., 2008a)[2].

As the approach presented in the GUM (BIPM et al., 2008a; BIPM et al., 2009) is intended to be generally applicable, it is not limited to specific measurements or any field of expertise. (Farrance and Frenkel, 2012) give an extensive review about uncertainty quantification based

[2]Exact values for a normal distribution are (BIPM et al., 2008a): 68.27 % ($k = 1$), 95.45 % ($k = 2$) and 99.73 % ($k = 3$). For a strict evaluation, the degrees of freedom need to be considered and the coverage factor k is then chosen based on the accompanying t-distribution, see (BIPM et al., 2008a; BIPM et al., 2008b) for details.

on functional relationships and summarized algebraic solutions of equation (D.10) for common measurement models. Furthermore, (Ellison and Williams, 2012) provide detailed information about applying the GUM framework for uncertainty quantification in analytical measurements.

As already elaborated, the basic GUM framework is not applicable to highly non-linear models and multiple-output models. To mitigate these insufficiencies, the GUM framework was extended by Supplement 1 (BIPM et al., 2008b) and Supplement 2 (BIPM et al., 2011)[3].

D.1.2. GUM Supplement 1: Monte Carlo Method

GUM Supplement 1 (BIPM et al., 2008b), which comprises Monte Carlo methods (MCM), is applicable to any arbitrary model with multiple inputs and a single output. Therefore, this approach can be used if the criteria of the GUM framework are not fulfilled due to complicated or highly non-linear models. While the law of propagation of uncertainty requires partial derivatives, the Monte Carlo approach can also be applied if such derivatives are unknown or cannot be determined.

Assuming that each input X_n of the generic measurand model introduced in equation (D.1) can be considered as a randomly distributed variable with possible values ξ_n and expectation x_n, the according model output Y is described by its estimate y resulting from η possible values. To estimate the probability distribution of the model output quantity, a suitable PDF $g_{X_n}(\xi_n)$ needs to be assigned to each input (Wübbeler, 2012). Assigning a suitable PDF to each input depends on the available information or data as well as the properties of the PDF. For inputs which are not independent of each other, a joint PDF can be used. A detailed overview of common PDFs and the according properties can be found in (BIPM et al., 2008b). PDFs relevant for the parameters considered in this work are extensively discussed by (BIPM et al., 2008b; Ellison and Williams, 2012).

The assigned PDFs are propagated through the model to obtain an output PDF $g_Y(\eta)$. The estimate of the output quantity y is represented by the expectation of the output PDF. The combined standard uncertainty of the output quantity $u_c(y)$ is given by the standard deviation of the estimated PDF. Furthermore, coverage probability and coverage interval can be determined from the obtained output PDF.

While assigned PDFs can be propagated in several ways, the MCM provides a convenient approach to estimate an approximated probability distribution function. Although being inexact by nature, the MCM is generally considered more sound than the conventional GUM framework for a large set of problems, since fewer requirements need to be satisfied (BIPM et al., 2008b). To obtain robust information about the output quantity and its associated uncertainty, the number of draws N_{MC} used for model evaluation in the MCM needs to be selected accordingly. While N_{MC} can be determined adaptively, see (BIPM et al., 2008b), $N_{\mathrm{MC}} = 1 \cdot 10^6$ is commonly sufficient to obtain a coverage interval of 95 %, which allows quantifying the model output

[3]GUM Supplement 2 will not be elaborated here as it covers Multiple-Output Models, which are not used in this work.

uncertainty to one or two significant digits (BIPM et al., 2008b).

D.1.3. Combining Type A and Type B Uncertainties

As already elaborated, measurement uncertainties within the GUM framework can be evaluated as uncertainties of Type A and Type B. Although, the combination of both types of uncertainties does not seem to be explicitly addressed in the GUM framework (BIPM et al., 2008a), an additive combination is commonly used in the literature, e.g. (Bell, 2001; Kirkup and Frenkel, 2006; Niemeier and Tengen, 2020). Considering i ($i = 1 \dots N$) uncertainty components of Type A and j ($j = 1 \dots M$) components of Type B with standard uncertainties $u_{\mathrm{A},i}$ and $u_{\mathrm{B},j}$, respectively, allows estimating the resulting combined standard uncertainty as (Niemeier and Tengen, 2020):

$$u_{\mathrm{c}}(y) = \left[\sum_i u_{\mathrm{A},i}^2 + \sum_j u_{\mathrm{B},j}^2 \right]^{\frac{1}{2}} \tag{D.12}$$

According to equation (D.8), $c_i = 1$ and $c_j = 1$ are valid for a purely additive model. Therefore, equation (D.12) can also be used to obtain the combined standard uncertainty $u_{\mathrm{c}}(y)$ for any number of additive uncertainty components disregarding their specific type (Type A or Type B). This generalization is especially useful when uncertainties are tabulated and analyzed using uncertainty budgets.

D.1.4. Identifying and Reporting Uncertainty

So-called *fishbone diagrams*, which are also known as *cause-and-effect diagrams* or *Ishikawa diagrams*, are commonly used to identify potential sources of uncertainties (Coskun and Oosterhuis, 2020; Ellison and Williams, 2012). To create such diagrams, each input of the measurand model is analyzed and branched out until negligible effects are considered in each subbranch. To identify effects which can be summarized in a single contribution or effects which cancel out each other, possible duplications are rearranged and resolved. Furthermore, effects of the same or a very similar category are relabelled to ensure consistent naming and simplify distinction from non-related effects. A detailed introduction about constructing fishbone diagrams is given by (Ellison and Williams, 2012).

For uncertainty calculation and reporting, however, *uncertainty budgets* in which uncertainty analysis results are summarized in a tabular form are commonly used (BIPM et al., 2008b). A basic procedure for creating uncertainty budgets is presented by (Bell, 2001). While not standardized, uncertainty budgets commonly state information about each quantity considered in the uncertainty quantification, its estimate x_i, the attributed standard uncertainty $u(x_i)$, the sensitivity coefficient c_i and its uncertainty contribution $|c_i| \cdot u(x_i)$ (Bell, 2001; BIPM et al., 2008b; Grykałowska et al., 2015). Furthermore, information about the assigned PDF or coverage factor k used to calculate the expanded uncertainty U should be provided.

Since equation (D.8) can only be used to calculate the required sensitivity coefficients if the partial derivatives of the measurand model are known, such coefficients cannot be easily estimated if PDFs are propagated with MCM. For such cases, (BIPM et al., 2008b) suggest keeping all but one input quantity constant during MCM to estimate a single variable PDF. Using this PDF, the related sensitivity coefficients can be calculated as the ratio of the standard uncertainty of the resulting model values and the standard uncertainty of the best estimate of the relevant input quantity (BIPM et al., 2008b). Although this approach is a generalization of equation (D.8), the obtained sensitivity coefficients differ, since higher-order terms of the Taylor series expansion are not neglected (BIPM et al., 2008b). Therefore, (BIPM et al., 2008b) emphasize to use uncertainty budgets as a qualitative tool to identify predominant uncertainty contributions.

For data reporting, providing two significant digits for both estimates and the associated uncertainties is commonly considered sufficient (BIPM et al., 2008a). Furthermore, (BIPM et al., 2008a) suggest to round up calculated uncertainties as this mitigates round-off errors. To state a numerical result y with its associated (combined) standard uncertainty $u_c(y)$, a compact bracket notation is used in this work; the expressions $(100.021\,47 \pm 0.000\,35)\,\mathrm{g}$ and $100.021\,47(35)\,\mathrm{g}$ are equivalent (BIPM et al., 2008a). Although uncertainties crossing the decimal point, e.g. $(100.2 \pm 1.1)\,\mathrm{g}$, are not explicitly addressed in (BIPM et al., 2008a), such measurements are often expressed as $100.2(1.1)\,\mathrm{g}$ or $100.2(11)\,\mathrm{g}$, since the bracket notation refers to the number of significant digits provided in the bracket.

D.2. Uncertainty Quantification and Propagation

D.2.1. Software-Assisted Uncertainty Quantification and Propagation

While uncertainty quantification and propagation is rather straightforward for purely additive uncertainty components or simple measurand models, determining the required partial derivatives for uncertainty components with more complicated measurand models can quickly become laborious and is prone to errors if done manually. Therefore, the uncertainty analyses performed for the data presented in this work are built on the *uncertainties* and *GUM Tree Calculator* packages for the *Python* programming language; see (Lebigot, 2017) and (Hall, 2022) for details about the respective packages. While the *uncertainties* package is especially helpful, since uncertainty propagation is automatically performed alongside the evaluation of the measurand model based on automatic differentiation, the *GUM Tree Calculator* package allows assessing the uncertainty attributed to sensor calibrations and provides extensive methods for uncertainty formatting and reporting. Despite the well-reviewed performance of both packages, obtained results were cross-checked against manual uncertainty calculations on a random basis. The partial derivatives required for these checks were calculated using the *SymPy* library (Meurer et al., 2017).

However, numerical or iterative calculation routines, such as calculation of feed boiling point,

number of theoretical stages, number of transfer units etc., do not rely on an algebraic measurand model $f(x_i)$ and the partial derivatives $\frac{\partial f}{\partial x_i}$, which are required for uncertainty quantification based on the law of propagation of uncertainty, see equation (D.10), are commonly unknown. Therefore, uncertainties are quantified using Monte Carlo methods based on (BIPM et al., 2008b; Veen et al., 2021) for these cases. Although advanced software tools are available for the corresponding simulations and uncertainty analyses, the Monte Carlo simulations performed in this work were fully integrated into the data evaluation workflow using the pseudo-random number generators and associated probability functions provided by the *NumPy* package, see (Harris et al., 2020).

Combining the aforementioned software packages with MCM allows a consistent propagation of relevant uncertainties through the data evaluation workflow, which is summarized in appendix E.5.1. As shown in table E.3, the automated uncertainty propagation requires information about the initial uncertainties attributed to sensor readings or calibration samples. Therefore, combined standard uncertainties associated with relevant plant sensor readings and calibration procedures as well as applied simplifications and assumptions are quantified manually and summarized in the following sections. Experimental results and their associated combined standard uncertainties are summarized in appendix F.1.

D.2.2. Sample Analysis and Mixture Composition

Sample analysis based on density measurements and the corresponding method calibration are commonly affected by impurities of the used chemicals. However, no information about relevant impurities are given in the certificates of analysis, see appendix B.

In addition, considering impurities in both chlorobenzene and ethylbenzene results in a multicomponent mixture for which simplified mixing rules may not apply. This is especially relevant since mixture density and mixture molar mass are related to the mixture composition but are also required to establish a density calibration curve. Due to the lack of the respective specifications, no reliable approach accounting for the potential impurities could be identified. Therefore, any impurities are neglected, and the chemicals used for the experimental investigations are assumed to be pure.

For the density calibration used for sample analysis, samples with known composition were prepared by mass using a laboratory scale of type *Practum 224-1S* (Sartorius, Göttingen/Germany). The sample composition and density data were already listed in table C.3. The uncertainty budget of the laboratory scale is given in table D.1. As (Sartorius, 2022) specified the scale's repeatability as a standard deviation, it can directly be used as a standard uncertainty (Ellison and Williams, 2012). Furthermore, the uncertainty component due to linearity is considered twice as it affects both tare and gross weight (Ellison and Williams, 2012). Temperature-induced sensitivity drift is neglected.

Table D.1.: Uncertainty budget for laboratory scale, specification as per (Sartorius, 2022)

uncertainty component	specification	PDF	divisor	standard uncertainty
-	mg	-	-	mg
readability	0.1	rectangular	$2 \cdot \sqrt{3}$	0.029
repeatability	0.1			0.1
linearity (tare)	0.2	rectangular	$2 \cdot \sqrt{3}$	0.058
linearity (gross)	0.2	rectangular	$2 \cdot \sqrt{3}$	0.058
combined standard uncertainty				0.13
expanded uncertainty ($k = 2$)				0.26

Using the *uncertainties* package, the combined standard uncertainties attributed to the weighed-in masses are propagated to the mixture compositions, which are represented by mass fractions w_{CB}, see equation (C.2a), and molar fractions x_{CB}, see equation (C.2b). Obtained results are summarized in table C.3, were randomly double-checked against manual calculations and showed good agreement with the automated uncertainty quantification.

Although uncertainties of the molar masses M_{CB} and M_{EB} can be determined based on (Veen et al., 2016; Veen et al., 2021), the respective values are assumed to be unaffected by any uncertainty. This assumption seems especially reasonable as mixture impurities, which would potentially result in additional uncertainty components affecting the molar mass of the mixture, are also neglected.

As described in section 3.4, the liquid mixture density of the prepared samples was measured using a *DMA 4100 M* digital density meter (Anton Paar Germany, Ostfildern/Germany) equipped with an autosampler *Xsample 530* (Anton Paar Germany, Ostfildern/Germany). Each measurement was performed at a constant nominal temperature of 20 °C. Prior to the density analyses, the system was checked using the device's air/water adjustment procedure. In addition, the manufacturer suggested assessing potential linearity effects by cross-checking the density reading of a high purity substance of molecular structure and density similar to the analyte. While ultrapure water and a water reference standard were used for the air/water adjustment procedure, the linearity assessment was performed with toluene, since its properties are similar to those of chlorobenzene and ethylbenzene. The specifications of the respective chemicals can be found in table B.2. The system passed both the air/water adjustment procedure and the toluene cross-check. No density adjustments were necessary and the least significant digit of the measured density was within the literature reference[4].

Regarding the accuracy of the digital density meter, (Anton Paar, 2021) provides information about both the density measurement itself and the temperature control of the measuring cell.

[4]As the density is not stated in the certificate of analysis (Fisher Scientific, 2022a), values from (Fisher Scientific, 2022b; National Center for Biotechnology Information, 2022) were used for reference.

Since repeatability and reproducibility of the density measurements are specified as standard deviations, the respective values can be interpreted as standard uncertainties; see (Ellison and Williams, 2012). The same applies for the repeatability of the measuring cell temperature. Furthermore, accuracies for both density and temperature readings are given in (Anton Paar, 2021). While density related information can directly be associated with the measured density value, the effect of temperature depends on the mixture composition.

The uncertainty attributed to the measuring cell temperature was evaluated as shown in table D.2. As all density measurements were performed at a nominal temperature of 20 °C, a cell temperature of 20.000(22) °C is obtained after propagating relevant uncertainty components.

Table D.2.: Uncertainty budget for measuring cell temperature of digital density meter, specification as per (Anton Paar, 2021)

uncertainty component	specification	PDF	divisor	standard uncertainty
-	K	-	-	K
repeatability	0.02			0.02
accuracy	0.03	rectangular	$2 \cdot \sqrt{3}$	0.0087
combined standard uncertainty				0.022
expanded uncertainty ($k = 2$)				0.044

The effect of the uncertainty in cell temperature on mixture density is evaluated based on the temperature dependent density of the pure mixture components and a density mixing rule, see equations (C.4) and (C.5). Without considering any deviations[5] in the density correlation given in equation (C.5), the combined standard uncertainty determined in table D.2 was propagated through equation (C.5) using the *uncertainties* package (Lebigot, 2017). For a temperature of 20.000(22) °C, pure component densities of $\rho_{\mathrm{L,CB}} = 1106.008(22)\,\mathrm{kg\,m^{-3}}$ and $\rho_{\mathrm{L,EB}} = 866.700(18)\,\mathrm{kg\,m^{-3}}$ are obtained. The effect of temperature on the uncertainty in mixture density was assessed by evaluating equation (C.4) over the complete concentration range[6] of $x_{\mathrm{CB}} = 0 \ldots 1\,\mathrm{mol_{CB}\,mol_{tot}^{-1}}$ which results in a maximum standard uncertainty of $u_{\mathrm{c}}(\rho_{\mathrm{L,mix}}) = 0.022\,\mathrm{kg\,m^{-3}}$, see table D.3. The molar masses of chlorobenzene and ethylbenzene are given in table C.1, uncertainties associated with the molar masses were neglected.

[5] As (Ottenbacher et al., 2011) give a mean deviation of 0.085 % between predicted and experimental values, deviations in the density polynomial defined in equation (C.5) are neglected.

[6] In accordance with (Bradtmöller, 2017; Ottenbacher et al., 2011), excess volume V^{E} is not considered in equation (C.4).

Table D.3.: Temperature effect on uncertainty associated with mixture density, $\rho_{\mathrm{L,mix}}$ calculated according to equation (C.4) for $\rho_{\mathrm{L,CB}} = 1106.008(22)\,\mathrm{kg\,m^{-3}}$ and $\rho_{\mathrm{L,EB}} = 866.700(18)\,\mathrm{kg\,m^{-3}}$

x_{CB}	x_{EB}	$\rho_{\mathrm{L,mix}}$
$\mathrm{mol_{CB}\,mol_{tot}^{-1}}$	$\mathrm{mol_{EB}\,mol_{tot}^{-1}}$	$\mathrm{kg\,m^{-3}}$
0.00	1.00	866.700(18)
0.05	0.95	876.725(19)
0.10	0.90	886.923(19)
0.20	0.80	907.856(19)
0.30	0.70	929.534(19)
0.40	0.60	951.999(20)
0.50	0.50	975.295(20)
0.60	0.40	999.468(21)
0.70	0.30	1024.570(21)
0.80	0.20	1050.653(21)
0.90	0.10	1077.778(22)
0.95	0.05	1091.751(22)
1.00	0.00	1106.008(22)

The uncertainty budget for the density measurements conducted with the digital density meter, see table D.4, is finally obtained by combining the uncertainty component of the measuring cell temperature as well as the manufacturer's specifications directly related to the density measurement itself.

Table D.4.: Uncertainty budget for density measurements, specification as per (Anton Paar, 2021), originally given in $\mathrm{g\,cm^{-3}}$, see tables D.2 and D.3 for effect of measuring cell temperature

uncertainty component	specification	PDF	divisor	standard uncertainty
-	$\mathrm{kg\,m^{-3}}$	-	-	$\mathrm{kg\,m^{-3}}$
repeatability	0.01			0.01
reproducibility	0.05			0.05
accuracy	0.1	rectangular	$2 \cdot \sqrt{3}$	0.029
cell temperature				0.022
combined standard uncertainty				0.063
expanded uncertainty ($k = 2$)				0.126

While table D.4 provides the maximum combined standard uncertainty to expect for density measurements at 20.000(22) °C, the values listed in table C.3 are calculated with composition dependent temperature effects. However, very similar uncertainties are obtained for both cases. As table C.3 also contains multiple density measurements of samples with identical composition, the standard deviation of the mean is considered as an additional uncertainty component. Respective Type A and Type B uncertainties are combined according to equation (D.12).

To finally quantify the uncertainty in mixture composition, the estimated combined standard uncertainty associated with the mixture density $u_c(\rho_{L,mix})$ is propagated through the regression polynomial of the density calibration curve illustrated in figure C.1 using the *uncertainties* package (Lebigot, 2017). Obtained uncertainties $u_c(\rho_{L,mix})$ were cross-checked against manual calculations according to equation (D.13):

$$\begin{aligned} u_c(x_{CB}) &= \frac{\partial x_{CB}}{\partial \rho_{L,mix}} \cdot u(\rho_{L,mix}) \\ &= \left(3\, a_3\, \rho_{L,mix}^2 + 2\, a_2\, \rho_{L,mix} + a_1\right) \cdot u(\rho_{L,mix}) \end{aligned} \tag{D.13}$$

As can be derived from equation (D.13), the maximum uncertainty in mixture composition is obtained for large liquid mixture densities which is given for $x_{CB} \to 1.0\,\mathrm{kmol_{CB}\,kmol_{tot}^{-1}}$ as $\rho_{L,CB} > \rho_{L,EB}$. Using an experimental setup similar to that used in this work, (Bradtmöller, 2017) obtained a maximum molar fraction of $x_{CB} \approx 0.87\,\mathrm{kmol_{CB}\,kmol_{tot}^{-1}}$ which corresponds to $\rho_{L,mix} \approx 1.07\,\mathrm{g\,cm^{-3}}$. Considering the combined standard uncertainty from table D.4, the maximum expectable uncertainty in mixture composition is estimated for a sample density of $\rho_{L,mix} = 1.070\,000(63)\,\mathrm{g\,cm^{-3}}$. Furthermore, an additional uncertainty component attributed to the maximum deviation of the density calibration polynomial ε_{max}, see equation (C.3b), was estimated assuming a rectangular PDF. The respective standard uncertainties are summarized in table D.5.

Table D.5.: Uncertainty budget for mixture composition, $\rho_{L,mix} = 1.070\,000(63)\,\mathrm{g\,cm^{-3}}$ ($x_{CB} = 0.868\,27(23)$ $\mathrm{mol_{CB}\,mol_{tot}^{-1}}$), uncertainty of density reading according to table D.4, maximum absolute deviation of regression polynomial according to table C.2

uncertainty component	specification	PDF	divisor	standard uncertainty
-	$\mathrm{mol_{CB}\,mol_{tot}^{-1}}$	-	-	$\mathrm{mol_{CB}\,mol_{tot}^{-1}}$
density analysis				0.000 23
regression polynomial	±0.000 36	rectangular	$\sqrt{3}$	0.000 21
combined standard uncertainty				0.000 31
expanded uncertainty ($k = 2$)				0.000 62

D.2.3. Molar Mass of Mixtures

As molar masses M_F, M_D, M_B, M_mb are calculated according to equation (C.1), associated combined standard uncertainties, $u_\mathrm{c}(M_\mathrm{F})$, $u_\mathrm{c}(M_\mathrm{D})$, $u_\mathrm{c}(M_\mathrm{B})$ and $u_\mathrm{c}(M_\mathrm{mb})$, are quantified by propagating the uncertainties of the corresponding molar fractions, $u_\mathrm{c}(x_\mathrm{F})$, $u_\mathrm{c}(x_\mathrm{D})$, $u_\mathrm{c}(x_\mathrm{B})$ and $u_\mathrm{c}(x_\mathrm{mb})$ or $u_\mathrm{c}(y_\mathrm{mb})$. Although uncertainties of the pure component molar masses, $u_\mathrm{c}(M_\mathrm{CB})$ and $u_\mathrm{c}(M_\mathrm{EB})$, can be determined based on (Veen et al., 2016; Veen et al., 2021), the respective molar masses are assumed to be unaffected by any uncertainty.

D.2.4. Excess Volume

Excess volume was not only determined based on density analyses, but also predicted the determined Redlich-Kister parameters. Therefore, the uncertainties associated with experimental and predicted values need to be assessed separately. As the *uncertainties* package (Lebigot, 2017) was consistently used to quantify uncertainties associated with mixture compositions and density readings, the uncertainty propagation for the excess volume was also fully automated based on the corresponding equations.

The composition of the prepared liquid samples as well as the results of the corresponding density analyses and the associated uncertainties are summarized in table C.3. While any uncertainty components attributed to the molar mass M_i are assumed to be negligible, the uncertainties in the molar fraction x_CB and the density readings $\rho_\mathrm{L,i}$ were propagated through equation (C.22). As highlighted in the context of figure C.2, a considerably larger uncertainty $u(V^\mathrm{E}_\mathrm{exp})$ was obtained at $x_\mathrm{CB} = 0.5\,\mathrm{mol_{CB}\,mol_{tot}^{-1}}$ which results from deviations in the least significant digit of the individual density readings, see table C.3 for explicit values.

Although the uncertainty of the determined Redlich-Kister parameters was not assessed, the uncertainty in the predicted excess volume $u(V^\mathrm{E}_\mathrm{pred})$ can be quantified similarly as the predicted excess volume is calculated by inserting both the regressed Redlich-Kister parameters from table C.12 and the mixture compositions from table C.3 into equation (C.23). To finally quantify deviations between experimentally observed and predicted excess volume, $V^\mathrm{E}_\mathrm{exp}$ and $V^\mathrm{E}_\mathrm{pred}$, absolute and relative deviations were determined, see appendix C.9 for details.

D.2.5. Column Geometry and Packing Specification

Calculating the column load and quantifying separation performance requires information on the column dimensions, packing specifications and the height of the packed bed. As already summarized in table A.1, uncertainties associated with geometric parameters are determined based on the general tolerances specified in (DIN ISO 2768-1, 1991).

Since the distillation column is made from borosilicate glass, which commonly shows considerable geometric deviations, tolerances of class *very coarse* are assumed. The same tolerance class was used for the height of the packing elements as the corrugated metal sheets were manually cut to size in the manufacturer's production routine. However, as wire EDM (electrical discharge

machining) was used to ensure consistent packing diameters with tight tolerances, *fine* tolerances are considered for this dimension. For both width and height of the corrugated packing channels, *medium* tolerances are taken into account.

As shown in equation (D.14), the height of the packed bed H_{bed} is calculated with the number of packing elements installed in the column, $N_{\mathrm{p}} = 24$, and the height of each element, $h_{\mathrm{p}} = 102\,\mathrm{mm}$. The associated uncertainty $u_{\mathrm{c}}(H_{\mathrm{bed}})$ is obtained from uncertainty propagation.

$$H_{\mathrm{bed}} = N_{\mathrm{p}} \cdot h_{\mathrm{p}} \tag{D.14}$$

Since the number of packing elements installed in the column is known exactly, $u(N_{\mathrm{p}}) = 0$ is used for the associated uncertainty. The uncertainty of the height of a packing element $u(h_{\mathrm{p}})$ is documented in table A.1. Uncertainties associated with void fraction $u_{\mathrm{c}}(\varepsilon_{\mathrm{p}})$, the fraction of surface area occupied by holes and $u_{\mathrm{c}}(\Omega_{\mathrm{p}})$ packing surface tension $u_{\mathrm{c}}(\sigma_{\mathrm{p}})$ are not stated in the used literature sources and thus neglected.

D.2.6. Operational Parameters

In general, uncertainty analysis should be performed for the measuring chain, which is used to acquire process data, as well as subsequent data processing or calculations. For sensors with digital communication interfaces, all signal processing and conversion is performed in the sensor itself and thus, covered by the manufacturer's specifications. However, for analog sensors, an additional signal transfer and acquisition is required which results in additional uncertainty contributions. Therefore, different uncertainty components need to be considered depending on the sensor configuration and data acquisition hardware.

The uncertainty analyses elaborated in this section cover the most common uncertainty contributions relevant for each sensor reading or measuring chain. Unless otherwise stated, all considerations cover a single sensor or instrument reading. As stated in section 3.5, operational parameters are evaluated during steady-state plant operation and averaged over the respective time period. Therefore, an additional uncertainty component attributed to calculating the respective mean value is considered as part of the data processing and evaluation, but not stated in the uncertainty budgets presented in this section.

D.2.6.1. Liquid Feed Density (Inline Measurement)

The inline measurement of the feed density obtained from sensor D101 was used to identify steady-state plant operation, see section 3.3.3.2. Albeit its exact numerical value is not needed for experiment evaluation, its associated uncertainty is evaluated in table D.6 to support the trends illustrated in figure A.1.

Table D.6.: Uncertainty budget for density readings from sensor D101, specification as per (Krohne, 2016)

uncertainty component	specification	PDF	divisor	standard uncertainty
-	$\mathrm{kg\,m^{-3}}$	-	-	$\mathrm{kg\,m^{-3}}$
sensor	± 2.0	rectangular	$\sqrt{3}$	1.15
combined standard uncertainty				1.15
expanded uncertainty ($k = 2$)				2.30

D.2.6.2. Temperatures and Pressures

In contrast to the used Coriolis mass flow meter or the scales, operating temperatures and pressures were measured by sensors with analog output signals. Therefore, the uncertainty analysis of the respective process values cannot solely rely on deviations as specified by the sensor manufacturer, and information about the signal processing and recording equipment need to be taken into account additionally. (Scheller and Krummeck, 2018) provide a detailed discussion about uncertainty analysis for temperature measurements and address relevant uncertainty components related to the sensor itself, sensor connection (cable), signal processing, analog-to-digital conversion, cold junction temperature etc. Although (Scheller and Krummeck, 2018) explicitly address uncertainties in temperature measurements, their approach can be generalized for any analog measuring chain.

Regarding the temperature readings used in this work and their associated uncertainties, digital and analog as well as calibrated and uncalibrated temperature sensors or measuring chains need to be distinguished. An overview of analog and digital sensor signals as well as sensor calibration is given in table D.7. Accuracies of used temperature sensors and, in case sensors were calibrated, calibration results were already summarized in appendices A.3 and A.5, respectively.

Table D.7.: Overview of temperature measuring chains

sensor tag	sensor signal		sensor calibration	
	analog	digital	calibrated	uncalibrated
T101		x		x
T604	x			x
T605	x			x
others	x		x	

Since temperature sensor T101 delivers a digital sensor signal, the attributed uncertainty is quantified based on the sensor accuracy specified by the manufacturer, which includes any

deviations or uncertainties due to signal processing and analog-to-digital conversion. The respective uncertainty evaluation for temperature sensor T101 is summarized in table D.8.

Table D.8.: Uncertainty budget for temperature sensor T101, specification as per (Krohne, 2016)

uncertainty component	specification	PDF	divisor	standard uncertainty
-	K	-	-	K
sensor	±1.0	rectangular	$\sqrt{3}$	0.58
combined standard uncertainty				0.58
expanded uncertainty ($k = 2$)				1.16

Since temperature sensors T604 and T605 were used uncalibrated, the general accuracy specified in (DIN EN 60751, 2009) is used for the respective uncertainty. The accuracy of the data acquisition module is specified by the manufacturer and includes all errors related to signal processing and conversion (Keysight Technologies, 2020). Potential deviations due to connection leads (cables) are not considered, since all RTDs were installed in 4-wire configuration which should eliminate any asymmetries in the measured resistances. Effects due to varying operating temperatures of the data acquisition modules, which can be considered by using the temperature coefficient specified by the manufacturer, see (Keysight Technologies, 2020), are neglected. Results of the uncertainty evaluation for temperature sensors T604 and T605 are listed in table D.9.

Table D.9.: Uncertainty budget for temperature sensors T604 and T605, specification for sensor as per (DIN EN 60751, 2009), specification for data acquisition as per (Keysight Technologies, 2020)

uncertainty component	specification	PDF	divisor	standard uncertainty
-	K	-	-	K
sensor	±0.5	rectangular	$\sqrt{3}$	0.29
data acquisition	±1.0	rectangular	$\sqrt{3}$	0.58
combined standard uncertainty				0.65
expanded uncertainty ($k = 2$)				1.30

All other analog temperature sensors were calibrated as described in appendix A.5. As the temperature sensor calibration covered the full measuring chain comprising the temperature sensor, the connection leads and the data acquisition, all relevant uncertainty components are included in the estimated maximum standard deviation of 0.14 K. For the sake of simplicity, and due to the high number of used temperature sensors, the estimated maximum standard deviation is attributed to all readings obtained from the calibrated temperature sensors. Similar

to the uncalibrated analog temperature sensors, effects due to varying operating temperatures of the data acquisition modules are neglected. The resulting uncertainty budget is given in table D.10.

Table D.10.: Uncertainty budget for calibrated temperature sensors, standard uncertainty estimated using the *GUM Tree Calculator* (Hall, 2022) based on sensor calibration data, see appendix A.5

uncertainty component	specification	PDF	divisor	standard uncertainty
-	K	-	-	K
measuring chain calibration and regression				0.14
combined standard uncertainty				0.14
expanded uncertainty ($k = 2$)				0.28

For the uncertainty associated with the pressure sensor readings, an ideal signal conversion in the sensor[7] and an ideal signal transfer from the sensor to the data acquisition is assumed. Furthermore, quantization errors due analog-to-digital conversion seem negligible[8] and are thus, not considered. The effect of operating temperature is not considered.

For absolute pressure sensors P201 and P204, a process pressure of $p = 0 \ldots 1.5\,\mathrm{bar(a)}$ is represented by a sensor output signal of $4 \ldots 20\,\mathrm{mA}$. Therefore, the sensor resolution is $1.5\,\mathrm{bar(a)}/16\,\mathrm{mA} = 0.093\,75\,\mathrm{bar(a)\,mA^{-1}}$. Assuming a nominal operating pressure of $p_\mathrm{h} = 100\,\mathrm{mbar(a)}$ results in a current signal of about 5.07 mA. The respective measurement uncertainty analysis for this operating point including uncertainty components due to data acquisition is summarized in table D.11.

Table D.11.: Uncertainty budget for pressure sensors P201 and P204, $p = 100\,\mathrm{mbar(a)}$ ($5.07\,\mathrm{mA}$), specification for sensor as per (E+H, 2004), specification for data acquisition as per (Keysight Technologies, 2020)

uncertainty component	specification	PDF	divisor	standard uncertainty
-	mA	-	-	mA
sensor	±0.02	rectangular	$\sqrt{3}$	0.012
data acquisition	±0.0045	rectangular	$\sqrt{3}$	0.0026
combined standard uncertainty				0.012
expanded uncertainty ($k = 2$)				0.024

[7] Measured pressure is internally converted into the output current signal.

[8] Common quantization error: ± 1 bit. Data acquisition: 22 bits. Output signal resolution of pressure sensors: 1 µA for sensors P201 and P204 (E+H, 2004), 6 µA for sensors P202 and P203 (VEGA, 2014). Measuring range: 100 mA ⟹ Resolution of data acquisition: 0.024 µA per bit.

Table D.11.: Uncertainty budget for pressure sensors P201 and P204, $p = 100\,\mathrm{mbar(a)}$ ($5.07\,\mathrm{mA}$), specification for sensor as per (E+H, 2004), specification for data acquisition as per (Keysight Technologies, 2020) (continued)

uncertainty component	specification	PDF	divisor	standard uncertainty
-	mA	-	-	mA
conversion based on sensor resolution				mbar(a)
combined standard uncertainty				1.11
expanded uncertainty ($k = 2$)				2.22

The uncertainty of differential pressure sensors P203 and P204 is analyzed similarly. The output signal of $4 \ldots 20\,\mathrm{mA}$ covers a measuring range of $\Delta p = -25 \ldots 25\,\mathrm{mbar}$ which results in a sensor resolution of $50\,\mathrm{mbar}/16\,\mathrm{mA} = 3.125\,\mathrm{mbar\,mA^{-1}}$. Since the maximum differential pressure along each section of the packed bed is reached for flooding, exemplary sensor readings of $\Delta p = \pm 15\,\mathrm{mbar}$ should be considered[9]. Although readings of $\Delta p = 15\,\mathrm{mbar}$ and $\Delta p = -15\,\mathrm{mbar}$ could generally be expected depending on the arrangement of the pressure lines, uncertainty analysis is only carried out for $\Delta p = 15\,\mathrm{mbar}$ (equivalent to a sensor signal of $16.8\,\mathrm{mA}$), which is the higher sensor output signal and thus, affected by the higher uncertainty. The uncertainty budget of pressure sensors P202 and P203 is given in table D.12.

Table D.12.: Uncertainty budget for pressure sensors P202 and P203, $\Delta p = 15\,\mathrm{mbar}$ ($16.8\,\mathrm{mA}$), specification for sensor as per (VEGA, 2014), specification for data acquisition as per (Keysight Technologies, 2020)

uncertainty component	specification	PDF	divisor	standard uncertainty
-	mA	-	-	mA
sensor	± 0.02	rectangular	$\sqrt{3}$	0.012
data acquisition	± 0.0057	rectangular	$\sqrt{3}$	0.0033
combined standard uncertainty				0.012
expanded uncertainty ($k = 2$)				0.024
conversion based on sensor resolution				mbar
combined standard uncertainty				0.038
expanded uncertainty ($k = 2$)				0.076

[9]The height of each bed section installed in the column is 1224 mm. Furthermore, a specific pressure drop of $12\,\mathrm{mbar\,m^{-1}}$ is commonly used for *Mellapak*-type packings at flooding (Lockett et al., 2006). Therefore, a maximum pressure drop of $\Delta p = 12\,\mathrm{mbar\,m^{-1}} \cdot 1.224\,\mathrm{m} \approx 15\,\mathrm{mbar}$ is obtained. A possible inverse arrangement of the pressure lines is considered by the respective negative value.

D.2.6.3. Feed Flow

As readings from the Coriolis mass flow meter F101 are acquired via its digital communication interface, all accuracy information required for the uncertainty analysis are directly obtained from the manufacturer's specification. According to the specification, see table A.4, the accuracy of the sensor reading depends on the actual value of the mass flow. The uncertainty analysis for a nominal mass flow of $\dot{m}_\mathrm{F} = 14\,\mathrm{kg/h}$, as used for experiment *604-2*, is summarized in table D.13.

Table D.13.: Uncertainty budget for mass flow meter F101, $\dot{m}_\mathrm{F} = 14\,\mathrm{kg\,h^{-1}}$, recorded data from experiment *604-2*, specification as per (Krohne, 2016)

uncertainty component	specification	PDF	divisor	standard uncertainty
-	$\mathrm{kg\,h^{-1}}$	-	-	$\mathrm{kg\,h^{-1}}$
sensor	± 0.021	rectangular	$\sqrt{3}$	0.012
combined standard uncertainty				0.012
expanded uncertainty ($k = 2$)				0.024

The molar feed flow $\dot{F}$ is calculated with the feed mass flow $\dot{m}_\mathrm{F}$ and the molar mass of the feedstock mixture M_F according to equation (3.16a), which allows propagating relevant uncertainties, $u_\mathrm{c}(\dot{m}_\mathrm{F})$ and $u_\mathrm{c}(M_\mathrm{F})$.

D.2.6.4. Distillate and Bottom Product Flows

As both distillate and bottoms mass flows are measured gravimetrically, the uncertainties of the scales W401 and W402 need to be analyzed. (Ellison and Williams, 2012) provide an extensive overview of the evaluation of common sources of uncertainties for scales and balances. However, the data required for a full uncertainty quantification were not available for the scales used in this work. Therefore, uncertainties are quantified with sparse specifications, see table A.4, and are only valid to a limited extent. The uncertainties of scales W401 and W402 are evaluated in tables D.14 and D.15. In contrast to (Kern & Sohn, 2021), (Sartorius, 2014) do not give any specifications for both the reproducibility and the linearity of the scale. Therefore, suitable approximations as suggested by (Ellison and Williams, 2012) are used.

Table D.14.: Uncertainty budget for scale W401, specifications as per (Kern & Sohn, 2021)

uncertainty component	specification	PDF	divisor	standard uncertainty
-	g	-	-	g
readability	0.1	rectangular	$2 \cdot \sqrt{3}$	0.03
reproducibility	0.1	rectangular	$2 \cdot \sqrt{3}$	0.03
linearity	± 0.3	rectangular	$\sqrt{3}$	0.17
combined standard uncertainty				0.18
expanded uncertainty ($k = 2$)				0.36

Table D.15.: Uncertainty budget for scale W402, specifications as per (Sartorius, 2014) or approximated according to (Ellison and Williams, 2012)

uncertainty component	specification	PDF	divisor	standard uncertainty
-	g	-	-	g
readability	1.0	rectangular	$2 \cdot \sqrt{3}$	0.29
reproducibility	approximation: half of readability			0.50
linearity	approximation: half of readability			0.50
combined standard uncertainty				0.76
expanded uncertainty ($k = 2$)				1.52

As elaborated in section 3.5.2 and illustrated in figure E.2, multiple weighing cycles are evaluated by linear regression. While the uncertainty components listed in tables D.14 and D.15 are passed to each regression, potential systematic offsets between scale readings are neglected as they should cancel out each other. After removing potential outliers by IQR, remaining mass flows are arithmetically averaged to obtain a single mass flow for the respective steady state. Therefore, the associated standard uncertainty is quantified by the standard deviation of the mean, see equation (D.5), and propagated to further calculations.

To be consistent with section 3.5 and figure E.2, exemplary uncertainty quantification is shown for experiment *604-2*. To calculate the uncertainty associated with the distillate and bottoms mass flows, $u(\dot{m}_\mathrm{D})$ and $u(\dot{m}_\mathrm{B})$, respective mass flows are recalled from figures E.2a and E.2b. The according arithmetic means and their standard deviations are summarized in table D.16.

Table D.16.: Uncertainty evaluation for distillate and bottoms mass flows, $\dot{m}_\mathrm{D}$ and $\dot{m}_\mathrm{B}$, regression results as per figures E.2a and E.2b

weighing cycle	$\dot{m}_\mathrm{D}$	$\dot{m}_\mathrm{B}$
-	$\mathrm{kg\,h^{-1}}$	$\mathrm{kg\,h^{-1}}$
1	12.67	0.85
2	12.62	1.04
3	12.65	1.04
4	12.61	1.32
5	12.63	1.40
6	12.68	1.18
arithmetic mean	12.642	1.14
(combined) standard uncertainty	0.030	0.20
expanded uncertainty ($k = 2$)	0.060	0.40

Molar distillate and bottom product flows, $\dot{D}$ and $\dot{B}$, are calculated according to equations (3.16b) and (3.16c), respectively, which allows propagating relevant uncertainties $u_\mathrm{c}(\dot{m}_\mathrm{D})$ and $u_\mathrm{c}(M_\mathrm{D})$ as well as $u_\mathrm{c}(\dot{m}_\mathrm{B})$ and $u_\mathrm{c}(M_\mathrm{B})$.

E. Data Evaluation

E.1. Algebraic Integration for NTU

The number of transfer units $\mathrm{NTU_{oG}}$ was introduced in equation (2.54a). While $\mathrm{NTU_{oG}}$ is often calculated numerically using discrete values, see section 2.2.3.2, an algebraic calculation of $\mathrm{NTU_{oG}}$ seems to be less common and was not found in the literature. Therefore, suitable procedures to solve equation (2.54a) algebraically are presented here. Although the respective procedure slightly varies depending on the reflux condition of the column (total vs. partial reflux), the underlying concepts are based on the same approach.

As the molar fraction in the bulk of the gas phase y^{b} is defined by the operating line(s), y^{b} is substituted with the term y^{op}. Furthermore, both the equilibrium curve y^{eq} and the bulk concentration y^{b} are functions of the molar fraction in the liquid phase x. Functions $f_1(x)$ and $f_2(x)$ are introduced to obtain a more general expression for $\mathrm{NTU_{oG}}$. Therefore, equation (2.54a) can be written as:

$$\begin{aligned}
\mathrm{NTU_{oG}} &= \int_{y_{\mathrm{bottom}}}^{y_{\mathrm{top}}} \frac{1}{y^{\mathrm{eq}} - y^{\mathrm{b}}}\,\mathrm{d}y \\
&= \int_{y_{\mathrm{bottom}}}^{y_{\mathrm{top}}} \frac{1}{y^{\mathrm{eq}} - y^{\mathrm{op}}}\,\mathrm{d}y \\
&= \int_{y_{\mathrm{bottom}}}^{y_{\mathrm{top}}} \frac{1}{f_1(x) - f_2(x)}\,\mathrm{d}y
\end{aligned} \tag{E.1}$$

The equilibrium curve y^{eq}, which is substituted by $f_1(x)$, was already introduced in equation (2.3) and is recalled here:

$$y^{\mathrm{eq}} = \frac{\alpha_{12} \cdot x_1}{1 + (\alpha_{12} - 1) \cdot x_1} \tag{2.3}$$

Equation (E.1) shows that the limits of integration as well as the integration variable are in y, while the integrand is a function of x. These can be homogenized by introducing the generalized function $y = f(x)$, the inverse function $x = g(y)$ and the first derivative $f'(x)$:

$$y = f(x) \tag{E.2a}$$

$$x = g(y) \tag{E.2b}$$

$$\mathrm{d}y = f'(x)\,\mathrm{d}x \tag{E.2c}$$

E.1.1. Total Reflux

Considering total reflux, the operating line is equal to the diagonal. Therefore, both $f_1(x)$ and $f_2(x)$ required to solve equation (E.1) are known:

$$f_1(x) = \frac{\alpha \cdot x}{(\alpha - 1) \cdot x + 1} \tag{E.3a}$$

$$f_2(x) = x \tag{E.3b}$$

Furthermore, equation (E.3b) is used to define the inverse function $g_2(y_i)$ as well as the derivative $f_2'(x)$:

$$g_2(y_i) = x_i \tag{E.4a}$$

$$f_2'(x) = 1 \tag{E.4b}$$

Combining equations (E.3a) and (E.4) with equation (E.1) results in an integral for $\mathrm{NTU_{oG}}$ which can be evaluated algebraically:

$$\begin{aligned} \mathrm{NTU_{oG}} &= \int_{g_2(y_{\mathrm{bottom}})}^{g_2(y_{\mathrm{top}})} \frac{1}{f_1(x) - f_2(x)} \cdot f_2'(x)\,\mathrm{d}x \\ &= \int_{x_{\mathrm{bottom}}}^{x_{\mathrm{top}}} \frac{1}{\frac{\alpha \cdot x}{(\alpha-1)\cdot x+1} - x}\,\mathrm{d}x \end{aligned} \tag{E.5}$$

E.1.2. Partial Reflux

For partial reflux, both the rectifying and the stripping section operating lines, y^{ROL} and y^{SOL}, need to be considered. Since both operating lines and the feed line y^{FL} intersect at $(x_{\mathrm{is}}, y_{\mathrm{is}})$, a non-smooth function $f_2(x)$ is obtained in the integrand requiring a sectionwise integration.

The respective operating lines were already defined in equations (2.23) and (2.27). In addition, the feed line y^{FL} is recalled from equation (2.34):

$$y^{\mathrm{ROL}} = \frac{\nu}{\nu + 1} \cdot x + \frac{1}{\nu + 1} \cdot x_{\mathrm{D}} \tag{2.23}$$

$$y^{\mathrm{SOL}} = \frac{\nu'}{\nu' - 1} \cdot x - \frac{1}{\nu' - 1} \cdot x_{\mathrm{B}} \tag{2.27}$$

$$y^{\mathrm{FL}} = \frac{q}{q - 1} \cdot x + \frac{1}{q - 1} \cdot x_{\mathrm{F}} \tag{2.34}$$

The reboil ratio ν', which is part of equation (2.27), is commonly not known explicitly, but

can be determined based on the intersection between the rectifying section operating line and the feed line:

$$
\begin{aligned}
& y^{\mathrm{ROL}} \overset{!}{=} y^{\mathrm{FL}} \\
& \quad \Longrightarrow (x_{\mathrm{is}}, y_{\mathrm{is}}) \\
& \quad \underset{(2.27)}{\Longrightarrow} \nu'
\end{aligned}
$$

The intersection $(x_{\mathrm{is}}, y_{\mathrm{is}})$ also defines the bounds for the sectionwise integration. Combining

$$f_1(x) = y^{\mathrm{eq}} \tag{E.7a}$$

$$f_3(x) = y^{\mathrm{SOL}} \tag{E.7b}$$

$$f_4(x) = y^{\mathrm{ROL}} \tag{E.7c}$$

with equations (E.1), (E.2b) and (E.2c) results in:

$$
\begin{aligned}
\mathrm{NTU}_{\mathrm{oG}} &= \int_{y_{\mathrm{bottom}}}^{y_{\mathrm{top}}} \frac{1}{f_1(x) - f_2(x)} \,\mathrm{d}y \\
&= \int_{y_{\mathrm{bottom}}}^{y_{\mathrm{is}}} \frac{1}{f_1(x) - f_3(x)} \,\mathrm{d}y + \int_{y_{\mathrm{is}}}^{y_{\mathrm{top}}} \frac{1}{f_1(x) - f_4(x)} \,\mathrm{d}y \\
&= \int_{g_3(y_{\mathrm{bottom}})}^{g_3(y_{\mathrm{is}})} \frac{1}{f_1(x) - f_3(x)} \cdot f_3'(x) \,\mathrm{d}x + \int_{g_4(y_{\mathrm{is}})}^{g_4(y_{\mathrm{top}})} \frac{1}{f_1(x) - f_4(x)} \cdot f_4'(x) \,\mathrm{d}x
\end{aligned}
\tag{E.8}
$$

Since $f_1(x)$, $f_3(x)$ and $f_4(x)$ are defined in equations (E.7a) to (E.7c), the inverse functions $g_3(y_i)$ and $g_4(y_i)$ as well as the derivatives $f_3'(x)$ and $f_4'(x)$ required for equation (E.8) can be determined. Integrating the obtained equation algebraically finally results $\mathrm{NTU}_{\mathrm{oG}}$.

E.2. Outlier Removal with IQR

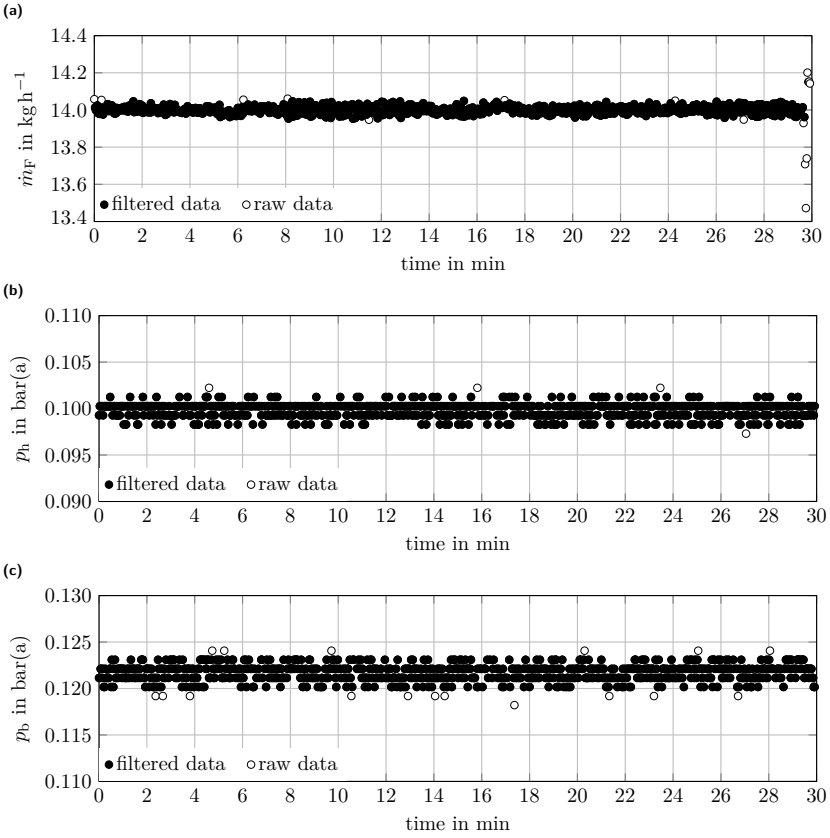

Figure E.1.: Exemplary outlier removal with IQR for recorded process data of experiment *604-2*;
(a): feed mass flow, sensor F101, $\dot{m}_F = 14.00(2)\,\mathrm{kg\,h^{-1}}$;
(b): column head pressure, sensor P201, $p_h = 0.0998(13)\,\mathrm{bar(a)}$;
(c): pressure below bed, sensor P204, $p_b = 0.1217(14)\,\mathrm{bar(a)}$;
combined standard uncertainties not indicated to improve readability

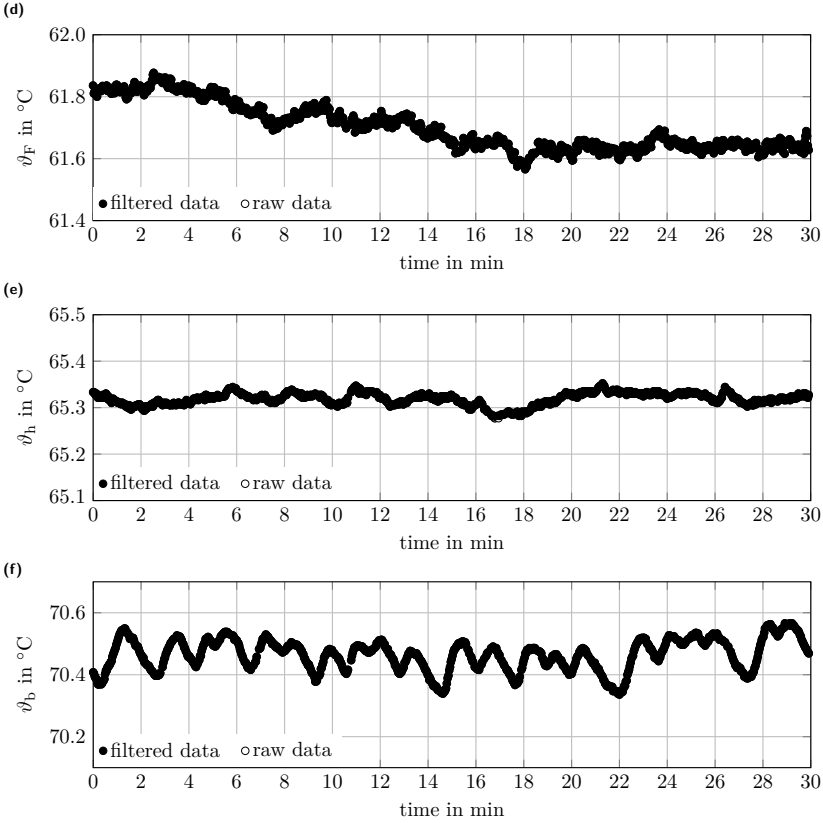

Figure E.1.: Exemplary outlier removal with IQR for recorded process data of experiment *604-2*;
(d): feed temperature, sensor T101, $\vartheta_F = 61.70(58)\,^\circ\mathrm{C}$;
(e): column head temperature, sensor T102, $\vartheta_h = 65.32(14)\,^\circ\mathrm{C}$;
(f): temperature below packed bed, sensor T214, $\vartheta_b = 70.46(15)\,^\circ\mathrm{C}$;
combined standard uncertainties not indicated to improve readability (continued)

Table E.1.: Comparison of raw and filtered time series of plant sensor readings, uncertainties not stated to ensure consistent statistical measures, exemplary evaluation of experiment *604-2*

tag	parameter	unit	dataset	values	mean	min	Q_1	Q_2	Q_3	max
F101	$\dot{m}_\mathrm{F}$	$\mathrm{kg\,h^{-1}}$	raw	816	13.9997	13.4719	13.9874	13.9992	14.0124	14.2011
			filtered	800	14.0000	13.9528	13.9875	13.9991	14.0118	14.0487
P201	p_h	bar(a)	raw	816	0.0998	0.0973	0.0993	0.1003	0.1003	0.1022
			filtered	812	0.0998	0.0983	0.0993	0.1003	0.1003	0.1012
P204	p_b	bar(a)	raw	816	0.1217	0.1182	0.1211	0.1221	0.1221	0.1241
			filtered	799	0.1217	0.1202	0.1211	0.1221	0.1221	0.1231
T101	ϑ_F	°C	raw	816	61.7016	61.5657	61.6387	61.6752	61.7586	61.8771
			filtered	816	61.7016	61.5657	61.6387	61.6752	61.7586	61.8771
T102	ϑ_h	°C	raw	816	65.3190	65.2773	65.3103	65.3213	65.3303	65.3523
			filtered	811	65.3192	65.2823	65.3103	65.3213	65.3303	65.3523
T214	ϑ_b	°C	raw	816	70.4644	70.3359	70.4279	70.4719	70.5049	70.5659
			filtered	816	70.4643	70.3359	70.4279	70.4719	70.5049	70.5659

E.3. Mass Flow Determination with Linear Regression

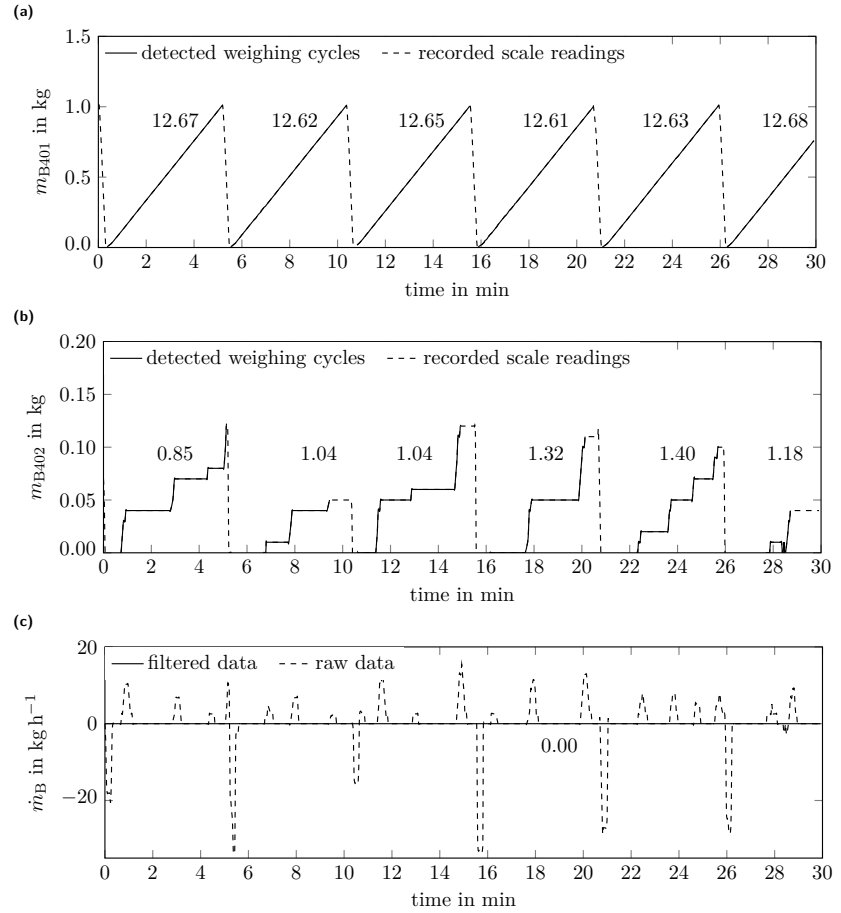

Figure E.2.: Exemplary determination of distillate and bottoms mass flow by linear regression for experiment *604-2*, numbers annotated in diagrams state determined mass flows in $\mathrm{kg\,h^{-1}}$;
(a): distillate mass flow determined from readings of scale W401, tank B401, $\dot{m}_D = 12.64(3)\,\mathrm{kg\,h^{-1}}$;
(b): bottoms mass flow determined from readings of scale W402, tank B402, $\dot{m}_B = 1.14(20)\,\mathrm{kg\,h^{-1}}$;
(c): bottoms mass flow calculated by the plant control system, $\dot{m}_B = 0.00\,\mathrm{kg\,h^{-1}}$ is obtained after filtering which does not represent steady-state operating conditions correctly

E.4. Constructability Check for McCabe-Thiele Approach

To exclude thermodynamically invalid sets of input parameters and to ensure constructability of McCabe-Thiele stage constructions, the conditions summarized in table E.2 are evaluated during data processing. Performed checks cover the order of mixture compositions x_F, x_B and x_D as well as the position of the intersection between feed line and stripping line (x_is, y_is) in relation to the equilibrium curve.

Table E.2.: Conditions of constructability check for McCabe-Thiele stage constructions

	condition to check
1	order of compositions
	1.1 $x_\mathrm{B} < x_\mathrm{F}$
	1.2 $x_\mathrm{F} < x_\mathrm{D}$
2	intersection between feed line and stripping line
	2.1 $y_\mathrm{is} < y^\mathrm{eq}(x_\mathrm{is})$
	2.2 $x^\mathrm{eq}(y_\mathrm{is}) < x_\mathrm{is}$

E.5. Software

To reduce manual errors in experiment evaluation, an automated data processing routine was implemented using the *Python* programming language (Python, 2022). In this section, core features and software structure are documented briefly. The code base can be retrieved from the supplemental data repository, see (Gutperl and Wolke, 2024).

E.5.1. Data Evaluation Workflow

The data evaluation procedure comprises multiple consecutive steps. The data loaded from data storage, see appendix E.5.6.3, and intermediate results are partially validated against each other to detect inconsistent datasets and to abort evaluation on critical errors. A brief overview of the implemented workflow is summarized in table E.3.

Table E.3.: Overview of data evaluation workflow with methods used for uncertainty quantification (UQ); LPU: law of propagation of uncertainty, see equation (D.10); MCM: Monte Carlo methods, see appendix D.1.2

	evaluation step	UQ	for reference, see
I.	load constant data and associated uncertainties[a]	LPU	
1	column geometry and packing specifications		table A.1
2	sensor specifications		appendices A.3 to A.5
3	density calibration curve		appendix C.3.1
4	molar masses of pure components		table C.1
5	NRTL parameters		appendix C.11
6	DIPPR parameters for physical properties		appendices C.3.2 to C.8.2
II.	prepare experiment evaluation	LPU	
1	metadata		
2	nominal operating conditions		
	2.1 $p_{\mathrm{h,nom}}$		
	2.2 $\dot{m}_{\mathrm{D,nom}}$ and $\dot{m}_{\mathrm{F,nom}}$		
3	plant data records and extract steady-state data		
4	results of sample analyses		
5	calculate steady-state liquid and vapor compositions		
	5.1 of in- and output streams x_{F}, x_{D} and x_{B}		section 3.5.1
	5.2 at mid-bed position x_{mb} and y_{mb}		equations (3.10a) and (3.10b)

Table E.3.: Overview of data evaluation workflow with methods used for uncertainty quantification (UQ); LPU: law of propagation of uncertainty, see equation (D.10); MCM: Monte Carlo methods, see appendix D.1.2 (continued)

	evaluation step	UQ	for reference, see
III.	evaluate operating conditions[b]	LPU	
1	mass flows $\dot{m}_\mathrm{D}$ and $\dot{m}_\mathrm{B}$		table 3.6
	1.1 feed mass flow $\dot{m}_\mathrm{F}$ (flow meter F101)		
	1.2 product mass flows $\dot{m}_\mathrm{D}$ and $\dot{m}_\mathrm{B}$ (underfloor weighing)		appendix E.3
2	molar flows $\dot{F}$, $\dot{D}$ and $\dot{B}$		equation (3.16)
3	temperatures		
	3.1 above and below bed, ϑ_h and ϑ_b		table 3.6
	3.1 at mid-bed position T_mb		equation (3.10c)
4	pressures		
	4.1 above and below bed, p_h and p_b		table 3.6
	4.2 at mid-bed position p_mb		equation (3.10d)
	4.3 specific pressure drop Δp_bed		equation (3.13)
5	stream ratios $\dot{m}_\mathrm{F}\,\dot{m}_\mathrm{D}^{-1}$ and $\dot{F}\,\dot{D}^{-1}$		equation (3.2c)
6	column load		
	6.1 liquid load w_L		equation (3.11)
	6.2 f-factor f_G		equation (3.12)
7	material balances and corresponding deviations		
	7.1 mass balance		equations (3.15) and (3.17)
	7.2 molar balance		equations (2.12) and (3.18)

Table E.3.: Overview of data evaluation workflow with methods used for uncertainty quantification (UQ); LPU: law of propagation of uncertainty, see equation (D.10); MCM: Monte Carlo methods, see appendix D.1.2 (continued)

	evaluation step	UQ	for reference, see
8	compare nominal and actual operating conditions		
IV.	perform McCabe-Thiele stage constructions	MCM/LPU	
1	prepare sets of random input parameters[c]	-	appendices D.1.2 and D.2.1
	1.1 liquid molar fractions x_F, x_D and x_B		
	1.2 stream ratio $\dot{m}_\mathrm{F}\,\dot{m}_\mathrm{D}^{-1}$		
	1.3 pressures p_h and p_mb		
	1.4 feed temperature ϑ_F		
2	stage construction for each set of input parameters	MCM	
	2.1 calculate feed properties		
	2.1.1 subcooling $T_{\mathrm{F,boil}}$		appendix C.12
	2.1.2 enthalpies h'_F and h_F		appendix C.4
	2.1.3 enthalpy of vaporization $\Delta h_{\mathrm{vap,F}}$		appendix C.5
	2.1.4 feed condition q		equation (2.16)
	2.2 determine operating lines		
	2.2.1 stripping line		equation (2.27)
	2.2.2 feed line		equation (2.34)
	2.2.3 liquid molar fraction x_is (at SOL/FL intersection)		figure 2.4
	2.4 check constructability, abort if check failed		appendix E.4
	2.5 quantify separation performance		section 3.5.4.1

Table E.3.: Overview of data evaluation workflow with methods used for uncertainty quantification (UQ); LPU: law of propagation of uncertainty, see equation (D.10); MCM: Monte Carlo methods, see appendix D.1.2 (continued)

	evaluation step	UQ	for reference, see
	2.5.1 number of theoretical stages N_{th} and $N_{\mathrm{th,dec}}$		equation (3.20) and figure 3.7
	2.5.2 $\mathrm{NTU_{oG}}$ by integration		equation (2.54a)
3	summarize obtained result distributions[d]	-	
	3.1 set of input parameters		
	3.2 result of constructability check		
	3.3 liquid molar fraction x_{is}		
	3.4 feed condition q		
	3.5 boiling point feed $T_{\mathrm{F,boil}}$		
	3.6 number of theoretical stages N_{th} and $N_{\mathrm{th,dec}}$		
	3.7 relative volatility $\overline{\alpha}_{12}$		
	3.8 $\mathrm{NTU_{oG}}$		
4	derive further intermediate results	LPU	
	4.1 feed subcooling ΔT_{F}		equation (3.14)
	4.2 HETP using N_{th} obtained from MCM		equation (2.44)
	4.3 relative volatility $\overline{\alpha}_{12}$		equation (3.26)
	4.4 slope of equilibrium curve m		equation (3.25)
	4.5 stripping factor λ		equation (3.24)
	4.6 $\mathrm{NTU_{oG}}$ from $N_{\mathrm{th,dec}}$		equation (2.69)

Table E.3.: Overview of data evaluation workflow with methods used for uncertainty quantification (UQ); LPU: law of propagation of uncertainty, see equation (D.10); MCM: Monte Carlo methods, see appendix D.1.2 (continued)

evaluation step		UQ	for reference, see
V. determine mass transfer		LPU	
1	calculate mid-bed liquid molar fraction $x_{\mathrm{mb,is}}$		equation (3.23)
2	calculate physical properties with $x_{\mathrm{mb,is}}$, y_{mb} and T_{mb}		
	2.1 densities		appendices C.3.2 and C.3.3
	2.2 viscosities		appendix C.6
	2.3 surface tension		appendix C.7
3	estimate diffusion coefficients $D_{\mathrm{L,12}}$ and $D_{\mathrm{G,12}}$		appendix C.8
4	evaluate model-specific fluiddynamics		equations (2.70) to (2.87)
5	estimate mass transfer coefficients k_{L} and k_{G}		table 3.8
	5.1 with original correlations		
	5.2 with revised correlations		
6	evaluate separation performance		
	6.1 $\mathrm{HTU_L}$, $\mathrm{HTU_G}$ and $\mathrm{HTU_{oG}}$		equations (2.57a) and (2.92)
	6.2 HETP from $\mathrm{HTU_{oG}}$		equation (2.65)
	6.3 bed height H_{bed} from $\mathrm{HTU_{oG}}$ and $\mathrm{NTU_{oG}}$		equation (2.54a)
	6.3.1 with $\mathrm{NTU_{oG}}$ from integration		
	6.3.2 with $\mathrm{NTU_{oG}}$ from $N_{\mathrm{th,dec}}$		

Table E.3.: Overview of data evaluation workflow with methods used for uncertainty quantification (UQ); LPU: law of propagation of uncertainty, see equation (D.10); MCM: Monte Carlo methods, see appendix D.1.2 (continued)

evaluation step	UQ	for reference, see
VI. save results to data storage	-	
1 convert data into storage format		
1.1 base data		
1.1.1 metadata		
1.1.2 nominal operating parameters		
1.1.3 density sample analysis results		
1.1.4 plant data records		
1.2 results data		
1.1.1 operating conditions		
1.1.2 mass balance		
1.1.3 molar balance		
1.1.4 separation performance		
1.1.5 mass transfer		
2 export data to HDF5 file		

[a] uncertainties determined based on manufacturer specifications and sensor calibrations are consistently propagated through data evaluation, see appendix D for details

[b] evaluation includes outlier removal with IQR, see equation (3.8) and appendix E.2

[c] $N_{\mathrm{MC}} = 1 \cdot 10^6$ sets of random input parameters sampled from probability density functions described by associated uncertainties

[d] arithmetic means and corresponding standard deviations are calculated for each result value and interpreted as estimates and associated combined standard uncertainty, see appendix D.1.2

E.5.2. Package Dependencies and Installation

Data processing and data handling are heavily based on *NumPy* (Harris et al., 2020), *pandas* (McKinney, 2010; Pandas, 2021) and *SciPy* (Virtanen et al., 2020). Uncertainty estimation and quantification, see appendix D.2, are partially based on the *GUM Tree Calculator* (Hall, 2022) and *uncertainties* (Lebigot, 2017) packages as well as the *SymPy* (Meurer et al., 2017) library. A command-line interface (CLI) for simplified mass imports and evaluation of multiple experiments was implemented using *Click* (Pallets Organization, 2014).

To set up the Python toolchain for data evaluation, using a *conda*-based environment is recommended. For this, required package dependencies are specified in the `environment.yaml` file, which can be used to automatically resolve and install all dependencies in a clean Python environment.

E.5.3. Usage

Common routines required for data import and evaluation are conveniently accessible through a command-line interface (CLI) provided by `cli.py`. An overview of available commands and details about how to use each command are available via the `--help` flag, see listings E.1 and E.2. To retrace or debug performed actions, the log file `processing.log` is created upon execution.

Listing E.1: Show usage information for command-line interface

```
$ python cli.py --help
Usage: cli.py [OPTIONS] COMMAND [ARGS]...

  CLI for data evaluation and management

Options:
  --help  Show this message and exit.

Commands:
  convert      Subcommands for converting data
  delete       Subcommands for deleting data
  evaluate     Subcommands for experiment evaluation
  import       Subcommands for experiment import
  list         Subcommands for listings
  postprocess  Subcommands for post-processing data
```

Listing E.2: Show usage information for experiment run evaluation

```
$ python cli.py evaluate run --help
Usage: cli.py evaluate run [OPTIONS]

  Evaluate specific run(s)

Options:
  -i, --identifier <INTEGER INTEGER>...
                                  [required]
  -m, --evaluation_mode TEXT
  -s, --number_of_samples INTEGER
  -w, --number_of_workers INTEGER
  -d, --debug_mode
  --help                          Show this message and exit.
```

E.5.4. Execution Time and Scalability

Since the data evaluation routine includes Monte Carlo simulations, the runtime required for data processing becomes non-negligible. However, as the underlying implementation supports multiprocessing, corresponding calculations are automatically distributed across all available logical CPU cores.

Data processing was initially performed on a 10 core CPU and later transferred to a 20 core CPU to speed up calculations. To evaluate the scalability of the data evaluation routine, the number of draws used for Monte Carlo simulations N_{MC} was varied. Runtimes achieved on both systems are illustrated in figure E.3. As generation and termination of worker processes dominate execution times for $N_{\mathrm{MC}} < 10^4$ due to the related system overhead, a non-linear correlation is obtained in the corresponding range. However, this influence decreases with an increasing number of calculations. Therefore, a linear correlation is obtained for $N_{\mathrm{MC}} \geq 10^4$ and data evaluation is approximately twice as fast when doubling the core count.

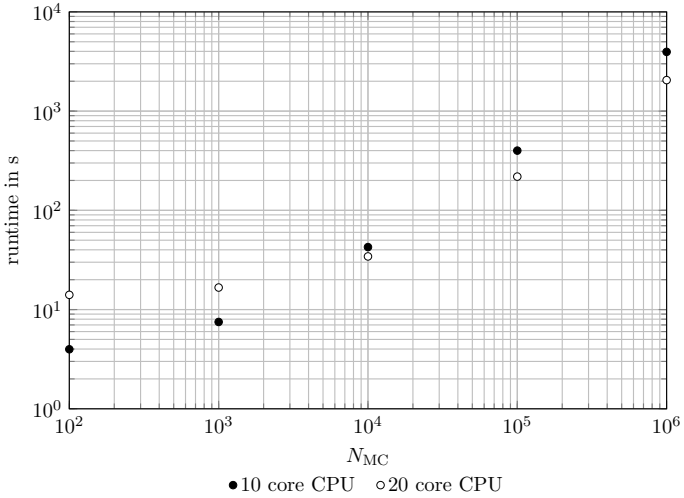

Figure E.3.: Runtime of data evaluation routine in dependence of the number of samples N_{MC} used for MCM, evaluation of single experiment, averages obtained from three consecutive executions, standard deviations smaller than marker size; 10 core CPU: Apple M1 Pro 10 Core, 32 GB memory (Apple MacBook Pro 2021, 14 in); 20 core CPU: Apple M1 Ultra 20 Core, 64 GB memory (Apple Mac Studio 2022)

E.5.5. Data Files

To ensure a consistent data format throughout all experiments, relevant raw data were parsed into a unified data structure and stored in the HDF5 format (Hierarchical Data Format, Version 5) before further evaluation. In addition, both intermediate values and final results obtained from data evaluation were added to the HDF5 file of the according experiment. Therefore, the HDF5 files available in the supplemental data repository, see (Gutperl and Wolke, 2024), contain all datasets relevant to re-evaluate or analyze a single experiment.

The data stored in each file is structured using the *PyTables* format[1]. Each filename is formatted as `P<experiment number>_<run number>.h5`. Although direct access to the stored data files should generally not be required, since common evaluation and post-processing functions are provided by the command line interface, see appendix E.5.3, the respective files can be opened with any HDF5-compatible software[2]. The structure of the data storage directory is briefly explained in appendix E.5.6.3.

[1] Data were stored using the `pandas.HDFStore` interface which is based on *PyTables*, see (PyTables, 2002) for details.
[2] *ViTables* was used in this work, see (Mas, 2008) for details.

E.5.6. Software and Directory Structure

To keep the codebase and the experiment datasets decoupled from each other, independent subdirectories are used. Details about the structure and the contents of the corresponding directories are summarized in the following sections.

E.5.6.1. Root Directory

A short description about each item provided in the root directory is given below:

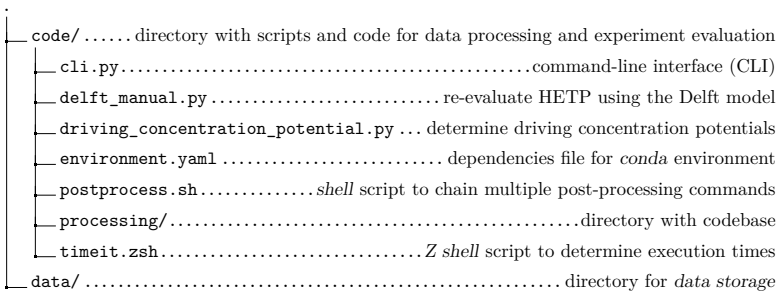

Figure E.4.: Structure of root directory

E.5.6.2. Codebase

The codebase is structured as Python packages and subpackages containing related calculation routines or functions. As the package names are considered self-descriptive, no additional explanations are given about the routines provided. The codebase is structured as follows:

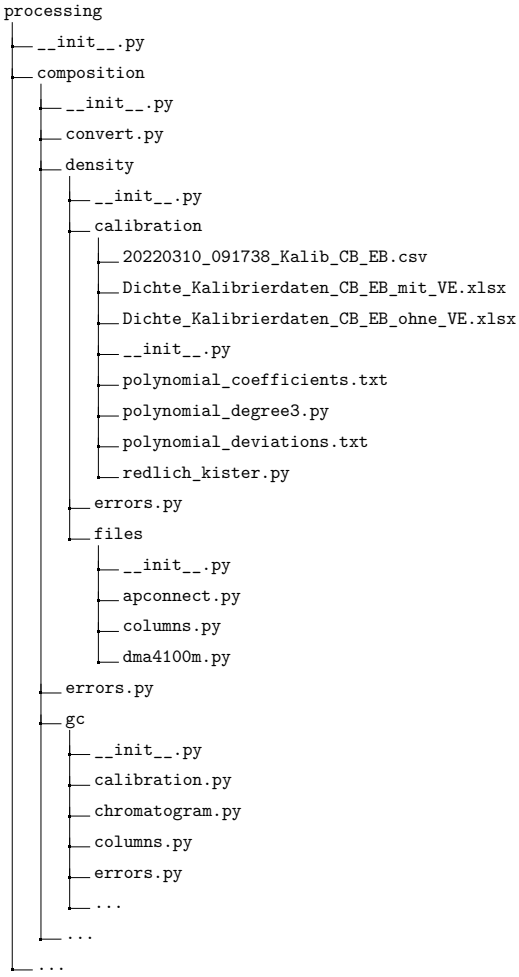

Figure E.5.: Structure of codebase

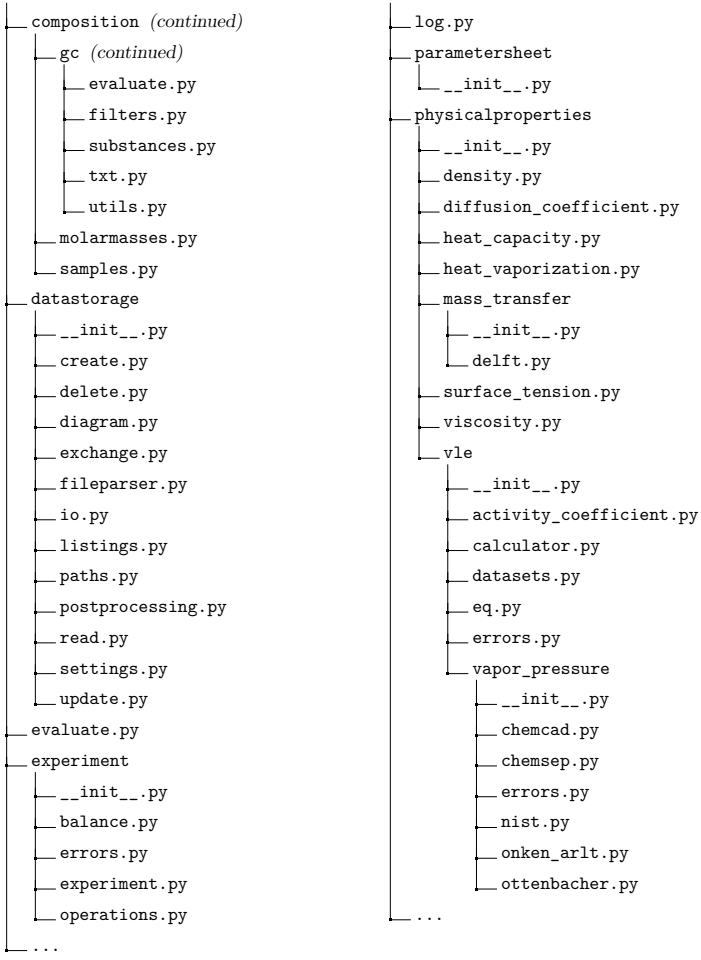

Figure E.5.: Structure of codebase (continued)

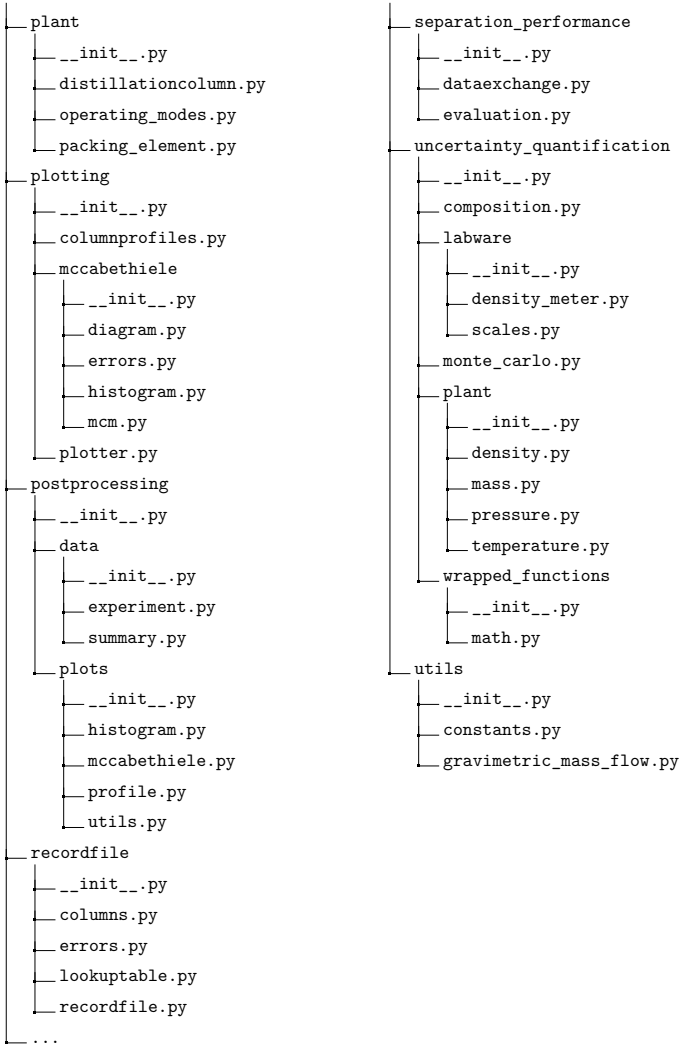

Figure E.5.: Structure of codebase (continued)

E.5.6.3. Data Storage

The data storage contains files of imported and/or evaluated experiments. Details about file format and file structure were already given in appendix E.5.5. The directory used for data storage is structured as follows:

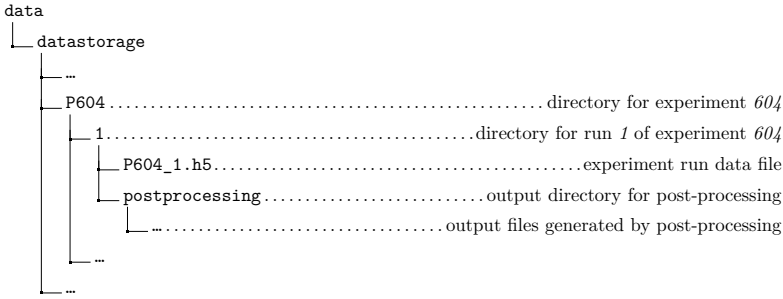

Figure E.6.: Structure of data storage directory

F. Experimental Results

A reduced set of intermediate and final results is tabulated in this appendix. Although missing data can be determined using the values given in the following tables and the calculation procedures presented in section 3.5, the complete set of exported results is available in the data repository of this work, see (Gutperl and Wolke, 2024).

In addition to the tabulated values, supplemental diagrams illustrating operating parameters, operational characteristics and separation performance as well as associated combined standard uncertainties $u_c(\cdot)$ are presented.

F.1. Tabulated Results

intentionally left blank

Table F.1.: Column load

no.	operating mode	$\dot{F}\,\dot{D}^{-1}$	f_G	w_L	$\dot{m}_F$	$\dot{m}_D$	$\dot{m}_B$	λ
-	-	-	$Pa^{0.5}$	$m^3\,m^{-2}\,h^{-1}$	$kg\,h^{-1}$	$kg\,h^{-1}$	$kg\,h^{-1}$	-
P500-1	simulated total reflux	0.987(16)	0.863(30)	2.063(77)	3.999(61)	4.053(18)	0.00	0.998(16)
P500-2	simulated total reflux	1.006(14)	0.848(30)	2.076(74)	4.001(41)	3.980(38)	0.00	0.986(14)
P501-1	simulated total reflux	1.004(12)	1.278(46)	3.13(11)	6.000(21)	5.977(70)	0.00	0.992(12)
P501-2	simulated total reflux	1.024(25)	1.251(52)	3.13(11)	5.999(26)	5.86(14)	0.00	0.976(24)
P502-1	simulated total reflux	0.9996(90)	1.891(66)	4.68(16)	8.998(59)	9.008(55)	0.00	0.9954(91)
P502-2	simulated total reflux	1.0031(95)	1.893(65)	4.69(16)	9.006(76)	8.979(38)	0.00	0.9938(95)
P503-1	simulated total reflux	1.0058(58)	2.480(85)	6.22(21)	12.004(69)	11.9397(73)	0.00	0.9846(60)
P503-2	simulated total reflux	1.011(22)	2.46(10)	6.24(21)	12.000(23)	11.87(26)	0.007(80)	0.984(22)
P504-1	simulated total reflux	1.0022(45)	2.812(97)	7.31(25)	13.997(42)	13.969(43)	0.00	0.9997(67)
P504-2	simulated total reflux	1.0031(45)	2.819(97)	7.20(25)	14.001(37)	13.961(50)	0.00	0.9770(44)
P600-2	partial reflux	1.1040(72)	0.782(27)	2.088(71)	4.000(11)	3.630(22)	0.328(15)	0.9011(61)
P601-1	partial reflux	1.107(12)	1.158(40)	3.13(11)	5.998(61)	5.428(21)	0.71(25)	0.8963(99)
P601-2	partial reflux	1.111(12)	1.160(42)	3.13(11)	5.999(26)	5.410(55)	1.6(2.9)	0.8955(99)
P602-1	partial reflux	1.1038(61)	1.726(59)	4.67(16)	9.001(48)	8.1665(86)	0.93(16)	0.8930(50)
P602-2	partial reflux	1.1177(68)	1.717(59)	4.70(16)	9.001(44)	8.068(29)	0.62(51)	0.8891(55)
P603-1	partial reflux	1.1062(92)	2.270(78)	6.26(22)	12.003(93)	10.871(33)	1.11(23)	0.8962(75)
P603-2	partial reflux	1.1044(52)	2.284(78)	6.24(21)	12.002(51)	10.887(22)	0.70(19)	0.8930(42)
P604-1	partial reflux	1.1053(38)	2.606(89)	7.30(25)	14.000(35)	12.693(29)	1.08(65)	0.8961(34)
P604-2	partial reflux	1.1095(32)	2.606(89)	7.33(25)	14.000(22)	12.642(30)	1.14(20)	0.8979(26)

Table F.1.: Column load (continued)

no.	operating mode	$\dot{F}\,\dot{D}^{-1}$	f_G	w_L	$\dot{m}_F$	$\dot{m}_D$	$\dot{m}_B$	λ
-	-	-	$Pa^{0.5}$	$m^3\,m^{-2}\,h^{-1}$	$kg\,h^{-1}$	$kg\,h^{-1}$	$kg\,h^{-1}$	-
P626-1	partial reflux	2.0019(77)	0.970(33)	4.73(16)	9.000(23)	4.508(13)	4.551(34)	0.4968(19)
P626-2	partial reflux	2.019(10)	0.965(33)	4.73(16)	9.000(30)	4.469(17)	6.3(3.0)	0.4925(26)
P627-1	partial reflux	2.004(11)	1.288(44)	6.32(22)	11.999(62)	6.0046(89)	6.06(11)	0.4973(27)
P627-2	partial reflux	2.0078(81)	1.289(44)	6.33(22)	12.005(47)	5.9959(58)	6.045(51)	0.4967(21)
P628-1	partial reflux	2.0098(82)	1.494(51)	7.37(25)	14.003(54)	6.9855(84)	7.115(15)	0.4948(20)
P628-2	partial reflux	2.0061(92)	1.496(52)	7.36(25)	14.000(45)	6.997(23)	7.054(36)	0.4953(23)
P632-1	partial reflux	2.751(62)	0.942(39)	6.31(21)	11.998(31)	4.373(98)	7.12(71)	0.3617(82)
P633-1	partial reflux	3.003(17)	1.005(35)	7.37(25)	13.998(32)	4.674(25)	9.376(90)	0.3314(19)
P633-2	partial reflux	3.034(19)	0.998(35)	7.37(25)	14.000(33)	4.627(27)	11.0(3.6)	0.3282(21)
P700-1	total reflux	0.9985(12)	0.900(40)	2.136(95)	4.25(12)	4.25(12)	0.00	0.9536(16)
P700-2	total reflux	0.999 99(37)	0.853(32)	2.042(75)	3.991(58)	3.991(58)	0.00	0.9752(10)
P701-1	total reflux	0.9994(10)	1.279(46)	3.05(11)	6.012(59)	6.012(59)	0.00	0.9651(10)
P701-2	total reflux	1.000 080(47)	1.256(47)	3.01(11)	5.907(91)	5.907(91)	0.00	0.967 93(14)
P702-1	total reflux	1.000 27(37)	1.873(67)	4.55(16)	8.958(94)	8.958(94)	0.00	0.9634(12)
P702-2	total reflux	0.999 79(54)	1.939(67)	4.67(16)	9.223(53)	9.223(53)	0.00	0.9615(15)
P703-1	total reflux	1.0008(14)	2.432(85)	6.04(21)	11.719(78)	11.719(78)	0.00	0.9821(41)
P703-2	total reflux	1.000 05(22)	2.459(91)	6.06(22)	11.89(17)	11.89(17)	0.00	0.969 82(56)
P704-1	total reflux	1.000 69(73)	2.82(10)	7.12(25)	14.03(12)	14.03(12)	0.00	0.9615(19)
P704-2	total reflux	1.0006(12)	2.867(99)	7.24(25)	14.239(58)	14.239(58)	0.00	0.9644(36)

Table F.2.: Temperatures and pressures

no.	p_h	Δp_bed	p_mb	T_mb	ΔT_F	q
-	mbar(a)	$\mathrm{mbar\,m^{-1}}$	mbar(a)	°C	°C	-
P500-1	100.4(1.4)	1.49(79)	102.32(97)	65.80(10)	0.13(67)	1.0007(38)
P500-2	100.2(1.4)	1.57(79)	102.18(97)	65.91(10)	1.69(67)	1.0097(38)
P501-1	99.0(1.4)	2.26(79)	101.83(97)	66.23(10)	0.83(67)	1.0048(39)
P501-2	99.5(1.4)	2.20(79)	102.24(96)	66.32(10)	1.01(66)	1.0058(39)
P502-1	100.4(1.3)	4.19(78)	105.55(96)	66.84(10)	0.41(69)	1.0024(40)
P502-2	99.7(1.4)	4.13(79)	104.77(97)	66.86(10)	1.31(67)	1.0075(38)
P503-1	99.1(1.4)	7.09(79)	107.81(97)	67.29(10)	0.69(67)	1.0039(38)
P503-2	99.5(1.4)	7.14(81)	108.32(99)	67.51(10)	1.07(67)	1.0061(38)
P504-1	100.6(1.4)	11.84(80)	115.14(97)	68.75(10)	1.29(67)	1.0073(38)
P504-2	100.3(1.3)	11.09(80)	113.97(98)	68.45(11)	1.08(82)	1.0059(45)
P600-2	99.1(1.4)	1.42(80)	100.85(98)	65.84(10)	0.91(67)	1.0054(40)
P601-1	100.4(1.3)	2.00(78)	102.84(95)	66.19(10)	1.02(66)	1.0061(40)
P601-2	99.3(1.4)	2.09(81)	101.9(1.0)	66.20(10)	1.73(67)	1.0104(40)
P602-1	100.3(1.3)	3.64(80)	104.85(98)	66.60(10)	1.24(66)	1.0073(39)
P602-2	99.1(1.4)	3.56(80)	103.56(98)	66.49(10)	0.88(67)	1.0053(40)
P603-1	100.1(1.4)	6.12(80)	107.69(98)	67.203(99)	1.94(67)	1.0116(40)
P603-2	99.2(1.3)	5.96(80)	106.53(97)	67.03(10)	1.48(66)	1.0088(39)
P604-1	100.5(1.4)	8.98(81)	111.52(98)	67.94(10)	1.94(67)	1.0115(40)
P604-2	99.8(1.3)	8.90(80)	110.76(97)	67.89(10)	2.61(67)	1.0157(40)

Table F.2.: Temperatures and pressures (continued)

no.	p_h	Δp_{bed}	p_{mb}	T_{mb}	ΔT_F	q
-	mbar(a)	mbar m^{-1}	mbar(a)	°C	°C	-
P626-1	100.1(1.4)	1.78(80)	102.30(98)	66.01(10)	1.68(66)	1.0106(42)
P626-2	99.4(1.4)	1.76(79)	101.61(97)	65.98(10)	1.95(66)	1.0124(42)
P627-1	100.1(1.4)	2.45(80)	103.14(98)	66.355(99)	2.09(67)	1.0132(42)
P627-2	99.5(1.4)	2.43(80)	102.54(98)	66.24(10)	1.94(67)	1.0123(42)
P628-1	99.8(1.4)	3.17(79)	103.76(97)	66.49(10)	2.67(67)	1.0169(42)
P628-2	99.7(1.4)	3.26(82)	103.8(1.0)	66.50(10)	2.80(67)	1.0177(42)
P632-1	99.8(1.4)	1.8(1.1)	102.2(1.3)	65.97(20)	2.57(68)	1.0163(43)
P633-1	100.2(1.4)	1.93(80)	102.62(98)	66.08(10)	2.83(67)	1.0180(42)
P633-2	99.7(1.4)	1.88(79)	102.00(96)	66.13(10)	2.79(67)	1.0177(42)
P700-1	100.6(1.4)	1.59(80)	102.57(97)	65.46(10)	0.43(66)	1.0023(36)
P700-2	99.3(1.4)	1.52(81)	101.19(99)	65.77(10)	0.64(67)	1.0036(37)
P701-1	99.3(1.4)	2.29(81)	102.13(99)	65.913(99)	1.04(67)	1.0056(36)
P701-2	99.4(1.3)	2.26(79)	102.24(96)	66.00(10)	0.88(66)	1.0048(36)
P702-1	100.5(1.4)	4.20(79)	105.70(96)	66.54(10)	0.59(67)	1.0032(36)
P702-2	99.3(1.4)	4.28(81)	104.61(99)	66.38(10)	0.34(67)	1.0019(36)
P703-1	99.2(1.4)	6.88(83)	107.7(1.0)	67.25(10)	1.33(68)	1.0074(38)
P703-2	99.3(1.4)	7.25(82)	108.2(1.0)	67.28(10)	1.06(68)	1.0057(37)
P704-1	100.3(1.1)	11.68(73)	114.61(89)	68.163(99)	1.06(64)	1.0056(34)
P704-2	99.2(1.4)	12.16(80)	114.16(97)	68.20(10)	1.28(67)	1.0068(36)

Table F.3.: Mixture compositions

no.	x_{F}	x_{is}	x_{D}	x_{B}	$x_{\mathrm{mb,is}}$
-	$\mathrm{kmol_{CB}\,kmol_{tot}^{-1}}$	$\mathrm{kmol_{CB}\,kmol_{tot}^{-1}}$	$\mathrm{kmol_{CB}\,kmol_{tot}^{-1}}$	$\mathrm{kmol_{CB}\,kmol_{tot}^{-1}}$	$\mathrm{kmol_{CB}\,kmol_{tot}^{-1}}$
P500-1	0.7409(43)	0.7409(43)	0.7411(35)	0.3073(65)	0.5241(39)
P500-2	0.7167(57)	0.7167(57)	0.7314(21)	0.2849(10)	0.5008(29)
P501-1	0.6975(49)	0.6975(49)	0.7061(28)	0.280 42(77)	0.4890(25)
P501-2	0.6916(47)	0.6917(47)	0.6989(25)	0.2658(14)	0.4787(25)
P502-1	0.7172(70)	0.7172(70)	0.7297(53)	0.2697(68)	0.4935(49)
P502-2	0.7117(53)	0.7117(53)	0.7154(46)	0.2635(14)	0.4876(28)
P503-1	0.741(11)	0.741(11)	0.7469(47)	0.2741(21)	0.5075(58)
P503-2	0.7356(49)	0.7357(49)	0.7384(39)	0.251 66(98)	0.4937(25)
P504-1	0.741(19)	0.741(19)	0.745(16)	0.206(22)	0.473(14)
P504-2	0.8024(43)	0.8024(43)	0.8067(42)	0.2751(12)	0.5388(22)
P600-2	0.6339(93)	0.6340(93)	0.6640(74)	0.3537(43)	0.4939(51)
P601-1	0.634(10)	0.634(10)	0.6642(58)	0.3687(12)	0.5014(53)
P601-2	0.6292(25)	0.6295(25)	0.6603(22)	0.356 93(76)	0.4932(13)
P602-1	0.6535(73)	0.6537(73)	0.6798(27)	0.387 51(61)	0.5206(36)
P602-2	0.6260(22)	0.6261(22)	0.6570(15)	0.3679(43)	0.4970(24)
P603-1	0.6386(44)	0.6389(44)	0.6694(12)	0.369 11(75)	0.5040(22)
P603-2	0.6521(19)	0.6523(19)	0.6833(21)	0.386 05(94)	0.5192(10)
P604-1	0.6461(94)	0.6464(94)	0.6819(53)	0.368 08(56)	0.5072(47)
P604-2	0.6270(24)	0.6275(25)	0.6598(30)	0.3525(12)	0.4900(14)

Table F.3.: Mixture compositions (continued)

no.	x_{F}	x_{is}	x_{D}	x_{B}	$x_{\mathrm{mb,is}}$
-	$\mathrm{kmol_{CB}\,kmol_{tot}^{-1}}$	$\mathrm{kmol_{CB}\,kmol_{tot}^{-1}}$	$\mathrm{kmol_{CB}\,kmol_{tot}^{-1}}$	$\mathrm{kmol_{CB}\,kmol_{tot}^{-1}}$	$\mathrm{kmol_{CB}\,kmol_{tot}^{-1}}$
P626-1	0.5145(13)	0.5149(13)	0.5609(22)	0.4738(24)	0.4944(14)
P626-2	0.5126(32)	0.5130(33)	0.5590(33)	0.4762(42)	0.4946(27)
P627-1	0.511 44(90)	0.512 05(93)	0.556 22(71)	0.4662(22)	0.4891(12)
P627-2	0.5065(51)	0.5071(52)	0.5554(14)	0.4655(26)	0.4863(29)
P628-1	0.516 32(41)	0.517 08(46)	0.561 03(41)	0.472 34(42)	0.494 71(31)
P628-2	0.519 39(90)	0.520 20(94)	0.564 74(41)	0.4745(20)	0.4973(11)
P632-1	0.506 68(59)	0.507 49(65)	0.551 81(53)	0.4793(18)	0.493 38(95)
P633-1	0.5022(19)	0.5029(19)	0.5493(36)	0.4825(32)	0.4927(19)
P633-2	0.500 94(33)	0.501 74(40)	0.5483(15)	0.479 62(96)	0.490 68(52)
P700-1	0.8482(58)	0.8482(58)	0.822(20)	0.3967(33)	0.6224(33)
P700-2	0.7903(40)	0.7903(40)	0.7902(50)	0.3133(41)	0.5518(29)
P701-1	0.8176(12)	0.8176(12)	0.808(17)	0.3509(12)	0.584 25(85)
P701-2	0.808 42(49)	0.808 42(49)	0.809 80(66)	0.338 94(56)	0.573 68(37)
P702-1	0.8223(64)	0.8223(64)	0.827 01(38)	0.3527(31)	0.5875(36)
P702-2	0.8279(74)	0.8279(74)	0.8243(59)	0.3612(42)	0.5945(43)
P703-1	0.773(23)	0.773(23)	0.7869(41)	0.2861(44)	0.529(12)
P703-2	0.8194(30)	0.8194(30)	0.8202(25)	0.318 46(96)	0.5689(16)
P704-1	0.8520(81)	0.8520(81)	0.8641(98)	0.3354(79)	0.5937(57)
P704-2	0.849(20)	0.849(20)	0.8604(13)	0.3201(64)	0.585(11)

Table F.4.: Separation performance

no.	S_{MC}	N_{th}	$HETP_{stages}$	$HETP_{Delft,4}$	$HTU_{oG,Delft,4}$	$NTU_{oG,stages}$	$NTU_{oG,integration}$	
-	%	-	m	m	m	-	-	
P500-1	100.00	10.14(95)	0.241(23)	0.1627(29)	0.1626(26)	10.16(95)	10.1(1.0)	
P500-2	100.00	11.3(1.1)	0.216(21)	0.1617(28)	0.1606(26)	11.4(1.1)	11.4(1.2)	
P501-1	100.00	10.70(81)	0.229(18)	0.1753(30)	0.1746(28)	10.74(82)	10.73(89)	
P501-2	99.17	13.1(3.2)	0.187(45)	0.1748(38)	0.1727(31)	13.2(3.2)	13(56)	[a]
P502-1	100.00	11.30(69)	0.217(13)	0.1889(31)	0.1884(30)	11.33(69)	11.31(75)	
P502-2	100.00	11.58(73)	0.211(13)	0.1887(31)	0.1881(30)	11.61(73)	11.60(79)	
P503-1	100.00	12.39(61)	0.1976(99)	0.1985(32)	0.1970(31)	12.49(62)	12.48(66)	
P503-2	99.27	14.1(3.2)	0.174(40)	0.1977(41)	0.1961(34)	14.2(3.2)	15(230)	[a]
P504-1	100.00	14.5(1.1)	0.168(13)	0.2004(32)	0.2004(32)	14.5(1.1)	14.5(1.1)	
P504-2	100.00	14.41(59)	0.1699(71)	0.2034(32)	0.2010(32)	14.58(60)	14.60(64)	
P600-2	99.44	12.5(1.5)	0.195(23)	0.1612(26)	0.1531(24)	13.2(1.6)	13.3(2.0)	
P601-1	99.23	11.8(2.1)	0.207(37)	0.1757(29)	0.1665(26)	12.5(2.2)	13(32)	[a]
P601-2	99.60	13.0(2.3)	0.188(34)	0.1754(30)	0.1661(27)	13.7(2.5)	14(55)	[a]
P602-1	99.96	11.6(1.0)	0.211(19)	0.1905(30)	0.1801(28)	12.3(1.1)	12.4(1.1)	
P602-2	100.00	12.1(1.1)	0.202(18)	0.1897(31)	0.1790(28)	12.8(1.2)	12.9(1.2)	
P603-1	99.99	12.2(1.4)	0.201(23)	0.1991(33)	0.1886(30)	12.9(1.5)	12.9(3.0)	
P603-2	100.00	11.67(65)	0.210(12)	0.1999(32)	0.1890(30)	12.34(69)	12.41(74)	
P604-1	99.95	13.0(1.2)	0.188(18)	0.2035(32)	0.1927(30)	13.8(1.3)	13.9(1.4)	
P604-2	100.00	12.89(56)	0.1900(83)	0.2029(32)	0.1923(30)	13.59(59)	13.68(62)	

Table F.4.: Separation performance (continued)

no.	S_{MC}	N_{th}	$HETP_{stages}$	$HETP_{Delft,4}$	$HTU_{oG,Delft,4}$	$NTU_{oG,stages}$	$NTU_{oG,integration}$	
-	%	-	m	m	m	-	-	
P626-1	69.51	4.4(1.5)	0.55(18)	0.1871(31)	0.1346(22)	6.2(2.0)	12(970)	[a]
P626-2	82.79	3.1(1.3)	0.80(35)	0.1871(31)	0.1341(22)	4.3(1.9)	5(110)	[a]
P627-1	8.84	6.0(1.7)	0.41(12)	0.1982(33)	0.1426(23)	8.3(2.4)	30(1000)	[a]
P627-2	56.09	3.7(1.5)	0.67(28)	0.1982(33)	0.1426(23)	5.1(2.1)	9(1200)	[a]
P628-1	0.02	8.8(2.0)	0.277(62)	0.2044(34)	0.1467(24)	12.3(2.8)	118(390)	[a]
P628-2	6.39	6.1(1.7)	0.40(11)	0.2045(34)	0.1469(24)	8.5(2.4)	30(1100)	[a]
P632-1	4.09	4.0(1.2)	0.62(19)	0.1950(41)	0.1224(23)	6.3(1.9)	29(2000)	[a]
P633-1	59.50	2.08(98)	1.17(55)	0.2002(34)	0.1212(20)	3.4(1.6)	5(170)	[a]
P633-2	16.61	3.8(1.1)	0.65(19)	0.2000(34)	0.1206(20)	6.2(1.8)	21(1400)	[a]
P700-1	100.00	12.28(26)	0.1993(46)	0.1687(28)	0.1648(27)	12.58(27)	12.61(28)	
P700-2	100.00	12.28(17)	0.1994(32)	0.1637(25)	0.1616(25)	12.43(17)	12.43(17)	
P701-1	100.00	12.25(11)	0.1999(25)	0.1793(28)	0.1762(27)	12.46(11)	12.48(12)	
P701-2	100.00	12.269(27)	0.1995(18)	0.1782(28)	0.1754(27)	12.470(28)	12.483(27)	
P702-1	100.00	12.52(23)	0.1955(40)	0.1927(30)	0.1892(29)	12.76(24)	12.78(24)	
P702-2	100.00	12.47(28)	0.1964(47)	0.1941(30)	0.1904(30)	12.71(29)	12.74(29)	
P703-1	100.00	12.62(67)	0.194(10)	0.1986(32)	0.1968(31)	12.74(68)	12.74(70)	
P703-2	100.00	13.33(11)	0.1836(21)	0.2006(32)	0.1975(31)	13.54(11)	13.56(11)	
P704-1	100.00	14.47(39)	0.1691(48)	0.2058(32)	0.2019(32)	14.76(40)	14.81(41)	
P704-2	100.00	14.78(81)	0.1656(92)	0.2059(32)	0.2022(32)	15.05(83)	15.10(86)	

[a] The associated combined standard uncertainty seems unreasonable. This could be related to the corresponding MCM success ratio S_{MC} and should be investigated in future activities.

F.2. Diagrams

F.2.1. Plant Operation

intentionally left blank

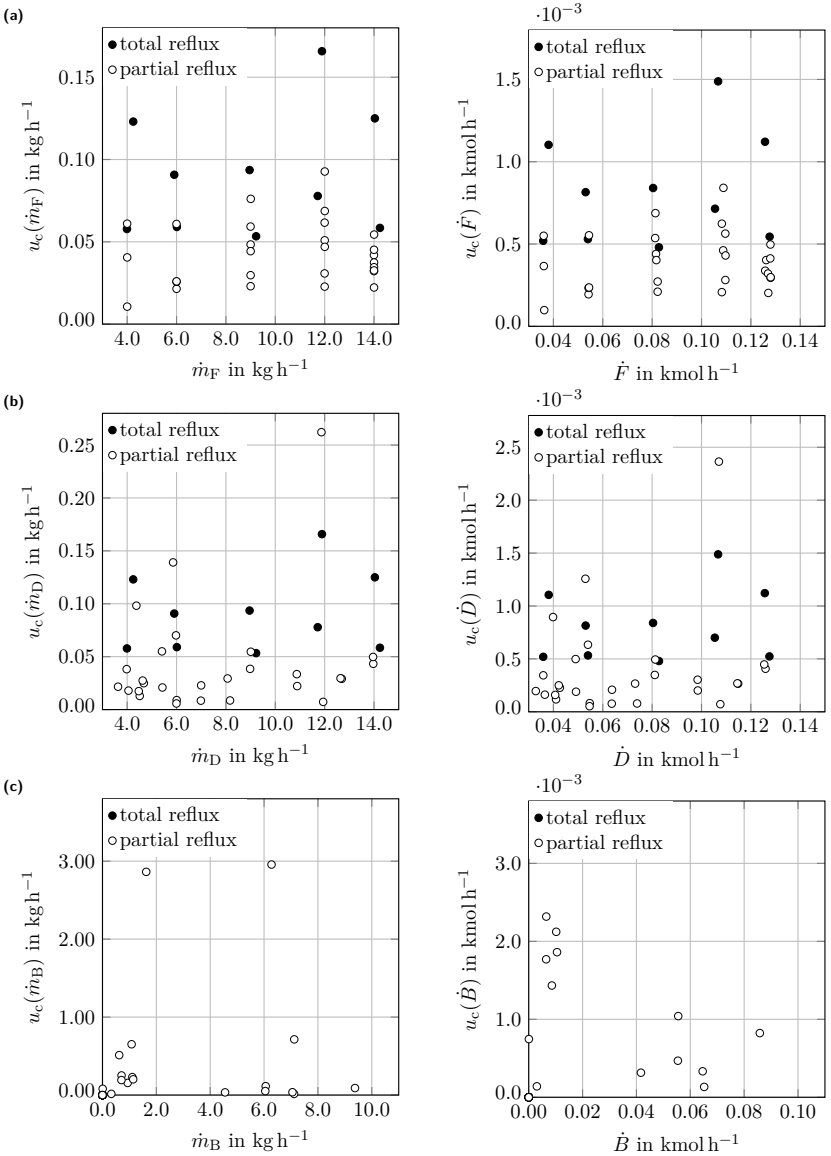

Figure F.1.: Combined standard uncertainty associated with feed mass and molar flow (a), distillate mass and molar flow (b), and bottoms mass and molar flow (c)

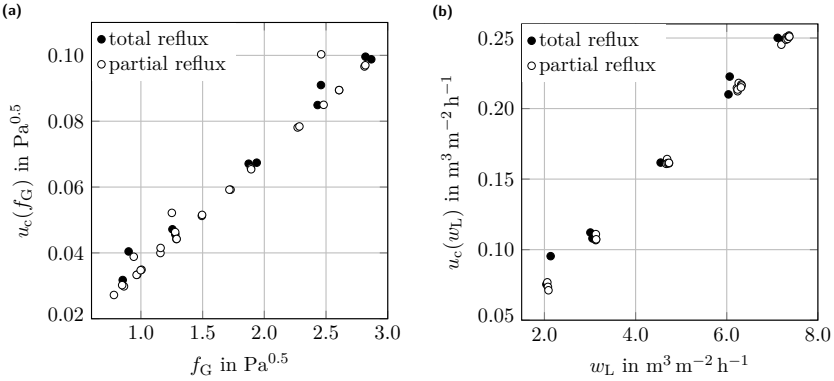

Figure F.2.: Combined standard uncertainty associated with f-factor f_G (a) and liquid load w_L (b)

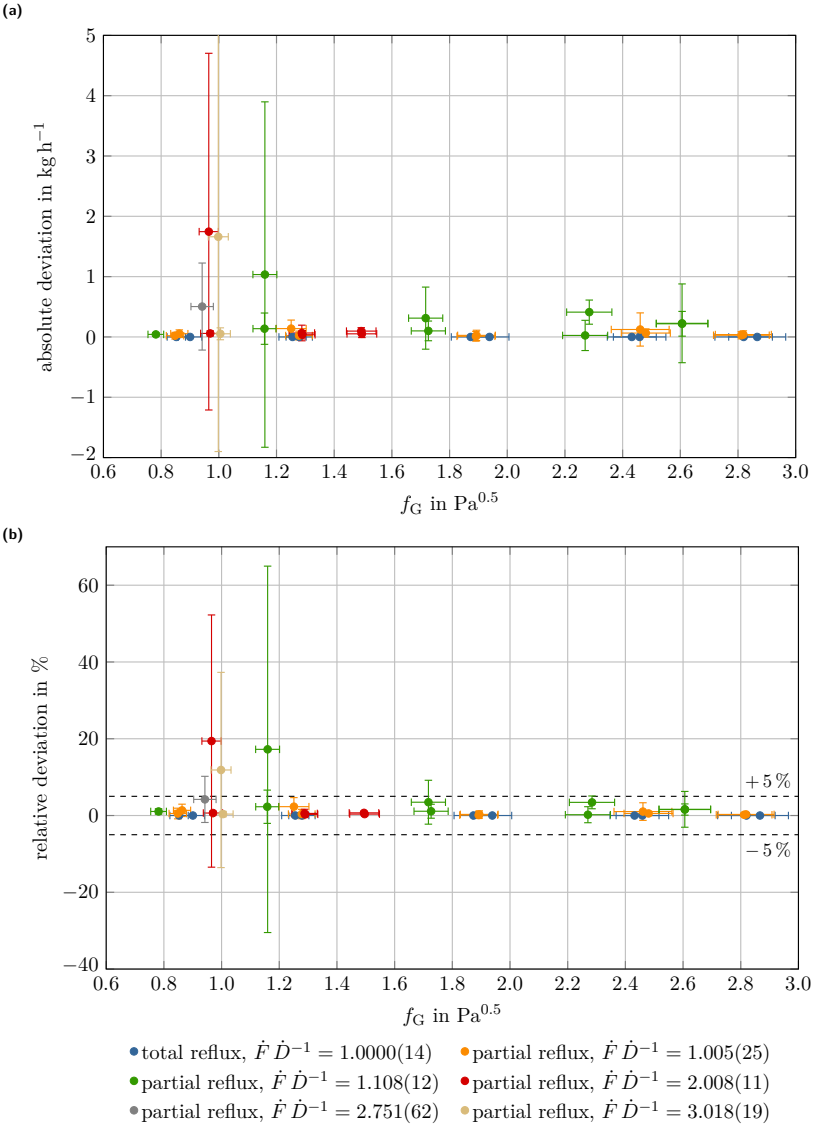

Figure F.3.: Absolute (a) and relative (b) deviations in mass balance in dependence of f-factor f_G and molar stream ratio $\dot{F}\,\dot{D}^{-1}$, indicated uncertainties are combined standard uncertainties $u_c(\cdot)$

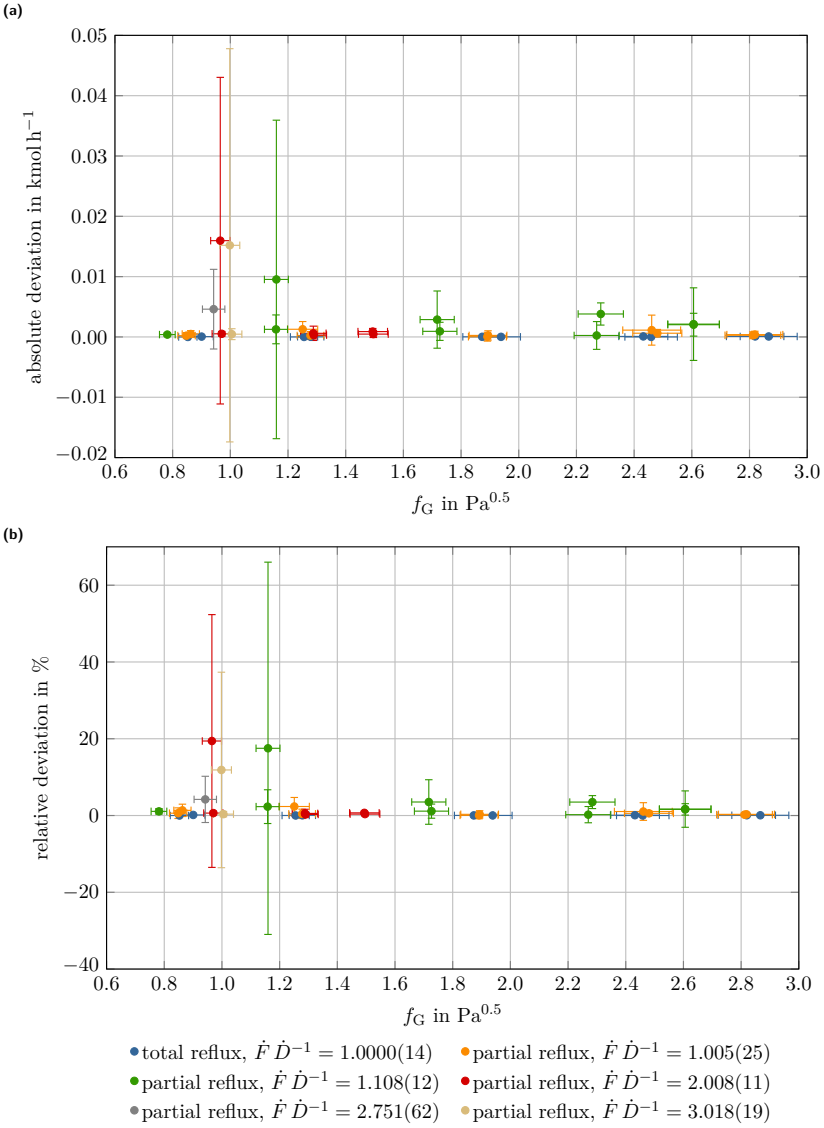

Figure F.4.: Absolute (a) and relative (b) deviations in molar balance in dependence of f-factor f_G and molar stream ratio $\dot{F}\,\dot{D}^{-1}$, indicated uncertainties are combined standard uncertainties $u_c(\cdot)$

F.2.2. Mixture Compositions

intentionally left blank

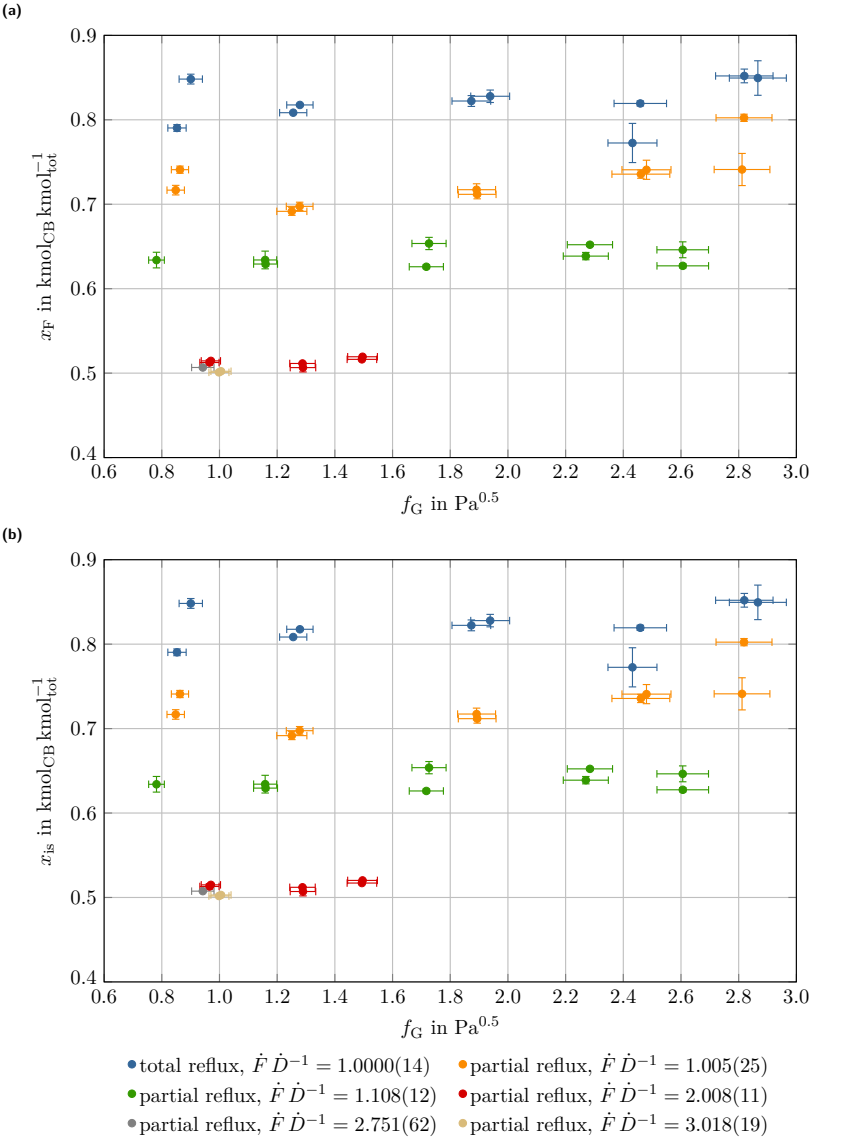

Figure F.5.: Molar fraction of chlorobenzene in feed in dependence of f-factor f_G and molar stream ratio $\dot{F}\,\dot{D}^{-1}$, (a): feedstock composition x_F, (b): calculated feed composition at intersection x_{is}; indicated uncertainties are combined standard uncertainties $u_c(\cdot)$

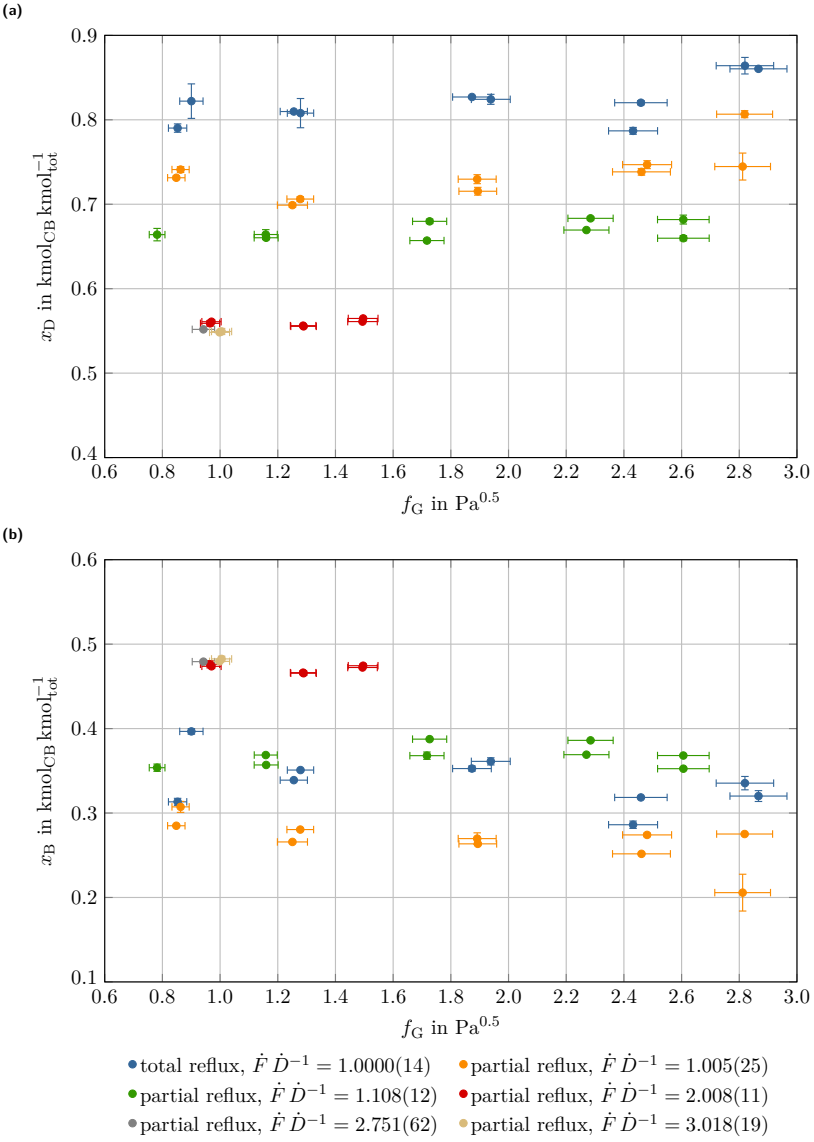

Figure F.6.: Molar fraction of chlorobenzene in distillate x_D (a) and bottom product x_B (b) in dependence of f-factor f_G and molar stream ratio $\dot{F}\,\dot{D}^{-1}$, indicated uncertainties are combined standard uncertainties $u_c(\cdot)$

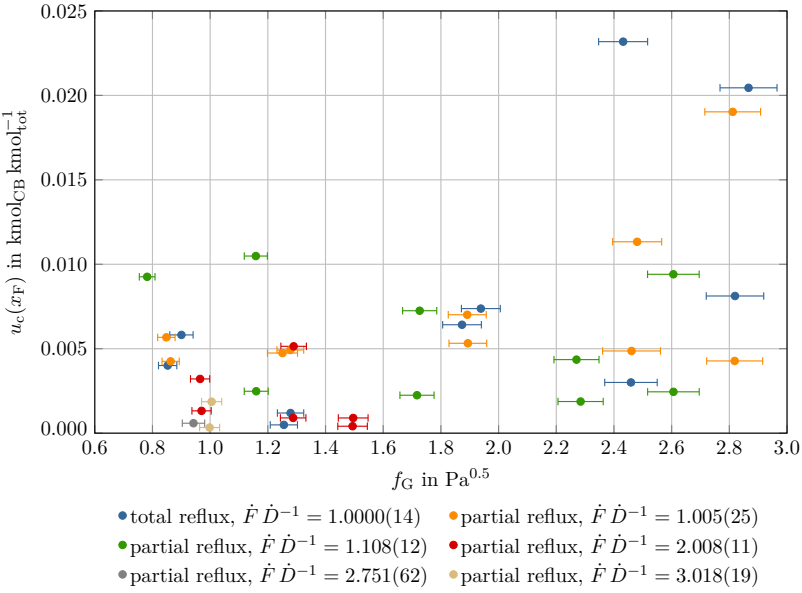

Figure F.7.: Combined standard uncertainty associated with feed molar fraction x_F in dependence of f-factor f_G and molar stream ratio $\dot{F}\,\dot{D}^{-1}$, indicated uncertainties are combined standard uncertainties $u_c(\cdot)$

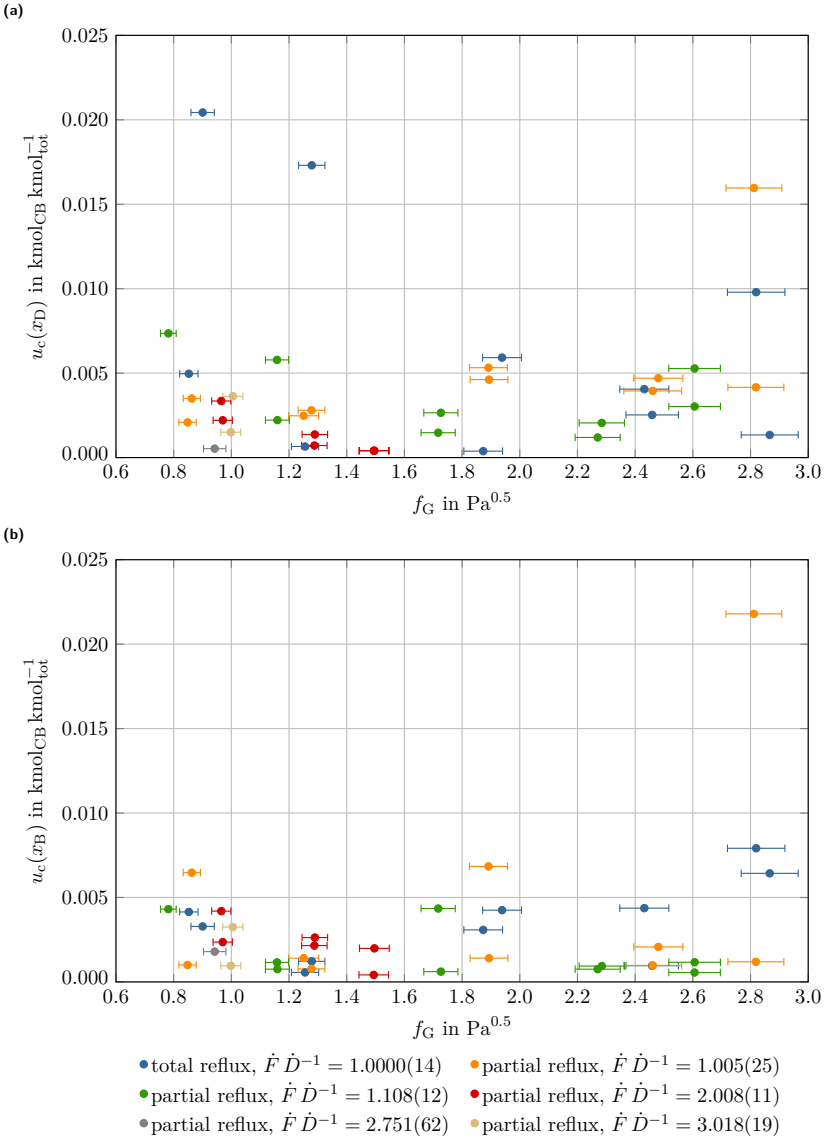

Figure F.8.: Combined standard uncertainty associated with distillate molar fraction x_D (a) and bottom product molar fraction x_B (b) in dependence of f-factor f_G and molar stream ratio $\dot{F}\,\dot{D}^{-1}$, indicated uncertainties are combined standard uncertainties $u_c(\cdot)$

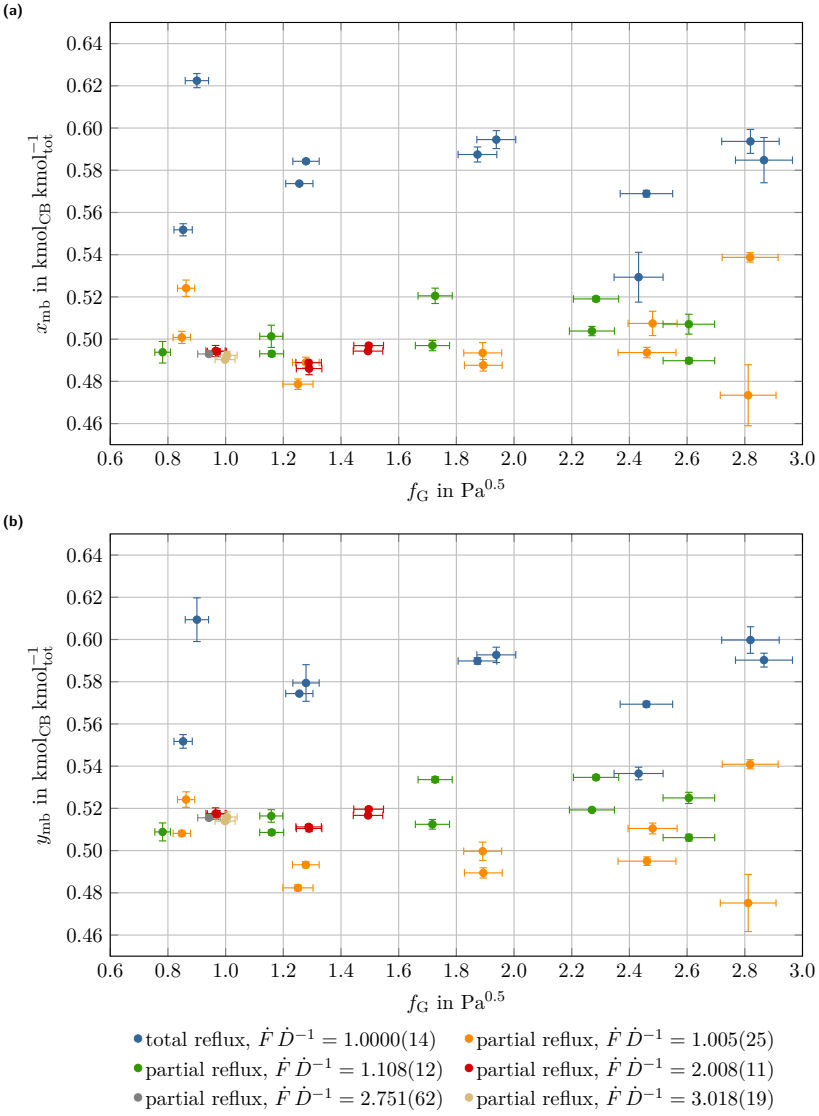

Figure F.9.: Molar fraction of chlorobenzene in liquid stream x_{mb} (a) and gas stream y_{mb} (b) at mid-bed position in dependence of f-factor f_G and molar stream ratio $\dot{F}\,\dot{D}^{-1}$, indicated uncertainties are combined standard uncertainties $u_c(\cdot)$

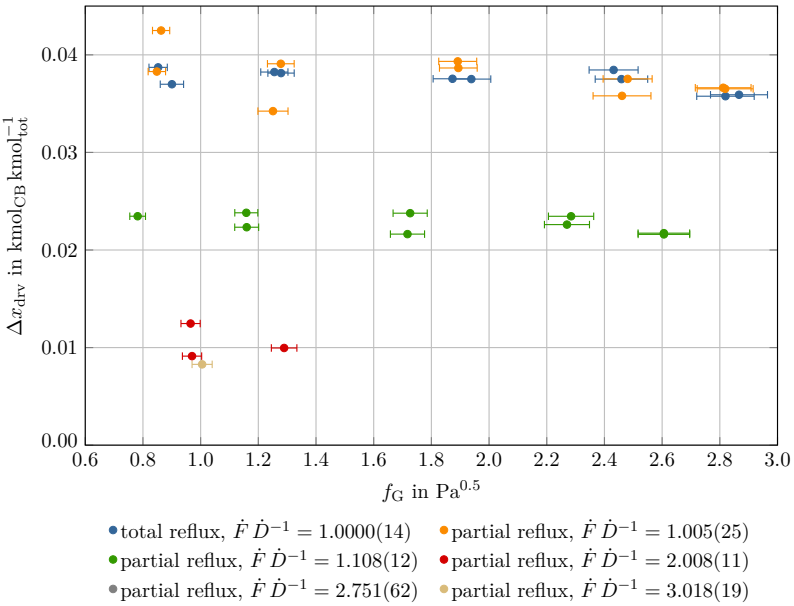

Figure F.10.: Mean driving potential on equilibrium stages Δx_{drv} in dependence of f-factor f_{G} and molar stream ratio $\dot{F}\,\dot{D}^{-1}$, indicated uncertainties are combined standard uncertainties $u_{\mathrm{c}}(\cdot)$

F.2.3. Pressures and Temperatures

intentionally left blank

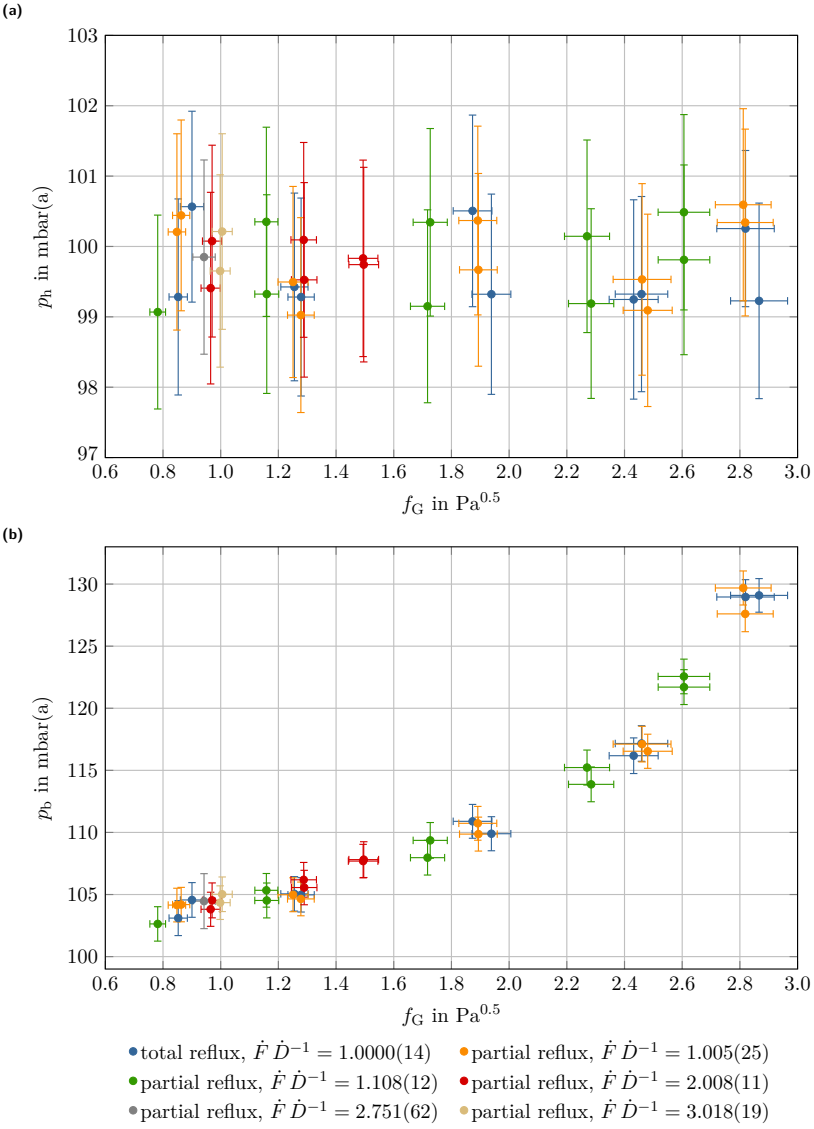

Figure F.11.: Head pressure p_h (a) and bottom pressure p_b (b) in dependence of f-factor f_G and molar stream ratio $\dot{F}\,\dot{D}^{-1}$, indicated uncertainties are combined standard uncertainties $u_c(\cdot)$

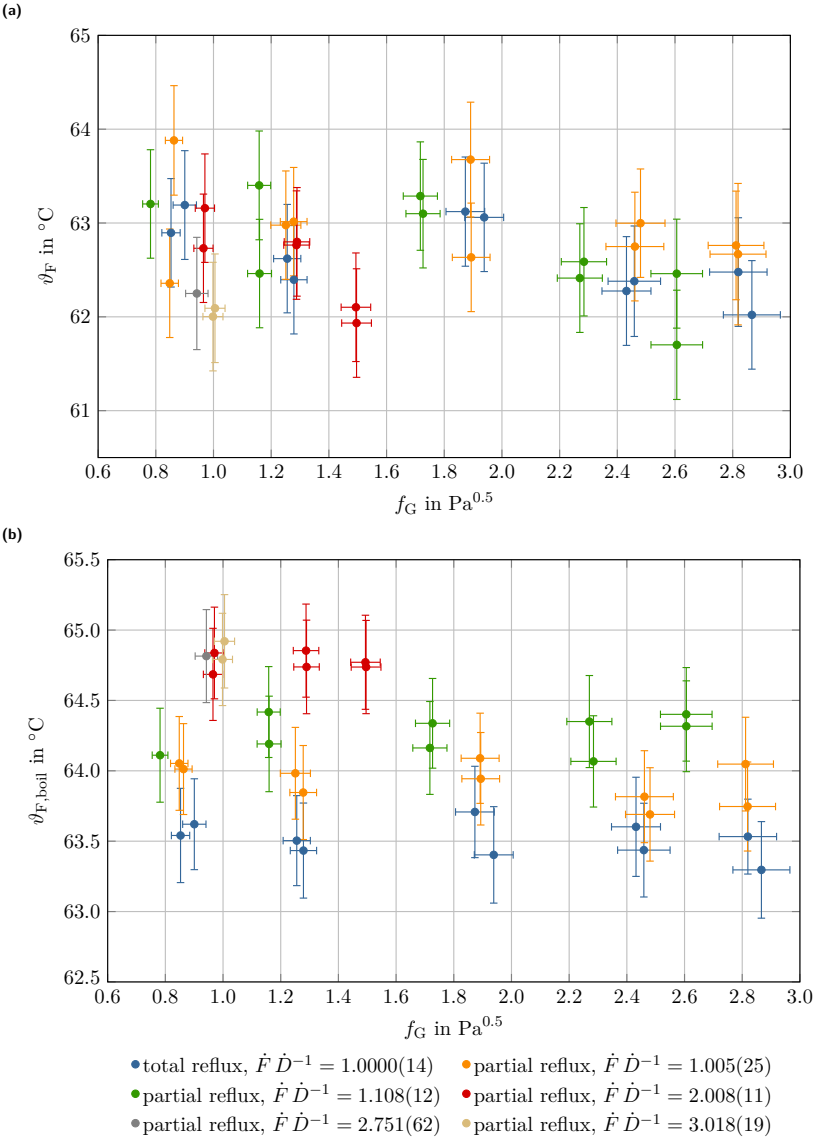

Figure F.12.: Feed inlet temperature ϑ_F (a) and feed boiling point $\vartheta_{F,boil}$ (b) in dependence of f-factor f_G and molar stream ratio $\dot{F}\,\dot{D}^{-1}$, indicated uncertainties are combined standard uncertainties $u_c(\cdot)$

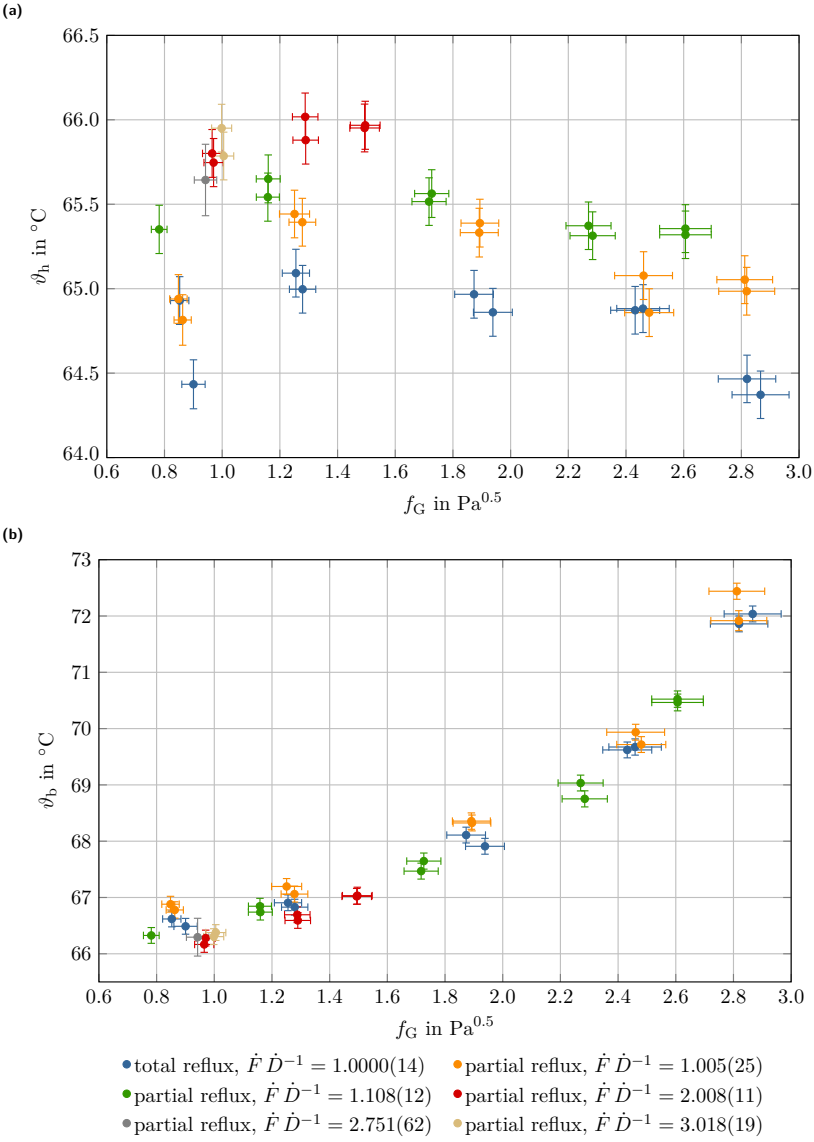

Figure F.13.: Head temperature ϑ_h (a) and bottom temperature ϑ_b (b) in dependence of f-factor f_G and molar stream ratio $\dot{F}\,\dot{D}^{-1}$, indicated uncertainties are combined standard uncertainties $u_c(\cdot)$

F.2.4. McCabe-Thiele Stage Constructions with Solution Space from Monte Carlo Methods

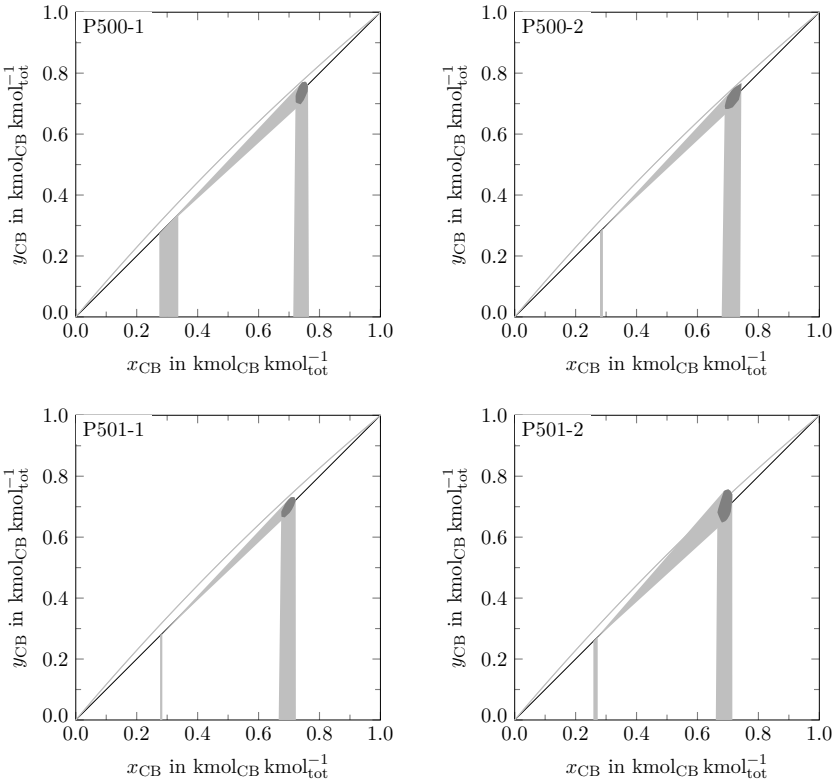

Figure F.14.: McCabe-Thiele stage constructions with Monte Carlo solution space

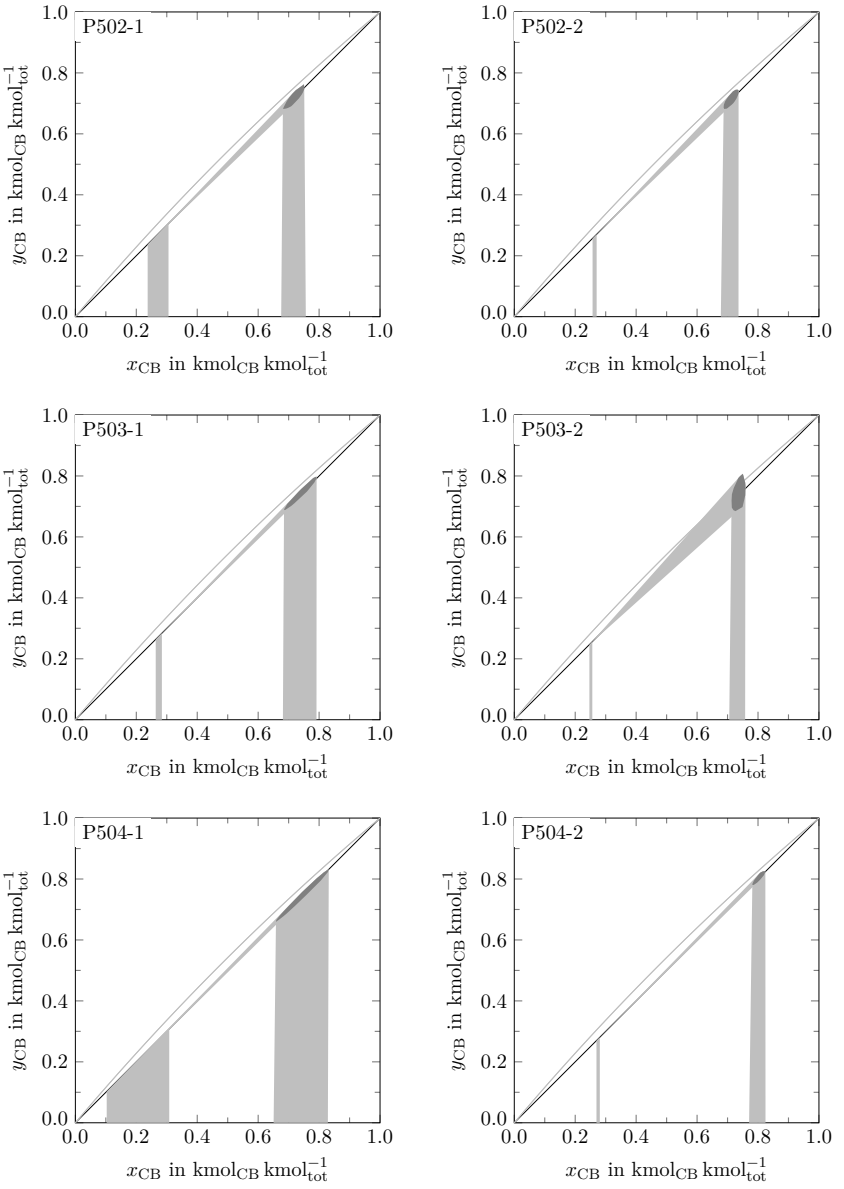

Figure F.14.: McCabe-Thiele stage constructions with Monte Carlo solution space (continued)

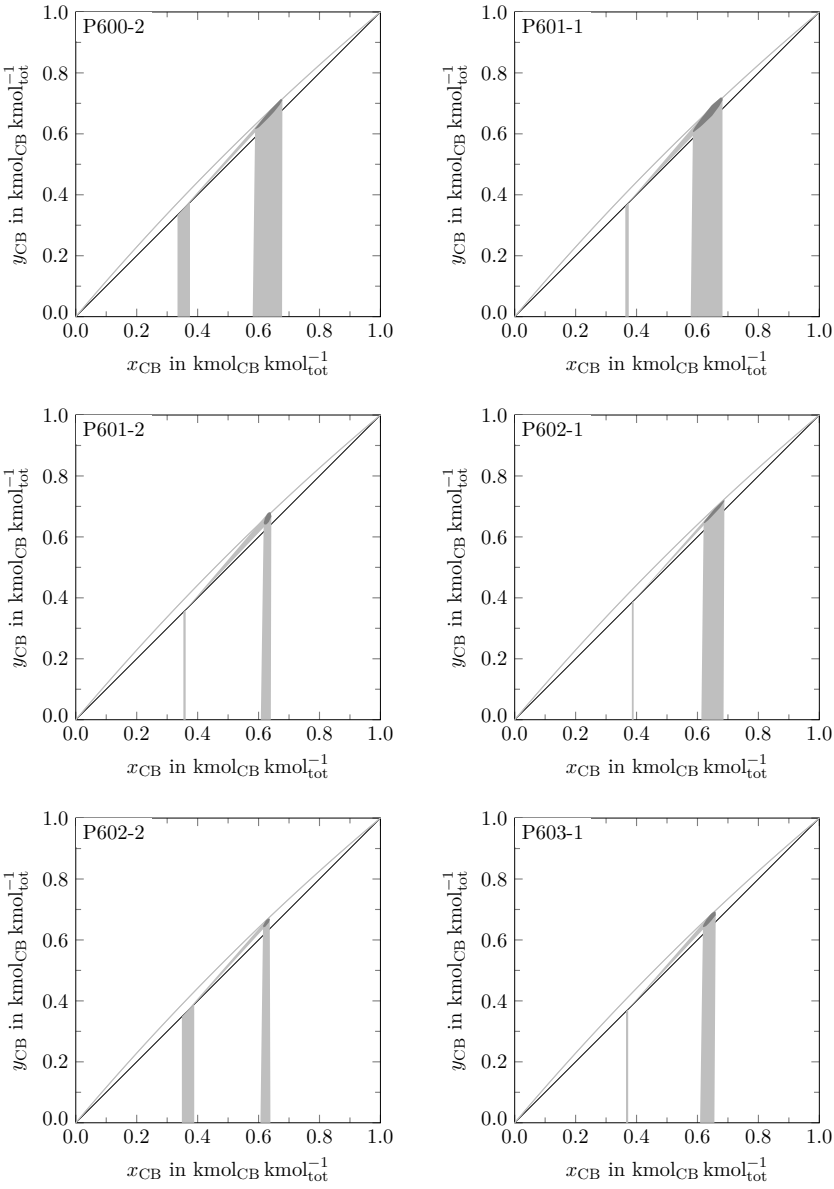

Figure F.14.: McCabe-Thiele stage constructions with Monte Carlo solution space (continued)

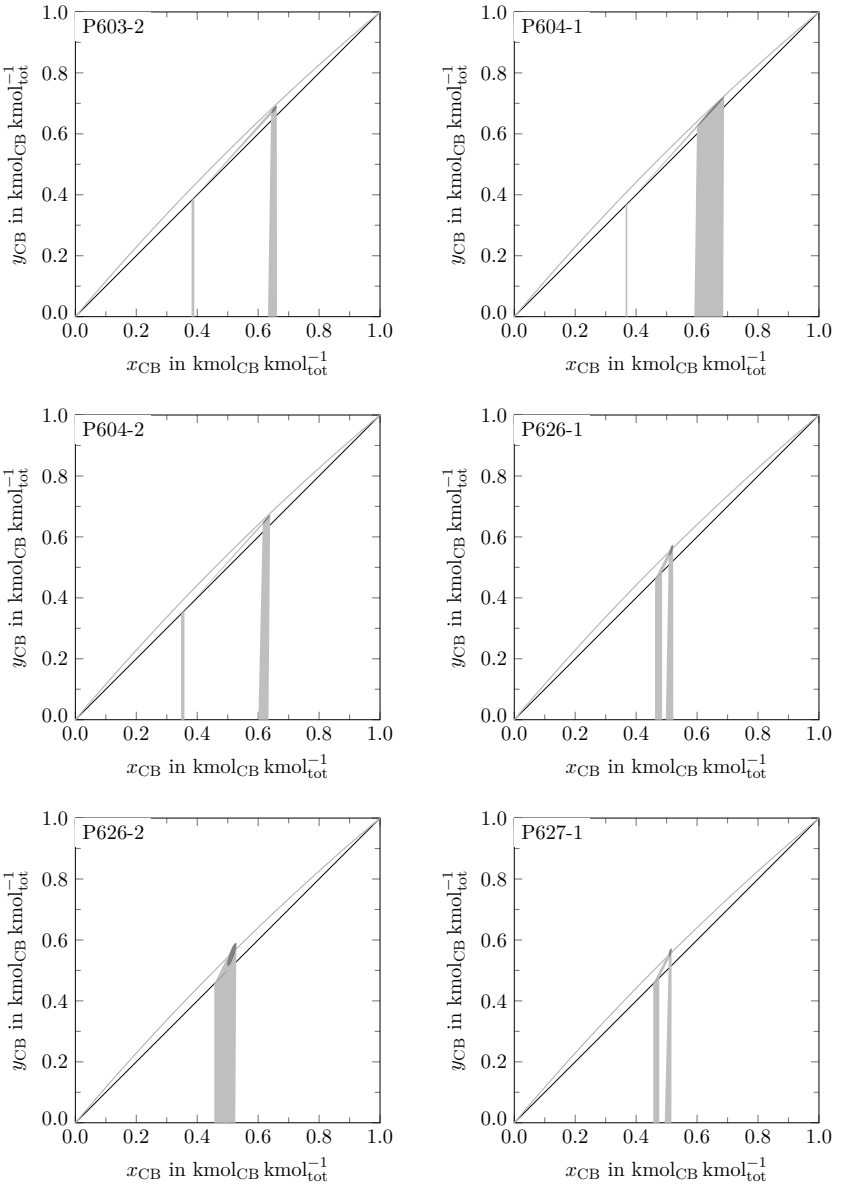

Figure F.14.: McCabe-Thiele stage constructions with Monte Carlo solution space (continued)

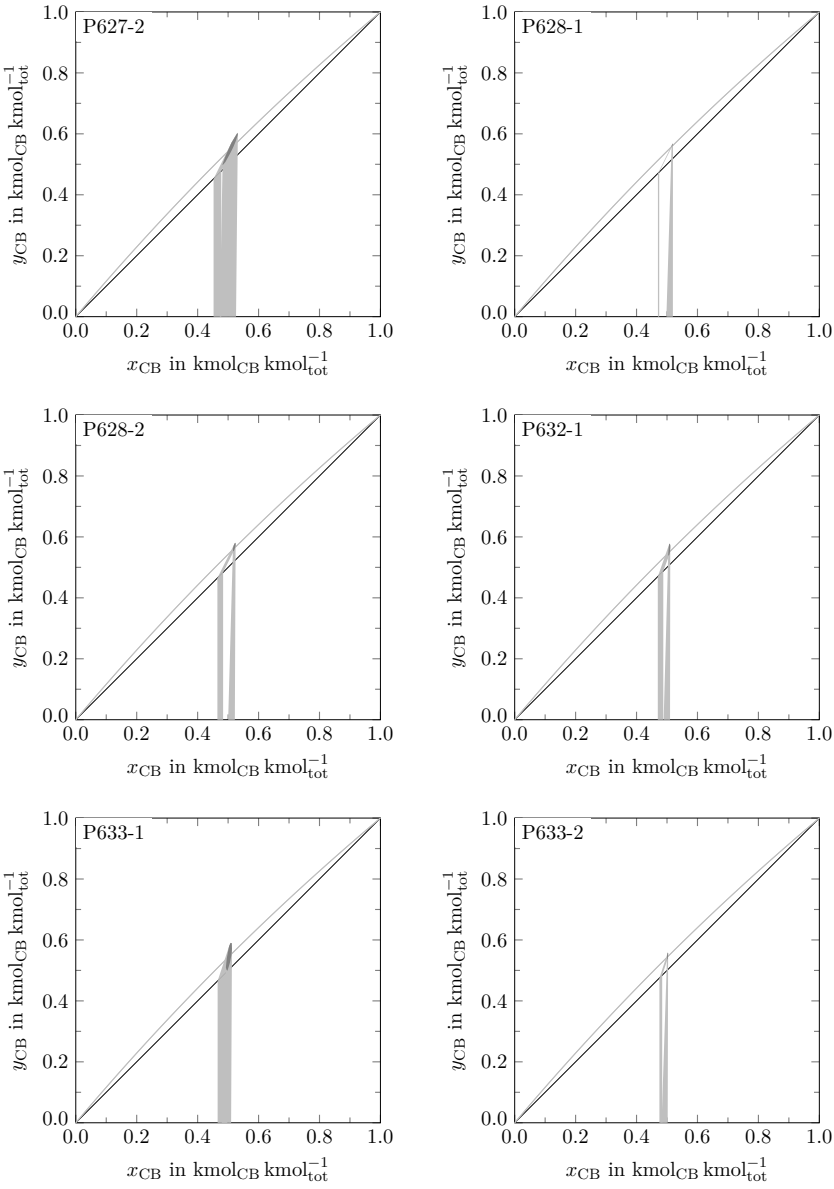

Figure F.14.: McCabe-Thiele stage constructions with Monte Carlo solution space (continued)

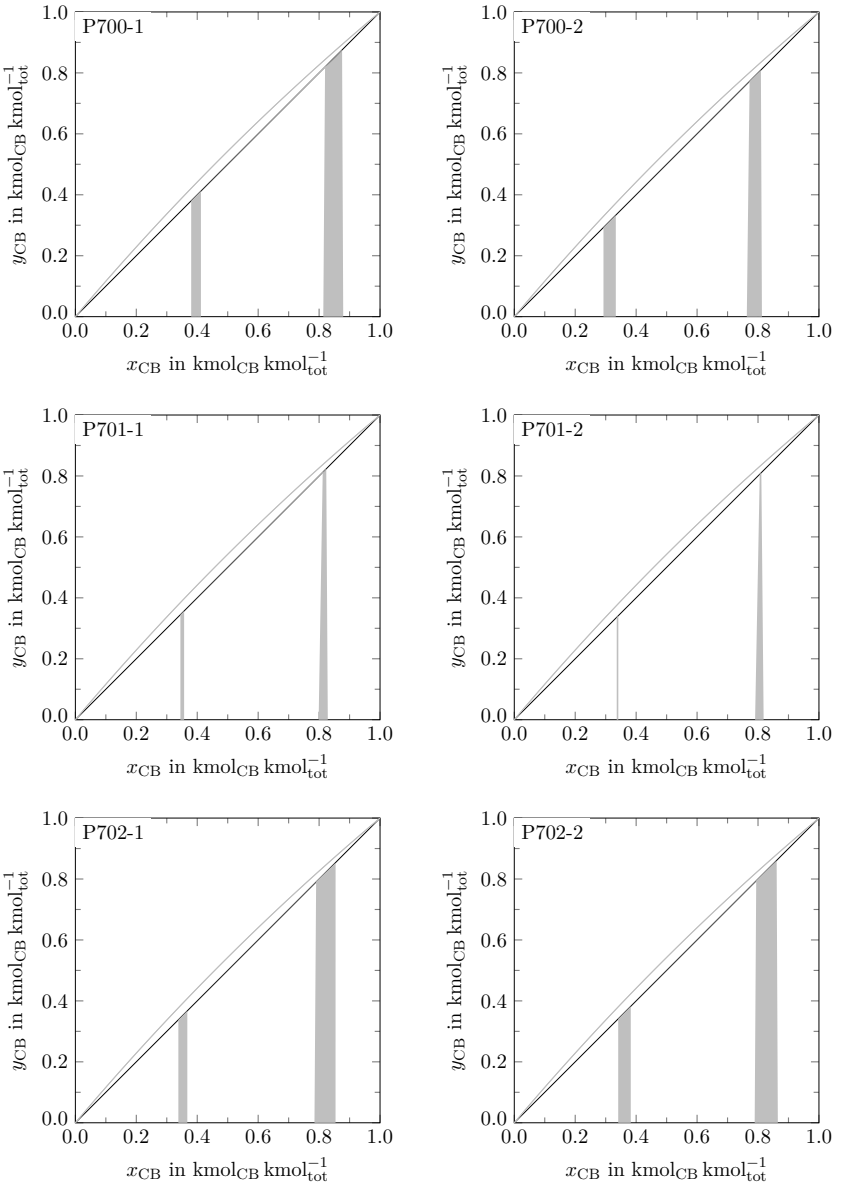

Figure F.14.: McCabe-Thiele stage constructions with Monte Carlo solution space (continued)

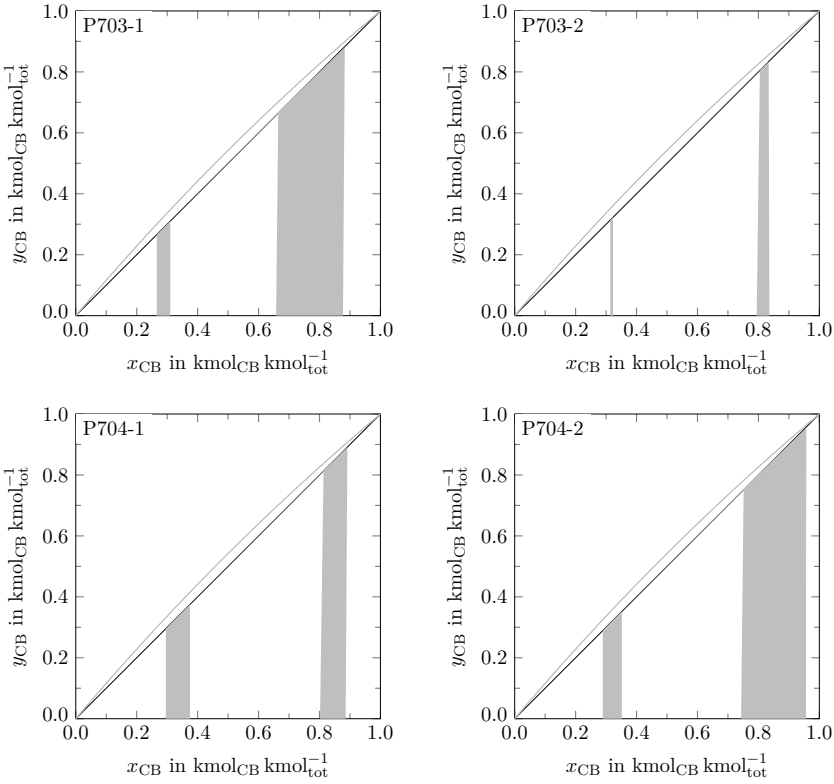

Figure F.14.: McCabe-Thiele stage constructions with Monte Carlo solution space (continued)

F.2.5. Separation Performance Predicted with Delft Mass Transfer Model

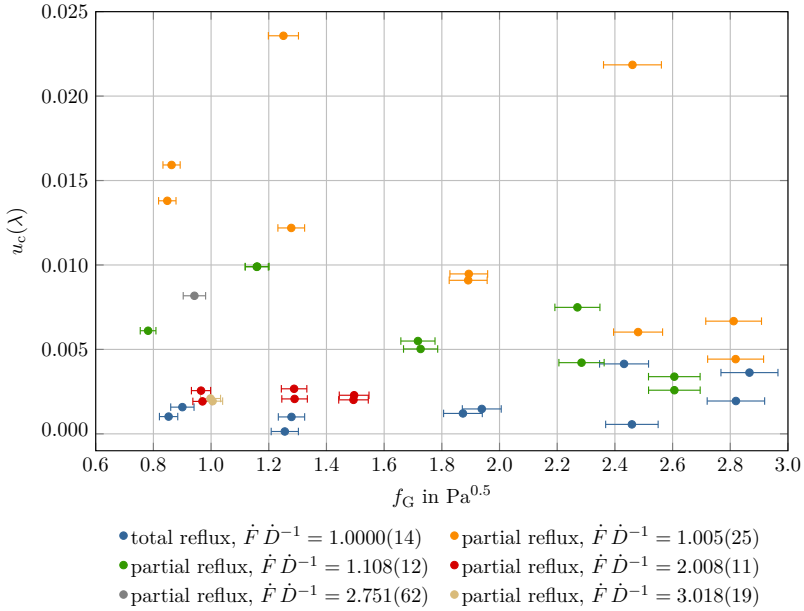

Figure F.15.: Combined standard uncertainty associated with stripping factor λ in dependence of f-factor f_G and molar stream ratio $\dot{F}\,\dot{D}^{-1}$, indicated uncertainties are combined standard uncertainties $u_c(\cdot)$

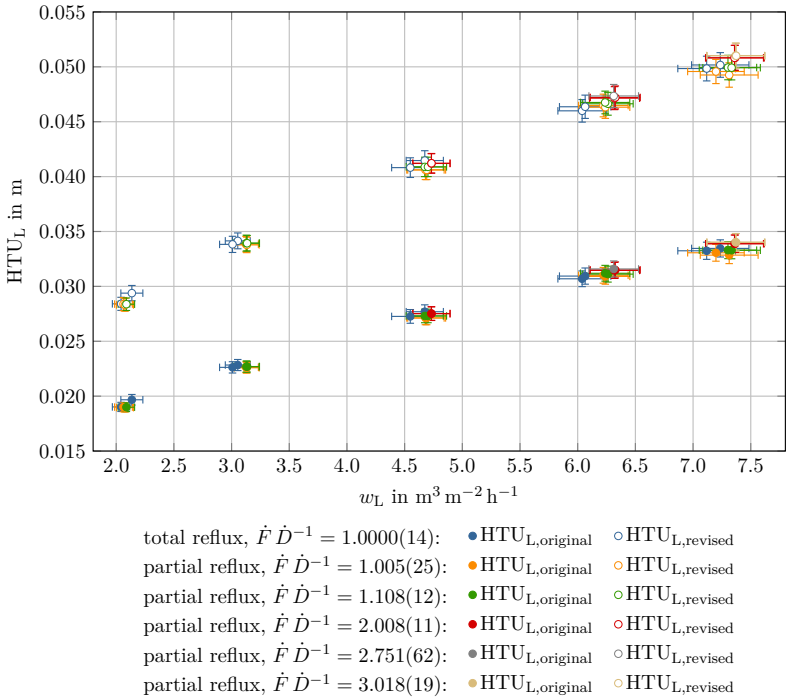

Figure F.16.: $\mathrm{HTU_L}$ predicted with Delft model in dependence of liquid load w_L and molar stream ratio $\dot{F}\,\dot{D}^{-1}$, indicated uncertainties are combined standard uncertainties $u_\mathrm{c}(\cdot)$

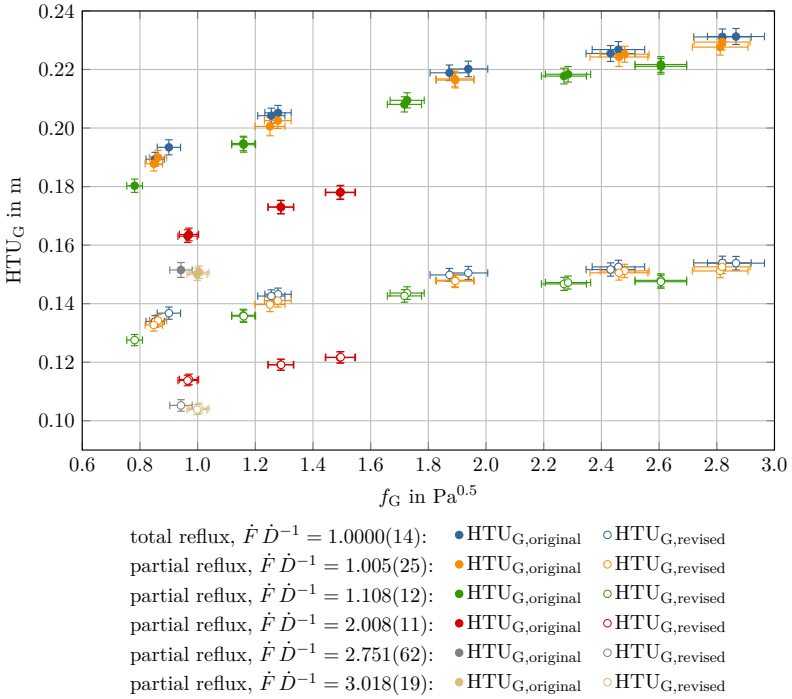

Figure F.17.: $\mathrm{HTU_G}$ predicted with Delft model in dependence of f-factor f_G and molar stream ratio $\dot{F}\,\dot{D}^{-1}$, indicated uncertainties are combined standard uncertainties $u_\mathrm{c}(\cdot)$

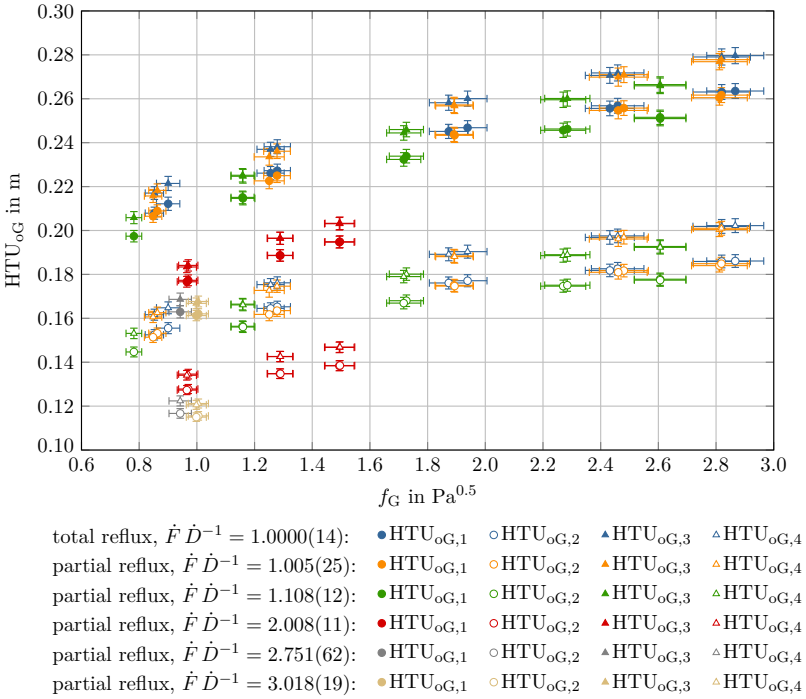

Figure F.18.: $\mathrm{HTU_{oG}}$ predicted with Delft model in dependence of f-factor f_G and molar stream ratio $\dot{F}\,\dot{D}^{-1}$, see table 4.3 for index notation of $\mathrm{HTU_{oG}}$, indicated uncertainties are combined standard uncertainties $u_c(\cdot)$

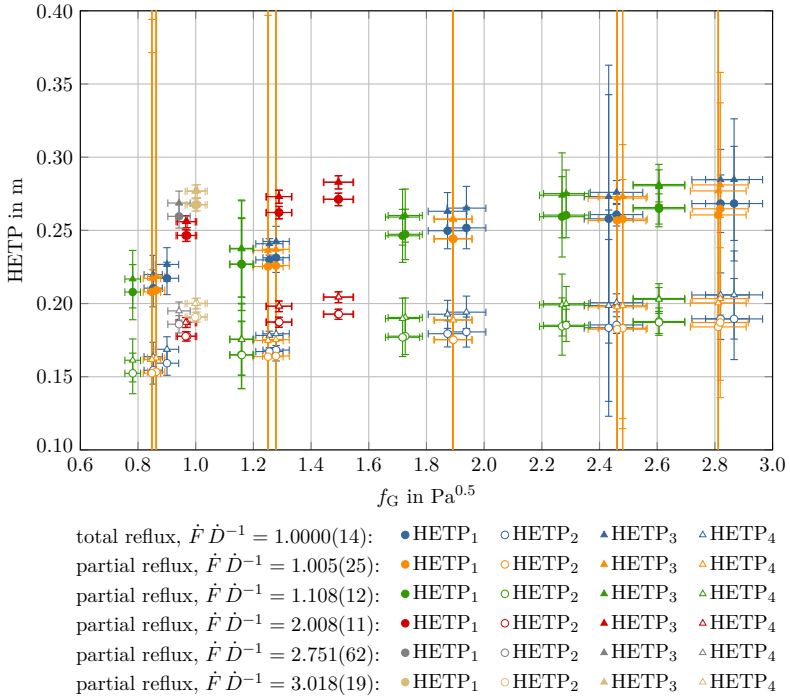

Figure F.19.: HETP predicted with Delft model in dependence of f-factor f_G and molar stream ratio $\dot{F}\,\dot{D}^{-1}$, see table 4.3 for index notation of HETP, indicated uncertainties are combined standard uncertainties $u_c(\cdot)$

G. Scientific Dissemination

G.1. Journals

Peer-Reviewed Contributions

Gutperl, S., Wolke, M., Jasch, K. and Scholl, S. (2022). "Separation Efficiency Measurements with Non-Volatile Components and Elevated Feed Viscosities". *Chemical Engineering and Technology* 45(8), pages 1414–1423. DOI: 10.1002/ceat.202200063.

Other Written Contributions

Gutperl, S., Jasch, K. and Scholl, S. (2020). "Trennleistungsmessungen der Rektifikation bei erhöhter Viskosität". *Chemie Ingenieur Technik* 92(9), page 1310. DOI: 10.1002/cite.202055113.

Gutperl, S. and Scholl, S. (2018). "Charakterisierung geeigneter Stoffgemische für Trennleistungsmessungen bei erhöhten Viskositäten". *Chemie Ingenieur Technik* 90(9), page 1315. DOI: 10.1002/cite.201855395.

G.2. Conferences

Presentations

Bolenz, L., Gutperl, S., Toye, D., Scholl, S. and Kenig, E. (2020). "Beschreibung der Rektifikation viskoser Systeme mit Hydrodynamischen Analogien". Jahrestreffen der ProcessNet-Fachgruppe Fluidverfahrenstechnik. Berchtesgaden.

Gutperl, S., Bolenz, L., Kriese, F., Jasch, K., Kenig, E. and Scholl, S. (2020). "Simulation und Bewertung eines Anlagenkonzeptes für Trennleistungsmessungen mit nicht-verdampfenden Komponenten". Jahrestreffen der ProcessNet-Fachgruppe Fluidverfahrenstechnik. Berchtesgaden.

Gutperl, S., Dierking, G., Bradtmöller, C. and Scholl, S. (2019). "Trennleistungsmessungen mit Stoffgemischen erhöhter Viskosität und nicht-verdampfenden Komponenten". Jahrestreffen der ProcessNet-Fachgruppe Fluidverfahrenstechnik. Potsdam.

Gutperl, S., Jasch, K. and Scholl, S. (2021a). "Betriebsverhalten eines neuartigen Anlagenkonzeptes für Trennleistungsmessungen mit viskosen Stoffgemischen". Jahrestreffen der ProcessNet-Fachgruppe Fluidverfahrenstechnik. Digital conference.

Gutperl, S., Jasch, K. and Scholl, S. (2021b). "Distillative separation efficiency measurements with non-volatile components at elevated viscosities". International Congress of Chemical and Process Engineering. Digital conference.

Gutperl, S., Jasch, K. and Scholl, S. (2021c). "Separation efficiencies at elevated mixture viscosities". 13th European Congress of Chemical Engineering and 6th European Congress of Applied Biotechnology. Digital conference.

Gutperl, S. and Scholl, S. (2018). "Charakterisierung geeigneter Stoffgemische für Trennleistungsmessungen bei erhöhten Viskositäten". ProcessNet-Jahrestagung. Aachen.

Gutperl, S. and Scholl, S. (2019). "Separation Efficiency Measurements for Viscous Mixtures". Current Topics on Packed Columns (Workshop). Liège.

Gutperl, S., Wolke, M., Jasch, K. and Scholl, S. (2023). "From viscous distillation to separation performance measurements at finite reflux ratios". 14th European Congress of Chemical Engineering and 7th European Congress of Applied Biotechnology. Berlin.

Poster

Gutperl, S., Bender, M., Jasch, K. and Scholl, S. (2020a). "Ein neuartiges Anlagenkonzept für Trennleistungsmessungen viskoser Stoffgemische mit nicht-verdampfenden Komponenten". Jahrestreffen der ProcessNet-Fachgemeinschaft Prozess-, Apparate- und Anlagentechnik. Digital conference.

Gutperl, S., Bradtmöller, C. and Scholl, S. (2018). "Verweilzeitmessungen zur fluiddynamischen Charakterisierung der Flüssigkeitsströmung in Packungskolonnen". Jahrestreffen der ProcessNet-Fachgruppe Fluidverfahrenstechnik. München.

Gutperl, S., Jasch, K. and Scholl, S. (2020b). "Stoffeigenschaften polymerhaltiger Stoffgemische für Trennleistungsmessungen bei erhöhter Viskosität". Jahrestreffen der ProcessNet-Fachgruppe Fluidverfahrenstechnik. Berchtesgaden.

Gutperl, S., Jasch, K. and Scholl, S. (2020c). "Trennleistungsmessungen der Rektifikation bei erhöhter Viskosität". ProcessNet-Jahrestagung. Digital conference.

Gutperl, S., Jasch, K. and Scholl, S. (2022). "Conducting Distillative Separation Efficiency Measurements with Elevated Feed Viscosities". 12th International Conference on Distillation and Absorption. Toulouse.

G.3. Research Data

Gutperl, S. and Wolke, M. (2024). *Separation Performance Measurements in Distillation: Finite and Infinite Reflux Ratio Operation - Data Evaluation Code and Results*. Research Data and Code. Braunschweig. DOI: 10.24355/dbbs.084-202407021136-0.

H. Supervised Students

H.1. Student Assistants

Table H.1.: Supervised student assistants

name	activity
Julian Dege	method development for sample analysis, distillation plant experiments
Gerrit Dierking	distillation plant commissioning
Renan Louro Cardoso Franco	mixture characterization, method development for sample analysis, distillation plant experiments
Lara-Marie Harting	distillation plant commissioning
Julia Hilbig	method development for sample analysis
Angela Kirchner	mixture characterization
Mathias Kirstein	process simulations, method development for sample analysis, data evaluation
Karoline Knospe	mixture characterization
Marie Kraus	mixture characterization, distillation plant experiments
Jara Leerkamp	mixture characterization
Hannes Schneider	distillation plant commissioning
Franziska Schwanz	mixture characterization
Friederike Schwarzer	process simulations
Luisa Stegemann	mixture characterization
Hanna Wiese	mixture characterization
Paul Wunder	method development for sample analysis

H.2. Student Theses

Bender, M. (2020). “Performance testing a plant concept for separation efficiency measurements of viscous mixtures with non-volatile components”. Student research internship.

Dierking, G. (2019). “Commissioning and performance testing a distillation plant for separation efficiency measurements of viscous mixtures”. Master’s thesis.

Kraus, M.-J. (2021). “Testing and characterization of a novel pilot plant for separation efficiency measurements of viscous mixtures with non-volatile components”. Master’s thesis.

Kriese, F. (2019). “Separation efficiency measurements for viscous mixtures – flow sheet simulation of a new process design”. Student research project.

Paruzel, N. (2019). “Developing and establishing a surface tension measurement routine for diluted solvent-based polymer solutions”. Bachelor’s thesis.

Wolke, M. (2021). “Quantifying the polymer influence on VLE and separation efficiency of a solvent mixture in distillation processes”. Master’s thesis.

Wolke, M. (2022). “Testing and characterization of a novel pilot plant for separation efficiency measurements with finite reflux ratio”. Student internship.

Bibliography

Abrams, D. S. and Prausnitz, J. M. (1975). "Statistical thermodynamics of liquid mixtures: A new expression for the excess Gibbs energy of partly or completely miscible systems". *AIChE Journal* 21(1), pages 116–128. DOI: 10.1002/aic.690210115.

Acros Organics (2022). *Certificates of Analysis*. URL: https://www.acros.com/portal/alias__Rainbow/lang__en/tabID__43/DesktopDefault.aspx (visited on September 2, 2022).

Amundson, N. R., Pontinen, A. J. and Tierney, J. W. (1959). "Multicomponent distillation on a large digital computer: II. Generalization with side-stream stripping". *AIChE Journal* 5(3), pages 295–300. DOI: 10.1002/aic.690050309.

Amundson, N. R. and Pontinen, A. J. (1958). "Multicomponent Distillation Calculations on a Large Digital Computer". *Industrial and Engineering Chemistry* 50(5), pages 730–736. DOI: 10.1021/ie50581a025.

Anton Paar (2021). *Reference Guide DMA 4100 M*. instrument software version: from 2.98, document number: XDLIB016EN-J. Graz.

Ashour, M. A., Neukäufer, J., Sarajlic, N., Klein, H., Rehfeldt, S., Paschold, J., Knösche, C. and Grützner, T. (2022). "Flexible 3D-Printed Test Rig for Liquid Distribution Characterization of Laboratory-Scale Packings". *Chemie Ingenieur Technik* 94(7), pages 1010–1016. DOI: 10.1002/cite.202200031.

Atkins, P. and Paula, J. de (2006). *Physical Chemistry*. 8th edition. W.H. Freeman: New York.

Bartolucci, A., Singh, K. P. and Bae, S. (2016). *Introduction to Statistical Analysis of Laboratory Data*. Wiley: Hoboken/NJ.

Bell, S. (2001). *NPL Good Practice Guide No. 11: The Beginner's Guide to Uncertainty of Measurement*. 2nd edition. National Physical Laboratory: Teddington/UK.

Beneke, D., Peters, M., Glasser, D. and Hildebrandt, D. (2013). *Distillation Process Design Using Column Profile Maps*. John Wiley & Sons: Hoboken/NJ.

Bennett, K. and Pilling, M. (2003). "Efficiency benefits of high performance structured packings". Texas Technology Showcase. Houston/TX.

Berg, J. C. (1988). "The Effect of Surface-Active Agents in Distillation Processes". *Surfactants in Chemical/Process Engineering*. Edited by D. T. Wasan, M. E. Ginn and D. O. Shah. Routledge: New York. Chapter 2. DOI: 10.1201/9780203737750-2.

Bezanson, J., Edelman, A., Karpinski, S. and Shah, V. B. (2017). "Julia: A fresh approach to numerical computing". *SIAM Review* 59(1), pages 65–98. DOI: 10.1137/141000671.

Billet, R. (1979). *Distillation engineering*. Translated by M. Wulfinghoff. Chemical Publishing Company: New York.

Billet, R. (1989). *Packed column analysis and design*. Ruhr University Bochum, Department for Thermal Separation Processes.

Billet, R. (1995). *Packed towers*. Translated by J. W. Fullarton. VCH: Weinheim. DOI: 10.1002/3527605983.

BIPM, IEC, IFCC, ILAC, ISO, IUPAC, IUPAP and OIML (2008a). *Evaluation of measurement data - Guide to the expression of uncertainty in measurement*. Joint Committee for Guides in Metrology, JCGM 100:2008.

BIPM, IEC, IFCC, ILAC, ISO, IUPAC, IUPAP and OIML (2008b). *Evaluation of measurement data - Supplement 1 to the Guide to the expression of uncertainty in measurement: Propagation of distributions using a Monte Carlo method*. Joint Committee for Guides in Metrology, JCGM 101:2008.

BIPM, IEC, IFCC, ILAC, ISO, IUPAC, IUPAP and OIML (2009). *Evaluation of measurement data - An introduction to the Guide to the expression of uncertainty in measurement and related documents*. Joint Committee for Guides in Metrology, JCGM 104:2009.

BIPM, IEC, IFCC, ILAC, ISO, IUPAC, IUPAP and OIML (2011). *Evaluation of measurement data - Supplement 2 to the Guide to the expression of uncertainty in measurement: Extension to any number of output quantities*. Joint Committee for Guides in Metrology, JCGM 102:2011.

BIPM, IEC, IFCC, ILAC, ISO, IUPAC, IUPAP and OIML (2012a). *Evaluation of measurement data - The role of measurement uncertainty in conformity assessment*. Joint Committee for Guides in Metrology, JCGM 106:2012.

BIPM, IEC, IFCC, ILAC, ISO, IUPAC, IUPAP and OIML (2012b). *International vocabulary of metrology - Basic and general concepts and associated terms (VIM)*. Joint Committee for Guides in Metrology, JCGM 200:2012. (3rd edition).

BIPM, IEC, IFCC, ILAC, ISO, IUPAC, IUPAP and OIML (2020). *Guide to the expression of uncertainty in measurement - Part 6: Developing and using measurement models*. Joint Committee for Guides in Metrology, JCGM GUM-6:2020.

Bittorf, L., Reichmann, F., Schmalenberg, M., Soboll, S. and Kockmann, N. (2019). "Equipment and Separation Units for Flow Chemistry Applications and Process Development". *Chemical Engineering and Technology* 42(10), pages 1985–1995. DOI: 10.1002/ceat.201900120.

Böcker, S. and Ronge, G. (2005). "Distillation of Viscous Systems". *Chemical Engineering and Technology* 28(1), pages 25–28. DOI: 10.1002/ceat.200407050.

Boggs, P. T. and Rogers, J. E. (1990). "Orthogonal Distance Regression". *Contemporary Mathematics* 112, pages 183–194.

Bolenz, L., Ehlert, T., Dechert, C., Bertling, R. and Kenig, E. (2021). "Modelling of a continuous distillation process with finite reflux ratio using the hydrodynamic analogy approach". *Chemical Engineering Research and Design* 172, pages 99–108. DOI: 10.1016/j.cherd.2021.05.025.

Bradtmöller, C. (2017). *Einfluss erhöhter Viskosität auf die Trennleistung von strukturierten Packungen in der Rektifikation*. Dissertation. TU Braunschweig, Cuvillier: Göttingen.

Bradtmöller, C., Janzen, A., Crine, M., Toye, D., Kenig, E. and Scholl, S. (2015). "Influence of Viscosity on Liquid Flow Inside Structured Packings". *Industrial and Engineering Chemistry Research* 54(10), pages 2803–2815. DOI: 10.1021/ie502015y.

Bradtmöller, C. and Scholl, S. (2015). "Geometry and viscosity effects on separation efficiency in distillation". *Chemical Engineering Research and Design* 99, pages 75–86. DOI: 10.1016/j.cherd.2015.03.013.

Bradtmöller, C. and Scholl, S. (2016). "Proposal for a Viscous Test Mixture—Densities, Viscosities, and Vapor-Liquid Equilibrium Data of the Binary Mixture 2-Methyl-2-butanol + 2-Methyl-1-propanol". *Journal of Chemical and Engineering Data* 61(1), pages 272–285. DOI: 10.1021/acs.jced.5b00537.

Cai, T. (2014). "Column Performance Testing Procedures". *Distillation: Operation and Applications*. Edited by A. Górak and H. Schoenmakers. Academic Press: London. Chapter 3, pages 103–154. DOI: 10.1016/B978-0-12-386876-3.00003-X.

Cai, Y., Yang, C., Xu, D. and Gui, W. (2018). "Baseline correction for Raman spectra using penalized spline smoothing based on vector transformation". *Analytical Methods* 10(28), pages 3525–3533. DOI: 10.1039/c8ay00914g.

Carrillo, F., Martín, A. and Roselló, A. (2000). "A Shortcut Method for the Estimation of Structured Packings HEPT in Distillation". *Chemical Engineering and Technology* 23(5), pages 425–428.

Chilton, T. H. and Colburn, A. P. (1935). "Distillation and Absorption in Packed Columns. A Convenient Design and Correlation Method". *Industrial and Engineering Chemistry* 27(3), pages 255–260. DOI: 10.1021/ie50303a004.

Čmelíková, T., Valenz, L., Vachková, E. L. and Rejl, F. (2021). "Basic separation efficiency and hydraulic data of MellapakPlus 452.Y structured packing under distillation conditions". *Chemical Engineering Research and Design* 172, pages 175–185. DOI: 10.1016/j.cherd.2021.05.026.

Colburn, A. P. (1939). "The Simplified Calculations of Diffusional Processes. General Considerations of Two-Film Resistances". *Transactions of the American Institute of Chemical Engineers* 35(2), pages 211–236.

Colburn, A. P. (1941). "Simplified Calculation of Diffusional Processes". *Industrial and Engineering Chemistry* 33(4), pages 459–467. DOI: 10.1021/ie50376a008.

Coskun, A. and Oosterhuis, W. P. (2020). "Statistical distributions commonly used in measurement uncertainty in laboratory medicine". *Biochemia medica* 30(1), pages 5–17. DOI: 10.11613/bm.2020.010101.

Coulson, E. A. and Herington, E. F. G. (1948). "Fractional distillation. I. The selection of test mixtures for estimating the efficiency of fractionating columns". *Transactions of the Faraday Society* 44, pages 629–636. DOI: 10.1039/tf9484400629.

Deibele, L. and Brandt, H.-W. (1985). "Fehlerbetrachtung bei der Messung der theoretischen Bodenzahl von Destillationskolonnen". *Chemie Ingenieur Technik* 57(5), pages 439–442. DOI: 10.1002/cite.330570510.

Dejean, B., Meyer, M. and Rouzineau, D. (2020). "Design and conception of an innovative packing for separation column - Part I: Hydrodynamic study on wire intersections". *Chemical Engineering Research and Design* 160, pages 11–19. DOI: 10.1016/j.cherd.2020.05.006.

Deldossi, L. and Zappa, D. (2009). "ISO 5725 and GUM: comparison and comments". *Accreditation and Quality Assurance* 14(3), pages 159–166. DOI: 10.1007/s00769-008-0478-3.

DIN EN 60584-1:2014-07 (2014). *Thermocouples - Part 1: EMF specifications and tolerances (IEC 60584-1:2013); German version EN 60584-1:2013*. Technical report. Berlin: DIN Deutsches Institut für Normung.

DIN EN 60751:2009-05 (2009). *Industrial platinum resistance thermometers and platinum temperature sensors (IEC 60751:2008); German version EN 60751:2008*. Technical report. Berlin: DIN Deutsches Institut für Normung.

DIN ISO 2768-1:1991-06 (1991). *General tolerances; tolerances for linear and angular dimensions without individual tolerance indications; identical with ISO 2768-1:1989*. Technical report. Berlin: DIN Deutsches Institut für Normung.

Dullien, F. A. L. (1971). "Statistical Test of Vignes' Correlation of Liquid-Phase-Diffusion Coefficients". *Industrial and Engineering Chemistry Fundamentals* 10(1), pages 41–49. DOI: 10.1021/i160037a009.

Duss, M. and Taylor, R. (2018). "Predict Distillation Tray Efficiency". *CEP Magazine*.

Düssel, R. and Stichlmair, J. (2006). "Rektifikation". *Fluidverfahrenstechnik*. Edited by R. Goedecke. Wiley: Weinheim. Chapter 8, pages 689–798.

Eckert, J. S. and Walter, L. F. (1964). "What Affects Packed Bed Distillation". *Hydrocarbon Processing* 43(2), pages 107–114.

Edmister, W. C. (1957). "Absorption and stripping-factor functions for distillation calculation by manual- and digital-computer methods". *AIChE Journal* 3(2), pages 165–171. DOI: 10.1002/aic.690030207.

Edwards, J. E. (2013). *Optimize Batch Distillation*. URL: https://www.chemicalprocessing.com/print/content/11344226 (visited on April 6, 2023).

Ellison, S. L. R. and Williams, A., editors (2012). *Eurachem/CITAC guide: Quantifying Uncertainty in Analytical Measurement*. 3rd edition. Eurachem: Gembloux.

Endress + Hauser (2004). *cerabar S Drucktransmitter Betriebsanleitung*. Weil am Rhein.

Fair, J. R., Steinmeyer, D. E., Penney, W. R. and Crocker, B. B. (2008). "Absorption". *Perry's Chemical Engineers' Handbook*. Edited by D. W. Green and R. H. Perry. 8th edition. McGraw-Hill: New York. Chapter 13, pages 14-1–14-98.

Fair, J. R. (2001). "Distillation". *Kirk-Othmer Encyclopedia of Chemical Technology*. Wiley. DOI: 10.1002/0471238961.0409192006010918.a01.pub2.

Fairley, T. (1907). "The Early History of Distillation". *Journal of the Institute of Brewing* 13(6), pages 559–582. DOI: 10.1002/j.2050-0416.1907.tb02205.x.

Farrance, I. and Frenkel, R. (2012). "Uncertainty of measurement: A review of the rules for calculating uncertainty components through functional relationships". *The Clinical Biochemist Reviews* 33(2), pages 49–75.

Fenske, M. R. (1932). "Fractionation of Straight-Run Pennsylvania Gasoline". *Industrial and Engineering Chemistry* 24(5), pages 482–485. DOI: 10.1021/ie50269a003.

Fisher Scientific (2022a). *Certificate of Analysis Toluene*. URL: https://www.fishersci.de/chemicalProductData_uk/coa?&itemCode=T/2306/17&batch=2180112&Submit=Search (visited on February 22, 2022).

Fisher Scientific (2022b). *Safety Data Sheet Toluene*. URL: https://www.fishersci.de/store/msds?partNumber=10040500&countryCode=DE&language=en (visited on February 22, 2022).

Flagiello, D., Parisi, A., Lancia, A. and Natale, F. D. (2021). "A Review on Gas-Liquid Mass Transfer Coefficients in Packed-Bed Columns". *ChemEngineering* 5(3), page 43. DOI: 10.3390/chemengineering5030043.

Fuller, E. N., Ensley, K. and Giddings, J. C. (1969). "Diffusion of halogenated hydrocarbons in helium. The effect of structure on collision cross sections". *The Journal of Physical Chemistry* 73(11), pages 3679–3685. DOI: 10.1021/j100845a020.

Fuller, E. N. and Giddings, J. C. (1965). "A Comparison of Methods for Predicting Gaseous Diffusion Coefficients". *Journal of Chromatographic Science* 3(7), pages 222–227. DOI: 10.1093/chromsci/3.7.222.

Fuller, E. N., Schettler, P. D. and Giddings, J. C. (1966). "New Method for Prediction of Binary Gas-Phase Diffusion Coefficients". *Industrial and Engineering Chemistry* 58(5), pages 18–27. DOI: 10.1021/ie50677a007.

Gmehling, J. (2003). *Grundoperationen*. Wiley: Weinheim.

Gmehling, J. and Kleiber, M. (2014). "Vapor-Liquid Equilibrium and Physical Properties for Distillation". *Distillation: Fundamentals and Principles*. Edited by A. Górak and E. Sorensen. Academic Press: Amsterdam. Chapter 2, pages 45–95. DOI: 10.1016/b978-0-12-386547-2.00002-8.

Gmehling, J., Kleiber, M., Kolbe, B. and Rarey, J. (2019). *Chemical Thermodynamics for Process Simulation*. 2nd edition. Wiley: Weinheim.

Górak, A. and Olujić, Ž., editors (2014). *Distillation: Equipment and Processes*. Academic Press: Amsterdam. DOI: 10.1016/C2010-0-66923-9.

Górak, A. and Schoenmakers, H., editors (2014). *Distillation: Operation and Applications*. Academic Press: London. DOI: 10.1016/C2010-0-67739-X.

Graf, K. (2011). *Determining Packing Height With Accuracy*. URL: https://www.chemengonline.com/determining-packing-height-with-accuracy/ (visited on March 11, 2023).

Grykałowska, A., Kowal, A. and Szmyrka-Grzebyk, A. (2015). "The basics of calibration procedure and estimation of uncertainty budget for meteorological temperature sensors". *Meteorological Applications* 22(S1), pages 867–872. DOI: 10.1002/met.1527.

Gutperl, S. (2016). "Fluid dynamic characterization of a packed column based on residence time measurements". Master's thesis. TU Braunschweig / TU Clausthal.

Gutperl, S. and Scholl, S. (2018). "Charakterisierung geeigneter Stoffgemische für Trennleistungsmessungen bei erhöhten Viskositäten". *Chemie Ingenieur Technik* 90(9), page 1315. DOI: 10.1002/cite.201855395.

Gutperl, S. and Wolke, M. (2024). *Separation Performance Measurements in Distillation: Finite and Infinite Reflux Ratio Operation - Data Evaluation Code and Results*. Research Data and Code. Braunschweig. DOI: 10.24355/dbbs.084-202407021136-0.

Gutperl, S., Wolke, M., Jasch, K. and Scholl, S. (2022). "Separation Efficiency Measurements with Non-Volatile Components and Elevated Feed Viscosities". *Chemical Engineering and Technology* 45(8), pages 1414–1423. DOI: 10.1002/ceat.202200063.

Haan, A. B. de, Eral, H. B. and Schuur, B. (2020). *Industrial Separation Processes*. 2nd edition. De Gruyter: Berlin. DOI: 10.1515/9783110654806-202.

Hall, B. D. (2022). "The GUM Tree Calculator: A Python Package for Measurement Modelling and Data Processing with Automatic Evaluation of Uncertainty". *Metrology* 2(1), pages 128–149. DOI: 10.3390/metrology2010009.

Hands, C. H. G. and Whitt, F. R. (1951). "Design of packed distillation columns. IV. An empirical method for the estimation of column height using the H.E.T.P. concept". *Journal of Applied Chemistry* 1(3), pages 135–140. DOI: 10.1002/jctb.5010010309.

Harris, C. R., Millman, K. J., Walt, S. J. van der, Gommers, R., Virtanen, P., Cournapeau, D., Wieser, E., Taylor, J., Berg, S., Smith, N. J., Kern, R., Picus, M., Hoyer, S., Kerkwijk, M. H. van, Brett, M., Haldane, A., Río, J. F. del, Wiebe, M., Peterson, P., Gérard-Marchant, P., Sheppard, K., Reddy, T., Weckesser, W., Abbasi, H., Gohlke, C. and Oliphant, T. E. (2020). "Array programming with NumPy". *Nature* 585(7825), pages 357–362. DOI: 10.1038/s41586-020-2649-2.

Harrison, M. E. (1990). "Consider three-phase distillation in packed columns". *Chemical Engineering Progress* 86, pages 80–85.

Kaibel, B. (2014). "Dividing-Wall Columns". *Distillation: Equipment and Processes*. Edited by A. Górak and Ž. Olujić. Academic Press: Amsterdam. Chapter 5, pages 183–199. DOI: 10.1016/B978-0-12-386878-7.00005-X.

Katayama, T. and Yoshida, F. (1968). "Relationship between H.E.T.P. and H.T.U." *Journal of Chemical Engineering of Japan* 1(1), pages 42–44. DOI: 10.1252/jcej.1.42.

Kenig, E. Y. (2022). "State-of-the-Art Modeling of Separation Columns: A Review". *Chemical Engineering Transactions* 94, pages 325–330. DOI: 10.3303/CET2294054.

Kenig, E. Y. and Blagov, S. (2014). "Modeling of Distillation Processes". *Distillation: Fundamentals and Principles*. Edited by A. Górak and E. Sorensen. Academic Press: Amsterdam. Chapter 10, pages 383–436. DOI: 10.1016/b978-0-12-386547-2.00010-7.

Kern & Sohn (2021). *Operating instructions precision/compact balances and platform scales KERN 572/573/KB/DS/FKB*. URL: https://dok.kern-sohn.com/manuals/files/English/572-573-kb-ds-fkb-ba-e-2176.pdf (visited on August 19, 2022).

Keysight Technologies (2020). *Technical Overview 34970A Data Acquisition/Switch Unit Family*. URL: https://www.keysight.com/us/en/assets/7018-06839/technical-overviews/5965-5290.pdf (visited on June 4, 2023).

King, C. J. (1980). *Separation Processes*. 2nd edition. McGraw-Hill: New York.

Kirkup, L. and Frenkel, R. B. (2006). *An Introduction to Uncertainty in Measurement*. Cambridge University Press: Cambridge. DOI: 10.1017/cbo9780511755538.

Kiss, A. A. (2013). *Advanced Distillation Technologies*. Wiley: Chichester.

Kiss, A. A. and Maleta, V. N. (2018). "Cyclic distillation technology - a new challenger in fluid separations". *Chemical Engineering Transactions* 69, pages 823–828. DOI: 10.3303/CET1869138.

Kiss, A. A., Maleta, V. N., Shevchenko, A. and Bedryk, O. (2021). *Cyclic distillation: A novel enhanced technology for processing hydrocarbons and derivatives*. URL: https://www.hydrocarbonprocessing.com/magazine/2021/january-2021/special-focus-sustainability/cyclic-distillation-a-novel-enhanced-technology-for-processing-hydrocarbons-and-derivatives (visited on April 6, 2023).

Kister, H. Z. (1990). *Distillation Operation*. McGraw-Hill: Boston/MA.

Kister, H. Z. (1992). *Distillation Design*. McGraw-Hill: Boston/MA.

Kleiber, M. (2020). *Process Engineering Addressing the Gap Between Study and Chemical Industry*. 2nd edition. De Gruyter: Berlin. DOI: 10.1515/9783110657685-201.

Kockmann, N. (2014). "History of Distillation". *Distillation: Fundamentals and Principles*. Edited by A. Górak and E. Sorensen. Academic Press: Amsterdam. Chapter 1, pages 1–43. DOI: 10.1016/B978-0-12-386547-2.00001-6.

Koshy, T. D. and Rukovena, F. (1986). "Reflux and surface tension effects on distillation". *Hydrocarbon Processing* 65.

Kraume, M. (2020). *Transportvorgänge in der Verfahrenstechnik*. 3rd edition. Springer: Berlin. DOI: 10.1007/978-3-662-60012-2.

Krohne Messtechnik (2016). *OPTIMASS 3400 Handbook*. serial no.: G170000000314171. URL: https://pick.krohne.com/ (visited on August 19, 2022).

Lam, S. K., Pitrou, A. and Seibert, S. (2015). "Numba: a LLVM-based Python JIT compiler". *Proceedings of the Second Workshop on the LLVM Compiler Infrastructure in HPC*. LLVM '15. Association for Computing Machinery: Austin, Texas. DOI: 10.1145/2833157.2833162.

Lebigot, E. O. (2017). *Uncertainties: A Python package for calculations with uncertainties*. URL: https://pythonhosted.org/uncertainties/ (visited on August 11, 2022).

Lee, J. W., Hauan, S. and Westerberg, A. W. (2000). "Extreme conditions in binary reactive distillation". *AIChE Journal* 46(11), pages 2225–2236. DOI: 10.1002/aic.690461114.

Levey, M. (1955). "Evidences of ancient distillation, sublimation and extraction in mesopotamia". *Centaurus* 4(1), pages 23–33. DOI: 10.1111/j.1600-0498.1955.tb00466.x.

Liley, P. E., Thomson, G. H., Friend, D. G., Daubert, T. E. and Buck, E. (2008). "Physical and Chemical Data". *Perry's Chemical Engineers' Handbook*. Edited by D. W. Green and R. H. Perry. 8th edition. McGraw-Hill: New York. Chapter 2, pages 2-1–2-204.

Lockett, M. J., Victor, R. A. and Billingham, J. F. (2006). "Structured Packing Flooding: Its Measurement and Prediction". *IChemE Symposium Series* 152, pages 400–408.

Lubin, M., Dowson, O., Garcia, J. D., Huchette, J., Legat, B. and Vielma, J. P. (2023). "JuMP 1.0: recent improvements to a modeling language for mathematical optimization". *Mathematical Programming Computation* 15, pages 581–589. DOI: 10.1007/s12532-023-00239-3.

Mahajan, A. R. and Mirgane, S. R. (2013). "Excess Molar Volumes and Viscosities for the Binary Mixtures of n-Octane, n-Decane, n-Dodecane, and n-Tetradecane with Octan-2-ol at 298.15 K". *Journal of Thermodynamics* 2013. DOI: 10.1155/2013/571918.

Manivannan, R. G., Cai, T., McCarley, K., Vennavelli, A. and Aichele, C. P. (2020). "Evaluation of the validity of tray and point efficiency correlations at elevated liquid viscosities and proposal of an improved point efficiency correlation". *Chemical Engineering Research and Design* 159, pages 27–35. DOI: 10.1016/j.cherd.2020.03.022.

Manivannan, R. G., Mohammad, S., McCarley, K., Cai, T. and Aichele, C. P. (2019). "A New Test System for Distillation Efficiency Experiments at Elevated Liquid Viscosities: Vapor–Liquid Equilibrium and Liquid Viscosity Data for Cyclopentanol + Cyclohexanol". *Journal of Chemical and Engineering Data* 64(2), pages 696–705. DOI: 10.1021/acs.jced.8b00929.

Manning, R. E. and Cannon, M. R. (1957). "Distillation Improvement by Control of Phase Channeling in Packed Columns". *Industrial and Engineering Chemistry* 49(3), pages 347–349. DOI: 10.1021/ie51392a022.

Mas, V. (2008). *ViTables: a GUI for PyTables*. URL: https://vitables.org/ (visited on April 12, 2024).

McCabe, W. L. and Thiele, E. W. (1925). "Graphical Design of Fractionating Columns". *Industrial and Engineering Chemistry* 17(6), pages 605–611. DOI: 10.1021/ie50186a023.

McKinney, W. (2010). "Data Structures for Statistical Computing in Python". *Proceedings of the 9th Python in Science Conference*. Edited by S. van der Walt and J. Millman, pages 56–61. DOI: 10.25080/Majora-92bf1922-00a.

Meier, R., Ruffert, G., Spriewald, J., Heimann, F., Kobus, A., Proplesch, R. and Stubbe, A. (2003). *Scale-up von Destillationskolonnen: Kolonnendurchmesser 50 mm – eine unüberwindbare Grenze*. Fachausschuss Thermische Zerlegung von Gas- und Flüssigkeitsgemischen. Weimar.

Meier, W., Hunkeler, R. and Stöcker, W.-D. (1979). "Sulzer Mellapak - Eine neue, geordnete Packung für Stoffaustausch-Apparate". *Chemie Ingenieur Technik* 51(2), pages 119–122. DOI: 10.1002/cite.330510210.

Mendes, M. F. (2011). "HETP Evaluation of Structured and Randomic Packing Distillation Column". *Mass Transfer in Chemical Engineering Processes*. Edited by J. Markoš. IntechOpen: Rijeka. Chapter 3, pages 41–68. DOI: 10.5772/19671.

Meurer, A., Smith, C. P., Paprocki, M., Čertík, O., Kirpichev, S. B., Rocklin, M., Kumar, A., Ivanov, S., Moore, J. K., Singh, S., Rathnayake, T., Vig, S., Granger, B. E., Muller, R. P., Bonazzi, F., Gupta, H., Vats, S., Johansson, F., Pedregosa, F., Curry, M. J., Terrel, A. R., Roučka, Š., Saboo, A., Fernando, I., Kulal, S., Cimrman, R. and Scopatz, A. (2017). "SymPy: symbolic computing in Python". *PeerJ Computer Science* 3, e103. DOI: 10.7717/peerj-cs.103.

Mix, T., Dweck, J., Weinberg, M. and Armstrong, R. (1978). "Energy Conservation in Distillation". *CEP Magazine*.

Molzahn, M. and Schmidt, R. (1975). "Belastungskennfelder von Trennkolonnen". *Verfahrenstechnik* 9(8), pages 388–395.

Moran, S. (2017). *Process Plant Layout*. 2nd edition. Elsevier: Oxford.

Morris, G. A. (1960). "The application of absorption tower design methods to packed distillation columns". *Proceedings of the International Symposium on Distillation*. Edited by P. A. Rottenburg, page 146.

Murphree, E. V. (1925a). "Graphical Rectifying Column Calculations". *Industrial and Engineering Chemistry* 17(9), pages 960–964. DOI: 10.1021/ie50189a033.

Murphree, E. V. (1925b). "Rectifying Column Calculations". *Industrial and Engineering Chemistry* 17(7), pages 747–750. DOI: 10.1021/ie50187a044.

National Center for Biotechnology Information (2021a). *PubChem Compound Summary for Chlorobenzene (CID 7964)*. URL: https://pubchem.ncbi.nlm.nih.gov/compound/Chlorobenzene (visited on December 8, 2021).

National Center for Biotechnology Information (2021b). *PubChem Compound Summary for Ethylbenzene (CID 7500)*. URL: https://pubchem.ncbi.nlm.nih.gov/compound/Ethylbenzene (visited on December 8, 2021).

National Center for Biotechnology Information (2022). *PubChem Compound Summary for Toluene (CID 1140)*. URL: https://pubchem.ncbi.nlm.nih.gov/compound/Toluene (visited on February 22, 2022).

National Institute of Standards and Technology (2023a). *NIST Chemistry WebBook Benzene, chloro-*. URL: https://webbook.nist.gov/cgi/cbook.cgi?ID=C108907&Units=SI&Mask=4#Thermo-Phase (visited on July 18, 2023).

National Institute of Standards and Technology (2023b). *NIST Chemistry WebBook Ethylbenzene*. URL: https://webbook.nist.gov/cgi/cbook.cgi?ID=C100414&Mask=4#Thermo-Phase (visited on July 18, 2023).

Neukäufer, J., Ashour, M. A., Sarajlic, N., Klein, H., Rehfeldt, S., Hallmann, H., Meinicke, S., Paschold, J., Knösche, C. and Grützner, T. (2022). "Development of enhanced three-

dimensional printed packings for scale-up of distillation columns: A successful case study". *AIChE Journal* 69(3), e17902. DOI: 10.1002/aic.17902.

Neukäufer, J., Sarajlic, N., Klein, H., Rehfeldt, S., Hallmann, H., Knösche, C. and Grützner, T. (2021). "Flexible distillation test rig on a laboratory scale for characterization of additively manufactured packings". *AIChE Journal* 67(11), e17381. DOI: 10.1002/aic.17381.

Niemeier, W. and Tengen, D. (2020). "Stochastic Properties of Confidence Ellipsoids after Least Squares Adjustment, Derived from GUM Analysis and Monte Carlo Simulations". *Mathematics* 8(8), page 1318. DOI: 10.3390/math8081318.

Olujić, Ž. (2008). *Standardization of Structured Packing Efficiency Measurements*. URL: https://aiche.confex.com/aiche/s08/techprogram/P105208.HTM (visited on March 28, 2023).

Olujić, Ž. (2014). "Types of Distillation Column Internals". *Distillation: Equipment and Processes*. Edited by A. Górak and Ž. Olujić. Academic Press: Amsterdam. Chapter 1, pages 1–34. DOI: 10.1016/b978-0-12-386878-7.00001-2.

Olujić, Ž., Behrens, M., Colli, L. and Paglianti, A. (2004). "Predicting the efficiency of corrugated sheet structured packings with large specific surface area". *Chemical and Biochemical Engineering Quarterly* 18(2), pages 89–96.

Olujić, Ž., Behrens, M. and Spiegel, L. (2007). "Experimental Characterization and Modeling of the Performance of a Large-Specific-Area High-Capacity Structured Packing". *Industrial and Engineering Chemistry Research* 46(3), pages 883–893. DOI: 10.1021/ie051146f.

Olujić, Ž., Kamerbeek, A. B. and de Graauw, J. (1999). "A corrugation geometry based model for efficiency of structured distillation packing". *Chemical Engineering and Processing: Process Intensification* 38(4), pages 683–695. DOI: https://doi.org/10.1016/S0255-2701(99)00068-9.

Olujić, Ž., Rietfort, T., Jansen, H., Kaibel, B., Zich, E., Frey, G., Ruffert, G. and Zielke, T. (2012). "Experimental Characterization and Modeling of High Performance Structured Packings". *Industrial and Engineering Chemistry Research* 51(11), pages 4414–4423. DOI: 10.1021/ie202585t.

Olujić, Ž. and Seibert, A. F. (2014). "Predicting the Liquid Phase Mass Transfer Resistance of Structured Packings". *Chemical and Biochemical Engineering Quarterly* 28(4), pages 409–424. DOI: 10.15255/cabeq.2014.19344.

Onda, K., Takeuchi, H. and Okumoto, Y. (1968). "Mass transfer coefficients between gas and liquid phases in packed columns". *Journal of Chemical Engineering of Japan* 1(1), pages 56–62. DOI: 10.1252/jcej.1.56.

Onken, U. and Arlt, W. (1990). *Recommended Test Mixtures for Distillation Columns*. 2nd edition. The Institution of Chemical Engineers: Rugby, England.

Orlando, A. E., Medina, L. C., Mendes, M. F. and Nicolaiewsky, E. M. A. (2009). "HETP evaluation of structured packing distillation column". *Brazilian Journal of Chemical Engineering* 26(3), pages 619–633. DOI: 10.1590/s0104-66322009000300017.

Ottenbacher, M., Olujić, Ž., Adrian, T., Jödecke, M. and Großmann, C. (2011). "Structured packing efficiency - Vital information for the chemical industry". *Chemical Engineering Research and Design* 89(8), pages 1427–1433. DOI: 10.1016/j.cherd.2011.02.012.

Pallets Organization (2014). *Click: A Python package for creating beautiful command line interfaces*. URL: https://click.palletsprojects.com/ (visited on November 14, 2021).

Pandas Development Team (2021). *pandas-dev/pandas: Pandas*. DOI: 10.5281/zenodo.7018966.

Peacock, D. G. (1967). "The selection of test mixtures for distillation columns". *Chemical Engineering Science* 22(7), pages 957–961. DOI: 10.1016/0009-2509(67)80160-x.

Peters, G. M., Sandin, G. and Spak, B. (2019a). "Environmental Prospects for Mixed Textile Recycling in Sweden". *Sustainable Chemistry and Engineering* 7(13), pages 11682–11690. DOI: 10.1021/acssuschemeng.9b01742.

Peters, G., Spak, B. and Sandin, G. (2019b). *LCA on recycling of blended fiber fabrics*. Technical report. Gothenburg: Chalmers University of Technology.

Peters, W. A. (1922). "The Efficiency and Capacity of Fractionating Columns". *Journal of Industrial and Engineering Chemistry* 14(6), pages 476–479. DOI: 10.1021/ie50150a002.

Pigford, R. L. and Colburn, A. P. (1950). "Packed Distillation Columns". *Perry's Chemical Engineers' Handbook*. Edited by J. H. Perry. 3rd edition. McGraw-Hill: New York. Chapter 9, pages 618–621.

Poling, B. E., Prausnitz, J. M. and O'Connell, J. P. (2001). *The properties of gases and liquids*. 5th edition. McGraw-Hill: New York.

Preißinger, U., Ränger, L.-M. and Grützner, T. (2019). "Design Considerations of a Simplified Multiple Dividing Wall Column Pilot Plant". *ChemEngineering* 3(2), page 34. DOI: 10.3390/chemengineering3020034.

Prohaska, T., Irrgeher, J., Benefield, J., Böhlke, J. K., Chesson, L. A., Coplen, T. B., Ding, T., Dunn, P. J. H., Gröning, M., Holden, N. E., Meijer, H. A. J., Moossen, H., Possolo, A., Takahashi, Y., Vogl, J., Walczyk, T., Wang, J., Wieser, M. E., Yoneda, S., Zhu, X.-K. and Meija, J. (2022). "Standard atomic weights of the elements 2021 (IUPAC Technical Report)". *Pure and Applied Chemistry* 94(5), pages 573–600. DOI: 10.1515/pac-2019-0603.

PyTables Developers Team (2002). *PyTables: Hierarchical Datasets in Python*. URL: https://www.pytables.org/ (visited on April 12, 2024).

Python Software Foundation (2022). *Python: Welcome to Python*. URL: https://www.python.org/ (visited on August 26, 2022).

Rasmussen, J. B., Mansouri, S. S., Zhang, X., Abildskov, J. and Huusom, J. K. (2020). "A mass and energy balance stage model for cyclic distillation". *AIChE Journal* 66(8), e16259. DOI: 10.1002/aic.16259.

Redlich, O. and Kister, A. T. (1948a). "Algebraic representation of thermodynamic properties and the classification of solutions". *Industrial and Engineering Chemistry* 40(2), pages 345–348. DOI: 10.1021/ie50458a036.

Redlich, O. and Kister, A. T. (1948b). "Thermodynamics of Nonelectrolyte Solutions - x-y-t relations in a Binary System". *Industrial and Engineering Chemistry* 40(2), pages 341–345. DOI: 10.1021/ie50458a035.

Reitze, A., Grünewald, M. and Riese, J. (2020). "Comparison of the Operating Range of a Wetted-Wall Column with a Packed Column for Distillation". *Chemie Ingenieur Technik* 92(12), pages 1968–1975. DOI: 10.1002/cite.202000065.

Renon, H. and Prausnitz, J. M. (1968). "Local compositions in thermodynamic excess functions for liquid mixtures". *AIChE Journal* 14(1), pages 135–144. DOI: 10.1002/aic.690140124.

Rieks, S., Preusser, N., Gambaryan-Roisman, T. and Kenig, E. (2018). "Zero-Gravity Distillation with Metal Foams: A Modelling Approach". *Chemical Engineering Transactions* 69, pages 283–288. DOI: 10.3303/CET1869048.

Sarajlic, N., Stadler, M., Ashour, M. A., Neukäufer, J., Grützner, T., Paschold, J., Knösche, C., Klein, H. and Rehfeldt, S. (2022). "Untersuchung der Flüssigkeitsverteilung in additiv gefertigten strukturierten Laborpackungen". *Chemie Ingenieur Technik* 94(7), pages 1002–1009. DOI: 10.1002/cite.202200024.

Sartorius (2022). *Product Datasheet Practum Laboratory Balances*. URL: https://www.sartorius.com/shop/medias/Practum-Laboratory-Balances.pdf?context=bWFzdGVyfGRvY3VtZW50c3w5MzMxOTN8YXBwbGljYXRpb24vcGRmfGRvY3VtZW50cy9oNTEvaGJjLzkxOTk1MjgxMTYyNTQucGRmfGZkNjJhNmY5YTdkODE4YzQxZTFlMzRkN2JhNjgwMzJiOWM1YzgxNDU2NzFlZGZhOTQ2MWY1NDM1NmU3ZjYyOWM (visited on May 15, 2023).

Sartorius Industrial Scales (2014). *Combics complete scales CAWP*. URL: http://www.blakeandboughton.co.uk/DS-CAWP-Complete_Scales-e.pdf (visited on August 19, 2022).

Sattler, K. (2001). *Thermische Trennverfahren*. 3rd edition. Wiley: Weinheim.

Scheller, G. and Krummeck, S. (2018). *Measurement Uncertainty of a Temperature Measuring Chain*. Technical report. Fulda: JUMO GmbH & Co. KG.

Schlumberger (2021). *PUREMEG Monoethylene glycol reclamation and regeneration system*. URL: https://www.slb.com/-/media/files/osf/brochure/puremeg-br.ashx (visited on April 6, 2023).

Schmit, C. E., Perkins, J. and Eldridge, R. B. (2004). "Investigation of X-ray imaging of vapor–liquid contactors. 2. Experiments and simulations of flows in an air–water contactor". *Chemical Engineering Science* 59(6), pages 1267–1283. DOI: https://doi.org/10.1016/j.ces.2004.01.001.

Schoenmakers, H. and Spiegel, L. (2014). "Laboratory Distillation and Scale-up". *Distillation: Equipment and Processes*. Edited by A. Górak and Ž. Olujić. Academic Press: Amsterdam. Chapter 10, pages 319–339. DOI: 10.1016/b978-0-12-386878-7.00010-3.

Schönbucher, A. (2002). *Thermische Verfahrenstechnik Grundlagen und Berechnungsmethoden für Ausrüstungen und Prozesse*. Springer: Berlin. DOI: 10.1007/978-3-642-56308-9.

Schultes, M. (2013). "Research on Mass Transfer Columns: passé?" *Chemical Engineering and Technology* 36(9), pages 1539–1549. DOI: 10.1002/ceat.201300192.

Seader, J. D. and Henley, E. J. (2011). *Separation Process Principles*. 3rd edition. Wiley: Hoboken/NJ.

Seader, J. D., Siirola, J. J. and Barnicki, S. D. (2008). "Distillation". *Perry's Chemical Engineers' Handbook*. Edited by D. W. Green and R. H. Perry. 8th edition. McGraw-Hill: New York. Chapter 13, pages 13-1–13-108.

Sherwood, T. K., Pigford, R. L. and Wilke, C. R. (1975). *Mass Transfer*. 3rd edition. Chemical Engineering Series. McGraw-Hill: New York.

Shokrkar, H. and Salem, A. (2008). "Effect of Structured Packing Characteristics on Styrene Monomer/Ethylbenzene Distillation Process". *Chemical Engineering and Technology* 31(10), pages 1453–1461. DOI: 10.1002/ceat.200800058.

Skiborowski, M. and Górak, A., editors (2022). *Process Intensification by Rotating Packed Beds*. 2nd edition. De Gruyter: Berlin. DOI: 10.1515/9783110724998.

Sorensen, E., Lam, K. F. and Sudhoff, D. (2014). "Special Distillation Applications". *Distillation: Operation and Applications*. Edited by A. Górak and H. Schoenmakers. Academic Press: London. Chapter 9, pages 367–401. DOI: 10.1016/b978-0-12-386876-3.00009-0.

Sorensen, E. (2014). "Principles of Binary Distillation". *Distillation: Fundamentals and Principles*. Edited by A. Górak and E. Sorensen. Academic Press: Amsterdam. Chapter 4, pages 145–185. DOI: 10.1016/b978-0-12-386547-2.00004-1.

Sosa, A., Ortega, J., Fernández, L., Pacheco, J. M., Wisniak, J. and Romero, A. (2019). "Further Advance to a Practical Methodology To Assess Vapor-Liquid Equilibrium Data: Influence on Binaries Rectification". *Journal of Chemical and Engineering Data* 64(9), pages 3933–3944. DOI: 10.1021/acs.jced.9b00344.

Spiegel, L. and Duss, M. (2014). "Structured Packings". *Distillation: Equipment and Processes*. Edited by A. Górak and Ž. Olujić. Academic Press: Amsterdam. Chapter 4, pages 145–181. DOI: 10.1016/B978-0-12-386878-7.00004-8.

Spiegel, L. and Meier, W. (2003). "Distillation Columns with Structured Packings in the Next Decade". *Chemical Engineering Research and Design* 81(1), pages 39–47. DOI: 10.1205/026387603321158177.

Spiegel, L. (2018). "The maldistribution story - an industrial perspective". *Chemical Engineering Transactions* 69, pages 715–720. DOI: 10.3303/CET1869120.

Starkweather, B., Agrawal, P. D. and Fisher, J., editors (2014). *AIChE Equipment Testing Procedure: Trayed and Packed Columns*. Wiley: Hoboken/NJ. DOI: 10.1002/9781118860250.

Staud, R., Sun, Z., Xu, S., Scholl, S. and Jasch, K. (2023). "Fluid dynamic and separation performance of foam loaded packed distillation columns". *Chemical Engineering Research and Design* 193, pages 801–809. DOI: 10.1016/j.cherd.2023.04.006.

Stec, M., Tatarczuk, A., Śpiewak, D. and Wilk, A. (2014). "Densities, Excess Molar Volumes, and Thermal Expansion Coefficients of Aqueous Aminoethylethanolamine Solutions at Temperatures from 283.15 to 343.15 K". *Journal of Solution Chemistry* 43(5), pages 959–971. DOI: 10.1007/s10953-014-0175-2.

Steffen, V. and da Silva, E. A. (2017). "Steady-State Modeling of Equilibrium Distillation". *Distillation - Innovative Applications and Modeling*. Edited by M. F. Mendes. IntechOpen: London. Chapter 1, pages 3–30. DOI: 10.5772/66833.

Stichlmair, J. G., Klein, H. and Rehfeldt, S. (2021). *Distillation: Principles and Practice*. 2nd edition. John Wiley & Sons: Hoboken/NJ.

Taylor, R. and Kooijman, H. A. (2014). "Mass Transfer in Distillation". *Distillation: Fundamentals and Principles*. Edited by A. Górak and E. Sorensen. Academic Press: Amsterdam. Chapter 3, pages 97–143. DOI: 10.1016/b978-0-12-386547-2.00003-x.

Trouton, F. (1884). "IV. On molecular latent heat". *The London, Edinburgh, and Dublin Philosophical Magazine and Journal of Science* 18(110), pages 54–57. DOI: 10.1080/14786448408627563.

Tsai, R. E., Schultheiss, P., Kettner, A., Lewis, J. C., Seibert, A. F., Eldridge, R. B. and Rochelle, G. T. (2008). "Influence of Surface Tension on Effective Packing Area". *Industrial and Engineering Chemistry Research* 47(4), pages 1253–1260. DOI: 10.1021/ie0707801.

Tsai, R. E., Seibert, A. F., Eldridge, R. B. and Rochelle, G. T. (2009). "Influence of viscosity and surface tension on the effective mass transfer area of structured packing". *Energy Procedia* 1(1), pages 1197–1204. DOI: 10.1016/j.egypro.2009.01.157.

Valenz, L., Haidl, J. and Linek, V. (2013). "The Effect of Column Diameter and Packing Height on the Pressure Drop and on the HETP of Structured Packings". *Industrial and Engineering Chemistry Research* 52(17), pages 5967–5974. DOI: 10.1021/ie302397q.

VDI 2761 Part 2 (2020). *Chemical separation processes - Measurement and evaluation of fluid dynamics and mass transfer in packed columns: Absorption and desorption*. Technical report. Düsseldorf: Verein Deutscher Ingenieure.

Veen, A. M. H. van der, Meija, J., Possolo, A. and Hibbert, D. B. (2016). *Guidelines for the Use of Atomic Weights*. Technical report. Research Triangle Park/NC: International Union of Pure and Applied Chemistry.

Veen, A. M. H. van der, Meija, J., Possolo, A. and Hibbert, D. B. (2021). "Interpretation and use of standard atomic weights (IUPAC Technical Report)". *Pure and Applied Chemistry* 93(5), pages 629–646. DOI: 10.1515/pac-2017-1002.

VEGA Grieshaber (2014). *Betriebsanleitung VEGADIF 34 ... 51*. Schiltach.

Vignes, A. (1966). "Diffusion in Binary Solutions. Variation of Diffusion Coefficient with Composition". *Industrial and Engineering Chemistry Fundamentals* 5(2), pages 189–199. DOI: 10.1021/i160018a007.

Virtanen, P., Gommers, R., Oliphant, T. E., Haberland, M., Reddy, T., Cournapeau, D., Burovski, E., Peterson, P., Weckesser, W., Bright, J., van der Walt, S. J., Brett, M., Wilson, J., Millman, K. J., Mayorov, N., Nelson, A. R. J., Jones, E., Kern, R., Larson, E., Carey, C. J., Polat, İ., Feng, Y., Moore, E. W., VanderPlas, J., Laxalde, D., Perktold, J., Cimrman, R., Henriksen, I., Quintero, E. A., Harris, C. R., Archibald, A. M., Ribeiro, A. H., Pedregosa, F., van Mulbregt, P. and SciPy 1.0 Contributors (2020). "SciPy 1.0: Fundamental Algorithms for

Scientific Computing in Python". *Nature Methods* 17, pages 261–272. DOI: 10.1038/s41592-019-0686-2.

Vogelpohl, A. (2021). *Distillation: The Theory*. 2nd edition. De Gruyter: Berlin.

Wächter, A. and Biegler, L. T. (2006). "On the implementation of an interior-point filter line-search algorithm for large-scale nonlinear programming". *Mathematical Programming* 106(1), pages 25–57. DOI: 10.1007/s10107-004-0559-y.

Wang, G. Q., Yuan, X. G., Tang, Z. L., Chen, J. B. and Yu, K. T. (2005a). "A Shortcut Method for Estimating the HETP of Structured Packed Distillation Columns at Elevated Pressure". *Chemical Engineering and Technology* 28(7), pages 767–772. DOI: 10.1002/ceat.200500065.

Wang, G. Q., Yuan, X. G. and Yu, K. T. (2005b). "Review of Mass-Transfer Correlations for Packed Columns". *Industrial and Engineering Chemistry Research* 44(23), pages 8715–8729. DOI: 10.1021/ie050017w.

Weiß, S., editor (1996). *Thermisches Trennen*. 2nd edition. Deutscher Verlag für Grundstoffindustrie: Stuttgart.

Wende, M., Fischer, F. and Kenig, E. Y. (2021). "Numerical and Experimental Investigation of Zero-Gravity Distillation Units". *Chemical Engineering Transactions* 88, pages 697–702. DOI: 10.3303/CET2188116.

Wilke, C. R. and Chang, P. (1955). "Correlation of diffusion coefficients in dilute solutions". *AIChE Journal* 1(2), pages 264–270. DOI: 10.1002/aic.690010222.

Willingham, C. B. and Sedlak, V. A. (1950). "Test Mixtures for Distillation at Atmospheric and Reduced Pressure". *Journal of Research of the National Bureau of Standards* 45(4), pages 315–317.

Wilson, G. M. (1964). "Vapor-Liquid Equilibrium. XI. A New Expression for the Excess Free Energy of Mixing". *Journal of the American Chemical Society* 86(2), pages 127–130. DOI: 10.1021/ja01056a002.

Wisniak, J. (1993). "A new test for the thermodynamic consistency of vapor-liquid equilibrium". *Industrial and Engineering Chemistry Research* 32(7), pages 1531–1533. DOI: 10.1021/ie00019a030.

Wisniak, J., Ortega, J. and Fernández, L. (2017). "A fresh look at the thermodynamic consistency of vapour-liquid equilibria data". *The Journal of Chemical Thermodynamics* 105, pages 385–395. DOI: 10.1016/j.jct.2016.10.038.

Wübbeler, G. (2012). *Messunsicherheitsbestimmung nach GUM S2 - Beliebige Zahl von Ausgangsgrößen*. 266. PTB-Seminar "Berechnung der Messunsicherheit". Berlin.

Yuan, H.-C. and Spiegel, L. (1982). "Theoretical and Experimental Investigation of the Influence of Maldistribution on the Performance of Packed Columns at Partial Reflux". *Chemie Ingenieur Technik* 54(8), pages 774–775. DOI: 10.1002/cite.330540820.

Zeck, S. (1990). "Einfluss von thermophysikalischen Stoffdaten auf die Auslegung und den Betrieb von Destillationskolonnen". *Chemie Ingenieur Technik* 62(9), pages 707–717. DOI: 10.1002/cite.330620904.

Zuiderweg, F. J., Hoek, P. J. and Lahm Jr., L. (1987). "The effect of liquid distribution and redistribution on the separating efficiency of packed columns". *IChemE Symposium Series* 104, A217.

ISSN 1860-1316
ISBN 978-3-68952-338-1

Cuvillier Verlag Göttingen
Internationaler wissenschaftlicher Fachverlag

Bibliografische Information der Deutschen Nationalbibliothek
Die Deutsche Nationalbibliothek verzeichnet diese Publikation in der Deutschen Nationalbibliografie; detaillierte bibliografische Daten sind im Internet über http://dnb.dnb.de abrufbar.
1. Aufl. – Göttingen: Cuvillier, 2026
Zugl.: (TU) Braunschweig, Univ., Diss., 2024

Herausgeber:
Stephan Scholl, Wolfgang Augustin
ICTV – Institut für Chemische und Thermische Verfahrenstechnik
Langer Kamp 7
38106 Braunschweig
Telefon + 49 (0)531 391 2781
Telefax + 49 (0)531 391 2792
ictv@tu-braunschweig.de
www.ictv.tu-bs.de

CUVILLIER VERLAG GmbH, Göttingen 2026
Nonnenstieg 8, 37075 Göttingen
Telefon: 0551-54724-0
Telefax: 0551-54724-21
www.cuvillier.de

Diese Publikation wurde durch Mittel aus dem Publikationsfonds NiedersachsenOPEN unterstützt, der von zukunft.niedersachsen finanziert wird.

1. Auflage, 2026
Gedruckt auf umweltfreundlichem, säurefreiem Papier aus nachhaltiger Forstwirtschaft.

ISSN 1860-1316
eISSN 3053-8300
ISBN 978-3-68952-338-1
eISBN 978-3-68952-339-8
ORCID https://orcid.org/0000-0002-6301-873X
DOI https://doi.org/10.61061/ISBN_9783689523381